RECRYSTALLISATION NUCLEATION AND MICROTEXTURE DEVELOPMENT IN ALUMINIUM–IRON ROLLED ALLOYS

By
Nicola Deards
St. Johns College, Cambridge

Department of Materials Science and Metallurgy
Pembroke Street
Cambridge
CB2 3QZ

A dissertation submitted for the degree of Doctor of Philosophy

October 1992

"I prepared myself for a multitude of reverses;
my operations might be incessantly baffled, and at least my work be imperfect:
yet, when I considered the improvement which every day takes place in science and mechanics,
I was encouraged to hope my present attempts would at least lay the foundations of future success."

Mary Shelley, *Frankenstein*

CONTENTS

Preface v

Acknowledgements vi

Abstract vii

Nomenclature and Abbreviations ix

Chapter 1: Recovery, Recrystallisation and Grain Growth

1.1 Recovery 1

1.2 Recrystallisation 2

1.2.1 *The Effect of Particles* 3

1.3 Nucleation Mechanisms 6

1.3.1 *Strain–Induced Boundary Migration* 7

1.3.2 *Subgrain Coalescence* 9

1.3.3 *SIBM versus Subgrain Coalescence* 12

1.4 Grain Growth 14

1.5 Secondary Recrystallisation 17

Chapter 2: Crystallographic Texture Development

2.1 Texture Measurement 22

2.1.1 *Transmission Electron Microscopy* 22

2.1.2 *Scanning Electron Microscopy* 24

2.1.3 *Neutron Diffraction* 25

2.2 Texture Representation 25

2.3 Grain Boundaries and Texture 32

2.4 Deformation Textures in Aluminium 34

2.5 Recrystallisation Textures 35

2.6 Oriented Growth vs Oriented Nucleation 36

2.6 Particle Deformation–Zones 39

2.7 Deformation–Zone Models 42

Chapter 3: Experimental Techniques

3.1 Experimental Programme for Al–Fe Alloys 47

3.1.1 *Alloy Chemistries* 47

3.1.2 *Rolling Schedules* 47

3.1.3 *Annealing Programmes* 47

3.2 Transmission Electron Microscopy 48

3.2.1 *Foil Preperation* 48
3.2.2 *Microscopy Methods* 48
3.2.3 *Microscope Calibration* 48
3.3 Data Interpretation 50
3.3.1 *Indexing Diffraction Data* 50
3.3.2 *Axis–Angle Pair Measurement* 50
3.4 Optical Analysis 52
3.4.1 *Specimen Preparation* 52
3.4.2 *Optical Microscopy* 52
3.5 Hardness Measurements 53
3.6 Al–Mn–Si Alloy Investigation 53

Chapter 4: Particle Deformation Zones

4.1 Recovery and Recrystallisation Kinetics 54
4.2 Particle Deformation–Zone Characterisation 64
4.3 Conclusions 77

Chapter 5: Recrystallisation Nucleation

5.1 Early Stages of Annealing 80
5.2 Preferred Nucleation–Sites 95
5.2.1 *Low Iron Content Alloy* 100
5.3 Conclusions 109

Chapter 6: Primary Recrystallisation

6.1 Later Recrystallisation Stages 110
6.2 Conclusions 130

Chapter 7: Annealing Mechanisms in a 6063 AA + Mn Alloy

7.1 Inhibition of Recrystallisation 131
7.2 Conclusions 157

Chapter 8: Conclusions and Further Work

8.1 Aluminium–Iron Alloys 159
8.2 Aluminium 6063 AA + Mn Alloy 160

References 162

Appendix 169

PREFACE

The investigation described herein was carried out under the supervision of Dr. H.K.D.H. Bhadeshia in the Department of Materials Science and Metallurgy, Cambridge, between October 1989 and August 1992.

Except where acknowledgement and reference to previous work is made, this work is, to the best of my knowledge, original and has been carried out without collaboration. Neither this nor any substantially similar dissertation has been, or is being submitted for any degree, diploma or other qualification at any other university.

This dissertation contains less than 60,000 words.

Nicola Deards

September 1992

ACKNOWLEDGEMENTS

I would like to thank Professor C.J. Humphreys for granting the use of the Department of Materials Science and Metallurgy laboratories and facilities. My grateful thanks go to Dr. H.K.D.H. Bhadeshia for his enthusiasm, encouragement and support during the project.

The technical assistance of John Leader (alloy preparation), David Duke (processing), Carol Best and Brian Barber (photography) and David Nicol (transmission electron microscopy) was much appreciated as was the financial acumen of Sara Taylor.

Thanks to the members of the Phase–Transformations group past and present for their help and friendship and also to Ian for looking after me during writing up.

My thanks also go to Dr. G. Marshall and Dr. R. Ricks at Alcan Laboratories, Banbury for their advice and to Alcan International for financial support.

My heartfelt thanks for their unfailing support go to my parents, to whom I would like to dedicate this work.

ABSTRACT

Crystallographic texture development during the thermo–mechanical processing of aluminium alloys determines their response to processing routes, such as superplastic forming or deep drawing. The research deals with a particular aspect of texture development; the role of particles in the mechanisms of recrystallisation during the heat–treatment of aluminium–iron alloys.

A series of extremely pure Al–Fe alloys containing 0.47–1.41 wt.% Fe have been studied with a view to revealing the role of $FeAl_3$ particles in stimulating recrystallisation. Transmission electron–microscopy of deformed and partially–recrystallised samples was used to characterise the deformation zones produced around the needle–like particles during deformation, and to observe the very early stages of recrystallisation. By measuring the orientations using electron diffraction, the crystallographic–orientation distributions from within particle deformation zones, which consist of highly–deformed subgrains. Recrystallisation nuclei tend to develop preferentially at the tips of the needle–shaped particles, where deformation gradients are largest. These then grow and consume the surrounding regions. The nucleation of recrystallisation was only found at particles. The evidence from transmission electron–micrographs and orientation measurements indicates that recrystallisation in these alloys occurs predominantly by a recovery mechanism. Once a recrystallisation nucleus has grown to consume the deformation zone, this recovery process is thought to be replaced by a more rapid subgrain boundary migration process, giving recrystallisation proper.

The lowest iron–content alloy, containing a low volume–fraction of particles (in thin bands aligned along the rolling–direction), behave slightly differently. Nucleation still occurs from particles, but due to the close proximity of particles within the bands, many potential nuclei are prevented from growing beyond the deformation zones. Only those nuclei at the band edges, or stranded away from bands, are capable of further growth.

A brief investigation was also carried out to study the development of an anisotropic recrystallised grain structure in a precipitate–containing Al–Mn–Si alloy. Such directional recrystallisation had previously been observed in alloys containing dispersions of oxide particles aligned along the rolling–direction, and was due to the anisotropic pinning of grain–boundaries during recrystallisation. This work investigates the mechanism which leads to the development of highly elongated grains in this alloy after deformation and isothermal heat–treatment. After deformation the alloy contains non–uniform distributions of precipitate particles, and the role of these particles in determining the morphology of the grain structure which develops on

annealing is followed using transmission–electron–microscopy techniques.

The elongated grains produced by annealing cast– and rolled–*6063 AA* originate directly from the recovery of the deformed microstructure. The anisotropy of grain structure thus arises from the flattening of the cast grains due to the rolling process. It is concluded that anisotropic pinning by dispersoids is not in the present case responsible for the development of anisotropy in the annealed microstructure.

NOMENCLATURE and ABBREVIATIONS

A	Activation energy
δA	Increase in boundary area when a volume δV is swept through by boundary
A_2	Constant
A_l	Logarithm of the angle θ at which E is a maximum
b	Burger's Vector of a dislocation
B_1	Constant
c	Constant
C_1	Constant
CSL	Coincidence site lattice
d	Spherical particle diameter
D	Grain diameter
D_a	Average grain diameter
D_{lim}	Limit of grain size after continuous grain growth
e	Base of natural logarithm (2.718)
E	Stored energy difference across boundary
E_o	Stored energy of grain boundary when $\theta = 0$
EBS	Electron back scattering
f	Volume fraction of particles in the material
ΔF	Driving force for grain boundary coalescence
f.c.c.	Face centred cubic
g	Crystal rotation in Euler space
g_i	Central (ideal) orientation of a Gaussian distribution
ΔG	Driving force for grain boundary migration (free energy per mole)
ΔG_{gn}	Free energy of growing nucleus
ΔG_i	Reduction in free energy of boundary motion due to pinning of particles
ΔG_{lb}	Free energy of low–angle boundary
ΔG_o	Driving force for grain–boundary migration at time zero
GMT	Grain Misorientation Texture
$\overline{h}$	Direction lying normal to the plane (hkl)
HV	Vickers hardness
HVEM	High voltage electron–microsopy
I	Measured intensity
I_c	Measured intensity of cube orientation
I^*	Measured intensity obtained for a standard specimen showing pure cube texture

k	Boltzmann's constant
K'	Constant for a given alloy
K''	Constant for a given alloy
K'''	Constant for a given alloy
$K_A(XYZ)$	Cube orientation co–ordinate system
$K_B(X'Y'Z')$	Crystal co–ordinate system lying parallel to K_A
K_G	Linear rate constant
K_R	Second–order recovery constant
K–W	Kronberg–Wilson boundaries
L	Radius of bulged grain–boundary
$\overline{L}$	Half–size of a subgrain wall
M	Mobility of a grain boundary
M_i	The volume fraction of a component in the Gaussian distribution
$N(*)$	Number of crystals in a particular orientation
$N(o)$	Number of crystals in the orientation o
ODF	Orientation distribution function
P_{hkl}	Pole figures by volume
$P_{\overline{h}}(y)$	Pole figure
Q_{hkl}	Pole figures by number
r	Particle radius
$\overline{r}$	Radius of a recrystallisation nucleus
R'	Diameter of a recrystallisation nucleus at the first contact between the nuclei and the surrounding particles
R_m	Mean radius of spherical grain boundary
R_r	Radius of the rotated zone around a particle
$R_y(\overline{h})$	Inverse pole figure
R_θ	Radius of a sphere containing each θ phase particle and its associated solid solution
RD	Rolling Direction
$S(\alpha°)$	Quantity of a particular orientation $\alpha°$
SACP	Selected Area Channeling Pattern
SEM	Scanning Electron Microscope
SIBM	Strain Induced Boundary Migration
t	Time
$t_{1/2}$	Time for 50 % recrystallisation
T	Temperature

T_c	Coarsening temperature
TD	Transverse direction
TEM	Transmission Electron Microscope
v	Velocity of a grain boundary
V	Volume
δV	Volume swept through by grain boundary
V_m	Molar volume
X	Fraction of recrystallised grains
y	Sample direction
Z	An axis of the crystal co–ordinates
Z'	An axis of the crystal co–ordinates after rotation
$\overline{\alpha}$	Tilting angle
$\alpha\beta$	A particular orientation in x-ray analysis
γ	Grain–boundary free–energy
γ_{lb}	Grain–boundary free–energy for a low–energy boundary
ϵ	Shear strain
ϵ_c, ϵ_c	Shear components
η_1	Geometric factor between 1 and 3
η_2	Geometric factor between 1 and 2
η_3	Geometric factor between 1 and 2
θ	Misorientation between two grains either side of a grain boundary
2θ	Angle between the incident and refracted beam in the TEM
θ_m	The angle of a boundary such that E is a maximum
θ_z	Magnitude of rotation of subgrains in the deformation zone of a particle
ρ	Dislocation density
Σ	Coincidence–site lattice–parameter
τ_n	Hardening stress due to a dispersed phase
ϕ_1, ϕ_2	Rotation of the boundary around two perpendicular axes
ϕ_1, Φ, ϕ_2	The three Euler angles lying in the boundary plane
ψ_i	The scattering width of a component of the Gaussian distribution
Ψ, Θ, Φ	Second definition of the Euler angles

Chapter 1

RECOVERY, RECRYSTALLISATION AND GRAIN GROWTH

A plastically deformed crystalline material has a large proportion of physical defects within its structure, and is therefore thermodynamically unstable. On increasing temperature the material can reduce its free energy by eliminating or rearranging these lattice defects via a number of processes. The work presented below is a survey of the current literature on the processes of recovery, recrystallisation and grain growth.

1.1 Recovery

If a specimen retains its original grain structure on an optical micrograph scale after annealing, then any physical or mechanical property changes must have been caused by recovery processes. Recovery occurs by the annihilation of point defects and dislocation dipoles, together with the rearrangement of like dislocations, giving lower energy configurations consisting of walls of dislocations, or subgrain boundaries, which lead to a break up of the original deformed grains into subgrains of almost identical orientation. This process is termed 'polygonisation', and is continuous throughout deformation, recovery and recrystallisation. It results in subgrain growth, leaving the original grain boundaries intact.

The name 'polygonisation' came from the experiments of Cahn (1949) in which single zinc crystals were bent about an axis normal to the slip direction and subsequently annealed. The crystal shape changed from a uniform curvature to a series of sharply tilted regions, with a sub–boundary at each tilt normal to the slip plane. This suggested that subgrains will form in any deformed specimen if the deformation is inhomogeneous. That is, local regions are bent even though no macroscopic bending moment is applied. Such local bending is to be expected wherever there is more than one operative slip system, and it is possible to produce sub-structures in most cubic metals after simple tensile deformation. In comparison, single crystals of hexagonal metals such as zinc can be given large deformations in single glide, and they will then recover their original properties without either recrystallisation or polygonisation mechanisms occurring.

The arrangement of polygonised dislocation walls after annealing depends largely upon the mode of deformation. More complicated deformation procedures result in more irregular dislocation arrangements. Hence the rate of formation of subgrain boundaries, and their type, depends strongly on the prior deformation.

Subgrain boundary formation is dependent upon the Burgers vectors and slip planes available for dislocation movement, and these are limited for each lattice type (Li, 1965). This means that there are only a limited number of subgrain boundaries which can be formed during

deformation. No stable dislocation networks can be formed on a slip plane in a face–centred cubic (fcc) metal from one set of slipping dislocations in that plane and another set from another slip system during deformation. However, networks can be formed on planes other than slip planes (Ball & Hirsch, 1955), and more complicated networks can be formed from dislocations of three slip systems (Ball, 1957). A few more dislocation networks can be formed if a long range stress field is present (Li, 1963a), and these will rearrange into stress–free stable networks during recovery. An example of a network formed during recovery is that which lies in the (001) plane with two sets of dislocations of [110] and $[1\bar{1}0]$ orientations. Some evidence has been found to suggest that at the intersection of these screw dislocations, small segments of dislocation of [100] Burgers vector are found (Lytton *et al.*, 1965).

Aluminium (as with some other high stacking–fault energy metals) polygonises during deformation. These observations have been amply substantiated by microbeam–analysis X-ray investigations (Keller, Hirsch & Thorp, 1950), and thin–film transmission electron microscopy (Hirsch, Horne & Whelan, 1957). When severely deformed, subgrain sizes of 2 μm may be observed at room temperature, and little or no subgrain growth occurs until temperatures of around 200°C are reached (Christian, 1965). Rather perfect subgrain structures are produced in aluminium after large deformations compared to the irregular networks observed in copper and similar metals, and the boundaries produced are much sharper. In copper at high deformations, regions relatively free from dislocations are separated by dense dislocation–walls or tangles. The high stacking fault energy of aluminium ensures a low activation energy for cross–slip. Dislocations therefore frequently cross–slip. Using vacancies formed during deformation, edge–dislocation climb may occur easily when the dislocations are not extended, and this helps to give the sharp polygonised structures.

Once a reasonably perfect structure has formed, the stored strain energy can be attributed to the surface energy of the subgrain boundaries. Subsequent subgrain growth is driven by the surface energy, and is analogous to ordinary grain growth.

1.2 Recrystallisation

Recrystallisation occurs by the absorption of defects and dislocations during grain boundary migration, and by the reduction in the total grain boundary area per unit volume.

Primary recrystallisation occurs when discrete 'nuclei' are formed which grow and consume the deformed material. The nucleus is a lattice region of a size corresponding to the deformed subgrains which is capable of growth and contains a much lower density of defects than the surrounding matrix. The nucleus is separated from the matrix by a high–energy grain boundary, the driving force for its growth being the difference in dislocation densities across the boundary (Haessner *et al.*, 1966).

In some cases, polygonisation can dissipate most of the available driving force, so that the microstructure then develops simply by the migration of subgrain boundaries, and recrystallisation proper is avoided entirely.

1.2.1 *The Effect of Particles*

It is generally found that widely spaced coarse particles enhance nucleation and rate of recrystallisation if present before deformation. Finely dispersed particles normally reduce recrystallisation kinetics with a greater retarding force on nucleation than on growth (Doherty & Martin, 1964). Recrystallisation in aluminium alloys is retarded by particles whose size and spacing are both less than approximately 0.5 μm, whereas larger particles which are coarsely dispersed, accelerate the process. In aluminium–iron systems, $FeAl_3$ particles of size 0.075 to 0.5 μm in diameter increase the dislocation density during deformation, thus decreasing the cell size and raising the wall density and misorientation. The particles anchor subgrain boundaries and junctions particles anchor sufficiently to retard migration and unravelling mechanisms and thus slow down subgrain coalescence and recrystallisation. Particles of larger than 0.6 μm in diameter are usually not shearable, and therefore matrix dislocations cannot penetrate them. As they do not change shape, the surrounding matrix flows around them, thus undergoing additional complex deformation. This results in cells much smaller than the average size adjacent to the particles, with dense, high misorientation walls. Thus these large particles act as nucleation stimulators, and promote smaller recrystallised grain sizes (Sandström, 1980). $FeAl_3$ particles in commercial aluminium add to the nucleation sites, and enhance the nucleation capacity of high–energy boundaries (Bay & Hansen, 1979). Needle–like particles which are not shearable allow the metal to flow easily around them, and are incapapable of nucleating recrystallisation. Dislocation accumulation along their length during deformation exerts bending stresses that can cause them to fracture into segments only a little longer than their diameter (McQueen *et. al.*, 1985).The fine particles thus produced lead to an increase in dislocation density during deformation and block dynamic recovery processes, giving a finer cell size with high dislocation density walls.

Elegant studies have been carried out on recrystallisation in a simple two–phase system (θ–phase dispersed in a solid solution of copper in aluminium) with a variety of particle spacings at constant matrix grain size (Doherty and Martin, 1963).

In a plot of the radius of the sphere containing each θ–particle and its associated solid solution (R_θ) against the time for 50 % recrystallisation ($t_{\frac{1}{2}}$), two different mechanisms of recrystallisation can be seen to be operating (figure *1.1*). The first linear section corresponds to those alloys which produced an acceleration in recrystallisation, and the second portion to those which produce retardation, the latter displaying a much greater sensitivity to interparticle

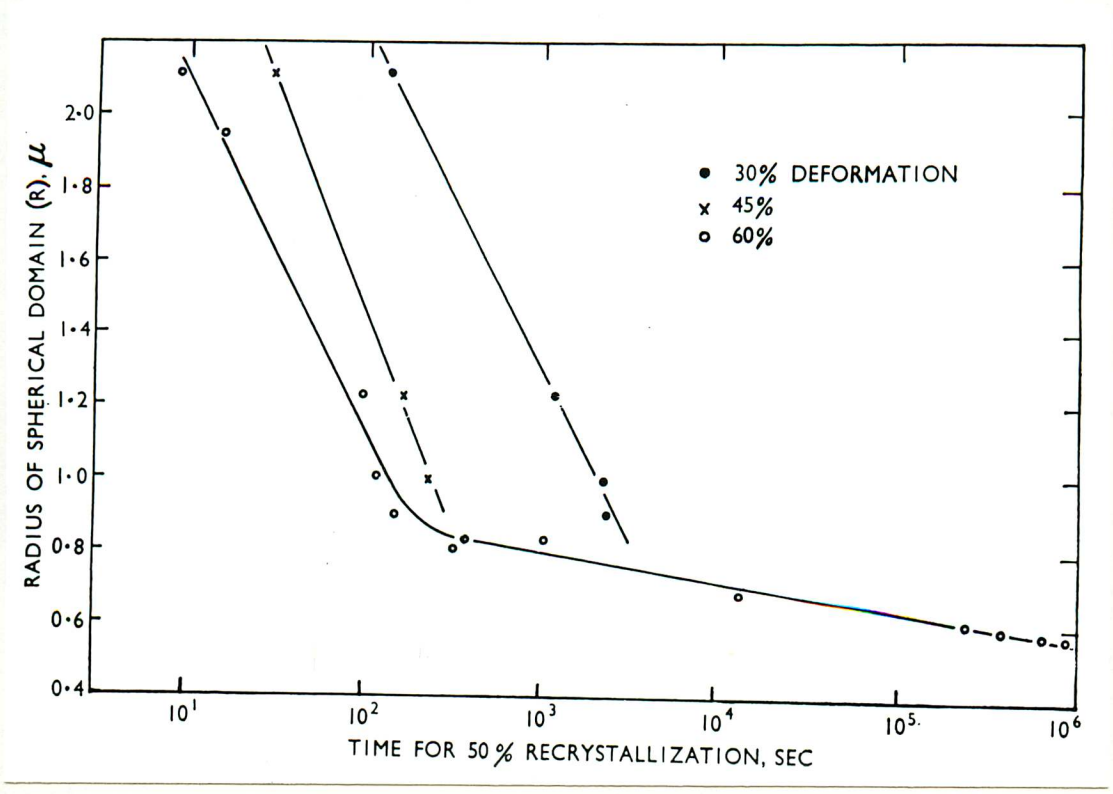

Figure 1.1 R_θ against $log_{10}t_{1/2}$ curves (Doherty and Martin, 1963).

spacing.

The recrystallisation kinetics may be considered to be influenced by three factors:

- Grain boundary pinning. The growth of new grains is retarded in proportion to f/r since this growth involves the migration of high energy grain boundaries, where f is the volume fraction of particles and r is the particle radius.
- Change in work hardening. Dew–Hughes and Robertson (1960) working on single crystals of aluminium containing dispersed θ phase, have discovered a hardening stress (τ_n) due to the presence of the dispersed phase given by

$$\tau_n = \frac{K'f}{r} \tag{1}$$

where K' is a constant for a given alloy. From this it can be predicted that the stored energy of cold work, and therefore the driving force for recrystallisation, would be given by an expression of the form

$$K'' + \frac{f}{r}K''' \tag{2}$$

where K'' and K''' are constants. It would seem that due to the opposing effects of $\frac{f}{r}$ upon the factors considered above, the rate of growth of recrystallisation nuclei would not be greatly affected by changes in the dispersion.

- Nucleation. An acceleration in nucleation rate in the presence of a coarse second phase may occur due to an increase in local lattice–curvature adjacent to the dispersed phase during

cold work. The dramatic retardation of nucleation by the presence of a fine dispersion can only be accounted for by considering the first contact between the growing nuclei and the surrounding particles. It is proposed that unless subgrain boundaries have attained a high–energy, high–mobility state before impingement on the θ phase occurs, nucleation will be difficult. From fig *1.2*, if the diameter of the nucleus is R' at this first contact (assuming a simple cubic array of particles), R' will be of the same order as R_θ, thus accounting for the fit of the points on the R_θ vs $\log t_{\frac{1}{2}}$ plot in figure *1.1*.

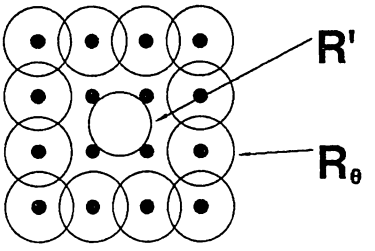

Figure 1.2 Dispersed particles in simple cubic array (black spots) showing: R_θ, spherical domain of the particle and associated solid solution; R', nucleus size at first contact with the dispersed phase (Doherty and Martin, 1963).

This theory is borne out by the transmission electron microscope images recorded in which nuclei are seen to be held up by θ particles, with each region eventually being consumed by a grain of a much larger radius of curvature. The above theory was confirmed by the experiments carried out by Doherty and Martin (1964) on artificial nucleation. As R_θ increased, the nucleation of recrystallised grains was observed to occur more easily.

For a given deformation, the rate of nucleation is always faster in two–phase alloys as compared to single phase alloys, the rate increasing with particle size. Growth rate is also increased with particle size, but to a lesser degree (Humphreys, 1977).

Humphreys (1977) used single–crystal experiments on aluminium containing 0.45 wt% Cu–0.5 wt% Si to show that after 10% recrystallisation a clear distinction could be seen between those specimens in which a substantial number of particles stimulated nucleation, and those where there was no such association. Nucleation at particles was observed to occur at high strains, with material containing larger particles. It was found that at these higher strains, the final grain size corresponded directly to the interparticle spacing.

Figure *1.3* shows the data for particle influence on recrystallisation in a graphical summary. To retard recrystallisation the necessary particle spacing decreases as particle size decreases. The effect of particles is not controlled solely by the average concentration of particles in the material studied; although many particles operate individually a strong effect due to clusters of closely spaced particles is frequently found. A further enhancement results from the fact that $FeAl_3$ particles pin the grain boundaries during the initial recrystallisation thereby increasing

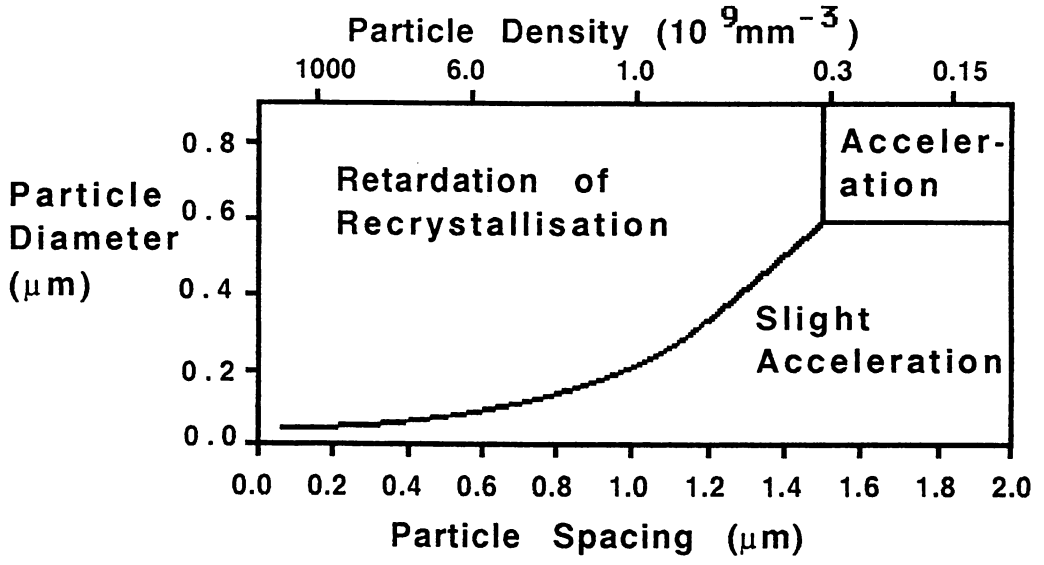

Figure 1.3 Summary of the effects of particles on recrystallisation. Only the particles sufficiently closely spaced, to the left side of the line, are able to effect retardation (McQueen, Chia and Starke, 1985).

the concentration of particles in the grain boundaries to far above the average concentrations (Bay & Hansen, 1979).

1.3 Nucleation Mechanisms

There are at present at least four suggested nucleation processes by which recrystallisation is initiated:

(a) The classical fluctuation theory by Burke and Turnbull (1952).

(b) Polygonisation, (Cahn, 1950; Beck *et al.*, 1949b).

(c) Subgrain coalescence, (Fujita, 1961; Hu, 1963).

(d) Strain induced boundary migration (Beck & Sperry, 1950; Bailey & Hirsch, 1962; Bailey, 1963,1960).

In each case, once a recrystallisation nucleus is formed, its ability to grow is dependent upon the mobility of its grain boundaries. The classical model of nucleation is based on the assumption that nuclei are formed as a result of thermal fluctuations. However, the critical nucleus size and activation energy based on this theory turn out to be unrealistically large.

Models b), c), and d) do not require the formation of a new orientation in the cold worked material. They are all variations on the same theme, distinct only in the mechanisms by which the recrystallisation nucleus is initiated. In aluminium the process of polygonisation is usually complete either by the end of the deformation process or after the early stages of annealing. It may then be expected that subgrain growth may be a problem equivalent to that

of normal grain growth where all the larger subgrains could grow at the expense of the small ones. This process, which is continuous recrystallisation or recrystallisation *in situ*, is rare. The usual process of nucleation is similar to abnormal grain growth in which only exceptional grains grow.

It is now therefore widely accepted that recrystallisation is only a growth process and that the process initiates after polygonisation. However, the definition of nucleation rate remains valid since there is an apparent incubation period found by extrapolation of experimental curves, although this may be indicative of an initial period of growth rather than of time to form a nucleus (Christian, 1965). The low angle (semi-coherent) grain boundaries are of relatively low mobility (except in special circumstances where a glissile boundary is possible), and move outwards 'picking up' individual dislocations and tangles, so that orientation of the surrounding matrix deviates increasingly from that of the recrystallised regions, giving a high angle boundary and increasing mobility.

There is some dispute as to which of the two processes, strain–induced boundary migration or subgrain coalescence, will produce the recrystallisation nuclei.

1.3.1 *Strain–Induced Boundary Migration*

Recrystallisation can begin from existing subgrains or from high energy grain boundaries present in the material before deformation. The boundary bulges to give an area of low dislocation density, and this becomes the recrystallisation nucleus. The process requires an appreciable area of grain boundary to exist, seperating an almost strain free region from the deformed matrix. Experiments have shown that there is no incubation period before bulging of the grain boundaries, and that the rate of boundary migration is highest initially and then decreases with annealing time.

Beck and Sperry (1950) have postulated a mechanism which accounts for these observations. Firstly they have assumed that the boundary is capable of high mobility by virtue of a large misorientation between the parent grain and the matrix. Secondly, they have assumed that there is a large strain difference between the two grains separated by the boundary. In these circumstances it was said that boundary migration is initiated by the part of the grain boundary which separates a large subgrain in the less strained grain from the matrix. The direction of migration is then away from this subgrain into the strained matrix. This leads to a reduction in internal energy which is equivalent to the difference between the stored energy released in the consumed region, and the energy required to extend the length of the migrating boundary. The basic driving force therefore is the difference in stored energy between the two grains.

The observations of workers such as Beck and Sperry strongly suggest that for mod-

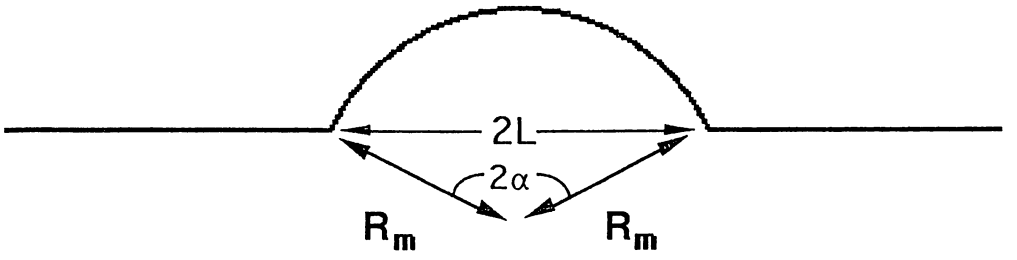

Figure 1.4 Model for grain boundary migration process (Bailey, 1960).

erate deformations, most polycrystalline metals recrystallise by this grain boundary migration mechanism. The problem therefore is to decide on the criterion for migration of the boundary. A simplified model was suggested by Bailey (1960), in which a circular area of grain boundary of diameter $2L$ bulges out into the shape of a spherical cap, as shown in figure *5.1*, and then migrates. The boundary will migrate provided that there is a difference in free energy ΔG across the boundary; that is, provided that the energy released by the migration more than compensates for the increase in the surface energy. Now the change in free energy will be given by:

$$\Delta G.\delta V = E\delta V - \gamma\delta A \tag{3}$$

where δA is the increase in boundary area when the volume δV is swept through by the grain boundary, E is the stored energy difference across the boundary, and γ is the grain boundary free energy per unit area. For migration ΔG must be positive, that is;

$$E > \gamma\frac{\delta A}{\delta V} \tag{4}$$

For the model shown in figure *1.4*

$$\frac{\delta A}{\delta V} = \frac{2\sin\alpha}{L} \tag{5}$$

Which has a maximum of $\frac{2}{L}$ when $R = L$ and hence:

$$E \geq \frac{2\gamma}{L} \tag{6}$$

Therefore, provided an area of radius larger than L moves forward there is a positive driving force. But the rate of advance of formation of the bulge depends on the nature of the migration process on an atomic scale.

The process of grain boundary migration can then be considered to proceed as follows. Migration may start at an area of boundary across which there is a fairly large difference in dislocation density. As soon as the boundary has moved, a relatively dislocation–free area is generated on one side of the boundary, and the driving force is then governed by the average

value of the stored energy. Although the stored energy of the dislocations provides the driving force for boundary migration, and produces a positive value for the free energy across the boundary, the main rate–determining factor is the activation energy which is only affected to a very small degree by the dislocations. The above model does not question the process of grain boundary migration on an atomic scale, and does not take into account any effect upon the activation process which may be caused by dislocations ending in the boundary. However, the activation energy is not expected to be greatly effected by dislocations, and can be expected to be approximately equal to that for grain boundary self–diffusion.

1.3.2 *Subgrain Coalescence*

Nielsen (1954) first proposed a mechanism of grain coalescence in secondary recrystallisation. He refers to this as 'geometrical coalescence' in which pairs of neighbouring grains (not contiguous grains) of close orientations are supposed to combine by boundary coalescence to form a recrystallisation nucleus. This process will involve no change in the initial orientation of the coalesced grains. However, Hu (1962) has observed from transmission electron microscopy that two neighbouring grains coalesce by the gradual disappearance of the boundary between them. Therefore a change in the initial orientation of the subgrains is produced.

Small angle tilt boundaries are able to coalesce by the formation of Y–junctions. This decreases the number of tilt boundaries whilst increasing the average angle of tilt, and after repetition large subgrains of high–angle boundaries are produced, capable of growth into surrounding small subgrains. Subgrain coalescence is a seperate phenomenon, and can be seen to form the basis for understanding many features in the nucleation of recrystallisation.

The free energy of a subgrain boundary, in terms of angle θ is given by

$$E = E_o\theta\,(A_l - \ln\theta) \text{ per unit area} \tag{7}$$

where E_oA_l is the free energy at $\theta = 1$, and A_l is the logarithm of the angle at which E is a maximum. Both E_o and A_l change with boundary type, and for the same E_o and A_l, two boundaries of angles θ_1 and θ_2 would coalesce into one boundary of angle $\theta_1 + \theta_2$ with the following driving force:

$$\Delta F = E_o \ln \left(\frac{\theta_1+\theta_2}{\theta_1}\right)^{\theta_1} \left(\frac{\theta_1+\theta_2}{\theta_2}\right)^{\theta_2} \text{ per unit area} \tag{8}$$

which is always positive. Thus it is always possible for boundaries of the same type to coalesce.

The subgrain coalesence theory was formulated by Hu (1962). He observed, using a hot stage in the transmission electron microscope, that in 3wt%-silicon-iron some neighbouring subgrains merged into a common orientation during recrystallisation whilst the boundary between them disappeared. The resulting subgrain was substantially larger than those surrounding it,

and its orientation differed from that of the original subgrains from which it was formed. No migration of high energy boundaries that are attached to certain polygonised subgrains was observed, and in addition, no recrystallised grains were observed prior to the completion of polygonisation. This mechanism has been observed in addition to the coalescence of subgrain boundaries by a number of workers (Fujita, 1961; Hu, 1962; Lytton *et al*, 1965). It can be seen to occur by the disappearance of boundaries between two subgrains, where the curvature of the remaining boundaries obviously suggest that the boundary did originally exist. It is thought that the mechanism occurs by the movement of dislocations away from the common sub–boundary into connecting or intersecting boundaries around the subgrains. The angular misfit of these connecting boundaries therefore increases as more subgrains coalesce, and eventually the boundary should be of a high enough energy to be capable of migration. Hence the period of incubation of recrystallisation corresponds to the time during which coalescences occur. The difference between this mechanism and that of subgrain boundary coalescence is that, in this case, it is possible to form a new orientation within the cold–worked matrix through the reorientation of existing subgrains. This accounts for recrystallisation orientations which are not present in the cold–worked matrix.

The criterion for the disappearance of a subgrain boundary, as suggested by Hu (1962), is dependent on the nature of the connecting boundaries. Subgrains which are slightly misoriented with one another are unlikely to coalesce, and this is consistent with the observation that the tendency for recrystallisation to occur is stronger in areas of less sharp deformation textures (Hu, 1959). Hence recrystallisation takes place more readily between crystallites of sufficient misorientation. In areas of a wide range of orientations an incubation period during which coalescence occurs is required.

The concept of subgrain rotation has been analysed by Li (1962a), who investigated the possibility of two subgrains being able to rotate during recrystallisation both from a thermodynamical and kinetic point of view. In his thermodynamic analysis, Li checked whether the process of rotation violated the second law of thermodynamics: *i.e.* the law that demands that the free energy of a system decrease with time. The free energy of a rotation (such as that shown in figure *1.5*) is the total free energy of all the surrounding boundaries of the rotating subgrain. Setting the size of the nth boundary as $2\overline{L}$ so that its area is $4\overline{L}^2$, and setting the free energy at E, the total free energy of all the boundaries relative to the perfect lattice is

$$\Delta F = \sum 4\overline{L}^2 E \tag{9}$$

Thus the change in free energy associated with a rotation (without any change in boundary type) is

$$\mathrm{d}\Delta F = \sum 4\overline{L}^2 E_o \ln\left(\frac{\theta_m}{\theta}\right)\mathrm{d}\theta \tag{10}$$

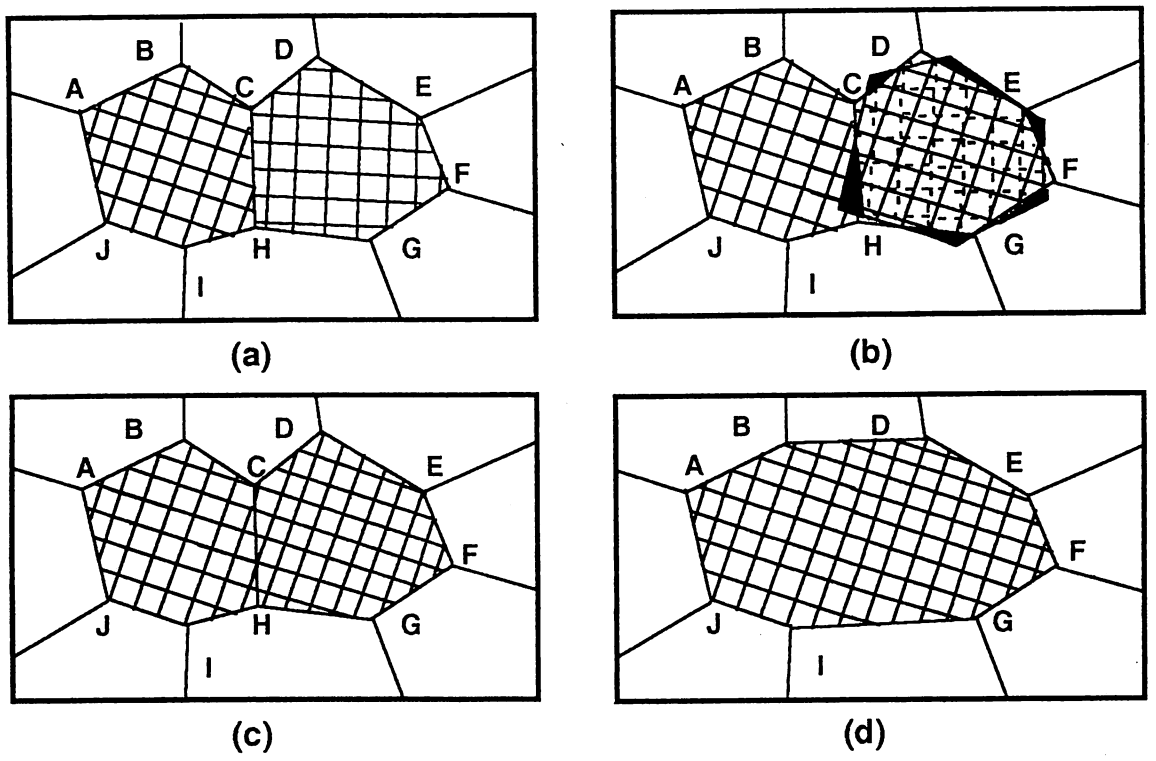

Figure 1.5 Coalescence of two subgrains by rotation of one. (a) The original subgrain structure before coalescence; (b) one subgrain undergoes a rotation; (c) the subgrain structure just after coalescence; (d) the final subgrain structure after some sub–boundary migration (Li, 1962a).

where θ_m is the angle of the nth boundary at which E is a maximum.

If the effect of the boundary type is ignored and it is assumed that the boundaries are of approximately the same size, the second law states that the following must be true:

$$\sum \ln(\theta_m/\theta)\,\mathrm{d}\theta \;<\; 0 \tag{11}$$

or

$$\pi\,(\theta_m/\theta)^{\mathrm{d}\theta} \;<\; 1 \tag{12}$$

This simplified result effectively means that rotation will occur favouring the elimination of low energy boundaries and the creation of high–energy boundaries. Both processes probably take place during recrystallisation, thus making the rotation thermodynamically possible.

Evidence supporting the subgrain coalescence theory has been found by Towner and Berger (1960) who observed an increase in subgrain boundary angle during subgrain growth of 2 to 6 minutes arc for an increase in subgrain size of x2. This is in accordance with the energetics described by Li, since under this mechanism subgrain boundaries of the smallest angle must disappear first.

Hu (1962) found that recrystallisation nuclei form preferentially in areas where a wide range of crystallographic orientations is present. It is suggested that this is because in areas of many orientations, the dislocation configurations are more complicated, and so the average distance for dislocations to move out of the boundary between the coalescing grains to other dislocation groups or subgrain boundaries will be shorter. Since there are many different orientations, the nucleated grains will also show a spread of orientations, and those grains displaying a favourable orientation for growth will consume the others. Areas in which few orientations are present lack these advantages and recrystallised grains are therefore more difficult to form.

1.3.3 *Strain Induced Boundary Migration vs Subgrain Coalescence*

In the past it has been unclear as to what is the important mechanism (or mechanisms) during nucleation, and as yet no overall view allows for the prediction of the type of nucleation which would be expected to occur in any given circumstances, and certainly no model capable of successfully predicting nucleation rates.

Bellier and Doherty (1977) found that after 40% deformation of aluminium, most new grains developed by SIBM of material either side of a transition band, which was surprising since the bands have a finite thickness of many μms. The simple model of SIBM due to Beck (1954) – that one grain with a larger subgrain size directly invades its neighbour grain which has a smaller subgrain size – does not seem capable of accounting for these results. This failure arises since a grain boundary seperating grains with subgrains of different sizes should be capable of bulging immediately into the grain with smaller substructure.

A large subgrain on one side of a transition band should only grow slowly at first since its boundary would initially be only of a low misorientation and therefore not very mobile. The boundary would have to cross the thickness of the transition band before it could acquire the full misorientation necessary for high mobility. From this it would appear that transition band SIBM would be at a disadvantage, not an advantage, with respect to grain boundary SIBM. Two–way SIBM, that is adjacent regions of the same grain boundary moving in opposite senses into the two grains, also conflicts with the classical model.

The most likely explanation for this is given by Li (1962a) in his analysis of subgrain coalescence. The process of coalescence is especially favoured adjacent to a high energy grain boundary. It is energetically favourable to eliminate a low–energy boundary by a rotation that increases the misorientation of a high energy boundary between a subgrain and its neighbour on the other side of a pre–existing high energy boundary. This has been found by Bellier and Doherty (1977).

Fujita (1961) studied subgrain growth in aluminium and found that the boundary of a recrystallised grain initially forms from the boundaries of a group of subgrains. As the

boundaries within the group disappear, vacancies and dislocations are deposited in the group boundary. Hu observed a similar process in rolled Si–Fe single crystals (Hu 1962, 1963). In this case the growth of subgrains appeared to proceed by a coalescence mechanism, with the boundary between two subgrains appearing to fade away. The process was seen to occur in parallel areas misoriented by a few degrees, termed 'microbands', which were present in the as-rolled structure. However, other workers using the same material concluded that nucleation takes place by the Cahn-Cottrell mechanism (Walter & Koch, 1962,1963). For example, Walter and Koch (1963) found that recrystallisation nuclei were initiated in transition bands, and that the new grains were of the same orientation as the sub–band from which they originated, suggesting that the nucleation occurred by sub–band boundary growth.

Michels and Rickets (1967) studied the recrystallisation of aluminium by heating cold-worked specimens in an electron microscope and producing moving pictures. This allowed the nucleation process to be traced back to its beginning in the cold-worked matrix represented in high resolution in the before-heating pictures. It was apparent from the moving pictures taken that a definite origin of the recrystallised grains during grain boundary migration and polygonisation cannot be determined since the process is rapid and is detected only after boundary migration has progressed relatively far.

Recrystallised grains were observed to originate from the smallest subgrains in the cold-worked structure, some of which displayed a zero incubation time, and their growth was rapid and non-uniform. Recrystallised grains were also observed to grow from large subgrains in the deformed specimens, but it was not possible to tell whether these subgrains were present in the as-deformed structure or had grown prior to observation. It was also found that the boundaries were high energy and that in several cases more than one nucleus contributed to the formation of one grain. The incubation periods found varied from 0 to 4 seconds and the grain boundaries migrated at between 1 and 10μm per second. This is similar to rates observed in bulk aluminium (Gordon & Vandermeer, 1962). This may be due to boundary formation and reorganisation of dislocation networks, and fine- scale boundary adjustments.

The range and distribution of misorientations among subgrains is apparently a major factor in determining the nucleation mechanism. In areas of small misorientation the subgrain coalescence model of Hu (1962, 1963) probably operates due to the low mobility of the boundaries. In regions of intermediate misorientations the Cottrell mechanism (Cahn, 1950, Cottrell, 1953) perhaps becomes important with grain boundary mobility increasing during a period of slow growth. However, in areas of high misorientations as studied by Michels and Rickets (1967), immediate and rapid boundary migration appears to be dominant.

Bay and Hansen (1984) found that the grain boundary region and the grain edges in

5 to 30% deformed aluminium were preferred sites for nucleation, although some intragranular nucleation was observed in all the specimens. Nuclei formed by SIBM were recognised since they were only partially surrounded by a high–energy boundary. Other nuclei were completely surrounded by high–energy boundaries. They were situated either on one side of a boundary or straddling it. It may be noted that nuclei surrounded by high–energy grain boundaries may arise either by growth of new orientations from a region outside of the foil, or by nucleation from a strongly misoriented region in the foil.

Both mechanisms, SIBM and subgrain coalescence, can take place at grain boundaries and grain edges, and their occurrence, either individually or in combination may explain the different types of recrystallisation nuclei observed. This contradicts Bellier and Doherty (1977) who found only SIBM. The occurrence of mechanisms other than SIBM in commercial purity aluminium as opposed to super–purity aluminium may be due to stronger pinning of grain boundaries.

1.4 Grain Growth

Grain growth can occur after the completion of primary recrystallisation. Grain growth is a term which covers a group of phenomena, which although related, have significant differences as discussed below.

The two most important forms of grain growth are 'normal' and 'abnormal'. The former occurs when the size of all the growing grains in the alloy increases uniformly with the annealing temperature. This often happens in single phase metals and solid solutions. In many alloys the addition of particular impurity elements causes 'inhibition' of grain growth due to the precipitation of fine particles. In inhibited alloys abnormal grain growth takes place, in which the grain size for a given temperature below a critical temperature T_c, is smaller than in an uninhibited alloy. Above T_c a few extremely large grains suddenly develop, mixed with regions of small grains. This is shown in figure *1.6* (Beck *et al.*, 1948) in which cobalt acts as an inhibitor in a Cu–Be alloy. An alloy containing 0.13 wt.% Co gave fine CoBe phase particles which caused inhibition, as compared to the 0.15 wt.% Co alloy which contained no such particles. The development of large grains above T_c can be seen by the vertical lines which branch off from the curve *b*, indicating a bimodal microstructure. For this reason, abnormal grain growth has also been termed 'discontinuous' (Beck *et al.*, 1948).

The dislocation density ρ is found to be inversely proportional to the annealing time t:

$$\rho^{-1} = ct \tag{13}$$

where c is a constant. These kinetics were observed for aluminium by Vandermeer and Gordon (1963), and judged to be consistent with subgrain growth.

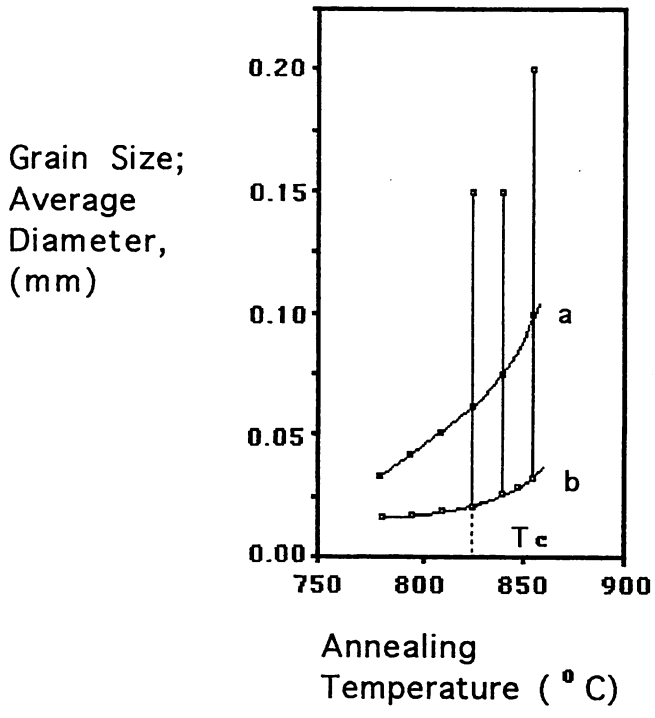

Figure 1.6 The grain size of Cu-Be alloy (a) with 0.15 wt.% Co and (b) with 0.13 wt.% Co, after annealing for 2 hours at various temperatures (Beck, Kremer, Demer and Holzworth, 1948).

A linear relationship is expected between the stored energy and dislocation density. Work–hardening theory (Li, 1962b) predicts that the square–root of the dislocation density should be linear with the flow stress. The stored energy is proportional to the square of the stress, so that the flow stress is directly proportional to the square–root of stored energy (Keh & Weissman, 1963). It follows that stored energy is proportional to the dislocation density.

If the stored energy due to dislocations is the driving force for grain growth, and if the growth rate is proportional to, and only affected by the driving force, then equation (13) shows that the growth rate during recrystallisation should be proportional to t^{-1} at long times. This has been observed several times (Leslie *et al.*, 1961; Speich & Fisher, 1965) and is more widely attributed to the simultaneous recovery of the cold–worked region. Thus, replacing ρ by the driving force, ΔG in equation (13), with ΔG changing with time through a second order recovery constant K_R, and growth rate v being proportional to the driving force ΔG through a rate constant K_G, it follows that

$$v^{-1} = K_G^{-1}\left(\Delta G_o^{-1} + K_R t\right) \tag{14}$$

where ΔG_o is the driving force at time zero (Li, 1965).

On plotting the growth rate against time on a log–log scale (figure *1.7*) the rate approaches t^{-1} at long times, but deviates considerably at shorter times. However, on plotting reciprocal growth rate against time (figure *1.8*) a linear plot is obtained. Integration gives

another linear relationship between the distance moved by the grain boundary and the log of time. This evidence suggests that there is a second order kinetics effect concurrent with grain growth, possibly due to the recovery of stored energy by the annihilation of dislocations.

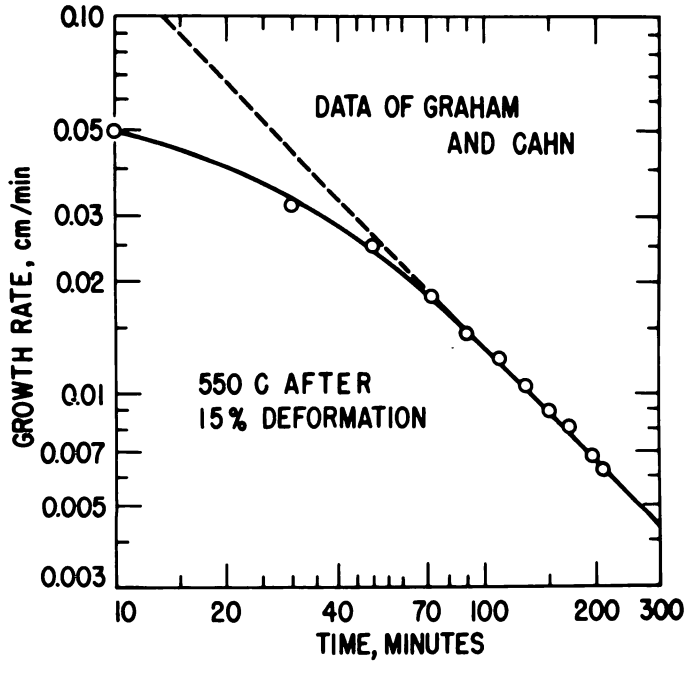

Figure 1.7 Grain growth rates in single crystal aluminium measured by repeated cycles of heating for a given time, cooling and etching to reveal boundary positions in a strained aluminium single crystal method (Li, 1965).

At long times the growth rate becomes

$$v = \frac{K_G}{K_R t} \tag{15}$$

indicating that if solute atoms affect K_G (*ie* grain–boundary mobility) as much as K_R, this equation becomes independent of solute–atom concentration. It is suggested that the overall effect of solute atoms on recrystallisation could arise from their effect on nucleation. In a similar manner, if temperature affects K_G as much as K_R, or if grain boundary mobility has the same activation energy as recovery, equation (15) will be independent of temperature. Again, the effect of temperature could be entirely on the rate of nucleation and not on the rate of growth.

However, other results have suggested that the growth rate is not proportional to the driving force – in particular from results which relate subgrain size to the velocity of grain boundaries. If this is the case, a power relation between growth rate and driving force may be considered:

$$v = K_G (\Delta G)^{C_1} \tag{16}$$

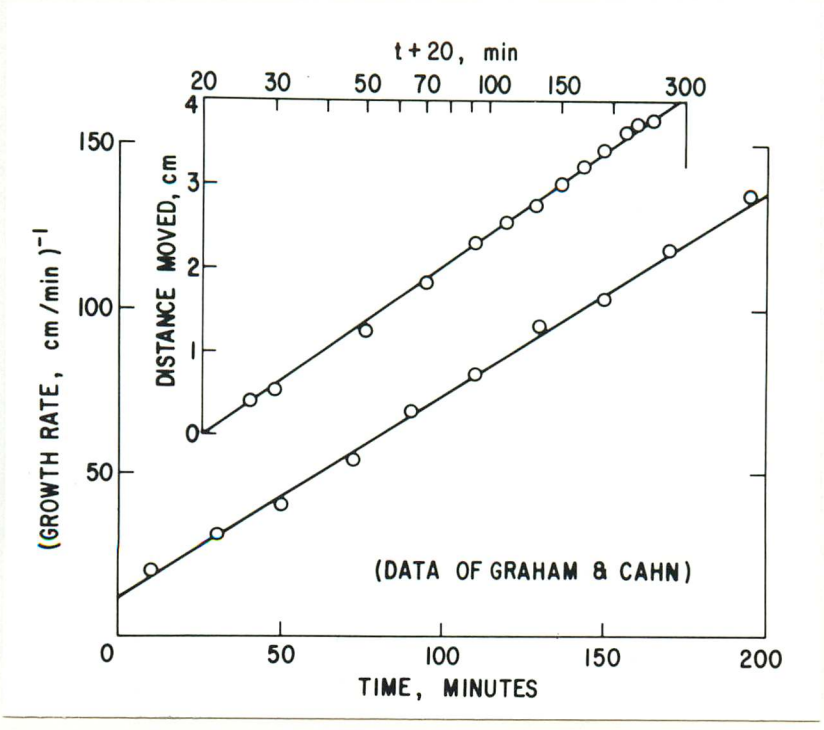

Figure 1.8 Grain growth rates in single crystal aluminuim measured by heat–cool–etch method (Li, 1965).

The relationship $v \approx t^{-1}$ indicates a recovery–kinetics relationship of the form

$$\frac{\mathrm{d}\Delta G}{\mathrm{d}t} = -K_R(\Delta G)^{C_1+1} \tag{17}$$

This is equivalent to

$$\frac{\mathrm{d}\Delta G}{\mathrm{d}t} = -\left(\frac{1}{K_R}\right)^{\frac{1}{C_1}}\left(\frac{C_1}{t}\right)^{\frac{(C_1+1)}{C_1}} \tag{18}$$

At large values of C_1,

$$\frac{\mathrm{d}\Delta G}{\mathrm{d}t} \approx t^{-1} \tag{19}$$

as is often observed (Astrom, 1955). Substituting equations (17) and (18) in to (19) gives, at long times

$$v = \frac{C_1 K_G}{K_R t} \tag{20}$$

Hence, due to a similar ratio between K_G and K_R, a single relation between v and t will be observed dependent on temperature or solute–atom concentration or both.

1.5 Secondary Recrystallisation

Secondary recrystallisation takes place in a primary recrystallised matrix, whereas primary recrystallisation occurs from a cold–deformed matrix. During continued annealing following primary recrystallisation, a few grains grow vigorously until they impinge on each other, and

a coarse–grained structure results. The progress of secondary recrystallisation can in principle be described by the Avrami equation (Avrami, 1941).

$$X = 1 - \exp(-A_1 t^{B_1}) \tag{21}$$

where X is the fraction of secondary recrystallised grains, and t is the annealing time (A_1 and B_1 are constants).

Secondary recrystallisation is, in effect, a special case of grain coarsening. The driving force, or free energy per mole ΔG, is provided by the presence of grain boundaries with a free energy per unit area γ (Detert, 1971). During coarsening the area of grain boundaries decreases, hence

$$\frac{\Delta G}{V_m} = \eta_1 \cdot \gamma \cdot \frac{1}{D_a} \tag{22}$$

where V_m is the molar volume, D_a is the mean grain diameter, and η_1 is a geometric factor between 1 and 3. The rate of grain growth can be expressed by the following equation

$$v = M \cdot \frac{\Delta G}{V_m} \tag{23}$$

where M is a mobility term.

Therefore, the time dependance of continuous grain coarsening is proportional to $\sqrt{t}$ since $v = \frac{dD_a}{dt}$. This holds for the mean grain diameter, but for individual grains the grain growth behaviour is more complicated.

The required conditions for secondary recrystallisation are that grain growth be strongly impeded, except for a few grains which act as nuclei. Pinning particles impede grain growth, as described by Zener (1948). A particle present on a grain boundary decreases its area by the particle cross section size. To find the limit of grain growth, the following method is applied. Spherical particles of a mean diameter d, and a grain boundary exposed to a dragging force (which decreases the free energy available for boundary motion by a term ΔG_i) are considered. ΔG_i is given by

$$\frac{\Delta G_i}{V_m} = \eta_2 \cdot \gamma \cdot \frac{f}{d} \tag{24}$$

where f is the volume fraction of particles, and η_2 is a geometric factor between 1 and 2. Consequently, continuous grain growth ceases when $\Delta G = \Delta G_i$, limiting the grain size to D_{lim}.

$$D_{\text{lim}} = \eta_3 \cdot \frac{d}{f} \tag{25}$$

where η_3 is a factor between 1 and 2.

Beck *et al.* (1949b) discovered that secondary recrystallisation in Al-Mn alloys was linked to the presence of $MnAl_6$ particles, but only over an annealing temperature range in

which the particles start to dissolve. Burke and Turnbull (1952) explained this phenomenon in the following way: for a grain diameter D, in order to produce a nucleus for secondary recrystallisation, the following must be true

$$\Delta G_{gn} + \Delta G_i < \Delta G \tag{26}$$

ΔG_{gn} determines the free energy of a growing nucleus

$$\frac{\Delta G_{gn}}{V_m} = \eta_1 \cdot \frac{\gamma}{D} \tag{27}$$

Therefore

$$\frac{\eta_1}{D} + \frac{\eta_3 \cdot \eta_2}{D_{\text{lim}}} < \frac{\eta_1}{D_a} \tag{28}$$

or if $\eta_1 = \eta_3 = \eta_2$

$$D > \frac{D_a}{\left(1 - \frac{D_a}{D_{\text{lim}}}\right)} \tag{29}$$

Two conclusions can be drawn from this. Firstly, all grains with a grain diameter larger than average may act as nuclei. Secondly, D_a should be smaller than D_{lim}. In the case of Fe–3wt.%Si with MnS particles, during annealing below 850°C continuous grain coarsening has come to an end as $D_a = D_{\text{lim}}$ has been reached. Annealing at temperatures at which the particles coarsen and dissolve causes an increase in D_{lim} and secondary recrystallisation is promoted. Rapid heating to higher temperatures causes faster dissolution of particles, and D_{lim} increases substantially, allowing more nuclei for recrystallisation.

Texture has a pronounced influence on secondary recrystallisation when a preferred crystal orientation is present in the matrix (Beck & Sperry, 1949a). This means that only low–energy boundaries exist between individual grains of preferred orientation. The energy of a low–energy boundary is much smaller than that of a high–energy grain boundary, and is less mobile. Exceptions from impeded grain growth will therefore exist when a few grains are present which have orientations which differ from that preferred. If these grains are of sufficient size *i.e.* $\simeq$ 2 or 3 times D_a, secondary recrystallisation will be promoted from them. Nucleation from these grains will not occur if

$$\frac{\Delta G_{gn}}{V_m} = \eta_1 \cdot \frac{\gamma}{D} > \frac{\Delta G_{\text{lb}}}{V_m} = \frac{(\eta_1\ \gamma_{\text{lb}})}{D_a} \tag{30}$$

And

$$D > \frac{\gamma}{\gamma_{\text{lb}}} \cdot D_a \tag{31}$$

where γ_{lb} and ΔG_{lb} are for the low–energy boundary, (Detert, 1971).

During the thermo–mechanical processing of aluminium alloys, all of the mechanisms described above play an important role in influencing the development of texture. Hence, in

order that a greater understanding may be reached of the factors affecting the fully–annealed bulk texture of rolled alloys, each of these mechanisms must be studied as deformation processes and heat treatments progress. The following chapters describe the experimental methods implemented in carrying out these studies. Areas of particular interest concerning the nucleation of primary recrystallisation and subsequent grain growth are looked at in detail.

Chapter 2

CRYSTALLOGRAPHIC TEXTURE DEVELOPMENT

On studying single crystals it can be seen that many mechanical properties are markedly anisotropic even in crystals with cubic symmetry. Anisotropy of the plastic properties occurs as a result of the behaviour of dislocations in crystals, and any directionality in properties such as yield stress occurs because stress must be resolved on the slip systems available. In addition, restraints which are imposed on the deformation of a component macroscopically will play a significant role. It may at first sight be argued that recrystallisation should give a random array of crystals in a polycrystalline material. However, this is generally untrue, since most deformation processes lead to anisotropy due to the crystallographic nature of slip and twinning. For example, there should be a natural tendency for slip planes to align along the rolling plane. Recrystallisation does not necessarily destroy the deformation texture since it often involves the movement of existing grain boundaries.

A fully recrystallised material containing non-random arrays of grains is referred to as possesing a preferred orientation or crystallographic texture. Many physical properties of the material vary with direction, therefore texture is an important feature from a technological point of view. In the deformation of a polycrystalline metal it is usual that most of the crystals in the aggregate will become oriented in a direction or plane parallel to that of deformation. Thus the preferred orientations developed will depend upon details of the deformation processes involved. Another factor will be the crystal structure of the metal, since this determines the crystallography of the operative slip systems.

After rolling, the texture produced not only has a specific crystallographic direction parallel to the rolling direction, but also a plane of low index tends to be parallel to the rolling plane. There is scatter about this ideal desription, but the scatter decreases with increasing cold deformation. As pointed out earlier, when a polycrystalline material displaying a texture is annealed, the recrystallised grains may also posses a preferred orientation: the recrystallised texture can be even stronger than the deformation texture. This recrystallisation texture may arise from:

(a) polygonisation

(b) primary recrystallisation of deformed grains, or

(c) subsequent growth of selected grains in the recrystallised material, termed secondary recrystallisation (Honeycombe, 1968).

There are a number of distinct facilities with which texture development in polycrystalline materials may be observed and analysed. The main categories of these experimental aids are

listed and discussed in terms of their applications below.

2.1 Texture Measurement

Optical microscopy can be used to identify areas of recrystallisation, and information on which nucleation mechanisms are active can often be gathered from optical microscopy, as well as the fraction of recrystallised grains present (Ito *et al.*, 1983). Many researchers have used bulk texture analysis methods to characterise deformation and recrystallisation textures in many alloys. The analysis, most commonly using X–ray diffraction goniometer equipment, is a fast and reliable method of acquiring texture information, but delivers little or no information on the mechanisms by which certain textures become dominant and why. Since successful recrystallisation nuclei, with high grain boundary mobilities, are the means by which particular misorientation types 'take over' a deformed structure to constitute the pronounced final recrystallisation texture, more detailed microstructural studies are necessary than these bulk methods. The most commonly employed X–ray methods involve the X–ray spectrometer and the pole–figure goniometer. Results of the determinations are reported on a pole–figure stereogram, as shown in figure *2.1.*

2.1.1 *Transmission Electron Microscopy*

The transmission electron microscope is used to produce grain boundary misorientation data by recording diffraction patterns for grains meeting at a boundary and subsequently analysing them to discover the axis–angle pair for the orientation relationship. In particular, small subgrains which constitute recrystallisation nuclei can be observed on the transmission electron microscope (TEM), and their orientation in relation to the deformed matrix (that is, their 'misorientation') measured using diffraction mode methods. The occurrence of particular misorientations can then be observed with reference to the microstructure of the deformed material in which they occur. That is, particular texture types can be related to specific deformed microstructure characteristics, such as deformation bands, transition bands, grain boundaries or precipitates. These features are potential nucleation sites due to the large spacial gradient of stored energy present at large lattice misorientations. This can then allow prediction of nuclei misorientations as long as deformation microstructures can be predicted in particular alloy types. The typical area under analysis is 5-10 μm in diameter.

Observations based on *in situ* recrystallisation of thin foils in the TEM must be viewed with some caution since thinning of the material affects the dislocation density and distribution. Ham (1962) found that dislocations are lost when thinning Al–Ag solid solution foils, and similar results hold for super–purity aluminium. Also the foil thickness affects vacancy concentration and causes surface tension effects.

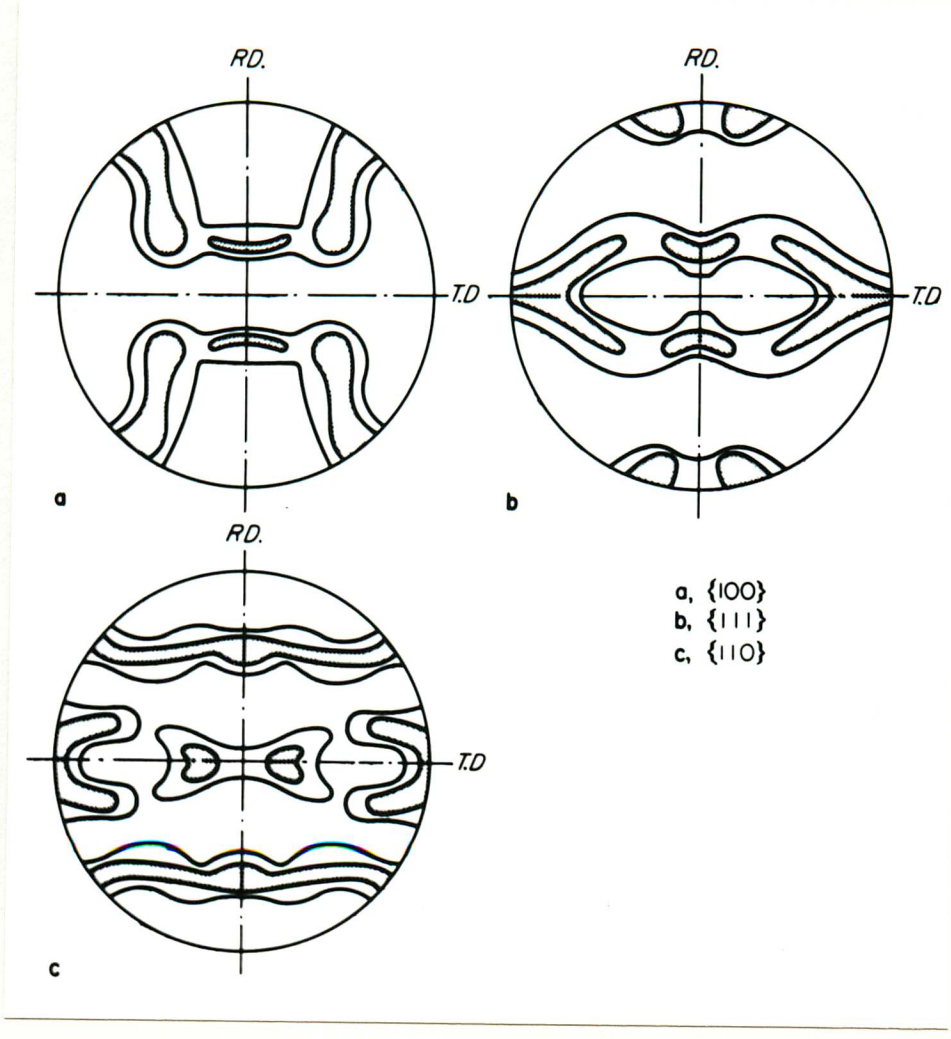

Figure 2.1 Pole figures of cold-rolled commercial aluminium after 99.5% reduction: (a) {100} (b) {111} (c) {110}, RD = rolling direction, TD = transverse direction (Honeycombe, 1968).

Ferran *et al.* (1971) pointed out that studies using electron microscopes can be difficult due to the small chance of finding a reasonable number of new grains in the region that can be examined in one foil. Although only small numbers of grains are required when dealing with microtexture, the method becomes extremely time–consuming if a statistically valid number of data points are required. Heavy deformation is therefore required, but this presents another problem, since it becomes easy to miss small subgrains that are most misoriented and therefore are the most likely potential nuclei. The foil size also limits the recrystallised grain size which may be observed, so that only the initial stages of recrystallisation, nucleation and early growth, can be studied in the TEM. In order to tell if the misorientations measured in the early stages are in fact the same misorientations which produce successful high mobility grains in the latter stages of recystallisation other methods are required.

The accuracy of TEM diffraction methods can be questioned since the thin area can be distorted, producing extraneous misorientation effects. However, inaccuracies such as these, as well as error in diffraction pattern measurements, only become important if the misorientations

are very small. For large angle misorientations the electron diffraction technique should be of adequate accuracy.

A method frequently used in the TEM is one which involves the production of Debye–Scherrer rings in the diffraction mode, and the subsequent measurement of the electron beam intensity for each ring using a transmission detector. This intensity is proportional to the volume fraction of crystallites having the normal to the (hkl) plane bisecting the angle 2θ between the incident and diffracted beam. The distribution of diffracted intensities around the centre (hkl) Debye–Scherrer ring is measured by making a circular deflection scan, and the data from such a scan are represented on a pole figure, the data falling on its edge. To produce a complete pole figure the process is repeated for a series of specimen tilt angles. Due to the movement of the study area during tilting and the increase in interaction volume with increasing tilt angle, the smallest area which can be examined by this method is 5μm.

The process can be computerised (Humphreys, 1984; Schwarzer & Weiland, 1986) and a complete run takes approximately ten minutes. Although in general X–ray techniques are superior to this method in measuring bulk orientations, this technique offers a unique option of being able to select a particular texture component within a measured pole figure and to image the corresponding structural components using the dark field mode.

High voltage electron microscopy can also be a useful technique in order to examine large areas of foil (Bay & Hansen, 1984).

2.1.2 *Scanning Electron Microscopy*

The scanning electron microscope is becoming increasingly important in recrystallisation texture measurement since it is possible to inspect large sample areas within which areas down to 0.5μm in diameter can be analysed. The method of orientation measurement employs back–scattered electron diffraction patterns. The specimen is positioned in the SEM to make an angle of typically 20^o with the incident beam so as to produce back–scattering. The backscattered diffraction patterns are imaged directly within the microscope chamber. Dingley (1984) used a low–light television and microcomputer to give a texture analysis system. The pattern produced is very large, allowing easy identification, and high spatial resolutions are obtained. Data collection and analysis from a selected region is semi–automatic. The operator must nominate two zone–axes and position the cursor on each of them in turn. From this point, and the specimen working height, the absolute orientation relative to the specimen co–ordinate system is computed to an accuracy of 0.5° in just 30 seconds. Subsequently axis–angle pairs, pole figures, *etc.* can be produced. Thus orientations between neighbouring grains can be measured, and the electron back–scattering (EBS) technique can be implemented in measuring the growth rate of particular orientations with the large field of view available. Already, with the semi–

automated system in operation, large numbers of data points can be gathered in a short period of time, grain sizes of less than 10μm can be studied, and specimen preparation may be easier. It must be noted however that large and small grains are indistinguishable in terms of orientation (Randle & Ralph, 1987).

The scanning electron microscope can be used to produce selected area channeling patterns such as those studied by Jensen *et al.*, (1985), to determine the size and orientation of individual grains simultaneously. Selected area channeling patterns (SACPs) were noted and defined as being from deformed material (a diffuse or non–existent pattern) or from recrystallised material. For recrystallised grains the patterns were compared to those given from several ideal orientations found in the recrystallised texture. If the observed grain orientation is within $\sim 5°$ of $\{hkl\}$ and the rotation pattern within $\sim 10°$ of $\langle uvw \rangle$ the grain can be designated $\{hkl\}\langle uvw \rangle$ (Hansen *et al.*, 1984). Those not corresponding to the specific orientation are recorded as being random. By noting the stage positions at which patterns changed, grain sizes may be calculated.

2.1.3 *Neutron Diffraction*

The in–situ neutron diffraction technique measures the bulk texture and the texture transformation during annealing of typically 1 cm^3 volume samples, allowing overall recrystallisation kinetics to be followed on–line as well as grain growth kinetics. Complete bulk textures can be measured within 30 minutes, but this texture analysis can be speeded up to follow reasonably fast annealing processes by measuring partial pole figures (typically 1/4) focussing on selected texture components, whereby a time resolution in the order of seconds is given.

2.2 Texture Representation

Textures are most conveniently represented on a stereographic projection where the centre of the projection represents a significant direction such as the normal to the sheet in rolling. Pole figures are a stereographic projection showing the variation in intensity of one particular set of crystal planes, in relation to specific directions in the specimen. Such a pole figure is constructed as follows:

One unit cell is located at the centre of the projection, and assuming cubic symmetry, the pole figure of the plane to be studied is obtained by taking the normal to the planes and projecting them upwards until they meet the projection sphere. As shown in figure *2.2*, the intersection of the normal to the plane with the sphere boundary is projected to the south pole, and the point at which the line intersects the horizontal plane is plotted. Each point in the stereographic projection represents a plane normal in the sample co–ordinate system, and in the notation of Bunge (1969), for a direction $\overline{h}$ lying normal to the plane hkl the pole figure $P_{\overline{h}}$

is defined by

$$\frac{dV}{V} = P_{\overline{h}}(y)dy \tag{1}$$

where $\frac{dV}{V}$ is the sample volume fraction with the crystallographic plane normal $\overline{h}$ lying parallel to the sample direction y. For a perfectly random texture, $P_{\overline{h}}(y) = 1$ for all directions y.

Since an *hkl* pole figure is a plot of the orientations of *hkl* plane normals, it is independent of crystal rotation about the normal. Pole figures are therefore two–dimensional and do not represent the full three–dimensional orientation relationship between the two co–ordinate systems. Pole figures measured directly by X–ray diffraction methods show $P_{\overline{h}}$ plotted as a series of contours of X–ray density. The intensity of the *hkl* reflection is measured at an array of directions in the sample space (*ie.* at an array of points on the pole figure). The diffracted intensity is corrected for background, absorption and extinction effects and then normalised to give an X–ray density for each orientation.

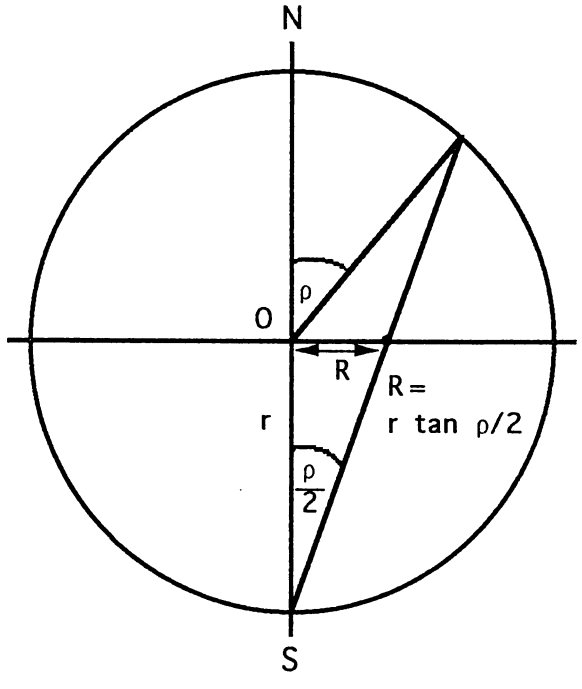

Figure 2.2 Stereogram construction (McKie & McKie, 1986).

Ito, Müsick and Lücke (1983) found the quantity of particular orientations by the following method (using the quantity I_c of the cube orientation as an example):

$$I_c = \frac{I}{I^*} \tag{2}$$

$$I = I(0°)S(0°) + I(5°)S(5°) + I(10°)S(10°) + I(15°)S(15°) \tag{3}$$

$$S(0°) = \int_0^{2.5} 2\pi \sin\theta d\theta \tag{4}$$

$$S(\overline{\alpha}^\circ) = \int_{\overline{\alpha}-2.5^\circ}^{\overline{\alpha}+2.5^\circ} 2\pi \sin\theta d\theta \qquad (5)$$

for $\overline{\alpha} = 5°$, $10°$ and $15°$ and where $I(\overline{\alpha}^\circ)$ is an average intensity on a small circle of the tilting angle $\overline{\alpha}$ in a {200}-pole figure whose centre corresponds to $\overline{\alpha} = 0°$. I^* is the intensity obtained in this manner for a standard specimen showing a pure cube texture (e.g. Al 99.98 wt.% pure, rolled to 95% reduction and annealed for 60 seconds at 360°C). This method assumes that the area considered ($\leq$ 17.5°) covers the spread of the orientations in the cube orientation and that no poles of other orientations fall into it. This is reasonable where the only other orientation is the R–orientation since no {100}–poles are close to each other, hence I_c should give the volume fraction of the cube component.

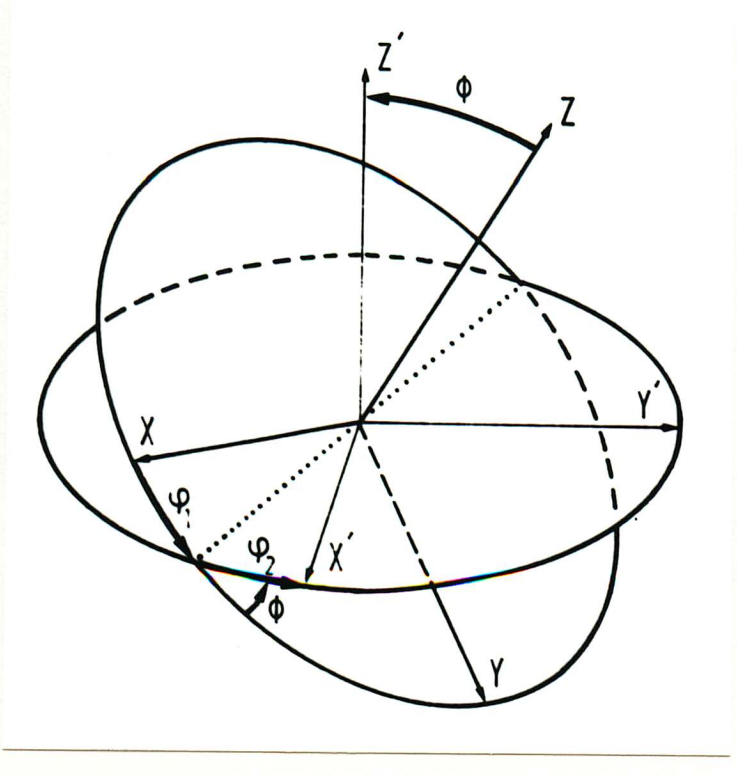

Figure 2.4 On the definition of Euler angles ϕ_1, Φ, ϕ_2. (Bunge, 1969).

Orientation distribution functions are a more precise method of measuring orientation intensities. They are derived using an expansion method as a function of the three Euler angles ϕ_1, Φ, ϕ_2 from four incomplete ($\overline{\alpha} \leq 85°$) pole figures ({111}, {200}, {220}, {311}) (Roe, 1965).

The Euler angles are a means of representing a crystal rotation, as follows: the crystal coordinate system begins with its axes parallel to those of the sample coordinate system. The crystal coordinate system is then first rotated about the Z' axis through the angle ϕ_1, then about the X' axis (in its new orientation) through Φ and, finally, once again about the Z' axis (in its new orientation) through the angle ϕ_2 (figure *2.3*). The rotation g is thus represented

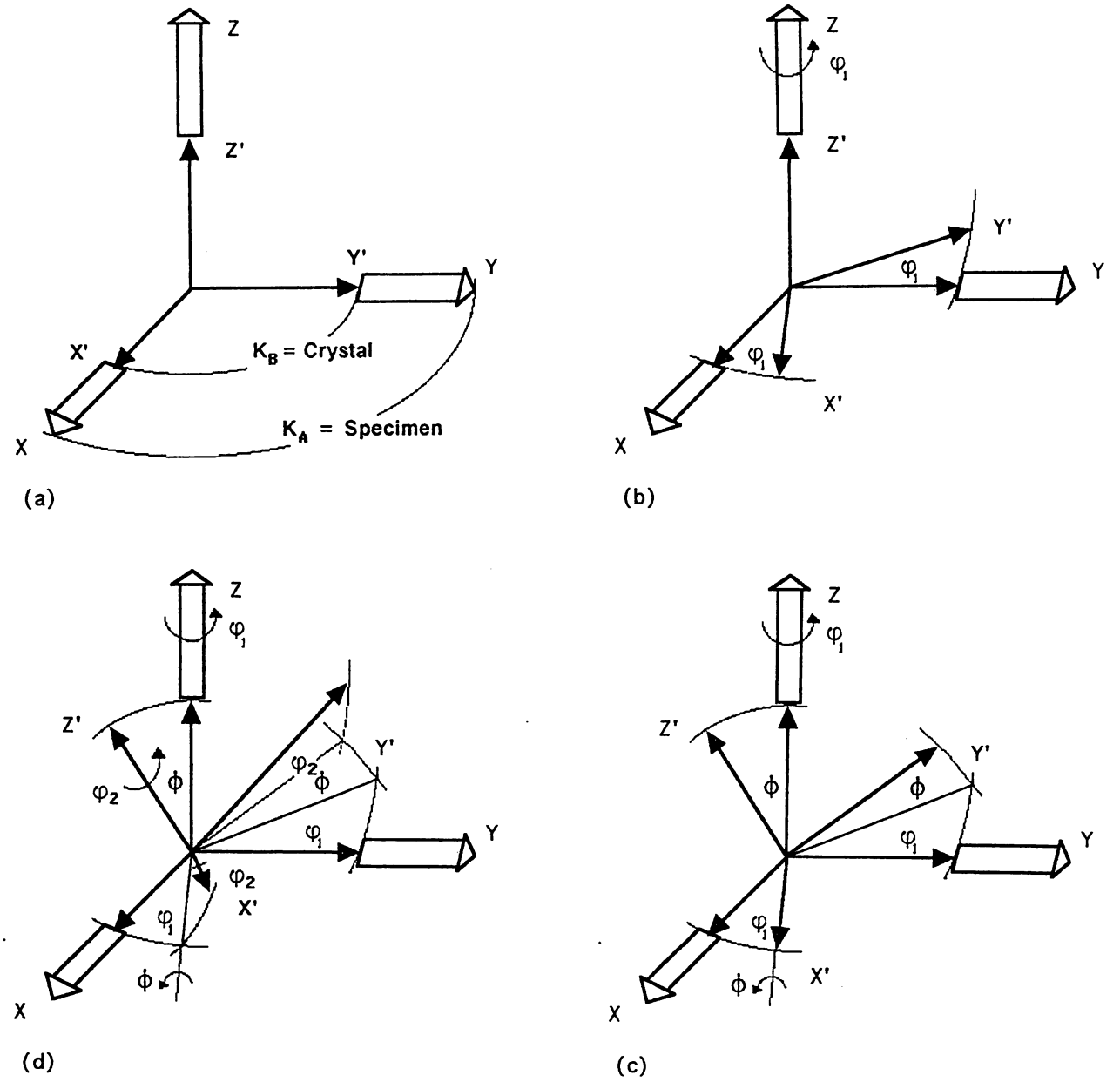

Figure 2.3 On the definition of the Euler angles ϕ_1, Φ, ϕ_2:
(a) The crystal coordinate system K_B $(X'Y'Z')$ lies parallel to the sample coordinate system K_A (XYZ) (the cube orientation).
(b) The crystal coordinate system is rotated about the Z'-axis through the angle ϕ_1.
(c) The crystal coordinate system K_B is rotated with respect to the orientation (b) around the X'-axis through the angle Φ.
(d) The crystal coordinate system K_B is rotated with respect to the orientation (c) around the Z'-axis through the angle ϕ_2 (Bunge, 1969).

by the three Eulerian angles ϕ_1, Φ, ϕ_2.

$$g = \{\phi_1, \Phi, \phi_2\} \tag{6}$$

If the Z axis of the two coordinate systems is considered as well as their $X-Y$ planes (figure *2.4*) it can be seen that the Euler angles are symmetric with respect to the coordinate systems. The angle Φ is the angle between the two Z axes, and ϕ_1 and ϕ_2 are the distances of the two X axes from the line of intersection of the two $X-Y$ planes.

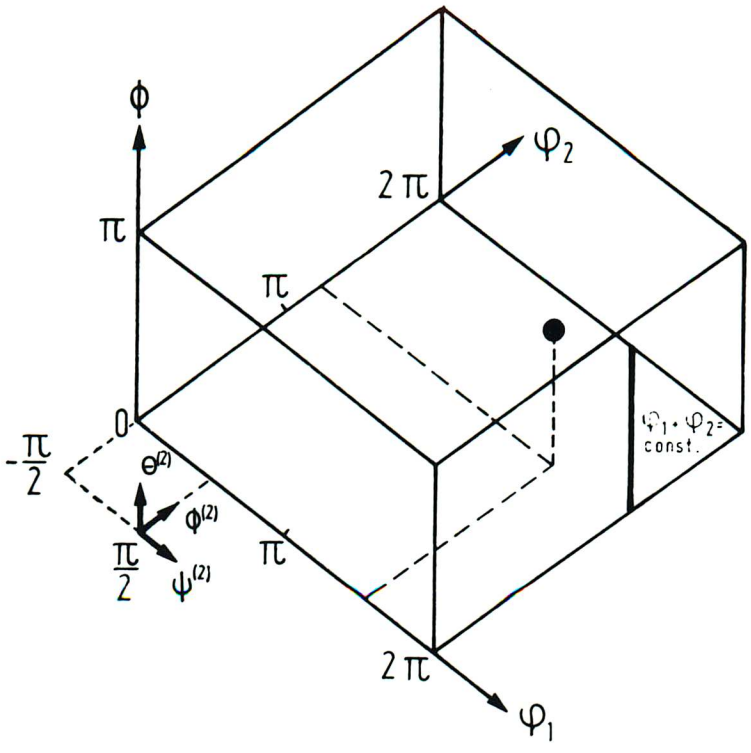

Figure 2.5 The orientation space (Euler space) corresponding to the two definitions of the Euler angles ϕ_1, Φ, ϕ_2 and Ψ, Θ, Φ. Points on the lines $\Phi = 0$, $\phi_1 + \phi_2 = \text{const.}$ represent the same rotation or orientation. (Bunge, 1969).

It is usual to represent the three parameters of the rotation g – namely ϕ_1, Φ, ϕ_2 – as Cartesian coordinates in a three dimensional space, the orientation space or Euler space (figure *2.5*). Each point of the Euler space then corresponds to a particular rotation, and conversely each rotation or crystal orientation leads to a point in the three dimensional space (Bunge, 1969). ODF's are occasionally represented as 3–dimensional models, but more normally as a series of sections (*e.g.* sections of constant ϕ_2 at 10° intervals). An example of such sections is shown in figure *2.6*.

The orientation distribution functions can be approximated to 'components', consisting of a superposition of a few isotropic Gauss-type scattering functions (Lücke *et al.*, 1981). The component (index i) is formed by rotating an orientation g_i around arbitrary axes by angles the frequency of which is given by a Gauss distribution.

The component is therefore described by

g_i - its central (ideal) orientation

ψ_i - its scattering width, and

M_i - its volume fraction

The advantages of these components are:

(a) Each texture can be described by just a few numbers, particularly for volume fractions.

(b) The error in frequency measurement of each orientation due to its multiplicity is eliminated. Multiplicity occurs due to the cubic crystal and orthorhombic specimen symmetry. Each general orientation appears 96 times in the complete orientation space $0° \leq \phi_1, \phi_2 \leq 360°$, $0° \leq \Phi \leq 180°$ due to the symmetry for an orthorhombic–cubic sample crystal. For especially symmetrical orientations, some of the 96 symmetrically equivalent positions fall on top of each other so that their multiplicity is reduced to 48 or even 24.

(c) The series expansion method leads to systematic falsifications of the ODF in the form of background fluctuations which reduce the height of the maxima and may even lead to physically unreal maxima and negative values of the ODF's. These can be eliminated using the component method. The 'ghost' peaks are produced when the terms with odd l of the series expansion are omitted if the ODF is read from pole figures. Hence a 'reduced' ODF is given. Using the Gauss-functions method, an approximation for the odd part of the ODF can be produced. This is because the different expansion coefficients from the superposition of Gaussain functions are not independent of each other but are all determined (including those of odd l) by the same model parameters, $g_i, \mathrm{M_i}, \psi_i$, making them true parameters. Hence the 'true ' ODF can be calculated (Lücke *et al.*, 1981).

An inverse pole figure $R_y(\overline{h})$ indicates the beginning with which a particular sample direction occurs in different crystal directions. $R_y(\overline{h})$ is defined by

$$\frac{\mathrm{d}V}{V} = R_y(\overline{h})\mathrm{d}\overline{h} \tag{7}$$

where $\frac{\mathrm{d}V}{V}$ is the volume fraction with the sample direction y lying parallel to the crystallographic plane normal $\overline{h}$. For a perfectly random texture, $R_y(\overline{h}) = 1$ for all directions $\overline{h}$. The inverse pole figure is plotted on a stereogram based on the crystal co–ordinate system, and gives complete representations of textures which are axisymmetric about the sample direction y.

It is useful to use inverse pole figures in addition to microtextural and grain misorientation texture (GMT) data, as pointed out by Randle and Ralph (1988) . This is because GMT can reveal the special boundaries in a set of grain boundaries, but inverse pole figures give evidence for soft– and hard–textured grain assemblies which also showed differing proportions of random boundaries. Hard orientations are those located in regions of a unit triangle where 2–slip systems (triangle edges) or 4–, 6–, or 8–slip systems ($\langle 011 \rangle$, $\langle 111 \rangle$, and $\langle 001 \rangle$ corners respectively) may operate. Soft orientations are associated with single slip. Ito *et al.*, (1983) also found pole figures useful in recognising particular textures. The R–component can be formed by two processes – continuous and discontinuous recrystallisation. In continuous recrystallisation the R–texture occurs as retained rolling texture (S–texture). In discontinuous

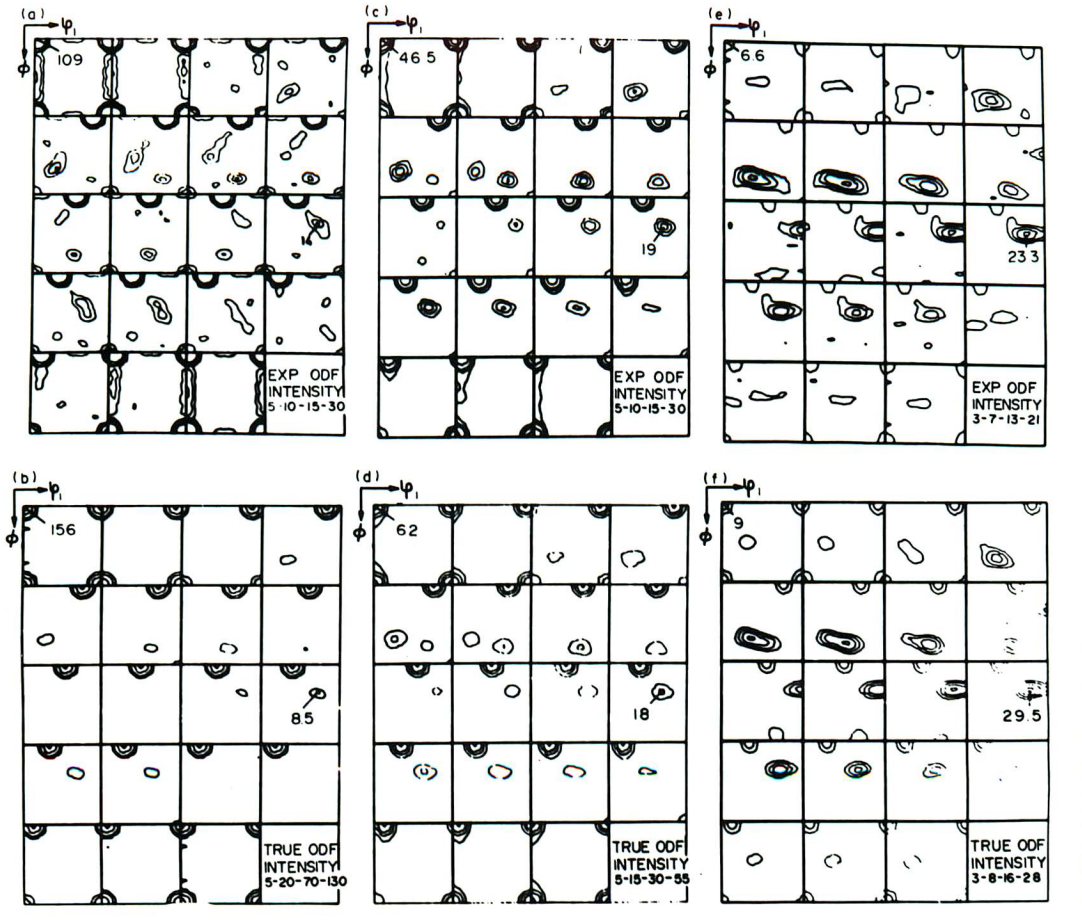

Figure 2.6 Examples for ODF's after primary recrystallisation.
(a,c,e) Experimental (reduced) ODF's
(b,d,f) Corrected (true) ODF's.
(a,b) 0.01 wt% Fe rolled 99% 500°C, cube orientation predominant.
(c,d) 0.01 wt% Fe rolled 95% 500°C, cube and R–orientations equally strong.
(e,f) 0.01 wt% Fe 360°C, R-orientation predominant, (Ito, Müsick and Lücke, 1983).

recrystallisation the R–texture is a ⟨111⟩–type growth texture since each of the 4 symmetrically equivalent components of the S–texture are related to the other three by a rotation of 40°⟨111⟩ giving high mobility boundaries. In the pole figures the R–texture sometimes occur as a smeared out maximum similar to a rolling texture, and sometimes as a sharp maximum. This suggests that the former was formed by continuous recrystallisation (e.g. 360°C anneal) and the latter by discontinuous recrystallisation (e.g. 500°C anneal).

Ferran *et al.* (1971) used an X–ray Kossel line technique coupled with the microfocus Laue technique to measure textures. However, they pointed out that the Laue technique may produce erroneous results in three ways:

(a) There is an appreciable error in measuring orientation ($\sim \pm 3°$ normally, but can be as large as 15°).

(b) The new grains occur at grain boundaries which are likely to be more distorted and misoriented with respect to the centre of a grain where the Laue patterns are obtained.

(c) If a new grain surrounded by more than one matrix grain has a meaningful orientation relationship with only one of these matrix grains, then the other reported relationships will be irrelevant and will make the results appear more random.

To obtain a complete, precise description of recrystallisation textures it is necessary to use several complementary techniques and combine the results. TEM texture measurements are useful in observing and quantitatively characterising lattice misorientations in bands, at particles and across subgrain clusters. There is an advantage in the TEM technique described above since texture is determined for a whole region (5–10μm) automatically. In general, nucleation, and the role of mictrotextural features in the process, is most easily observed in the TEM. Electron back scattering (EBS) measurement is also good for the observation and characterisation of nuclei since extremely small grains can be seen. Also, nuclei growth and grain growth are easily followed due to sample area and semi–automatic data–collection, and grain boundary geometry and spacial variations in texture can be measured. Neutron diffraction is particularly useful in the measurement of growth rate and recrystallisation kinetics. In addition, although X–ray analysis has not been reviewed in this paper, texture measurements taken by this method can give useful in formation. In particular, the interaction volume produced in an X–ray goniometer is much smaller than that in a neutron diffraction device, and this therefore allows inhomogeneities through the thickness of rolled plate to be measured. Also, there are X–ray goniometers in use at the present time which can measure textures during recrystallisation by annealing within the goniometer, giving dynamic texture measurements.

2.3 Grain Boundaries and Texture

Grain boundaries in partially recrystallised and fully recrystallised material can be characterised using geometrical criteria, for example by describing the proportion of shared sites from each grain meeting at the boundary, or by an analytical description of the packing of polyhedral units. Boundaries which posses markedly differing properties, such as diffusivity and mobility, from the majority of the boundaries in the material are termed 'special boundaries'. These special boundaries frequently display particular misorientations in terms of the coincidence site lattice model. It is these boundaries, which due to their extraordinary nature, encourage abnormal grain growth and the evolution of recrystallisation microtextures. It is therefore possible to gather useful information towards the understanding of microtexture development by measuring the distribution of grain misorientations (this being the grain misorientation texture) with respect to the geometrically special types.

The misorientation parameters across the boundary between recrystallised and de-

formed material give a guide to the physical properties of these interfaces, for example mobility, energy, and the ability to absorb dislocations, which are all key factors in influencing the control of recrystallisation. Hence the study of recrystallisation textures necessarily becomes focussed upon the distribution of the boundaries themselves. Apart from glissile interfaces, low angle boundaries should migrate less readily than high–angle grain boundaries because the structures are semi-coherent across the boundary. However, not all high angle boundaries are equivalent – some boundaries migrate much more rapidly than the majority of boundaries, due to either solute, precipitate or texture effects. On the assumption that boundary migration is controlled by grain boundary diffusion, it would be expected that boundary migration should be more rapid for high–angle boundaries than for smaller misorientations. This is generally true, but evidence has been found that the orientation dependence of high–angle boundary migration is a more specifically selective effect. That is, certain high–angle boundaries have much higher mobilities under some conditions than others.

The phenomenon of particular boundaries migrating faster than other boundaries during recrystallisation has been studied with respect to its promotion of particular annealing textures. The observation of increased grain–boundary mobility in certain high–angle boundaries does not mean that differences in mobilities between various boundaries are necessarily responsible for growth selection in single crystals or preferred orientation in general. Aust and Rutter (1960,1961,1962) and Ibe and Lücke (1964), demonstrated that twinning during growth can result in the replacement of a migrating boundary by a second boundary and a coherent twin boundary whenever this can produce a decrease in total interfacial energy. The interfacial energy of grain boundaries varies with orientation: grains oriented so that they have a low angle may well be favoured by the interfacial energy factor during the nucleation or the growth stage of any development of new grains. Growth selectivity based only upon orientation measurements implies only that there is an orientation dependence of boundary mobility and/or energy. It seems probable that mobility is a dominating factor in growth selection, since any new boundary of lower interfacial energy would not survive unless its mobility is among the highest.

Grain growth may be inhibited by:

- Segregation of solute species to grain boundaries, leading to a solute 'drag' effect (Aust & Rutter, 1962, Lücke & Stuwe, 1967, Cahn, 1962, Hillert & Sundman, 1976).
- Strong texture (Beck, 1949, Dunn & Walter, 1965).
- Interaction between grain boundaries and fine particles.

These factors which inhibit grain growth will in turn encourage abnormal grain growth (secondary recrystallisation) since a few favourable grains will exist to act as nuclei for the process.

Second–phase particles must be present to cause abnormal grain growth in a material with random grain orientation (Haessner, 1971). Abnormal growth may also occur if there are particularly large grains present in the microstructure which are then able to grow.

The study of grain–misorientation texture affords the possibility of improving the behaviour of polycrystalline materials by promoting the selection of specific boundaries which display better than average properties. However, materials design requires a detailed understanding of the individual effects of chemistry, thermomechanical history, boundary geometry and boundary properties on grain–misorientation texture development as well as their interrelation. Sufficient data must be collected in order to characterise and model the parameters which have been observed to influence the behaviour of grain boundaries.

2.4 Deformation Textures in Aluminium

Deformation of aluminium and its alloys proceeds by crystallographic slip that normally occurs on the $\{111\}$ planes in the $\langle 1\bar{1}0\rangle$ directions. Large amounts of deformation at ambient temperature leads to some strengthening through the development of textures, the nature of which depends in part on the mode of working. Textures evolved during cold working cause directionality in certain mechanical properties. Texture hardening causes moderate increases in both yield and tensile strength in the direction of working. Forming characteristics of the sheet may be controlled by controlling the 'R–value', which is the ratio of the strain in the width direction to that in the thickness direction. A large R–value means that there is a lack of deformation modes oriented to provide strain in the through thickness section. This will make the sheet resistant to thinning, which is desirable in forming processes (Polmear, 1981).

The rolling texture of aluminium is primarily composed of a 'tube' of preferred orientations running from the brass type orientation $\{011\}\ \langle 21\bar{1}\rangle$ through the S–orientation $\{123\}\ \langle 63\bar{4}\rangle$ to the copper type $\{112\}\ \langle 11\bar{1}\rangle$ (Erbslöh *et al.*, 1984). The tube can be represented in three dimensional Euler space as shown in figure *2.7*. The line down the centre of the tube along G-B-S-C is that corresponding to maximum orientation density. The area labelled I, II and III correspond to the three Taylor type models where group I models involve the relaxation of the shears ϵ_c and ϵ_s, group II involve the relaxation of the ϵ_b shear and group III involve the relaxation of the ϵ_c shear.

Ito *et al.*, (1983), using the orientation distribution function method found that the main components were:

Cu – component	$\{112\}\langle 11\bar{1}\rangle$	at $\phi_1 = 90°$	$\Phi = 35°$	$\phi_2 = 45°$
S – component	$\{124\}\langle 21\bar{1}\rangle$	at $\phi_1 = 57°$	$\Phi = 29°$	$\phi_2 = 63°$
Brass - component	$\{011\}\langle 21\bar{1}\rangle$	at $\phi_1 = 34°$	$\Phi = 45°$	$\phi_2 = 90°$

where ϕ_2 is one of the angles in Euler space. The positions of the Cu– and S–components were

found to vary from the ideal positions for each specimen. For example the S–component was found to be at $\phi_2 = 56°$, and was hence named the S/Cu–component.

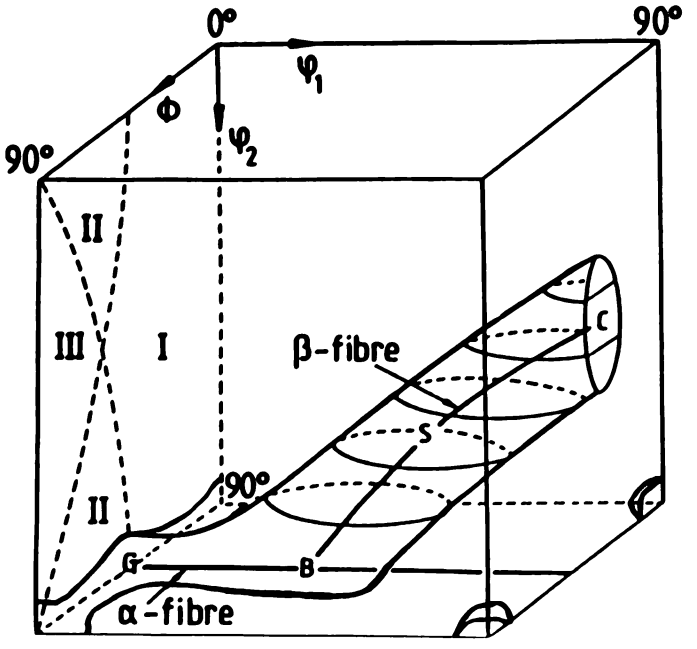

Figure 2.7 Schematic representation of the f.c.c. rolling texture in the first subspace of the three dimensional Euler angle space (Hirsch, 1990).

2.5 Recrystallisation Textures

Recrystallisation occurs in materials in sheet form, and in face centred cubic metals such as aluminium a texture is obtained which is related to the primary texture in the same way as the primary texture is related to the cold–worked matrix. The as–rolled textures of aluminium consist primarily of the brass type orientation $\{011\}\ \langle 21\bar{1}\rangle$, the S–orientation $\{124\}\ \langle 21\bar{1}\rangle$ and the copper type $\{112\}\ \langle 11\bar{1}\rangle$. Recrystallised textures obtained in commercially pure aluminium are related to the as–deformed textures by rotations around the $\langle 111\rangle$ axis of approximately 40° since grains of this orientation grow rapidly (Leibmann & Lücke, 1956a; Leibmann *et al.*, 1956b).

Since recrystallisation occurs from sub–grains and pre–existing grain boundaries, the orientation of the nuclei that will grow to give the annealing texture must be present in the deformed structure (although sometimes in vanishingly small amounts). Studies of recrystallisation by TEM have been carried out directly on thin foils, and contradictory results obtained in different experiments. For example, studies of single crystals deformed by hardness indentations produced new grains which were not appreciably misoriented with respect to the matrix (Haase & Granzer, 1961). However, later work on heavily deformed single crystals gave new

grains with intermediate to large misorientations, and the orientations of the grains appeared to be random since disorientations between recrystallised material and the cold–worked matrix (considering grains smaller than 5μm diameter) were $12 - 58°$ about the axis $\{112\}\langle 111\rangle$. This disorientation was measured about a rotation axis common to both the recrystallised and deformed grains (Michels & Ricketts, 1967).

The main texture components which have been observed in fully recrystallised aluminium sheet are as follows (Ito *et al.*, 1983):

Cube	$\{100\}$	$\langle 001\rangle$
R	$\{123\}$	$\langle 63\bar{4}\rangle$
Goss	$\{110\}$	$\langle 001\rangle$

The texture obtained must depend upon both the nucleation frequency and the growth rate of nuclei, and their dependence on the deformation structure.

Grain growth is accompanied by macroscopic textural changes, and its onset is a complex function of particle pinning, solute, surface and residual strain effects, and grain size distribution and texture, since each of these effect boundary mobility. However, macroscopic orientation measurements only reveal overall textures. It is necessary to measure texture on a microstructural level in order to deduce misorientation textures for individual grain boundaries.

2.6 Oriented Growth vs Oriented Nucleation

Two simplified theories of recrystallisation texture development have been proposed in previous studies. The 'oriented nucleation theory' postulates that texture formation is attributed solely to a selection of certain orientations in the nucleation process. Once the grains have been nucleated, it is assumed that they grow at the same rate, independent of the orientation (Burgers, 1941). The 'oriented growth theory', however, assumes that the orientation of the nuclei be random and that growing grains undergo a selection process according to their different growth rates due to different crystal orientations (Beck & Hu, 1966). Both of these theories lead to a larger volume fraction of the recrystallised material in the vicinity of the preferred orientations, that is they both give a recrystallisation texture. The difference between the two theories is that the oriented nucleation theory suggests that texture is caused by a larger number of crystals in the preferred orientations, whereas the oriented growth theory suggests that texture is due to bigger crystals of the preferred orientations.

Bleck and Bunge (1981) have studied these two theories quantitatively in order to establish their relevance. The mean grain size of the orientation o may be defined by the volume fraction $f(o)$ of crystals in o divided by the number of crystals $N(o)$ in this orientation.

$$D(o) = \frac{f(o)}{N(o)} \tag{8}$$

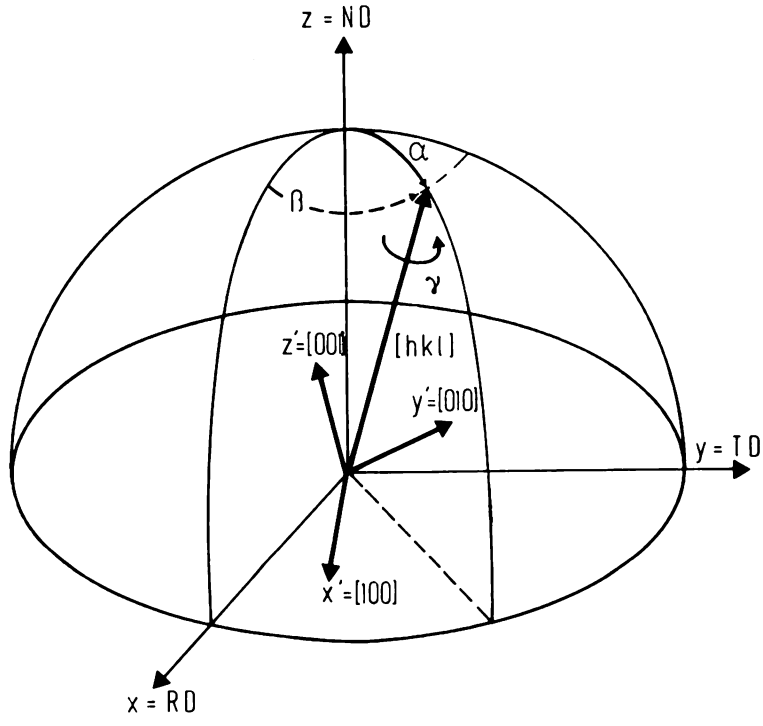

Figure 2.8 The orientation of a specified crystal direction $[hkl]$ relative to the sample coordinate system $K_A = \{XYZ\}$ is described by the polar coordinates α, β. A rotation of the crystal coordinate system about $[hkl]$ is described by a third angle γ (Bunge, 1969).

with

$$\frac{\mathrm{d}V}{V} = f(o)\,\mathrm{d}o \tag{9}$$

being the orientation distribution function of the volume and

$$\frac{\mathrm{d}N(*)}{N(*)} = N(o)\,\mathrm{d}o \tag{10}$$

being the orientation distribution function of the number of crystallites (irrespective of their grain sizes).

Usually only the pole figures for a metal are measured (that is, the orientation distribution functions of individual crystal directions). The complete orientation distribution function $f(o)$, which depends on three orientation parameters symbolised by o, is therefore not obtained. The pole figures depend on two orientation parameters only:

$$\frac{\mathrm{d}V}{V} = P_{hkl}(\alpha\beta)\sin\alpha\;\mathrm{d}\alpha\;\mathrm{d}\beta \tag{11}$$

Bleck and Bunge used X-ray diffraction to obtain a powder diffraction line consisting of individual spots belonging to the individual crystallites of an Al-Mn alloy. This was done using a texture goniometer. The registered X-ray intensity is thereby proportional to the volume fraction of crystals in the respective orientation $\alpha\beta$ (figure *2.8*). These pole figures are 'pole

figures by volume'. Analogously 'pole figures by number' can be defined

$$\frac{\mathrm{d}N(*)}{N(*)} = Q_{hkl}(\alpha\beta)\sin\alpha\ \mathrm{d}\alpha\ \mathrm{d}\beta \tag{12}$$

From both these pole figures the mean grain size of the crystals in the orientation $\alpha\beta$ were obtained using

$$D(\alpha\beta) = \frac{P_{hkl}(\alpha\beta)}{Q_{hkl}(\alpha\beta)} \tag{13}$$

The pole figures by number were compared with the conventional pole figures by volume, in order to deduce whether a preferred orientation in the recrystallised texture is due to a larger number of crystals or to bigger crystals.

In the high temperature range, above 400°C, recrystallisation took place by nucleation of grains in the Cube orientation with a considerable spread about the ideal orientation. After annealing the alloy at 450°C for 10 seconds it was found that the maximum densities (in the Cube orientation) are nearly the same for both types of pole figure. The larger volume fraction of recrystallised material in the vicinity of the Cube orientation is thus due to a larger number of crystals in this orientation, rather than to bigger crystals. The results are thus in good agreement with the oriented nucleation theory, since according to the oriented growth theory, the pole figure by number should be random. The situation is similar after 100 seconds annealing time.

In the low temperature range, below 400°C, two different nucleation processes can be distinguished. The earliest grains visible were found in the orientations similar to the rolling texture, and according to the optical observations are nucleated by strain induced boundary migration. These grains became elongated in the rolling direction during annealing since their growth is impeded by the banded structure of the deformed alloy. Later, grains of the Cube orientation were nucleated and they were approximately equiaxed. It was evident that the Cube grains were larger than grains in other orientations. From the distribution curves of the grain diameters it was concluded that the growth rate in the rolling direction for both of these groups of grains is nearly the same, whereas the first group of grains is impeded at the boundaries of the banded structure. In this case, two groups of grains can be distinguished which are formed by oriented nucleation, however, the second becomes larger due to a growth preference. In this case, elements of both the oriented nucleation and oriented growth theories must be taken into account.

The origin of the cube texture, in recrystallised aluminium alloys has been argued for many years. The theory of oriented growth, as put forward by Beck and Hu (1966) and Ibe and Lücke (1965) suggests that the cube texture is formed by the growth of grains having a misorientation of $30-40°$ about a common $\langle 111\rangle$ axis. Burgers and Louwerse (1931) postulated

the oriented nucleation theory, in which they suggested that cube oriented crystallites exist in the deformed structure which are able to change into low–energy grains capable of growth by rapid recovery mechanisms. Such nuclei have been observed in copper by Ridha and Hutchinson (1982), who showed that the cube oriented blocks have a particular morphology; that of elongated crystallites up to 50μm long, and $0.2 - 1\mu$m thick. It has been proposed that this shape is critical in allowing the successful nucleation of cube grains, since small lateral bulges give the volume highly favourable characteristics. It was also suggested that the cube oriented crystallites are of naturally low energy due to their particular slip geometry.

Lücke (1984) first advanced the theory that the cube texture formation in copper is not solely controlled by oriented nucleation, but that there is also a growth selection and particularly the S component of the deformed matrix plays a decisive role in this process. This is because any of the four S components ($\{123\}\langle 63\bar{4}\rangle$) have the correct orientation relationship for maximum growth rate (40° $\langle 111\rangle$), so that rapid growth of the cube also with respect to the global distribution is secured. This is supported by the observation of the effect of rolling strain on the cube texture strength in subsequently annealed copper. As strain increases many orientations rotate towards S, improving the growth situation of the cube grains so that the cube texture strength after annealing increases. However if the strain is increased further, the S rotates further to give a stable 'C' component ($\{112\}\langle 11\bar{1}\rangle$) which is less favourably oriented for cube texture and the cube texture strength decreases again (Duggan *et al.*, 1990).

It would therefore appear that the mechanisms of oriented growth and oriented nucleation both have an important role to play in the formation of recrystallisation textures, and that they are likely to both be operating in one alloy system.

2.7 Particle Deformation Zones

The study of particle–containing alloys has shown that the local deformation zones at particle/matrix interfaces are important in the nucleation of recrystallisation at these sites.

With increasing deformation the misorientations between matrix grains near particles are known to increase (Bay & Hansen, 1979, 1984; Humphreys, 1979). The misorientations may also be dependent on the particle size, shape, spacing and position relative to grain boundaries. Recrystallisation is nucleated near particles in deformation zones where the lattice is substantially misoriented with respect to the matrix well away from particles (Humphreys, 1977). Where the particles are present in a cluster, interactions during deformation may lead to a joint deformation zone, as has been observed at small strains in $Cu - SiO_2$ single crystals (Brown & Stobbs, 1971). Further interactions may take place if the particles, or the particle clusters, are situated at high energy boundaries, giving unusually large rotations (Bay & Hansen, 1979).

Humphreys (1977) observed 'lobes' at each side of the particles which were found

to comprise of subgrains of diameter $\sim 0.05 - 0.1$ μm. The effect of the particles on the lattice rotations was found to be confined to their immediate environment, and the rotation was a function of alloy, particle size and strain, since these parameters govern the activity of slip systems. Recrystallisation then occurs in these zones on subsequent annealing by rapid growth of particular subgrains (Humphreys, 1977, Bay & Hansen, 1979). It is therefore to be expected that the orientations of the recrystallised grains will be from within the spread of the deformation zones (Humphreys, 1978).

Humphreys (1977) found that in an alloy with a 60% cold roll, well away from particles of a diameter greater than 0.1 μm, subgrains were plate–shaped with broad faces lying approximately parallel to the rolling plane, typically 0.5 μm in thickness and 1.5 μm in diameter. Close to the particles however, the structure differed considerably. There was a region extending about a diameter from the particle which contained large numbers of very small equiaxed subgrains of diameter ~ 0.15 μm, which often occurred in groups of similar orientation. By plotting the orientations of the subgrains on a stereographic projection, they were found to be related by a rotation about an axis near the perpendicular to the rolling plane and rolling direction. By plotting angle of misorientation about this axis as a function of distance from the particle, the orientations were found to lie in a band of $\sim 10°$ at large distances, but at distances below ~ 4 μm, misorientations of up to 35° occurred, the maximum rotation being a function of particle size and strain.

Using hot stage electron microscopy, Humphreys sometimes observed nucleation away from the particle/matrix interface but within the deformation zone of the particle, and these subgrains were seen to grow towards the particles to become recrystallisation nuclei. In areas where the particles had been etched away during foil preperation, it was observed that recrystallisation was still nucleated, suggesting that its associated deformation structure is the important factor in nucleation and not the particle itself.

The nucleation process appeared to have three stages:

(a) Recrystallisation originated at a subgrain present in the deformation zone of a particle, quite often a group of subgrains of similar orientation. Subgrain growth occurring in this small area resulted in a large subgrain consisting of the total composite subgrain size.

(b) The nucleus then spread around the particle and consumed the deformation zone.

(c) Recrystallisation often stopped at this point – nuclei originating at the particles either consumed the stopped nuclei entirely, or other nuclei completed the recrystallisation process leaving a duplex microstructure. The former process is more likely to occur in a bulk specimen due to the extra curvature of grain boundaries in a 3–dimensional

specimen. No evidence of duplex microstructures was found in fully annealed bulk specimens.

The boundary between a stopped nucleus and the deformed matrix was found to be a high energy one (> 10°). Those nuclei which grew beyond this barrier did so at an irregular rate until all the deformed material was consumed.

Relating this retardation effect to bulk specimens is difficult, although it is unlikely that thermal grooving occurred in the samples, with the recrystallisation temperature being so low (250°C). In bulk specimens there was no strong evidence for there being a large number of nuclei of $2 - 4$ μm diameter corresponding to the end of stage (b) in the *in situ* experiments.

The linear growth rate of the recrystallised regions, determined by measuring the largest nucleus size as a function of annealing time, showed that after $\sim$ 10 seconds the growth rate was effectively a constant at 4.3 10^{-2} μms^{-1}. The nucleation rate (the percentage of particles initiating nucleation as a function of annealing time) was found to be initially rapid, but fell off substantially after approximately 40 seconds.

Investigation into the origin of texture in particle-nucleated grains shows that deformation zone nuclei can be classed according to orientations displayed (Nes, 1980). This suggests that particle stimulated recrystallisation is associated with structurally different types of sites. Bay and Hansen (1979) found that 80% of recrystallisation nuclei originated from particles situated on grain boundaries and in transition bands. Taking into account the observations made by Humphreys (1977), the recrystallisation process can be divided into two steps:

- Nucleation of subgrains occurring preferentially at particles located at grain boundary or transition–band–type heterogeneities.
- The nucleated particles grow rapidly around the particles and consume the deformation zone. However, growth out of the deformation zone is expected to be the rate controlling step.

Es-Said and Morris (1986) found that the shape of stable dispersion particles in unhomogenised aluminium alloys determined the shape of the subsequently recrystallised grains and, to some extent, determined the kinetics of recrystallisation. They found that after deformation, the particles were surrounded by deformation zones wich were not uniformly distributed, the highest curvature points being at the particle tips (also Humphreys, 1979; Liu *et. al.*, 1989; Bay and Hansen, 1984). As a result, recrystallised grains nucleate preferentially at the ends of the particles, and since the particles are nearly parallel to the rolling direction, the recrystallised grains also become elongated along the rolling direction. However, during a homogenising anneal two processes occur:

- The solute supersaturation level is decreased, reducing the effects of solute segregation

and dynamic precipitation in subsequent recrystallisation processes.

- The geometry and size of the intermetallic compounds are altered, usually becoming globular and coarsened. This results in more uniform deformation zones around the particles, and multiple nucleation of recrystallised grains occurs more easily. The end result is that the recrystallised grains are fine and equiaxed (Es-Said *et al.*, 1988).

Bay and Hansen (1984) measured the lattice rotations near $FeAl_3$ particles in thin foils. The component of the rotation measured was that about the foil normal, and the largest rotations were found at the ends of very elongated particles. The lattice rotations increased with amount of prior deformation, and were greater in coarse grained material (which may be due to less homogeneous slip in coarse grains). Also, particles situated at grain boundaries gave larger rotations than particles in the grain interiors. There was no clear relationship between particle size and magnitude of rotation, but groups of particles were observed to be more effective than single particles in producing large lattice rotations. (Areas of small subgrains were produced between two closely situated particles). Herbst and Huber (1978) found large orientation spreads at particle surfaces lying normal to the rolling direction, and at sharp particle angularities.

2.7.1 *Deformation Zone Models*

Humphreys (1977) has produced a detailed model of the deformation behaviour of the matrix immediately adjacent to dispersed hard particles by combining the models proposed by Ashby (1970), Brown and Stobbs (1976) and Humphreys and Stewart (1972).

As shown in figure *2.9a* a single–crystal matrix is deformed along a slip plane AB intersecting a particle. If the matrix is deformed by a vector $n\mathbf{b}$ and the particle is deformed with it, the situation is as in figure *2.9b*. If the particle is non–deformable then the local plastic deformation must restore the particle to its original shape leaving the matrix sheared. There are many possible solutions to this problem which have been tackled by the workers mentioned above, but it is necessary that this solution must produce a local reverse shear of $n\mathbf{b}$ across the plane CD. This is possible if a portion of the matrix is rotated locally in the sense shown in figure *2.9c*. In a three dimensional model, the rotation of a suitable portion of matrix about any axis normal to $\mathbf{b}$ can produce the required local shear across CD. These rotations are facilitated by the movement of dislocations, therefore the viability of any such process is dependent upon the available slip systems of the crystal.

The rotation process shown in figure *2.9c* can be predicted from a consideration of the dislocations involved in the deformation. Deforming the matrix around a hard particle results in the formation of Orowan loops as shown in figure *2.9d*, and these are unstable due to their high energy and the high local stresses produced in the matrix. An effective way of neutralising the loops is to form more loops of opposing sign, thus cancelling the first array of loops out.

This is shown in figure *2.9e* where loops **O** are cancelled out by X and Y. The creation of secondary loops at the interface by glide processes requires the formation of additional outer loops as in figure *2.9f* (schematic), resulting in the dislocations X' and Y' in the matrix (figure *2.9g*). The sign and configuration of these dislocations is such as to produce a subgrain with the same type of rotation as that in the continuum model (figure *2.9c*), showing the equivalence of the two approaches.

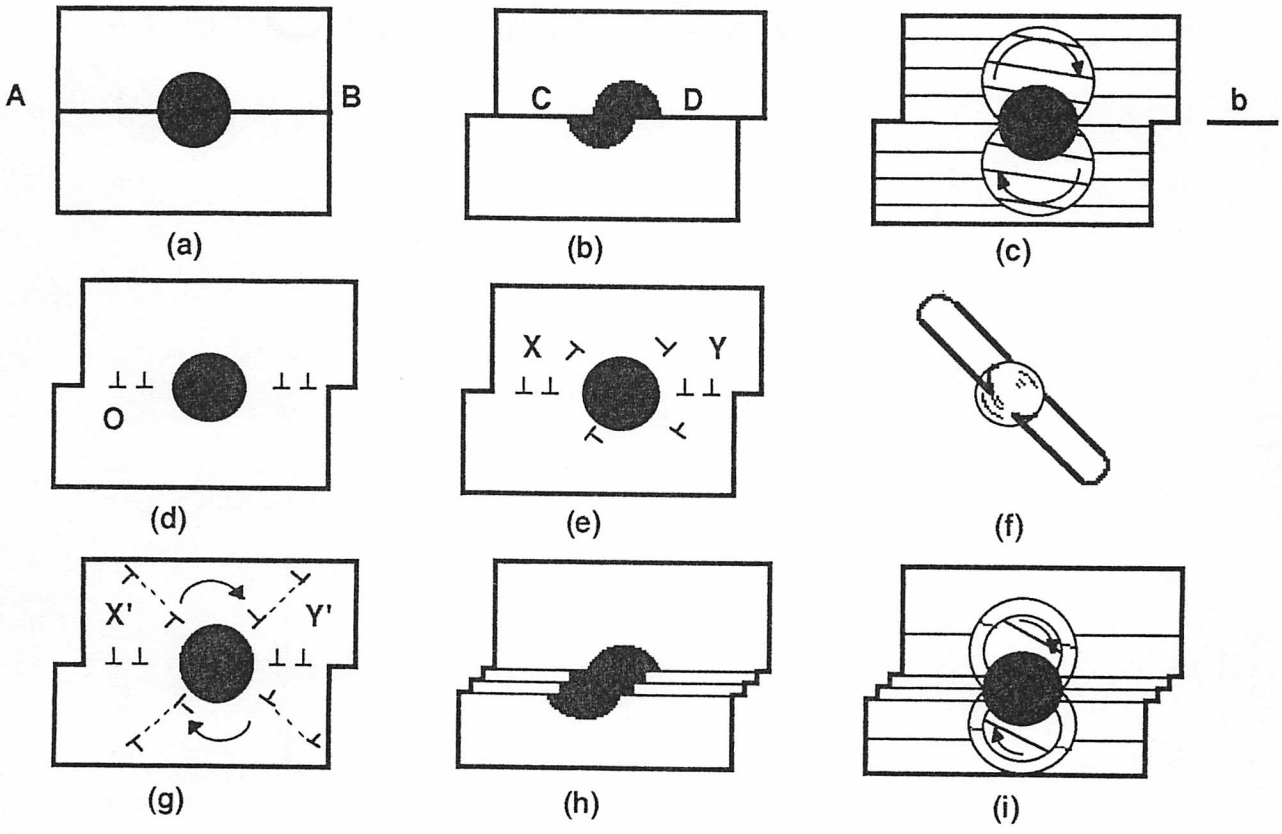

Figure 2.9 The origin of a deformation zone at a particle (Humphreys, 1977).

The early stages in the formation of these rotated regions have been investigated (Humphreys and Stewart, 1972; Chapman and Stobbs, 1969) in fcc alloys and with a primary Burgers vector of $a/2[\bar{1}01]$, regions with rotation axes $[1\bar{1}1]$, $[010]$ and $[111]$ have been identified. In practice, unlike the ideal case of figure *2.9a* several slip planes intersect a particle (figure *2.9h*). This can be taken into account in the continuum model by producing a series of inner subgrains with progressive misorientations (figure *2.9i*). Using the continuum model of figure *2.9* the magnitude of the rotation θ_z is related to the shear strain ϵ, the particle diameter d and the radius of the rotated zone R_r by:

$$\theta_z = \frac{\epsilon d}{2R_r} \tag{14}$$

The value of R_r is difficult to predict, but previous observations (Brown and Stobbs, 1971) suggest $R_r \sim d/2$, and thus $\theta_z \sim \epsilon$. However, if several regions rotate about different axes,

the rotations about any one axis will be less. For the case of fcc metals where three axes have been identified, a value of θ_z corresponding to $\epsilon/3$ might be expected.

In order that particle stimulated nucleation may occur, large deformations are required and therefore the consideration of only one slip system is unrealistic. In principle, the model can take this into account by relating the final orientations around the particle to the amount of slip occurring on each system. The information gathered in the work by Humphreys (1977) investigating the nature of the deformation zones is not sufficient to test the validity of the model, but the results are consistent with it, since a rotation away from the average matrix orientation is found as the particle is approached.

The idealised deformation zone shown in figure *2.9h* is obviously simplified, since in addition to the dislocations required to produce the rotation (geometrically–necessary dislocations), many extra dislocations will occur (statistically stored dislocations (Ashby, 1970)). Thus the total dislocation density within the zone is very high. Using the data of subgrain rotation and distance from the particle, Humphreys has calculated that for a 35° rotation across the deformation zone, a geometrically–necessary dislocation density of 10^{12}cm^{-2} is required.

Many of the statistically stored dislocations are eliminated upon recovery during deformation and annealing, and many of the geometrically–necessary dislocations are rearranged into sub–boundaries, giving a zone such as that shown in figure *2.10a*. Figure *2.10b* shows the substructure coarsening expected upon further annealing, where regions such as A grow to consume surrounding subgrains under the driving force of the reduction in dislocation and boundary energy. Doherty and Cahn (1972) have shown, however, that these rearrangements are opposed by a force arising from long–range elastic interactions. These occur due to the incompatibility between the deformed matrix and the deformation zone which would arise upon a transition from *2.10a* to *2.10b*, and must be accomodated by diffusion processes at the particle/matrix interface.

The experimental evidence suggests that a transition such as this does occur, by non–uniform subgrain growth within the deformation zone through a process of sub–boundary migration and the movement of Y junctions. These stages are essentially similar to the process of polygonisation, the essential difference in the deformation zone process being one of scale. The larger dislocation densities and smaller subgrain sizes in the deformation zone allow a much increased rate of polygonisation, and this is apparent since the deformation zone is seen to coarsen before recovery takes place in regions away from the particles.

The nucleus originating in the deformation zone is shown growing towards and around the particle in figures *2.10c* and *d*. This mechanism may arise from the constraints already outlined, and may be assisted by a higher diffusion rate at particle surfaces, but is also favoured

thermodynamically because by this path the nucleus can grow with the minimum increase in boundary energy. A similar situation occurs in thin films, where nuclei grow towards and along the surfaces.

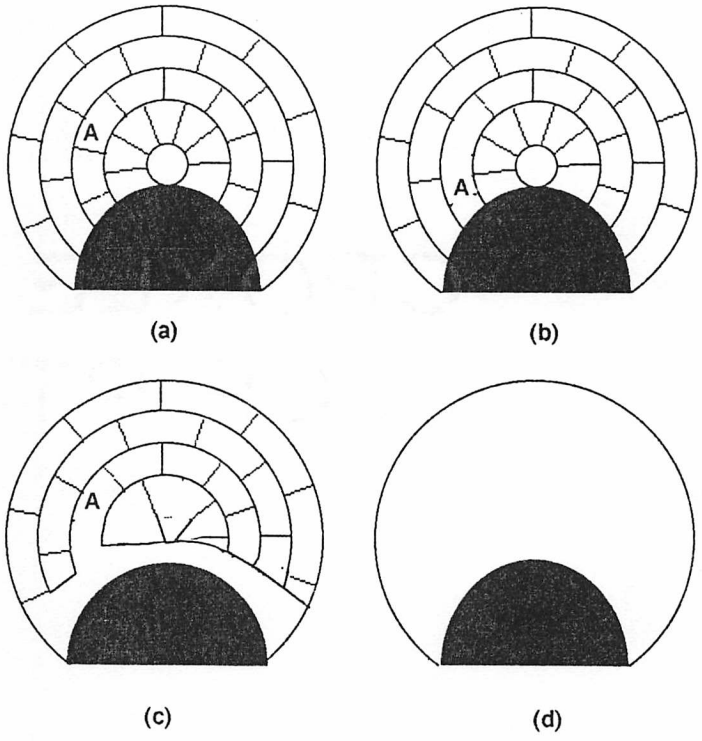

Figure 2.10 The annealing behaviour of a deformation zone (Humphreys, 1977).

The observation of a barrier to growth, after the deformation zone around a particle has been consumed, is assumed to occur due to the lower density of dislocations in the matrix outside of this zone. The driving force for recrystallisation is dependent upon a high energy difference across the recrystallisation boundary, and cannot proceed unless the driving force can overcome the retarding force due to the grain boundary. The general equation for nucleation expresses this:

$$\overline{r} > \frac{2\gamma}{E} \tag{15}$$

where $\overline{r}$ is the radius of the nucleus, γ the grain boundary energy and E the stored energy. Taking $E \sim 6$ erg/g atom and $\gamma \sim 625$ erg cm^{-2}, then $\overline{r} \sim 0.5$ μm. If $\overline{r}$, the radius of curvature of the deformation zone, is taken to be half the particle diameter, then this analysis leads to a critical particle diameter of 1 μm which decreases with increasing stored energy. This prediction is borne out by the results shown by Humphreys (1977). The results suggest that whilst the high dislocation energy and large lattice rotations of the deformation zone provide a viable mechanism for nucleation, the onset of particle–stimulated nucleation is controlled by the thermodynamic criterion.

Humphreys has also found evidence that where particles occur very close together they can form a joint deformation zone with a large effective radius of curvature compared with particle radius, thus decreasing the critical particle radius. Gawne and Higgins (1971) have found evidence to support this in their observations of preferred nucleation at particle clusters and pairs.

The dislocation structures formed around large particles during large strain deformation of polycrystals are highly complex. Each active slip system may produce an independent rotation zone. Multiple zones have been observed at particles, lending weight to the independent–zone model (Humphreys and Kahn, 1990; Kahn and Humphreys, 1988).

The evidence of the experimental work carried out by Humphreys suggests that the orientation of a recrystallised grain is that of a subgrain present in the deformation zone of a particle, and so recrystallisation textures depend upon the range of orientations present in these zones. As mentioned previously, there is a range of related orientations in each zone and there are likely to be several zones with different rotation axes. Therefore, several grains of differing orientations may nucleate from one particle, and this has been observed in alloys with large inclusions (English and Backofen, 1964). In the results of Humphreys' experiments only one nucleus was seen to initiate at each particle, and it is assumed that it does so from a single type of deformation zone, presumably that which has undergone the most rotation.

The misorientation between deformed and recrystallised grains increases with strain, as is to be expected in the deformation zone model. It is interesting to note that this is at variance with the observations of many workers that nuclei supposedly nucleated at precipitates are of random orientations. Doherty (1974) has observed that in single phase materials, nucleation occurs at areas associated with high local lattice misorientations and accelerated local recovery. This is consistent with the model presented by Humphreys, and suggests that it is unlikely that nucleation at second phase particles differs significantly from recrystallisation occurring at other microstructural features.

Chapter 3

EXPERIMENTAL TECHNIQUES

3.1 Experimental Programme for Al–Fe Alloys

As an introduction to the compilation of microtexture data, it was proposed that two rolling schedules be applied to three alloys, each of very high purity, with varying weight percentages of iron. Each alloy was to be given a series of heat treatments after rolling in order to produce varying degrees of recrystallisation. The degree of recrystallisation produced in each specimen was monitored by taking hardness measurements, which are shown in the results chapters. The solubility of iron is illustrated by the aluminium–iron phase diagram in figure *3.1*, and it can be seen that each of the three alloys contain sufficient iron to allow precipitation of intermetallic particles to occur. This is important, since it was intended to investigate the effect of particle–stimulated nucleation on microtexture development.

3.1.1 *Alloy Chemistries*

The three alloy compositions were as follows;

Super–Purity Aluminium with added Iron
(less than 0.0001 wt% impurities)

1.41 wt% Fe 1.06 wt%Fe 0.47wt%Fe

3.1.2 *Rolling Schedules*

The alloys were received in the as-cast state in slabs of 4 cm thickness. A width of 3 cm was removed from each slab for further working. In order to produce material of a sufficient rolling reduction to initiate recrystallisation at relatively low temperatures, rolling schedule I was designed. This consisted of hot rolling at 580°C down to 15 mm, followed by annealing for 1 hour at 380°C. The strips were then cold rolled down to 0.2 mm. A second schedule was designed to allow transmission electron microscopy foils (3 mm diameter) to be taken from the long transverse section and thereby contain enough particles per foil for easy data compilation. Rolling schedule II consisted of hot rolling from a 1 hour anneal at 400°C down to 15 mm and then annealing at 380°C for a further 1 hour before cold rolling down to 4 mm thickness.

3.1.3 *Annealing Programmes*

Each alloy from rolling schedule I was divided into strips of approximately 10 cm in length to carry out heat treatments. A muffle furnace was used to apply heat treatments of 30 minutes, at temperatures of 150°C, 200°C, 250°C, 300°C, 350°C and 400°C. At the end of the annealing

period the specimens were quenched in a salt water bath. A thermocouple was used in all cases to monitor the temperature. For rolling schedule II each alloy was annealed at 200°C and 250°C for periods of 30 minutes, 60 minutes and 90 minutes in a muffle furnace.

3.2 Transmission Electron Microscopy

3.2.1 *Foil Preparation*

Transmission electron microscopy (TEM) specimens were produced from the rolled sheets. Initially, 3 mm diameter discs were removed from close to the centre of the sheets in the case of the specimens from rolling schedule I (*i.e.* in the rolling plane) using a spark erosion technique. For the rolling schedule II specimens (in the long transverse section) discs were taken from within the rolling surfaces. All spark erosion was performed under paraffin in order to minimise specimen heating. The discs were then ground down manually on 1200 grit silicon carbide paper to approximately 75 μm thickness. In order to produce a thin area on the foils, an electro jet-polishing machine was used. The polishing solution used was made up of 85% methanol, 10% perchloric acid, 5% concentrated nitric acid. It was used at approximately -10°C, with a voltage of 25 V applied, giving a current of 100 mA.

3.2.2 *Microscopy Methods*

Each annealed specimen, and also the as-rolled material, was examined using a Phillips 400T transmission electron microscope, operated at 120 kV. On each sample, areas were selected in which grains were clearly defined and reasonably easy to identify. By taking bright and dark field image photographs, a record of the area analysed was obtained in order to identify grains from which diffraction patterns were produced, and also to identify positions of adjacent grains and distinguish between recrystallised and as-deformed material.

Using selected area apertures, diffraction patterns for each individual grain in the area of interest were obtained. Although tilting of the foil was often used to produce a well defined pattern in the first grain of each group, no further tilting was implemented on translating from one grain to the next.

Each foil yielded on average 3 subgrain groups, which consisted of between 5 to 12 subgrains each. It was often the case that the particles were completely or partially removed from the foil during jet polishing, leaving a particle–shaped hole in the foil, as shall be seen in the results sections.

3.2.3 *Microscope Calibration*

In order to identify the rolling direction on the micrographs taken, and also to measure the orientation of the diffraction patterns in relation to the rolling direction, it was necessary to calibrate the transmission electron microscope.

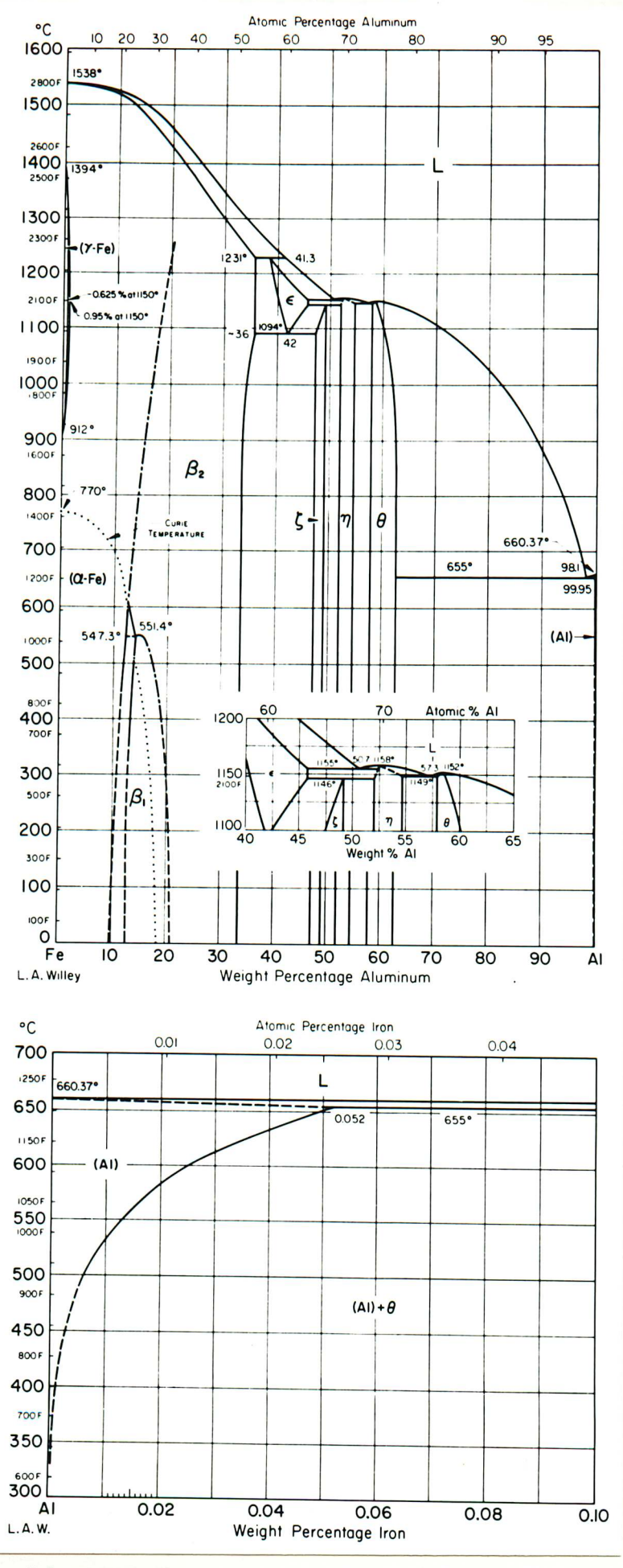

Figure 3.1 The Aluminium–Iron phase diagram (ASM Metals Handbook (Vol 8), 260).

On each foil, the rolling direction was marked by means of notches, added to the disc edges before grinding and polishing took place. The foils could then be placed in the transmission electron microscope specimen holder with the rolling direction aligned along the holder tilt axis, which is also the direction along which the specimen can be moved using one of the specimen shift screws.

The projection of the rolling direction onto the photographic plate was identified by taking double exposure prints; the first with an easily identified feature at one position, and the second with the feature displaced slightly using the specimen shift screw which moves the holder along its tilt axis. The direction of displacement then corresponded to the rolling direction. This procedure was carried out for each magnification that was used in the scope of this analysis.

The rotation of the rolling direction on producing the diffraction pattern then had to be calibrated for each magnification. This was done using molybdenum trioxide crystals placed on a copper grid in the specimen holder. One reasonably perfect crystal was chosen to carry out the analysis, and by again taking double exposure prints, a bright field image could be superimposed upon a diffraction pattern of the crystal. It was then simple to measure the rotation of the rolling direction from the bright field to the diffraction image by identifying the diffracted spot which corresponded to the crystal edge and measuring the rotation angle needed to bring the direction of that spot from the centre spot into coincidence with the crystal edge in the bright field image. This angle of rotation could then be applied to the previously measured rolling directions for the corresponding magnifications to obtain the rolling direction position in the diffraction mode. Care was taken throughout the calibration to ensure accurate focusing.

3.3 Data Interpretation

3.3.1 *Indexing of Diffraction Data*

For each alloy at each annealing temperature, an average of 8 subgrain clusters of 8 to 25 subgrains were analysed, yielding a reasonable cross-section of data with over 60 subgrains analysed. The diffraction pattern for each grain was indexed, and the rolling direction identified using the above calibration.

3.3.2 *Axis–Angle Pair Measurement*

Grains which were seen to be adjacent to one another were used to carry out axis–angle pair measurements, in order to gain information about grain boundary misorientations.

The orientation relationship between a pair of like crystals, the crystallographic bases of which are defined from a common origin, can be described using an axis–angle pair. From this it can be inferred that if one of the crystals is rigidly rotated through the origin, through a right–handed angle of rotation θ, its orientation coincides with that of the other. The axis–angle

pair between two grains was measured by superimposing the diffraction pattern from grain 2 over grain 1, and then using two vectors on each pattern and the angles between vectors 2A and 2B (as shown in figure *3.2*), the common axis for each pattern and the angle required to bring each grain into coincidence can be calculated.

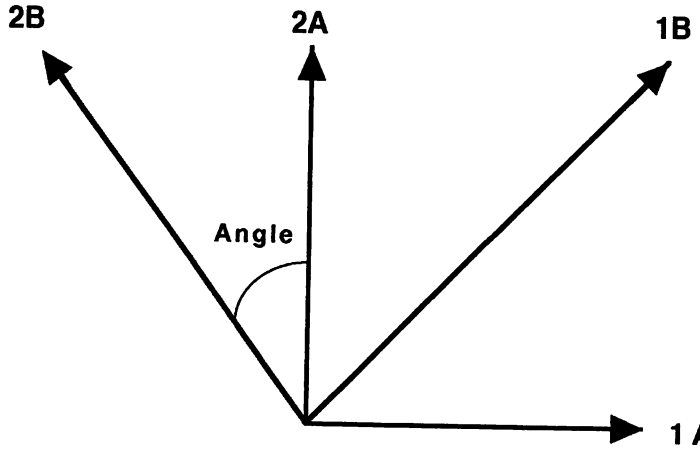

Figure 3.2 Vector positions of two superimposed diffraction patterns from grains 1 and 2.

The preferred method for the calculation of axis–angle pairs from transmission electron microsopy data is through the use of Kikuchi lines, since this affords the greatest accuracy. However, this method proved to be difficult in the present work since the extremely thin samples only yielded very weak Kikuchi line patterns. It was decided that the increase in accuracy given by using the Kikuchi line method was unnecessary in the research carried out here, and the experimental data are based on the conventional selected area diffraction patterns. The zone axis of the pattern can then deviate typically 5° from the optic axis of the microscope, and this can be used as an estimate of error. In fact, this error should be reduced somewhat since the orientations were deduced by examining not the zone axes, but the relationship between pairs of reciprocal lattice vectors from each of the two crystals concerned.

The symmetry of the crystal structure of aluminium (being face–centred cubic, or f.c.c.) means that there are in general 24 crystallographically equivalent descriptions (in terms of axis–angle pairs or rotation matrices) of any orientation relationship calculated. These 24 equivalent operations were generated by multiplying the rotation matrix by the symmetry operations of the f.c.c. structure. Following convention, where listed, the axis–angle pair with the highest angle of rotation is quoted.

The nature of a coincidence site lattice (CSL) boundary can be described by a discrete value known as the Σ value. It represents the reciprocal density of coincidence sites relative to ordinary lattice sites. Thus a boundary which has 1 in 3 of its boundary atoms common to both grains has a Σ value of 3. The value of Σ is a function of the relative orientation of the

two grains, and not of the orientation of the boundary plane. Some CSL relations for cubic crystals are listed in table *3.1.*

By using a computer program (listed in Appendix I) to compare the 24 axis angle pairs produced to a list of CSL relations and their equivalent Σ values, the approximate Σ value for each pair of grains was deduced. It was then easier to display the frequency of low– or high–angle boundaries observed in each sample by means of histograms.

Table 3.1 Some CSL relations for Cubic crystals (Christian, 1965).

Σ	Angle	Axis	Twin axes
3	60.0	⟨111⟩	⟨111⟩, ⟨112⟩
5	36.9	⟨100⟩	⟨012⟩, ⟨013⟩
7	38.2	⟨111⟩	⟨123⟩
9	38.9	⟨110⟩	⟨122⟩, ⟨114⟩
11	50.5	⟨110⟩	⟨113⟩, ⟨233⟩
13a	22.6	⟨100⟩	⟨023⟩, ⟨015⟩
13b	27.8	⟨111⟩	⟨134⟩
15	48.2	⟨210⟩	⟨125⟩
17a	28.1	⟨100⟩	⟨014⟩, ⟨035⟩
17b	61.9	⟨221⟩	⟨223⟩, ⟨334⟩
19a	26.5	⟨110⟩	⟨133⟩, ⟨116⟩
19b	46.8	⟨111⟩	⟨235⟩
21a	21.8	⟨111⟩	⟨235⟩, ⟨145⟩
21b	44.4	⟨211⟩	⟨124⟩

Another possible error in measuring axis–angle pairs other than that accounted for in the omission of Kikuchi lines, is that incurred when twinning is present. The ambiguity in the interpretation from bicrystals is however only present if the same diffraction pattern is produced from both crystals and in an identical orientation, and if the zone axis of the pattern is not an even axis of rotation symmetry.

3.4 Optical Analysis

3.4.1 *Specimen Preperation*

Optical microscopy was conducted by mounting the specimens in a two–fluid–mixing type epoxy resin which hardened within 8 hours at room temperature. The alloys were then ground on 1200 grit silicon carbide paper, and electropolished using the Struers electropolishing solution, and an anodising treatment was carried out using a solution of 0.4% HBF_4 in distilled water at 10 V for 60 seconds.

3.4.2 *Optical Microscopy*

Photographs were taken of the alloy microstructures using a Zeiss Optical microscope with reflected polarised light.

3.5 Hardness Measurements

Hardness measurements were carried out using a load of 10 kg, and an average of at least 7 readings was taken for each specimen.

Microhardness measurements were made on each of the specimens in order to give an idea as to the extent of recrystallisation which had occurred at each temperature. The machine used was a Leitz Miniload, and a load of 245.2 mN was implemented in all cases. For each specimen, 15 indents were recorded over an area of approximately 2 cm^2 and the average result taken as the microhardness value for that specimen.

3.6 Al–Mn–Si Alloy Investigation

A rolled strip of 6063 + Mn alloy was provided by Alcan on which to carry out some preliminary heat treatment experiments to induce directional recrystallisation. The strip was 3 mm thick, and had been homogenised prior to rolling to remove any casting inhomogeneities. The chemical composition of the alloy was as follows:

Mg	Si	Fe	Mn	Ti	in wt%
0.50	0.34	0.20	0.29	0.01	

Two sets of samples of the rolled alloy were heat treated in a muffle furnace (as used previously) at 350°C and 450°C respectively for periods of 30, 60, 120 and 240 minutes. These samples, as well as an as–rolled specimen, were examined optically using methods described above. Micrographs were taken in both the rolling plane and in the short and long transverse sections. Hardness measurements were also taken, in this case using a macrohardness indentor.

Chapter 4

PARTICLE DEFORMATION ZONES

A dispersion of hard particles in a matrix interferes with the normal reorientation processes that occur during deformation, and the texture can be distorted or in some cases prevented from being developed (Thurber & McHargue, 1960). The question of how second phases influence recrystallisation is a complex one, since the effect depends upon the size and dispersion of particles as well as on the stage of precipitation, that is; before or after deformation; before or during recrystallisation (Hutchinson, 1974).

Any inhomogeneities in dislocation density, subgrain size, or subgrain–boundary misorientations produced in a metal matrix during deformation are likely to promote recovery and recrystallisation due to stored–energy gradients produced. Thus it is of great importance that these inhomogeneities are fully understood and characterised.

Other than the qualitative work of Humphreys (chapter 2) in which a picture of the basic mechanisms responsible for local lattice orientation gradients in deformation zones is given, no model has been developed which is capable of predicting the important characteristics of the deformation zone. A recent attempt at this (Humphreys & Kalu, 1990) assumes a soft matrix containing a hard equiaxed particle being deformed in single slip. In the model described, the orientation gradient away from a particle is explained by the formation of an impenetrable zone which spreads out as plastic strain increases.

Most of the models already developed however, deal only with the case of spherical or equiaxed particles, and it is necessary in the case of $FeAl_3$ particles to take into account the anisotropic nature of the deformation zones produced at the needle–shaped particles. This work, therefore, seeks to characterise more fully the nature of the deformation zones at $FeAl_3$ particles in the 1.41 wt% Fe and 0.47 wt% Fe alloys.

4.1 Recovery and Recrystallisation Kinetics

Before a more detailed study of the deformation zones at particles is carried out, a knowledge of the effect of particles on the recovery and recrystallisation kinetics of the alloys is necessary in order to illucidate the role of particles as either enhancing or retarding these processes.

Rolling schedule I was carried out on the three aluminium–iron alloys (in which the alloys were cold rolled from 15 mm down to 0.2 mm) and then annealing treatments of 30 minutes were carried out at 150°C, 200°C, 250°C, 300°C, 350°C and 400°C. Microhardness measurements were then made on the thin strips in order to produce a general overview of the kinetics of recovery and recrystallisation in the alloys.

The drop in hardness as recovery and recrystallisation proceeded could be observed from these results. In figure *4.1(a)* the hardness curve for the 1.41 wt% Fe alloy is seen to take the form of an inverted S–curve, displaying an upper plateau which corresponds to the as–deformed matrix, and a lower plateau corresponding to 100% recrystallisation. The curves for both the 0.47 and 1.06 wt% Fe alloys (figures *4.1(b)* and *4.1(c)*) do not display a lower plateau, suggesting that recrystallisation has yet to be completed even at this temperature of 400°C. The data points show the average of 15 microhardness recordings for each specimen, using standard deviation.

Figure *4.1(d)* shows the three curves superimposed, and illustrates that the upper plateau of each approximately coincide at a similar microhardness value. The lower section of the curve for the 1.41 wt% Fe alloy, however, levels off at a higher microhardness value than the other two alloys. This difference is most likely to be due to the additional precipitate–hardening effects produced by the higher iron content.

The position of the slopes for each alloy is intriguing since the 1.06 wt% Fe alloy slope is displaced towards higher temperatures, with the 0.47 wt% Fe alloy falling between the 1.06 curve on the right and the 1.41 curve on the left. If the precipitates present simply aid recrystallisation, it would be expected that the 0.47 curve would be further to the right than the 1.06 alloy. By comparing the temperature at the midpoint of each curve's slope between the upper and lower plateaux of microhardness values as in table *4.1*, this shift can be seen more clearly. Since, from optical microscopy of the three alloys, it is apparent that the particles are accelerating recrystallisation kinetics as weight percent iron increases, it is suggested that the kinetics of recovery must be playing a major role in producing the hardness curves observed. The shift may be due to the transition from one recovery/recrystallisation mechanism to another from the 0.47 wt% Fe alloy to the 1.06 wt% Fe alloy concentration.

Table 4.1 Midpoint temperature values for the slope of each of the 1.41, 1.06 and 0.47 wt% Fe alloy curves, illustrating shift in curve positions.

Weight Percent Iron	Temperature at 50% Drop in Microhardness	Approximate % Recrystallisation from Metallography
1.41	268°C	25 – 30
1.06	340°C	5 – 8
0.47	288°C	0 – 2

Rolling schedule II was then carried out on just the 0.47 wt% Fe and the 1.41 wt% Fe alloys (in which the alloys were cold rolled from 15 mm down to 3 mm). Annealing was conducted at 250°C for periods of 30, 60, 90 and 120 minutes and microhardness measurements again used as

an indication of the degree of recovery and recrystallisation produced in each specimen. Since only a small amount of recrystallisation was reached even after 120 minutes of annealing, similar alloy specification samples were later heat–treated at higher temperatures to give an idea of the fully recrystallised hardness value for comparison, and this was found to be approximately 30 HV.

The hardness curves for the 0.47 and 1.41 wt% Fe alloys are shown in figure *4.2*, all measurements having been taken in the long transverse section. The data points show that the 1.41 wt% Fe alloy displays a higher overall Vickers hardness as compared to the 0.47 wt% Fe alloy. As expected from the higher precipitate hardening effect, the difference is exaggerated as compared to the data of rolling schedule I because the measurements are taken in the long transverse section in the second rolling schedule, as opposed to the rolling plane, and any change in iron content will produce a more pronounced change in particle separation and area fraction. The effects of these parameters are discussed later in this chapter.

In both the alloys deformed under rolling schedule II, the early stages of annealing shown in the hardness data produce primarily recovery processes, in which subgrains undergo a 'cleaning up' process with the movement of dislocations towards subgrain and grain boundaries. It was observed that subgrains remained at approximately their original as–deformed sizes for at least the first 60 minutes of annealing in the case of the 1.41 wt% Fe alloy, and for longer periods in the 0.47 wt% Fe (illustrated in chapter 5). During this time however, one or two subgrains adjacent to precipitates within a subgrain cluster appeared to be in a favourable state for subsequent recrystallisation nucleation due to their relatively dislocation–free condition. These subgrains, during data collection, and in the literature below are described as 'potential nuclei'. In only the 1.41 wt% Fe alloy were signs of true recrystallisation observed within the temperature–time scale illustrated in figure *4.2*, and this contributed to the further drop in hardness from 90 to 120 minutes annealing time.

In comparing the hardness values for rolling schedule I with rolling schedule II, the lower interparticle spacing necessarily produced in the greater rolling reduction of the former, and its effect on recovery and recrystallisation kinetics can be assessed. The drop in hardness from the as–rolled samples of the two classes of specimens, to an anneal of 250°C for 30 minutes was compared by calculating the following:

$$\frac{HV_{initial} - HV}{HV_{initial} - HV_{final}} \qquad (1)$$

and these values are displayed in table *4.2*. The larger the value given, the quicker the kinetics involved. A larger drop can be seen for the rolling schedule I alloys, suggesting an acceleration in recovery and recrysallisation mechanisms with increased rolling reduction. This is expected since schedule one is associated with a higher as–deformed hardness and hence a larger stored

Table 4.2 Comparison of hardness drops from as-rolled to 250°C, 30 minute anneal samples for rolling schedules I and II.

Weight Percent Iron	Vickers Hardness Drop (HV) Rolling Schedule I	Vickers Hardness Drop (HV) Rolling Schedule II
1.41	0.4	0.03
0.47	0.1	0.03

energy.

The interparticle spacings and distributions for each of the alloys of rolling schedule II are shown in figures *4.3* and *4.4*. The particles in the 1.41 wt% Fe alloy as shown in figure *4.3* were characterised as being approximately $1-7$ μm in length and $0.2-0.5$ μm in width. They were not uniformly dispersed, but occurred in bands of approximately $10-20$ μm in width and $20-40$ μm apart along the normal direction of the long transverse plane. The mean particle spacings (again along the normal direction) within the bands were found to be $1-6$ μm. The particles are non-shearable and it would therefore be expected that the matrix close to each particle would of necessity have to undergo quite complex deformation to accomodate the general deformation processes during rolling, and that the deformation gradient would be greatest close to the particle/matrix interface. In comparison, the particles in the 0.47 wt% Fe alloy were $0.8-4.0$ μm in length and $0.1-0.4$ μm in width occurring in bands of approximately $2.0-5.0$ μm in width and $100-200$ μm apart in the normal direction. The mean particle spacings (again along the normal direction) within the bands were $0.4-1.2$ μm (figure *4.4*).

Transmission electron micrographs of the 1.41 wt% Fe and 0.47 wt% Fe alloys of rolling schedule II, taken at very low magnification, are shown in figures *4.5* and *4.6* respectively, the particles showing up as bright on the dark thin area (since they have been prefentially etched out), giving a map of their distribution. The data in table *4.2* illustrate a deceleration in kinetics for both alloys as the deformation is reduced, and this is expected due to the accompanying decrease in stored energy. In rolling schedule I however, the transition from as-rolled to a 250°C, 30 minute anneal results in recrystallisation, whereas in the second rolling schedule only recovery has occurred. This fact may explain the apparent reversal in kinetics between the two alloys for the different rolling schedules, since the smaller interparticle spacing inherent in the higher iron alloy, which has already been mentioned, and the larger average particle size as compared to the lower iron content alloy accelerates recrystallisation, but retards general recovery. This phenomenon is probably related to the unusual shift in the position of the 1.06 wt% Fe alloy hardness curve shown previously. This alloy may have a particle dispersion which although able to retard recovery, is not able to accelerate recrystallisation sufficiently to cancel this effect.

Figure *4.7* shows an optical micrograph taken of the 1.41 wt% Fe alloy rolled under schedule I and annealed at 400°C for 30 minutes giving complete recrystallisation. As can be seen, the grain sizes produced correspond to the particle spacings, and in areas relatively free of particles the grain sizes increase. This suggests that recrystallised grains are pinned by particles. A specimen exhibiting partial recrystallisation after an anneal at 300°C for 30 minutes is shown in figure *4.8* in which it can be seen that the recrystallised grains are most frequently associated with $FeAl_3$ particles, suggesting that nucleation is stimulated by the presence of particles.

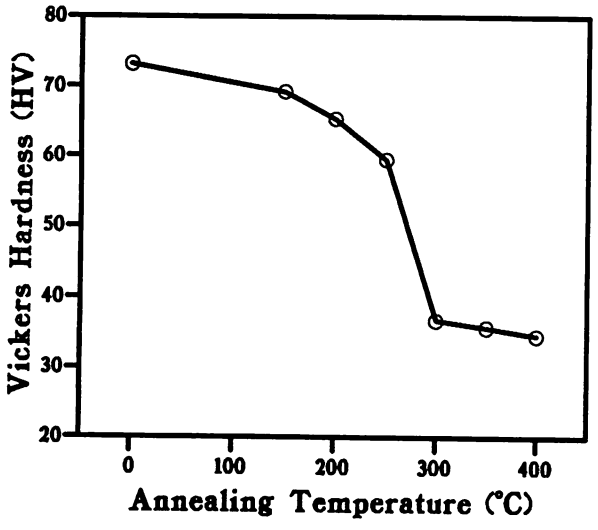

(a)

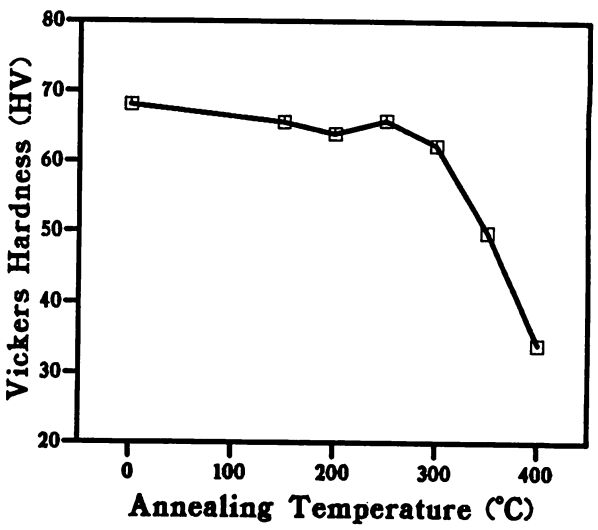

(b)

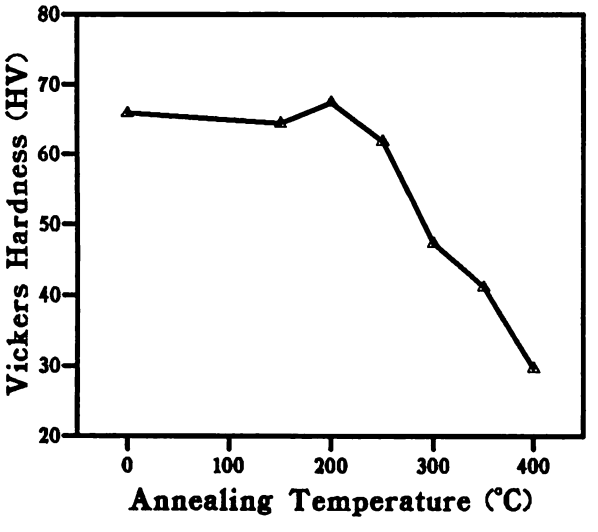

(c)

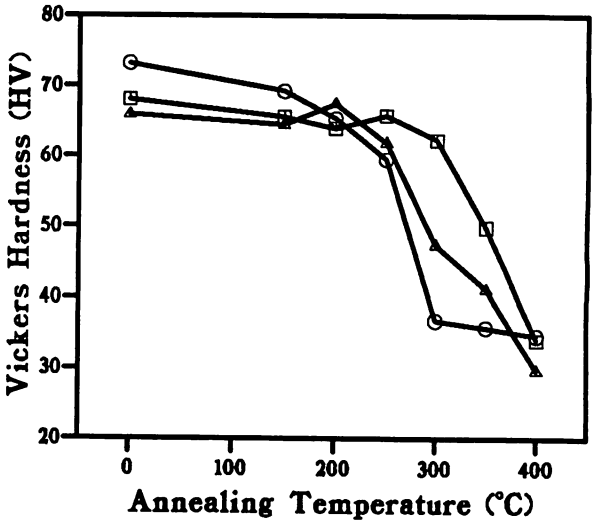

(d)

Figure 4.1 Microhardness data for (a) the 1.41 wt% Fe alloy, (b) the 1.06 wt% Fe alloy, (c) the 0.47 wt% Fe alloy, and (d) the 1.41, 1.06, and 0.47 wt% Fe alloys combined, rolling schedule I. Legend: Circle - 1.41 wt% Fe, Square - 1.06 wt% Fe, Triangle - 0.47 wt% Fe.

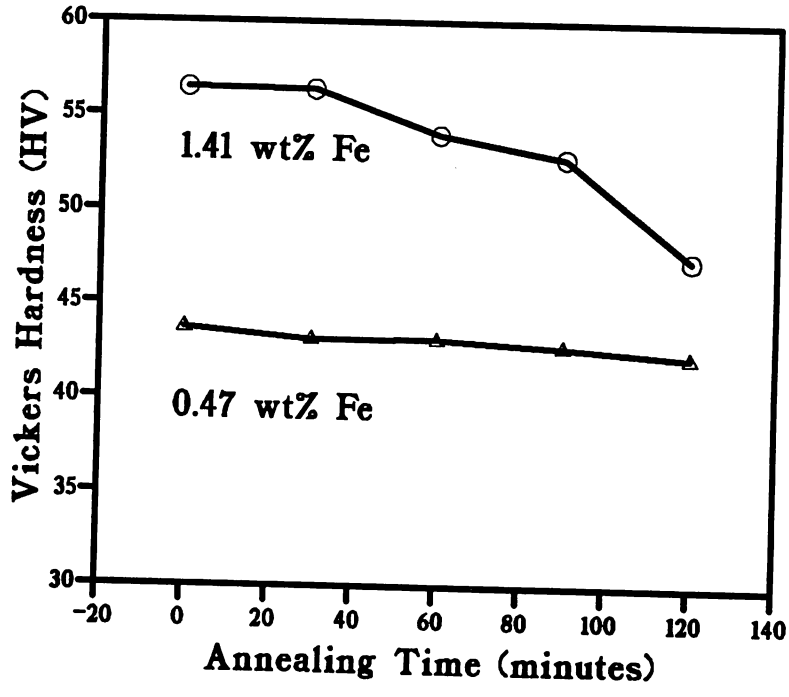

Figure 4.2 Hardness data for the 1.41 wt% Fe and 0.47 wt% Fe alloys, rolling schedule 2.

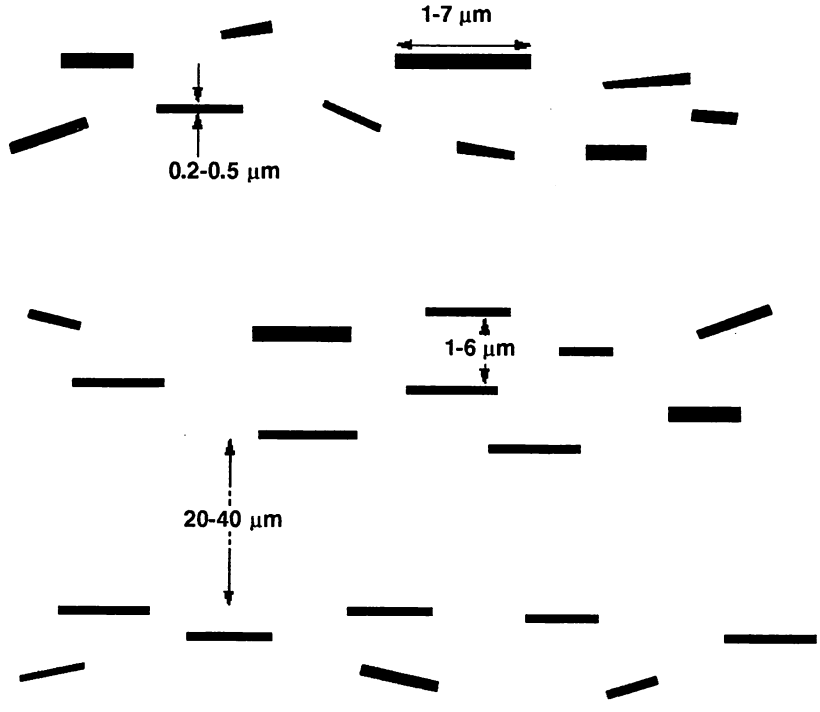

Figure 4.3 Schematic diagram showing particle distribution for the 1.41 wt% Fe alloy, rolling schedule II.

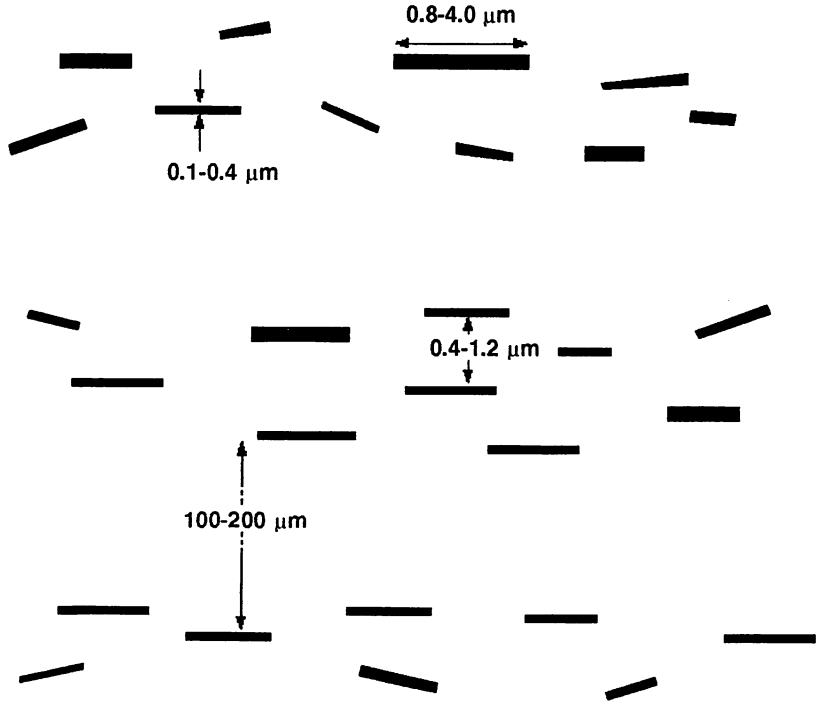

Figure 4.4 Schematic diagram showing particle distribution for the 0.47 wt% Fe alloy, rolling schedule II.

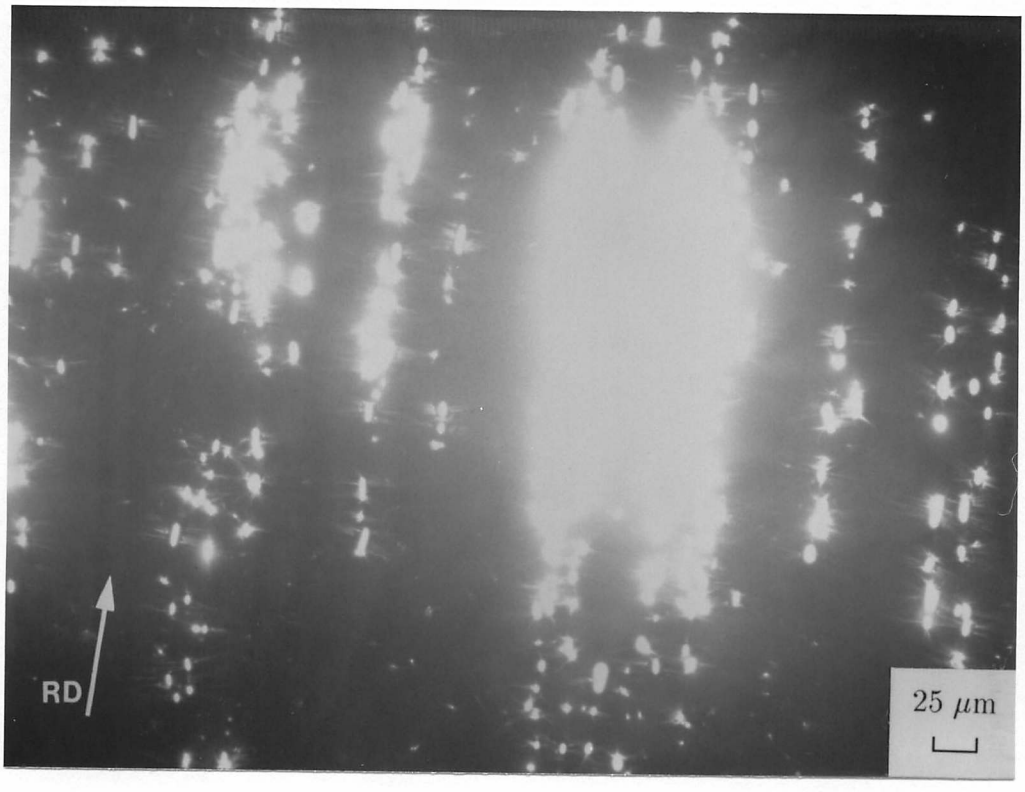

Figure 4.5 Transmission electron micrograph taken in the long transverse section showing particle distribution for the 1.41 wt% Fe alloy, rolling schedule II.

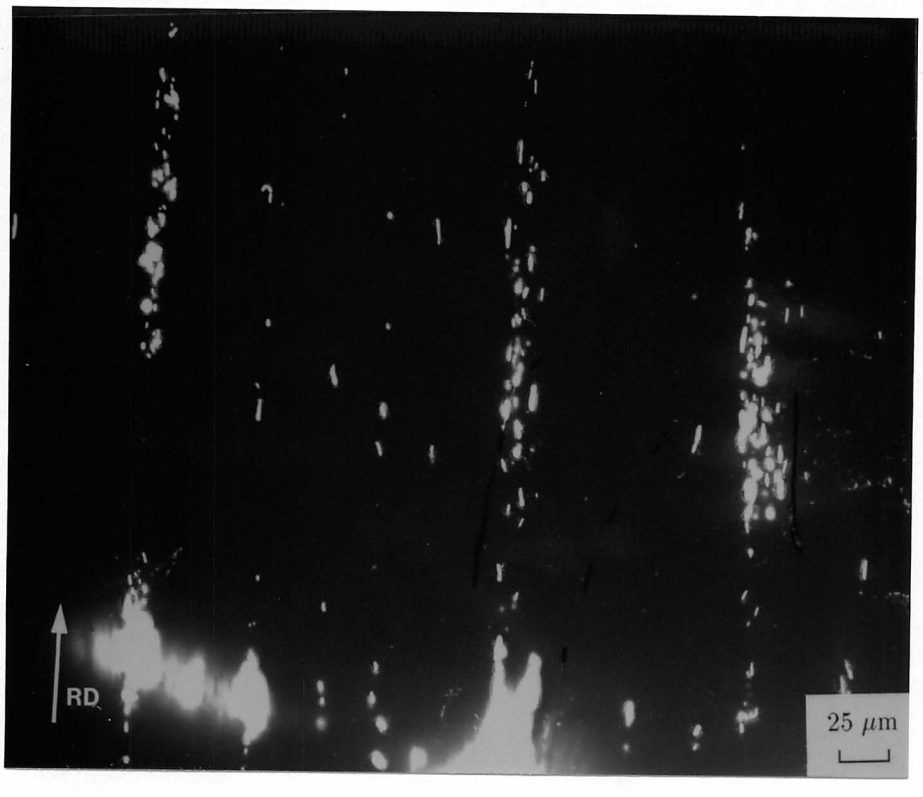

Figure 4.6 Transmission electron micrograph taken in the long transverse section showing particle distribution for the 0.47 wt% Fe alloy, rolling schedule II.

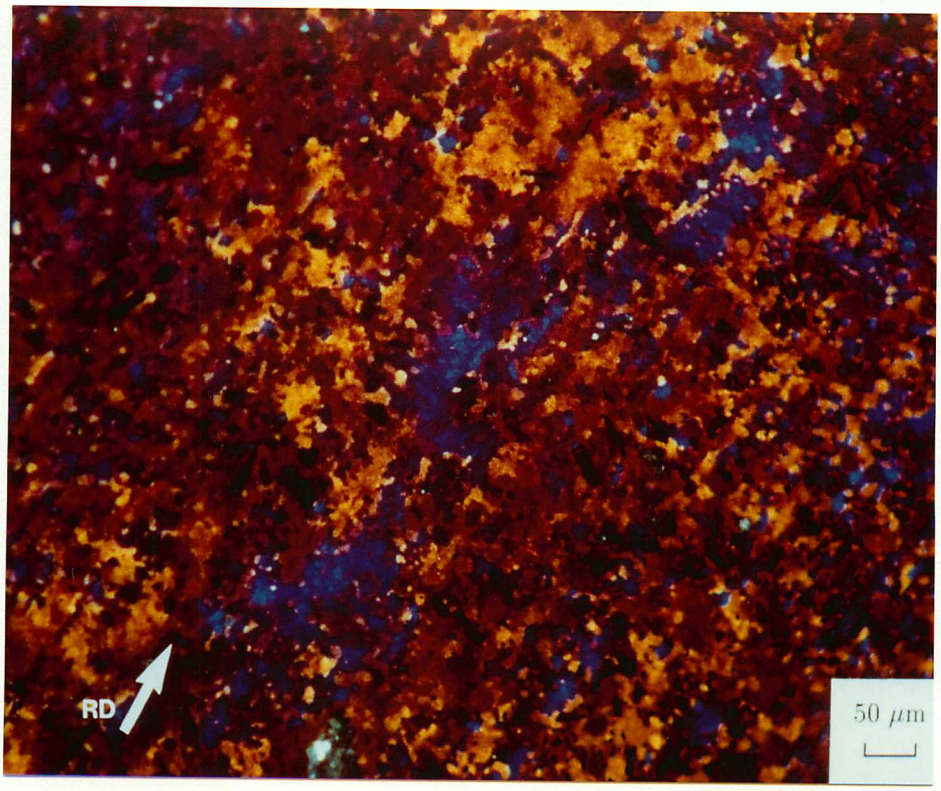

Figure 4.7 Optical micrograph in the rolling plane showing the 1.41 wt% Fe alloy, annealed at 400°C for 30 minutes giving partial recrystallisation, rolling schedule I.

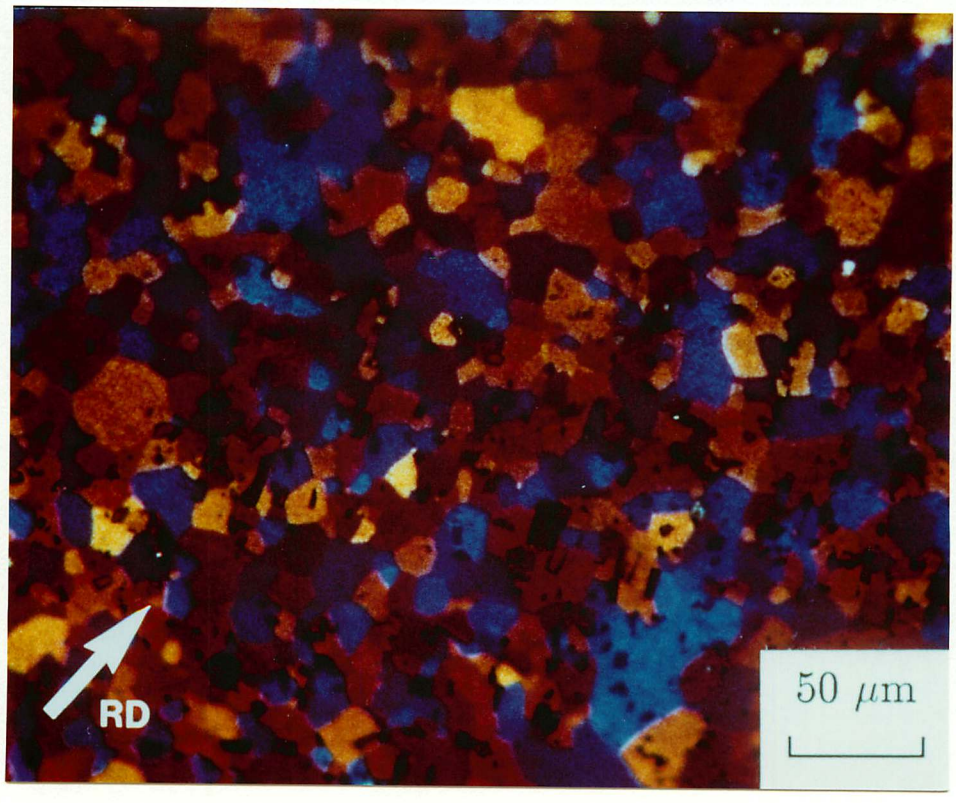

Figure 4.8 Optical micrograph in the rolling plane showing the 1.41 wt% Fe alloy, annealed at 300°C for 30 minutes giving full recrystallisation, rolling schedule I.

4.2 Particle Deformation Zone Characterisation

The deformation zones around needle–shaped $FeAl_3$ particles in the 1.41 wt% Fe alloy were characterised by studying the as–rolled microstructure from the second rolling schedule (cold rolled from 15 mm down to 3 mm). In these specimens it was possible to take transmission electron microscopy foils from the long transverse section to allow a sufficient number of particles to be observed in a given foil.

Areas free from precipitates, that is between the precipitate bands, displayed the normal elongated subgrain and grain structure typical of heavily cold rolled aluminium alloys. Some light shear banding was also observed, as shown in figure *4.14*. Within precipitate bands, the normal deformation accomodation process has obviously been interrupted by the precipitates, and the elongated subgrain structure is disturbed in the vicinity of particles (figure *4.15*). It was noted that most of the particles were approximately aligned along the rolling direction, but occasionally particles occurred with their long dimensions at an angle to the rolling plane of as much as 45°. These particles appeared to cause a much greater disturbance to the deformed microstructure (figure *4.16*).

In figure *4.17* the region surrounding an $FeAl_3$ particle aligned along the rolling direction is shown. There appears to be a greater degree of deformation at the particle tips, which is deduced from the relatively small subgrain size and high dislocation density as compared to the regions adjacent to its longer dimension. In the 1.41 wt% Fe alloy a typical deformation zone at a particle consisted of subgrain clusters of 0.4 μm average diameter up to a distance of 0.8 μm from the particle/matrix interface at particle ends, and of an average size 0.6 μm up to a distance of 1.5 μm from the interface at particle sides. Away from particles, subgrains were typically $0.2 - 0.55$ μm thick and $1 - 2$ μm long.

As has been suggested in much of the previous work outlined, there will be a deformation and crystallographic orientation gradient in a direction away from the particle/matrix interface. To characterise these factors in the particle deformation zones in this alloy, measurements of the orientations of the subgrains close to the particles were made. This was done by comparing the orientation of these subgrains with a subgrain located in the particle free matrix at a distance of $1 - 2$ μm from the particle/matrix interface. Referring to figure *4.12*, which shows a schematic view of a particle and its associated deformation zone, a diffraction pattern from the subgrain in question, A, was compared to an elongated subgrain diffraction pattern at B. The orientation relationship between these two grains was termed the 'remote orientation'. In order to give a simple classification of these misorientations, which would indicate the presence of low or high energy boundaries, each remote orientation was expressed in the form of a coincidence site lattice value, Σ, as described in chapter 3.

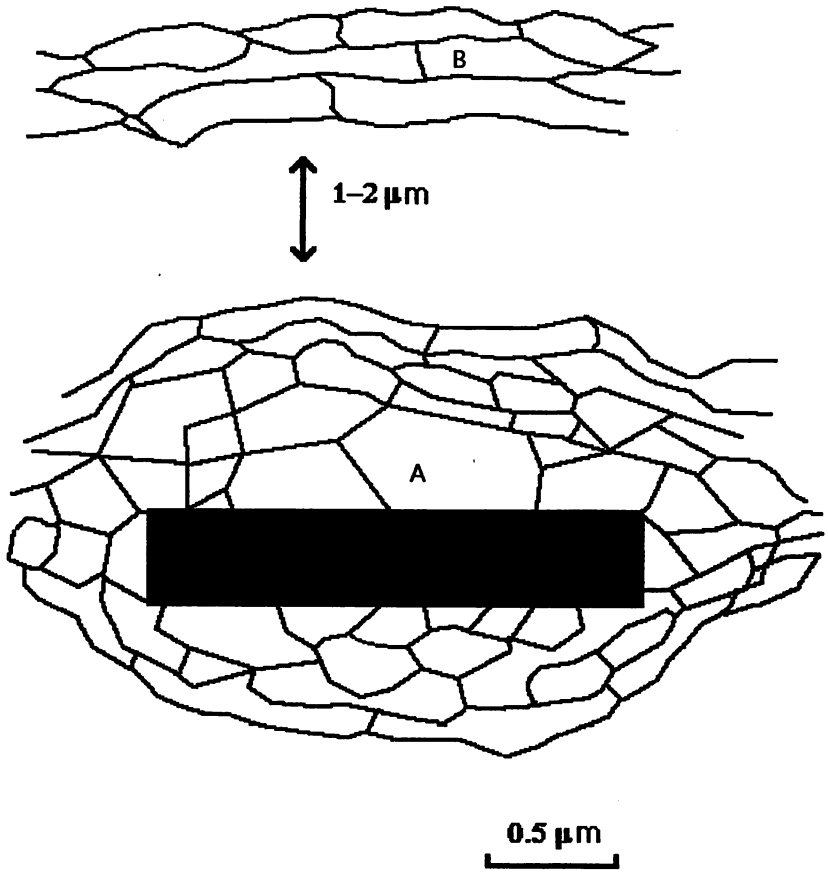

Figure 4.9 Schematic diagram showing a particle and deformation zone, with the positions of diffraction data recorded to calculate 'remote orientations'.

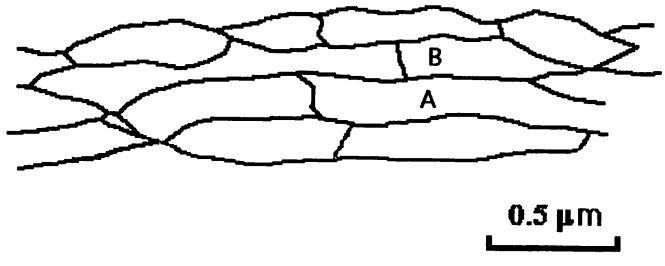

Figure 4.10 Schematic diagram showing the deformed matrix away from particles, with the positions of diffraction data recorded to calculate neighbouring subgrain orientations.

Figure *4.16* shows a histogram of experimentally measured remote orientation Σ–values for subgrains adjacent to particles. It is evident that the misorientations are frequently quite large. This can be compared to figure *4.17* which shows Σ–values measured between neighbouring elongated subgrains in the remote matrix (shown schematically in figure *4.10*). The elongated subgrains in this case display predominantly only small misorientations (large misorientations arise from axis angle pair measurements taken across grain boundaries as opposed to subgrain boundaries), and so the effect of particles on the subgrain misorientations becomes more apparent - a major perturbation is caused by the presence of particles.

It was observed also that for a given particle, the Σ–values (corresponding to the remote

orientations) for a group of subgrains lying close together at a particle tended to be similar. This is illustrated schematically in figure *4.11* where each of the subgrains A,B,C,D and E when compared to subgrain F to give a remote orientation value, all display the same Σ–value. This might be expected since the deformation gradient may not vary much along the length of a particle. Each cluster was then identified by the dominant Σ–value for the cluster and recorded as a single data point. A distinction was then made between clusters located along the long dimension of a particle (or side, as in subgrains A,B,C,D and E of figure *4.14*) and those occurring at the particle ends (subgrains G,H,I and J).

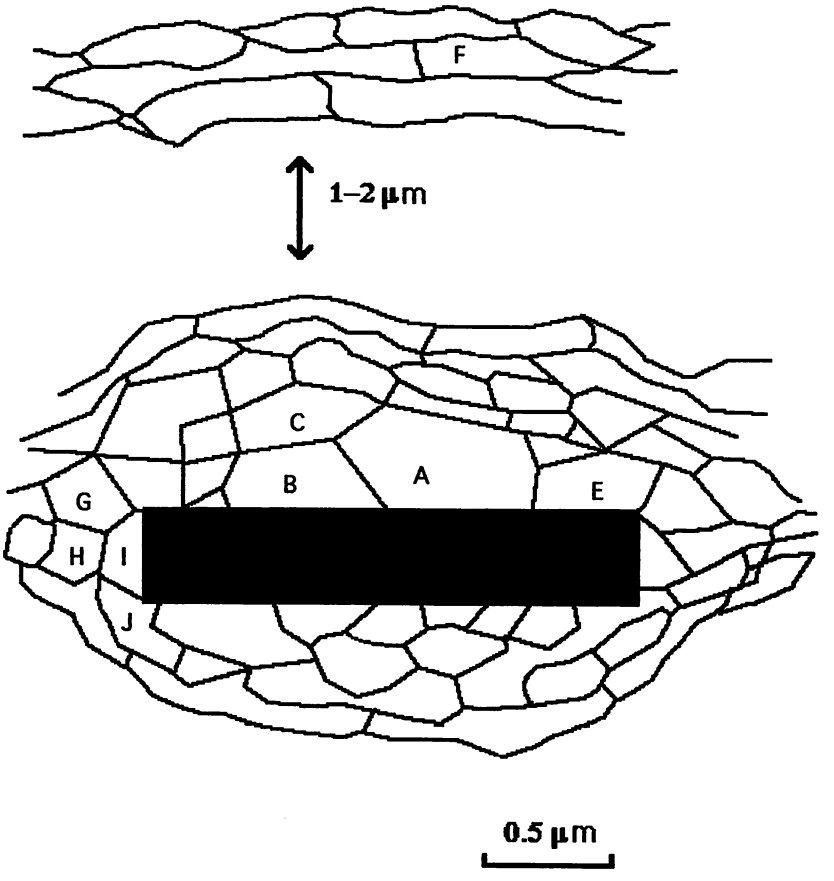

Figure 4.11 Schematic diagram showing a particle and deformation zone, with the positions of diffraction data recorded to calculate 'remote orientations' for clusters of subgrains.

From histograms for these results (figure *4.18*) it can be seen that there is a sharp distinction between end clusters, which contain large Σ–values, and side clusters, which are predominantly of low Σ–value. This is another indication that the matrix close to particle ends suffers greater deformation than at the sides. In subsequent annealing treatments it was observed that potential nuclei, and subsequent primary recrystallisation, occurred more frequently at particle tips rather than at particle sides. This is expected due to the higher dislocation density and greater rotation of subgrains associated with higher deformation strains occurring at particle ends during deformation.

On studying the 0.47 wt% Fe alloy in the as–rolled condition it was found that the smaller particle sizes gave a less pronounced deformation zone around individual particles, as shown in figure *4.19.* Also, few particles were found which were oriented at an angle greater than 20° to the rolling direction. However, particles within bands of the 0.47 wt% Fe alloy displayed a much smaller particle separation than within the bands of the 1.41 wt% Fe alloy, and the combined effect of the particles produced 'strips' of subgrains which, rather than being elongated with a high dislocation density, were much more equiaxed, and relatively free of dislocations. This is shown in figure *4.20.*

The 'remote' orientations for subgrains occurring within the strips of the 0.47 wt% Fe as–deformed alloy are shown in figure *4.21* and display a similar distribution to those in the 1.41 wt% Fe alloy, although there is a higher incidence of low sigma–value misorientations than high. Presumably this is due to the subgrains within the strips mentioned, which appear to be protected form high deformation. Misorientations between elongated subgrains in the as–deformed areas away from particle bands are shown in figure *4.22* and again there are very few high sigma–value misorientations, these being attributable to grain boundaries. These two graphs show that the particles in the 0.47 wt% Fe alloy again produce a perturbation of deformation in the matrix, but that this is less pronounced than in the 1.41 wt% Fe alloy. This is expected as a result of the smaller deformation zones found at individual particles and also due to the low deformations within strips.

'Remote' orientation cluster data for the 0.47 wt% Fe as–deformed alloy are shown in figure *4.23* with the usual distinction between end and side subgrains. This distinction however, in the case of the 0.47 wt% Fe alloy, was difficult to make due to the close proximity of particles - a subgrain could be close to the end of two particles, or close to the end of one and side of another. As a result, the frequency distributions for the two cluster–types are similar. The results given are again similar to those for the 1.41 wt% Fe alloy if the distinctions between end and side in the lower iron–content alloy are ignored. It may be that in the case of the shorter particles in the 0.47 wt% Fe alloy, similar degrees of deformation are produced along the sides of particles as at the ends, and so a distinction between the two is unnecessary. Upon annealing of the 0.47 wt% Fe alloy, potential nuclei appear reasonably uniformly throughout the strips of equiaxed subgrains described, and distinction between end and side clusters became more difficult.

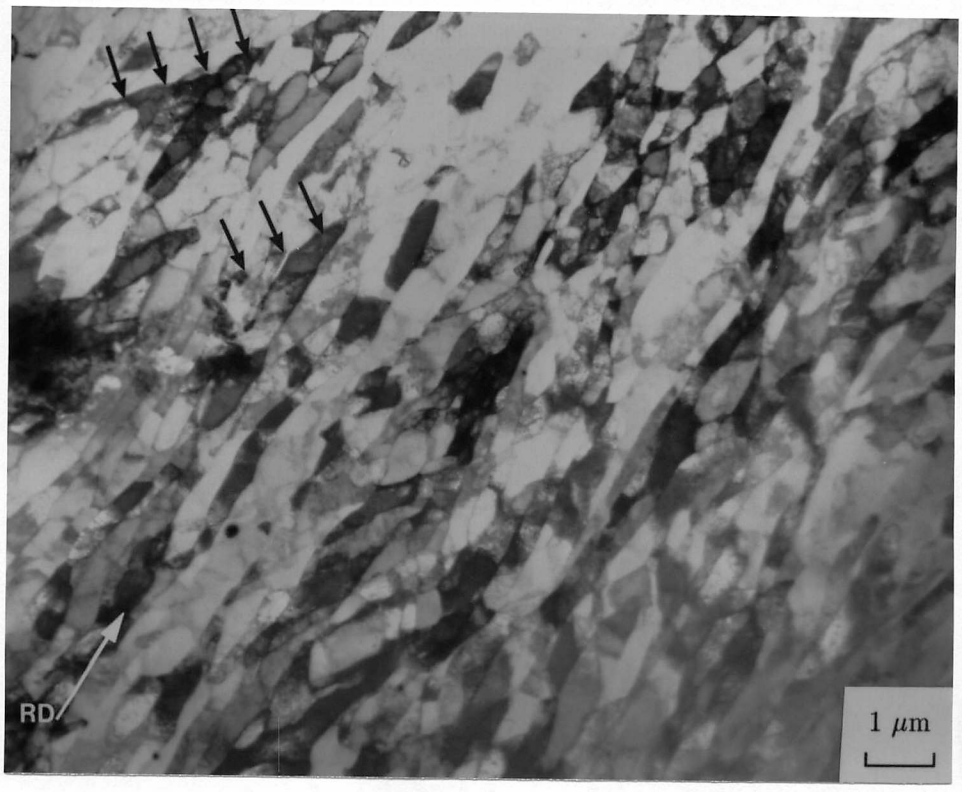

(a)

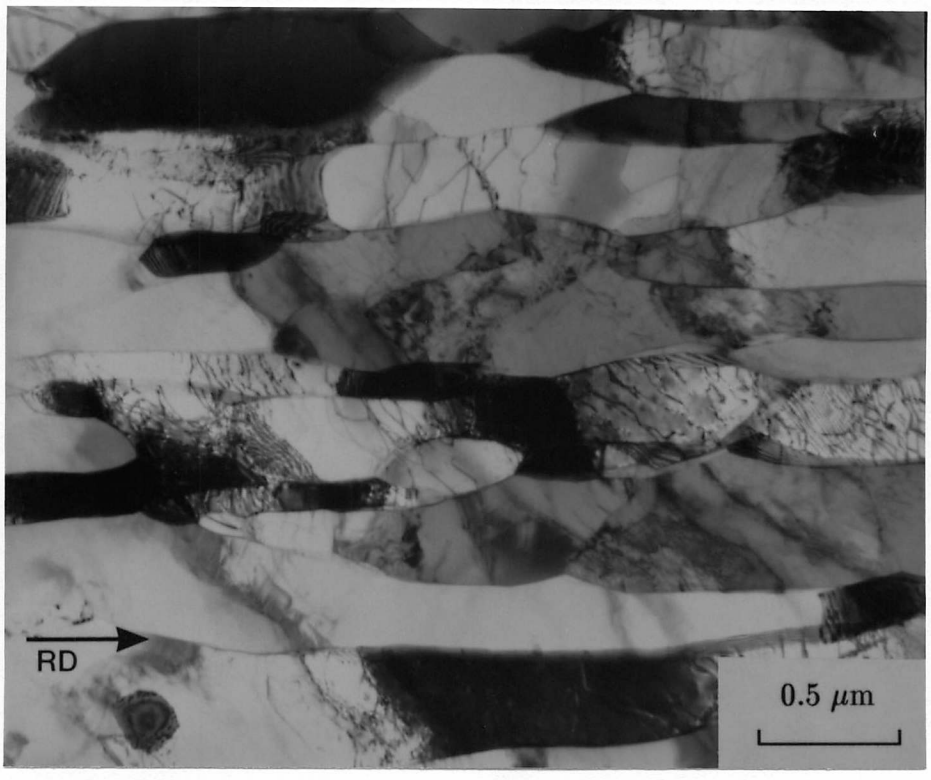

(b)

Figure 4.12 (a)Transmission electron micrograph taken in the long transverse section showing the microstructure of the 1.41 wt% Fe alloy in the as–rolled condition away from particles (shear banding indicated). (b) A similar area shown in the 1.41 wt% Fe alloy annealed at 250°C for 30 minutes showing some recovery. (Rolling schedule II).

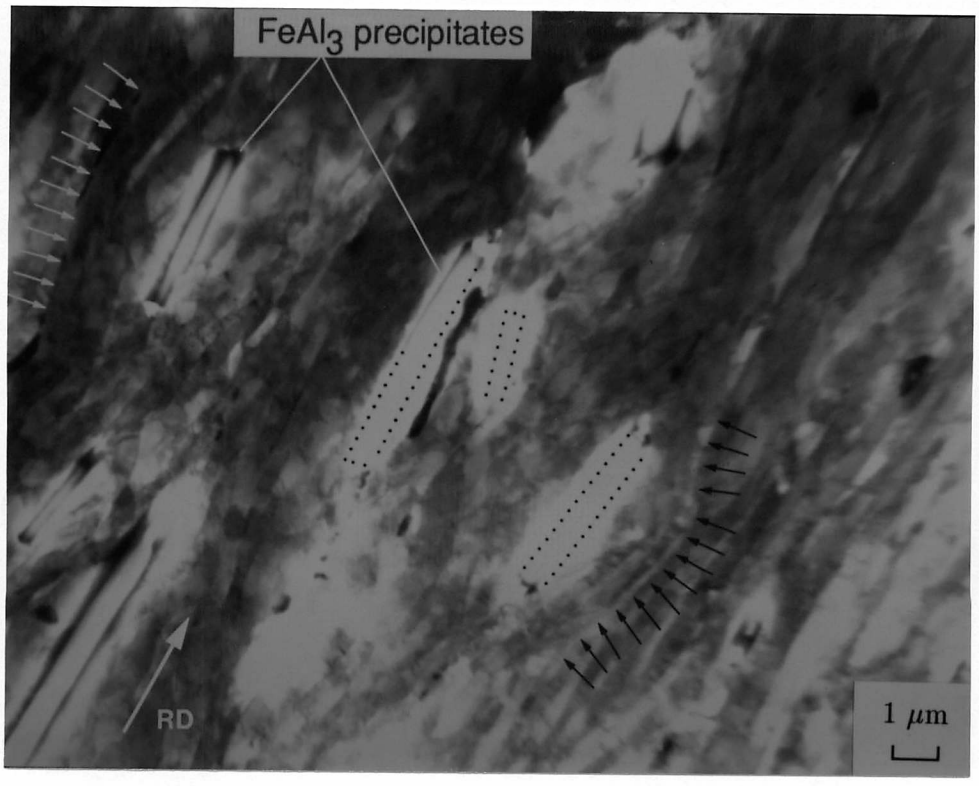

Figure 4.13 Transmission electron micrograph taken in the long transverse section showing the microstructure of Al–1.41 wt%Fe alloy in the as–rolled condition within a particle band with discontinuities in deformation indicated. Note that some precipitates are fully or partially etched out during polishing, and their original positions are shown with dotted lines. (Rolling schedule II).

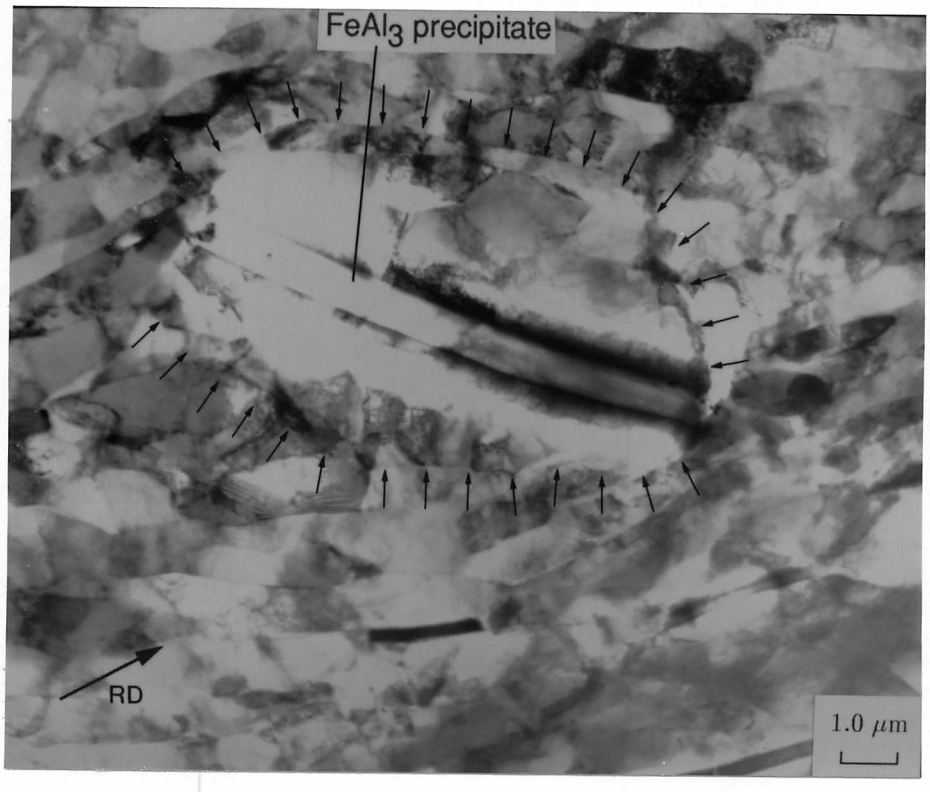

Figure 4.14 Transmission electron micrograph taken in the long transverse section showing the microstructure of Al–1.41 wt%Fe alloy in the as–rolled condition within a particle band where a particle is oriented at 40° to the rolling direction (edge of deformation zone indicated).

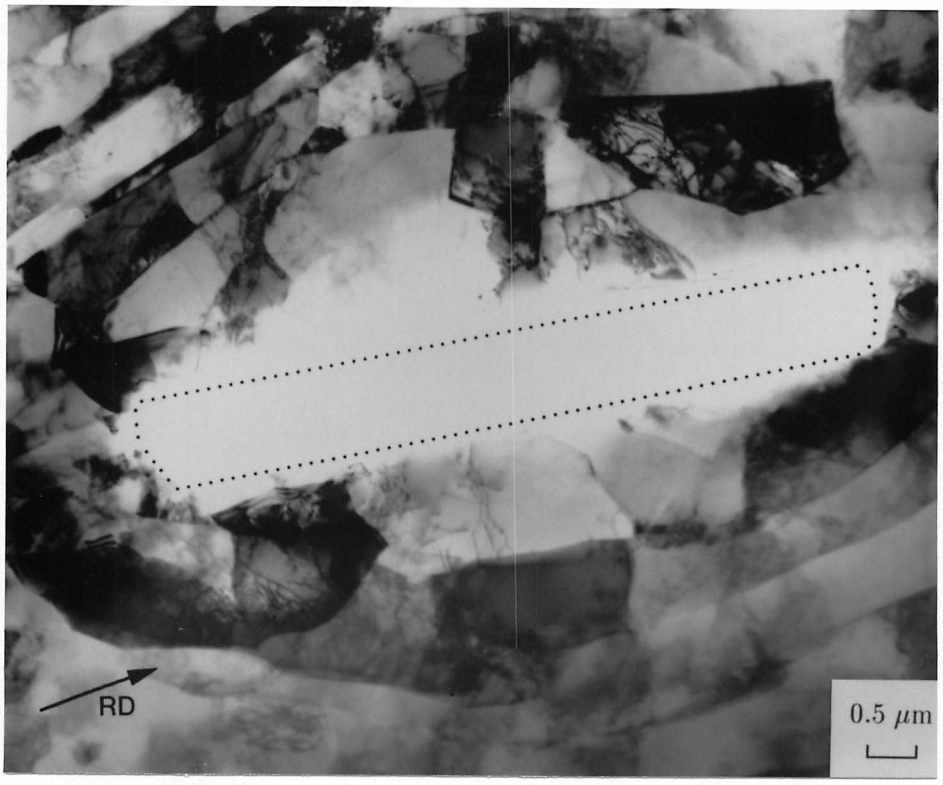

(a)

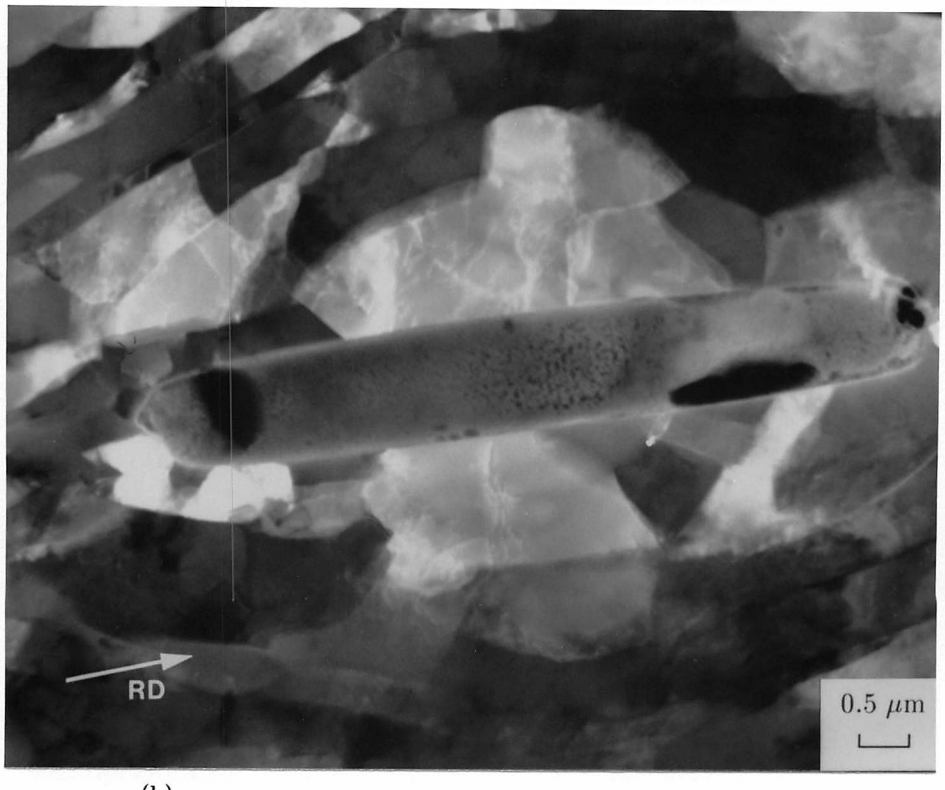

(b)

Figure 4.15 Transmission electron micrograph taken in the long transverse section showing the microstructure in the proximity of a $FeAl_3$ particle aligned along the rolling direction in the 1.41 wt% Fe alloy in the as–rolled condition. (a) Bright field, (b) dark field.

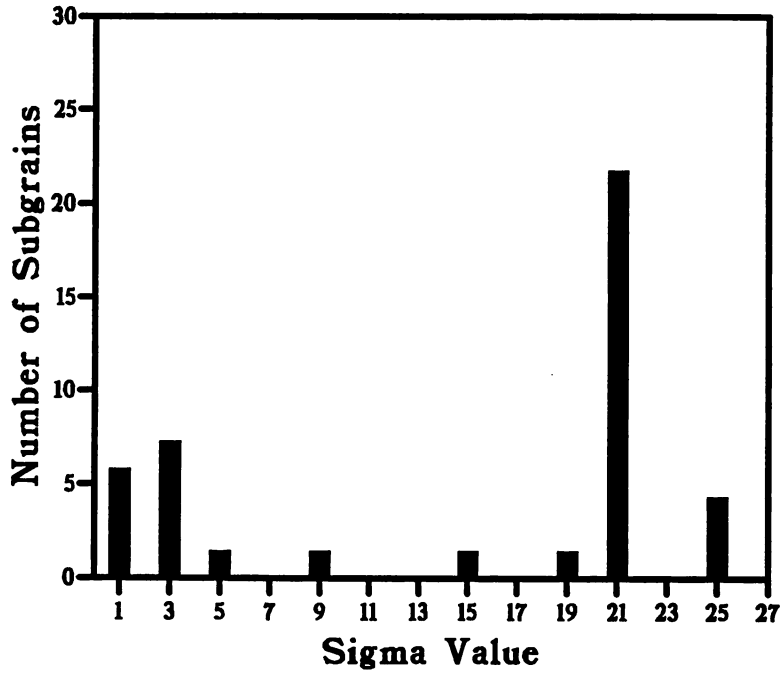

Figure 4.16 'Remote orientations' for subgrains adjacent to particles in the as–deformed 1.41 wt% Fe alloy.

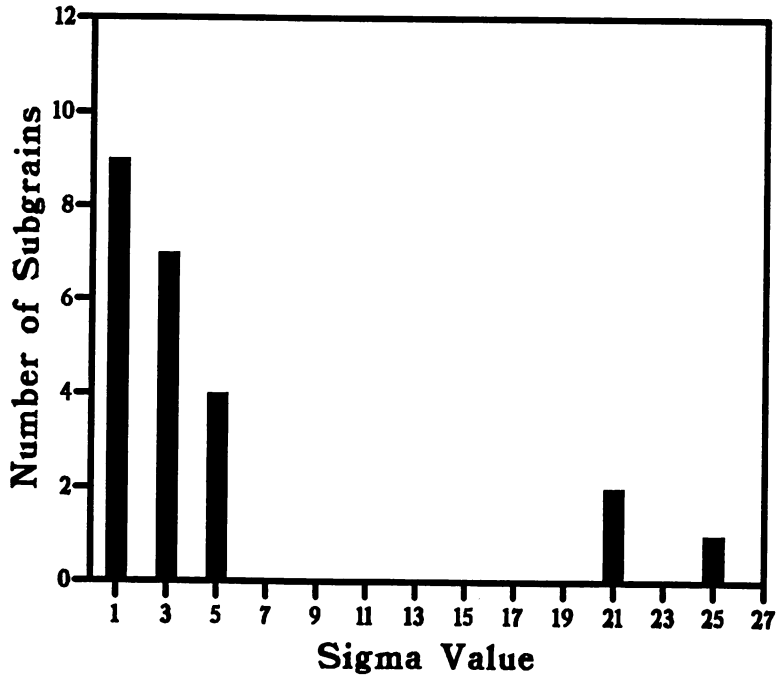

Figure 4.17 Misorientations between adjacent neighbouring subgrains in the deformed matrix away from particles in the as–rolled 1.41 wt% Fe alloy.

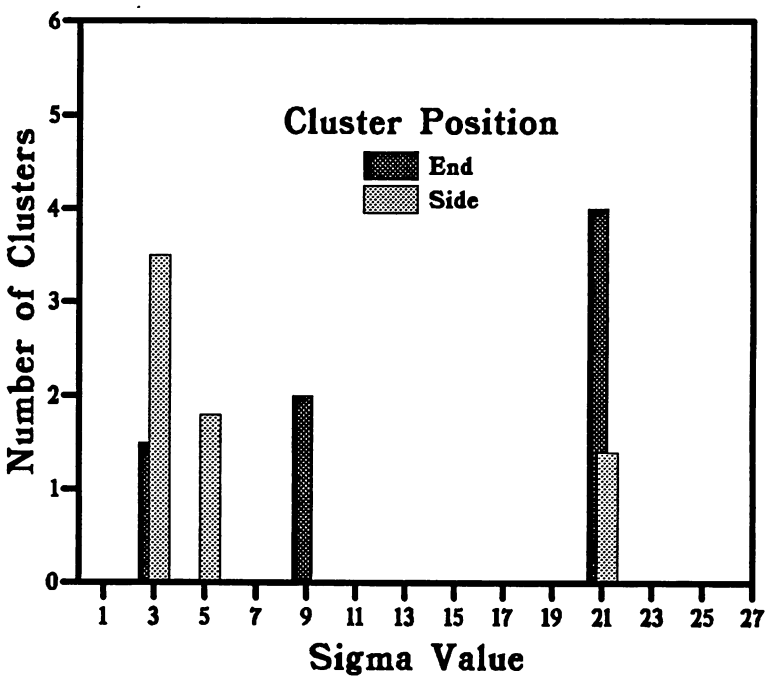

Figure 4.18 The frequency of subgrain–cluster 'remote orientations' adjacent to particles in the as–deformed matrix of the 1.41 wt% Fe alloy.

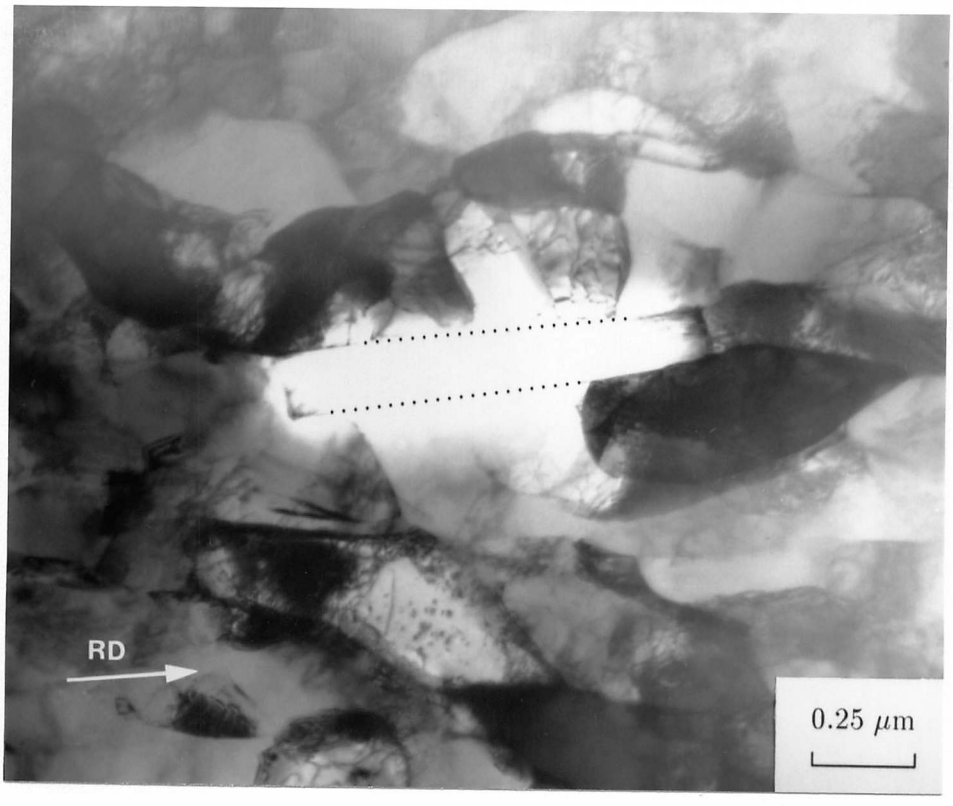

Figure 4.19 Transmission electron micrograph taken in the long transverse section showing the deformation zone around a particle in the 0.47 wt% Fe as–rolled alloy (rolling schedule II).

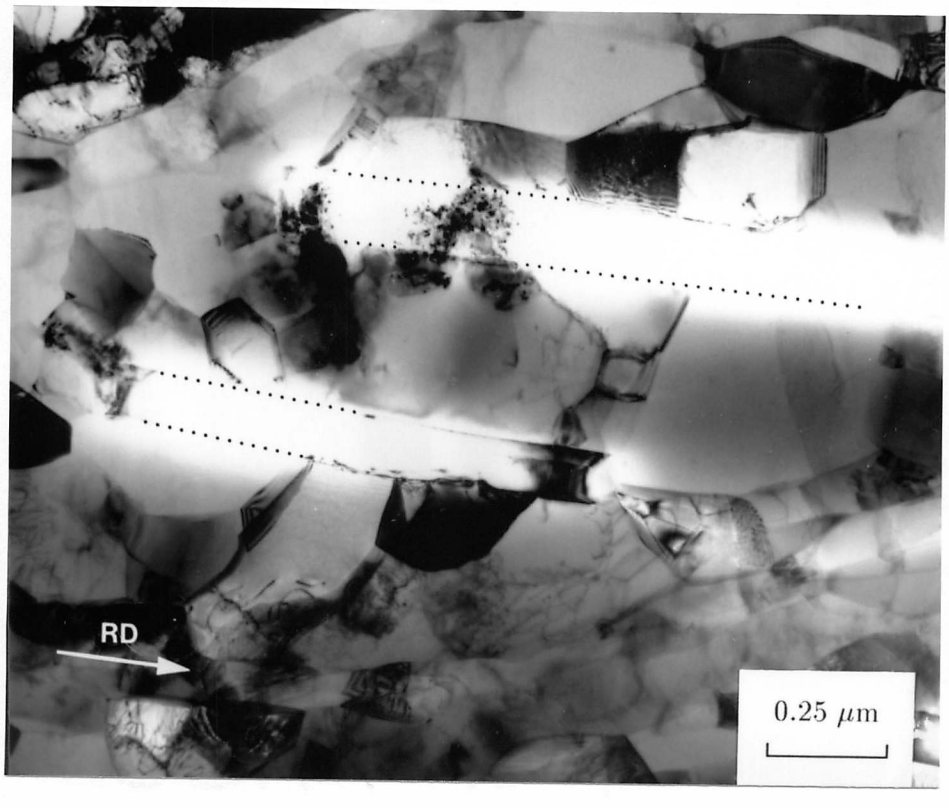

Figure 4.20 Transmission electron micrograph taken in the long transverse section showing the equiaxed subgrains within a particle band in the 0.47 wt% Fe as–rolled alloy (rolling schedule II).

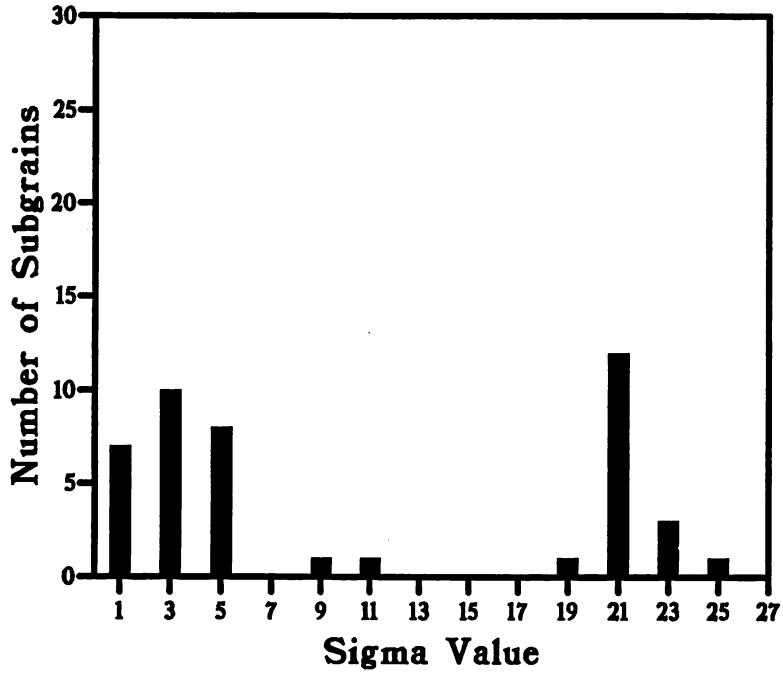

Figure 4.21 The frequency of subgrain 'remote orientations' adjacent to particles in the as–deformed matrix of the 0.47 wt% Fe alloy.

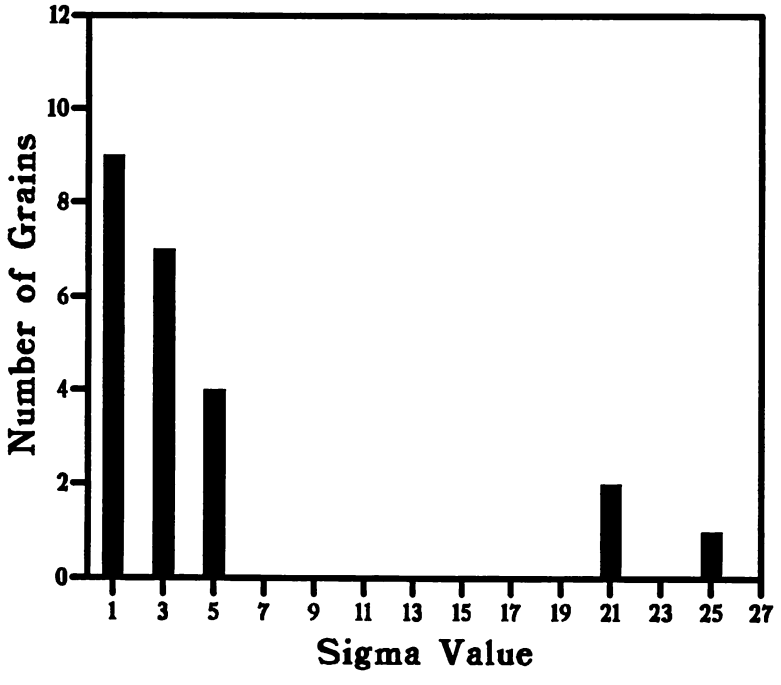

Figure 4.22 The frequency of subgrain 'remote orientations' between elongated subgrains away from particles in the as–deformed matrix of the 0.47 wt% Fe alloy.

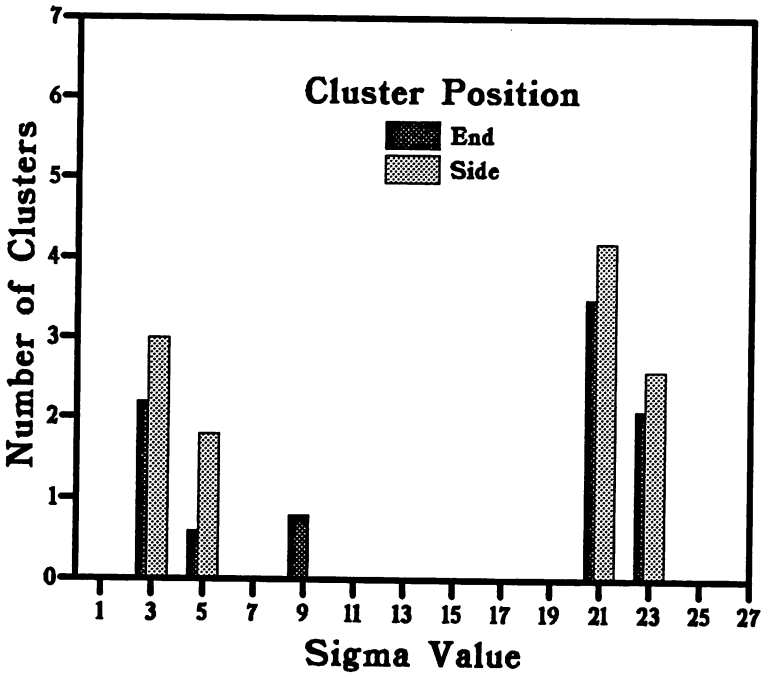

Figure 4.23 The frequency of subgrain cluster 'remote orientations' adjacent to particles in the as–deformed matrix of the 0.47 wt% Fe alloy.

4.3 Conclusions

It has been shown that the size of the $FeAl_3$ particles in the matrix, and the distribution of those particles, are extremely important factors in influencing the recovery and recrystallisation kinetics of the Al–Fe alloys, since it is these factors which influence the nature of the particle deformation zones. The smaller particle deformation zones in the 0.47 wt% Fe alloy are less effective in promoting recrystallisation, but their wider separation allows quicker recovery in the matrix. In both the high and low iron content alloys, the deformation zones are seen to produce a major perturbation in matrix deformation, and hence in dislocation density and boundary misorientations, but the extent of this in terms of volume fraction of disturbed matrix and volume of individual zones is greater in the high iron content alloy. It is also noted that the subgrain sizes are smaller and dislocation densities greater at the ends of the elongated particles than at the sides in the 1.41 wt% Fe alloy, but in the 0.47 wt% Fe alloy (in which particles are shorter) this distinction is less obvious.

Chapter 5

RECRYSTALLISATION NUCLEATION

The nature of the deformation zones of the $FeAl_3$ particles and the fact that these particles accelerate recrystallisation has been established in the previous chapter. It is now necessary to investigate the ways in which these zones promote recrystallisation nucleation. The clustering of particular subgrain orientation types within the zones is thought to play a role in the facilitation of nucleation, and these clusters are studied in detail here during the early stages of annealing to assess their role.

Fujita (1961) observed that during the recovery of high purity cold–worked aluminium, groups of subgrains formed which were subsequently observed to be important in recrystallisation as well as the conventional process of sub–boundary migration. It was noted that the groups were characterised in that the misfit angles between subgrains comprising the group were very small, and the boundary surrounding the composite subgrain was not smooth, but merely connected the individual boundaries of the small subgrains. It could be seen that this boundary was gradually stabilised by the absorption of the sub–boundaries within the group. By observing grain boundaries under differing glancing–angles of incident beam, boundaries consisting of many sub–boundaries which appeared to be the beginning of a recrystallisation boundary were found to have the following characteristics:

- the boundary was smooth despite being a composite one;
- the subgrain size within the boundary was large compared to that without;
- the misfit angles between the subgrains within the boundary were much smaller than those without;
- within the boundary, recovery was much more developed and subgrains were more easily discerned.

It was also noted that in some cases, a faint area of boundary traversed a particular subgrain existing across the boundary, and that this subgrain displayed a large misfit angle relative to the subgrains within the composite grain (see figure *5.1*).

Fujita came to the conclusion that such boundaries were formed by the deposition of vacancies and dislocations which had existed near the boundary. At this stage of annealing it was difiicult to observe the recrystallisation front optically since the contrast between recrystallised material and the matrix was not strong enough.

Fujita suggests that the position of recrystallisation is originally decided at the time of cold working, *ie.* that subgrain growth plays an important role in the disappearance of stored energy, but is not so important in the formation of recrystallisation boundaries, which require

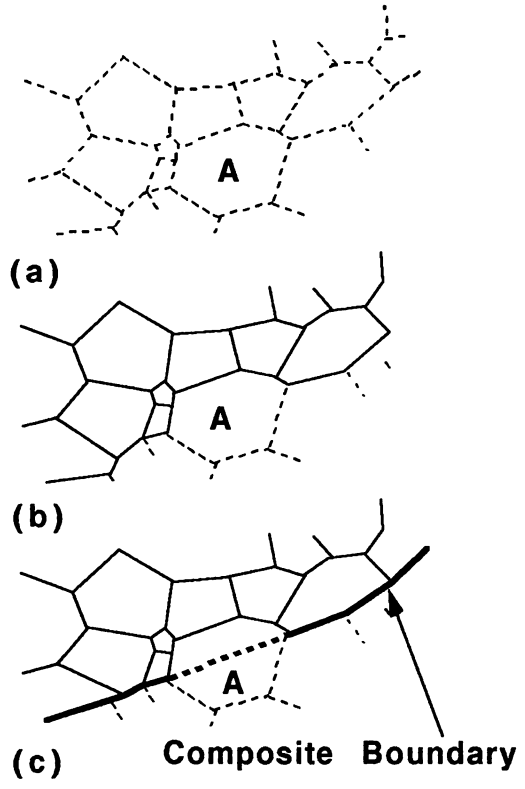

Figure 5.1 Schematic illustration the formation of a recrystallisation boundary (Fujita, 1961).

the absorption of lattice defects. The boundary surrounding a subgrain group has a larger misfit angle than those contained within it, and so it becomes a strong sink for lattice defects, allowing the overall disappearance of subgrains within the group.

The inhomogeneity of deformation in the Al–Fe alloys produces groups of subgrains occurring at particles wich differ in dislocation density, subgrain shape and size, and boundary misorientations from the normal elongated subgrains of the matrix. These groups may be compared to those found by Fujita, and it is not unreasonable to imagine that similar recovery phenomenon may be observed in these alloys as were observed in the high–purity aluminium which he studied.

In the present work the microstructural development within the deformation zones of particles in the 1.41 wt% Fe alloy during the early annealing stages was followed closely in order to ascertain the mechanisms involved in forming a recrystallisation nucleus. In addition, the annealing mechanisms occurring in the 0.47 wt% Fe alloy particle deformation–zones are studied in order to assess the role of these smaller zones in recrystallisation, and to highlight differences between the two alloys.

5.1 Early Stages of Annealing

In chapter 4, the particle deformation zones were characterised after rolling. In order to study the very early stages of recrystallisation, anneals were carried out at 250°C for 30, 60, 90 and 120 minute periods. The development of potential nuclei was observed at particles in the long transverse section using transmission electron microscopy. Recrystallisation was not observed at microstructural features other than particles, and the rate of polygonisation appeared to be much higher within particle deformation zones than in the remote deformed matrix. Figures *5.5* and *5.6* show examples of such potential nuclei at $FeAl_3$ particles. Remote orientations as used in chapter 4 were again measured for the subgrains adjacent to the particles and these were recorded as coincidence site lattice Σ–values. A distinction was made between those subgrains which appeared to be potential nuclei, (with low dislocation densities) and those subgrains which appeared dormant (as–deformed). When these data were plotted in histogram form for the 30 and 60 minute annealing times at 250°C (figures *5.7(b)* and *5.7(c)*) it became clear that the potential nuclei have more or less the same remote orientations as the deformed subgrains adjacent to the particles – the data points for the two roughly coincide.

Comparing the Σ distributions to the as–rolled data in figure *5.7(a)* also shows that little change is produced over these early stages of heat treatment. This is consistent with the structural changes observed within the particle–deformation zones, since the results simply reflect the stages of recovery and polygonisation during which subgrains are preparing for competition to become successful recrystallisation nuclei. Any misorientation change produced by possible subgrain coalescence would be unlikely to be detected in the Σ–value measurements due to the approximate nature of the data involved.

Figure *5.7(d)* shows the data for the 90 minutes anneal sample (at 250°C), and at this point no great change has yet occurred. The deformed subgrains have similar characteristics to the potential nuclei, and the Σ–value frequency distribution is similar to that for the 60–minute anneal.

As can be seen in figure *5.8* which shows a transmission electron micrograph of a potential nucleus at a particle tip in the sample annealed for 90 minutes at 250°C, the subgrains involved have increased in size considerably. However, the potential nucleus has not yet grown beyond the original particle deformation zone. This was found to be true of all the potential nuclei found at this annealing time, and it is suggested that the ability to grow beyond the deformation zone must be an important criterion in determining the success of a recrystallised grain, more so perhaps than the importance of its original state before growth to consume other subgrains within the zone.

A second method of displaying Σ–data, not mentioned in chapter 4, is by the 'nearest

neighbour' method in which the relationship between the adjacent subgrains is recorded rather than the relationship between a subgrain and the remote matrix. This is illustrated in figure *5.2* in which axis–pair measurements are taken between subgrains A and E, A and B, B and C, *etc.* The Σ–data for the as–rolled and annealed specimens of the 1.41 wt% Fe alloy measured between neighbouring subgrains as described, are shown in figures *5.9(a)* to (d). The Σ–value distributions for these measurements display little difference to the 'remote' orientation measurements for the as–rolled, 30 minute and 60 minute anneal samples. However, in the 90 minute anneal data, the number of potential nuclei displaying high misorientation with respect to their nearest neighbours has reduced dramatically.

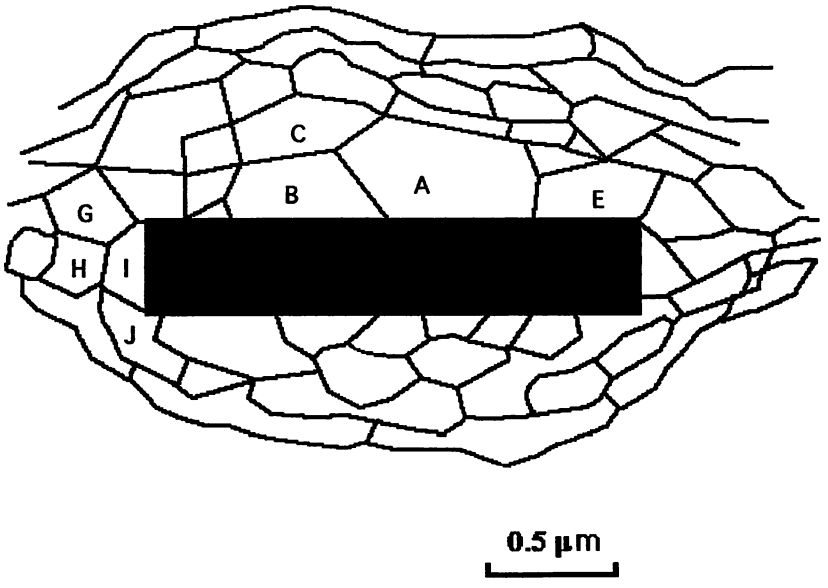

Figure 5.2 Schematic diagram showing a particle and its associated deformation zone in which diffraction data are recorded.

This result can be explained in terms of the growth of potential nuclei to consume areas of the deformation zone of their associated particle. Initially, the measurements for annealed samples are always recorded from clusters of subgrains (for example, cluster ABCDE in figure *5.3a*) in which at least one potential nucleus is present. In the case of the 90 minute anneal specimens, many nuclei had grown to consume whole clusters of subgrains, as shown in figure *5.3b*. In the case of the 'remote orientation' measurements, the number of individual potential nuclei with high misorientations will have remained constant despite their increased size. However, in nearest neighbour measurements this size increase is detected since the potential nuclei now impinge on fewer subgrains within the deformation zone (because few have survived) and many of the high misorientation data points are eliminated. This of course suggests that it is

those potential nuclei whose nearest neighbours share a high misorientation relationship with them which are successful in consuming the surrounding deformation zone.

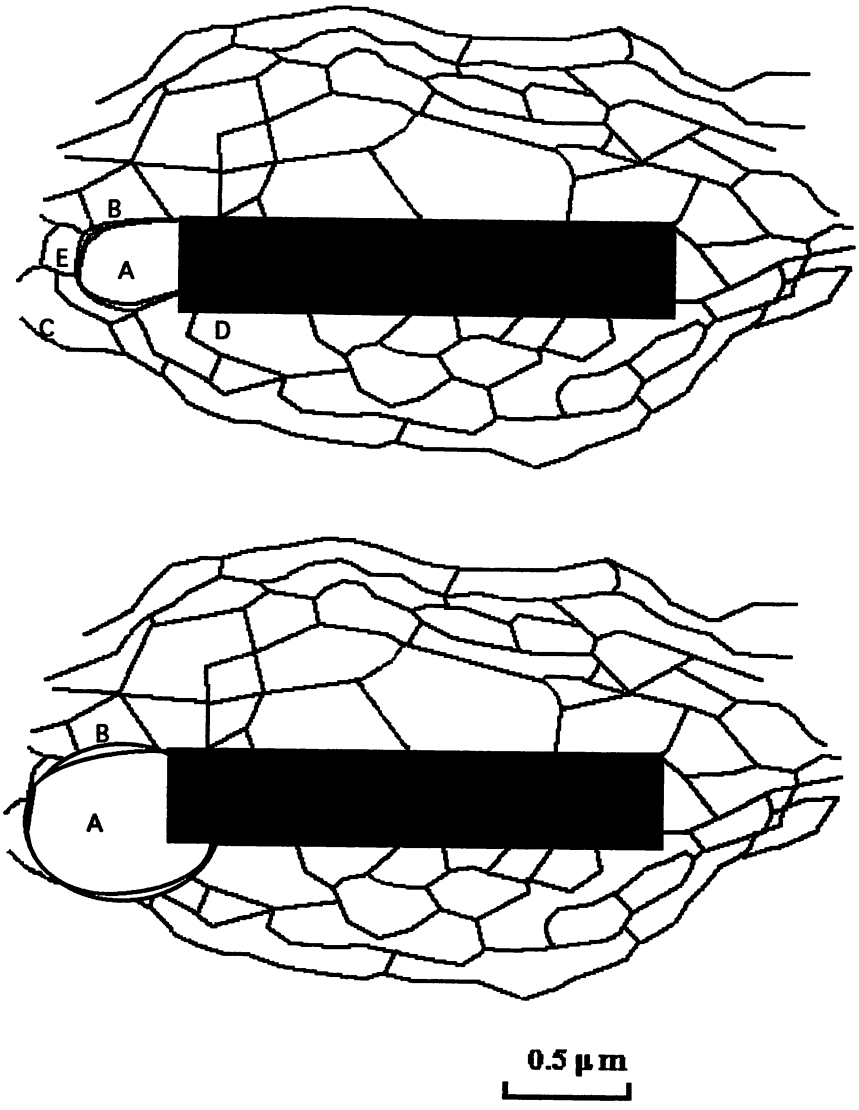

Figure 5.3 Schematic diagram showing (a) a recrystallisation nucleus, A, at a particle tip amongst a cluster of subgrains A,B,C,D and E, and (b) the subsequent growth of the nucleus A, swallowing up subgrains C,D and E.

The literature suggests that large misorientations between neighbouring grains are generally unfavourable for subgrain coalescence to occur. It would be expected therefore that in clusters where high Σ–value boundaries are predominant, this mechanism of nucleus development would not be observed. However, physical evidence for the mechanism of strain–induced boundary migration during the early stages of annealing was also scarce. Some bowing of boundaries was observed in the subgrain clusters at particles, but the intersection of a bowed subgrain boundary across two or more subgrains (as shown schematically in figure *5.4*) was never observed, and there was little evidence for grain boundary migration in these early annealing

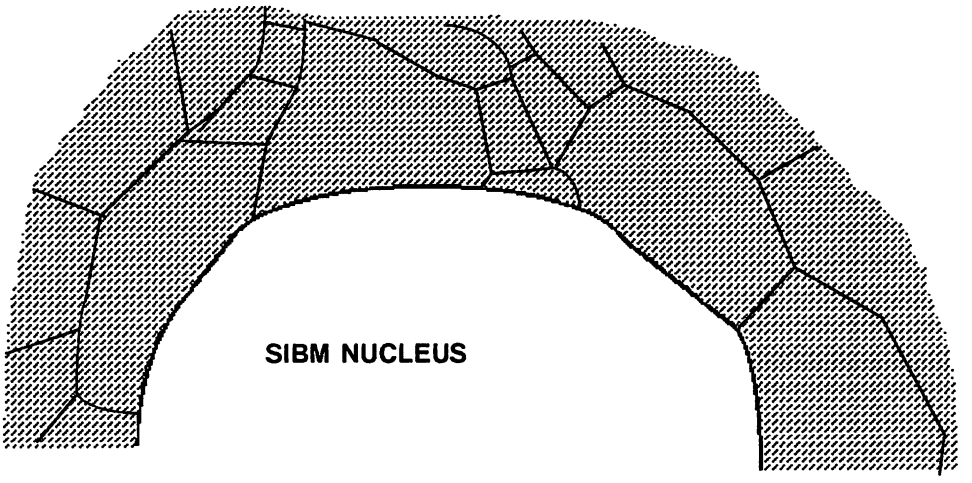

Figure 5.4 Schematic diagram showing bowing of a potential nucleus boundary expected during strain induced boundary migration.

stages.

In addition to this, some evidence was found of the movement of dislocations out of subgrain boundaries between potential nuclei and neighbouring subgrains. In figure *5.10* a transmission electron micrograph shows dislocation lines in the process of moving within a boundary. In figure *5.11* a transmission electron micrograph shows a potential nucleus, A, displaying sharp boundaries between all neighbouring subgrains except B, where individual dislocations can almost me discerned. The dark field image of the same subgrain cluster (figure *5.12*) underlines the difference between the subgrain boundaries in the cluster further, with the boundary between subgrains A and B occurring only faintly.

As was discussed in chapter 4, remote orientation measurements were made for the clusters of subgrains adjacent to particles after annealing. A distinction was again made between clusters at particle ends and those at particle sides. Figure *5.13(a)* shows the original Σ–value profile for the as–rolled alloy (chapter 4) which can then be compared to figures *5.13(b)*, *(c)* and *(d)* showing the Σ–values for the alloy after annealing for 30, 60 and 90 minutes respectively.

It should be noted that in the 60 minute and 90 minute annealed specimens, only those clusters containing potential nuclei were recorded. Therefore entirely as–deformed clusters were eliminated from the data. In figure *5.22* it can be seen that when the 90 minute anneal is reached, the potential nuclei (which by now had increased in size and were easier to identify) appeared exclusively at particle ends. It can be deduced from the drop in Σ–3 remote–orientation clusters that potential nuclei occurred preferentially at clusters with a high misorientation with respect to the deformed matrix. Therefore, the combination of high misorientation with respect to the deformed matrix and end of particle situation distinguished the preferred sites for potential nuclei to develop.

If cluster Σ–value data are studied again, but in this case using nearest neighbour data as described previously, a distinction between end and side clusters is again observed in the as–rolled alloy (figure *5.14(a)*). However, as annealing proceeds a greater number of end clusters displaying low Σ–value boundaries are recorded under the nearest neighbour criterion. As annealing proceeds further, completely as–deformed cluster data are eliminated as before, and eventually when the 90 minute anneal is reached (figure *5.14(d)*) the profile of Σ–values given for the end clusters containing potential nuclei is in fact opposite to that recorded for the 'remote' data. That is, there is a higher incidence of low Σ–values than high sigma values. These results are summarised in table *5.1.*

Table 5.1 Preferred sites for nucleation in particle deformation zones for the 1.41 wt% Fe alloy in terms of cluster CSL values and positions.

Site	'Remote' Misorientation	Nearest Neighbour Misorientation
End of Particle	High Σ	Low Σ

This difference between the remote and neighbouring orientation data can be explained if it is assumed that a modified form of subgrain coalescence is the dominant mechanism in producing a potential nucleus. It would then be expected that the subgrains within a cluster would rotate towards the potential nucleus, giving an increase in the number of low Σ–value data as annealing proceeds and a decrease in high Σ–value data. In conjunction with this, however, it is natural to see a large misorientation with respect to the deformed matrix since subgrain–coalescence type mechanisms can only occur in areas where there has been sufficient deformation for a wide spread of misorientations to develop over a small spacial area, a typical example of this being at particle ends.

If the individual Σ–value data are now referred to again, bearing in mind this new interpretation, the increase in Σ–3 orientations during annealing is again observed in the nearest–neighbour data. Figure *5.15* shows the hardness curves for the 1.41 wt% Fe alloy over the early stages of annealing which are studied in this section. For comparison, note that the hardness value recorded for a fully annealed specimen is about 30 HV. It is evident that only relatively small drops in hardness occur, consistent with the fact that only the very early stages of re-crystallisation and recovery are observed. In fact, recovery is the dominant process for these time periods. In addition, bulk texture measurements (figure *5.16* and table *5.2*) also show only small changes over 60 minutes annealing time, since the degree of recrystallisation is very small.

It must be noted at this stage that the mechanism assumed for the formation of potential nuclei is not strictly a subgrain–coalescence theory. Since the subgrains within clusters are of

Table 5.2 Changes in bulk texture types in 1.41 wt% Fe alloy after annealing at 250°C for up to 120 minutes.

Texture Type	As-rolled	30 minutes	60 minutes	90 minutes	120 minutes
$\{100\}\langle 001\rangle$ (Cube)	1.95	1.76	1.48	1.45	0.98
$\{110\}\ \langle 1\bar{1}2\rangle$ (Brass)	15.48	16.20	16.22	16.81	18.03
$\{121\}\ \langle 1\bar{1}1\rangle$ (Cu)	15.85	15.47	15.04	15.22	19.18
$\{110\}\ \langle 001\rangle$ (Goss)	5.72	4.47	4.33	4.79	4.98
$\{231\}\ \langle 3\bar{4}6\rangle$ (S)	28.09	28.52	30.83	28.44	32.97

similar orientations, only very small local rotations will be necessary for boundaries to disappear between two subgrains. Essentially it is the movement of dislocations out of those boundaries which is the dominant process, and this means that the mechanism can be more accurately described as being one of recovery.

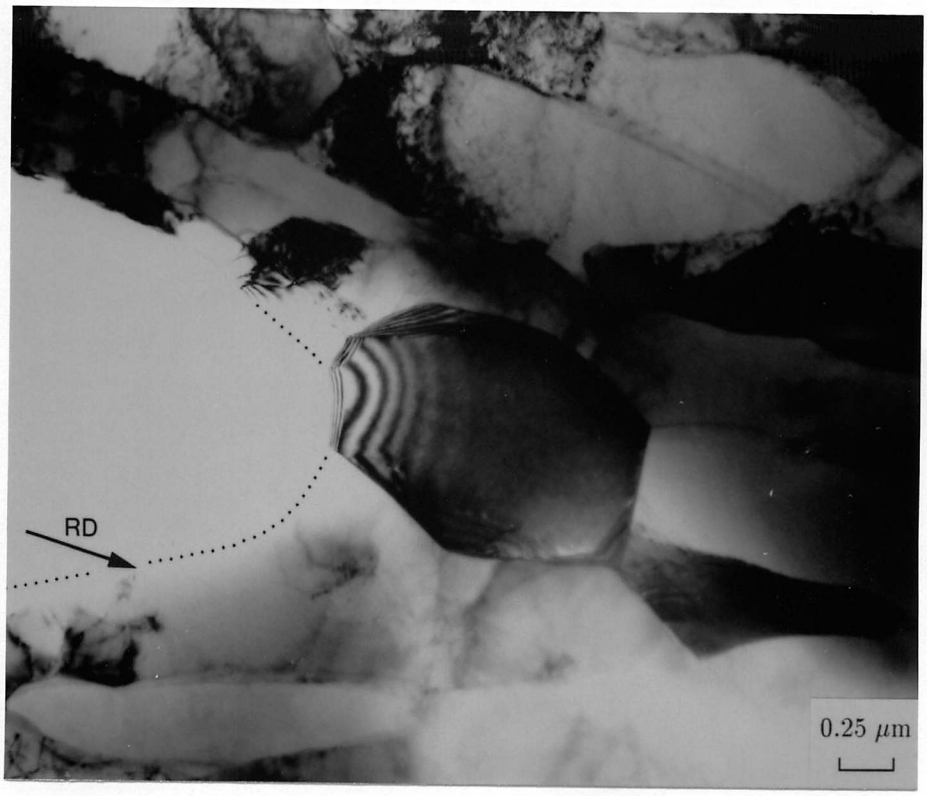

Figure 5.5 Transmission electron micrograph showing a potential nucleus at an $rmFeAl_3$ particle tip in the Al–1.41 wt% Fe alloy annealed at 250°C for 60 minutes.

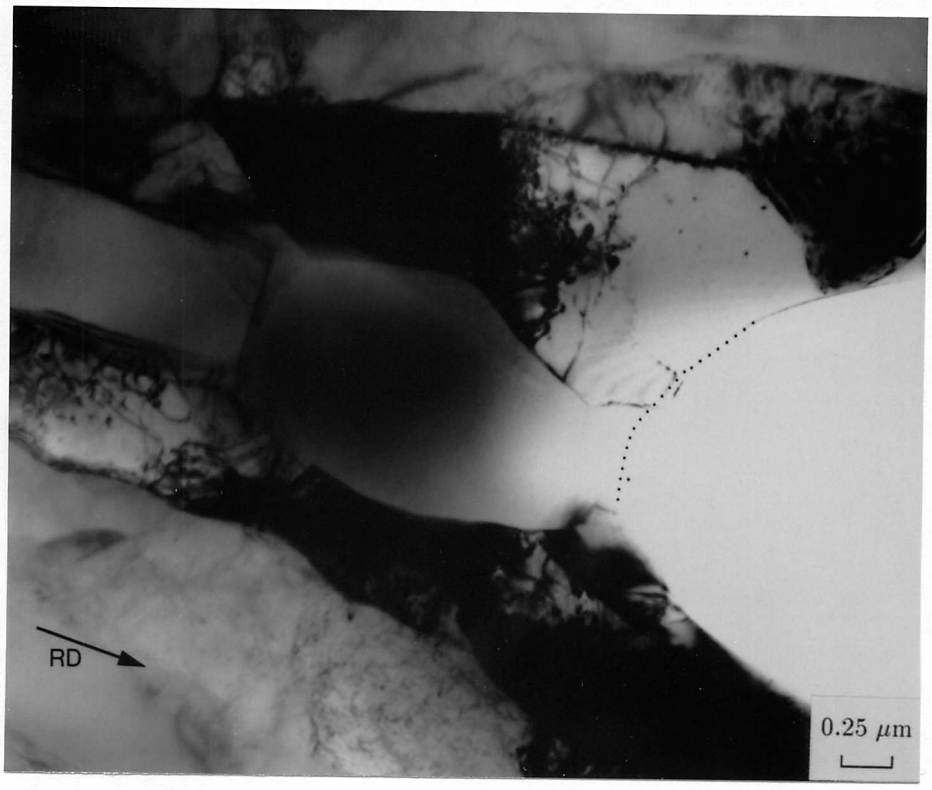

Figure 5.6 Transmission electron micrograph showing a potential nucleus at a particle tip in the Al–1.41 wt% Fe alloy annealed at 250°C for 60 minutes.

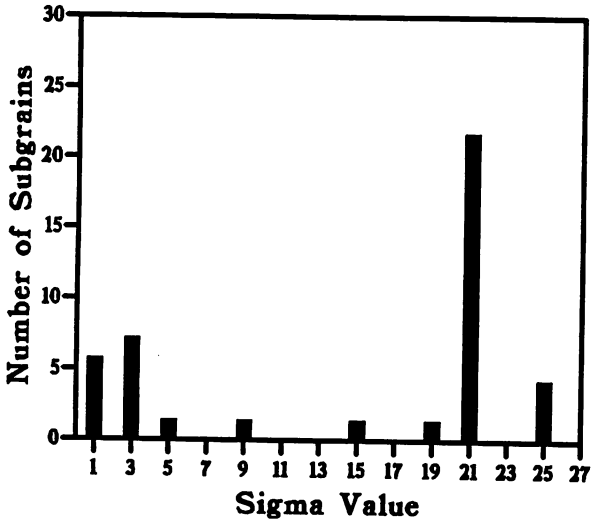

(a)

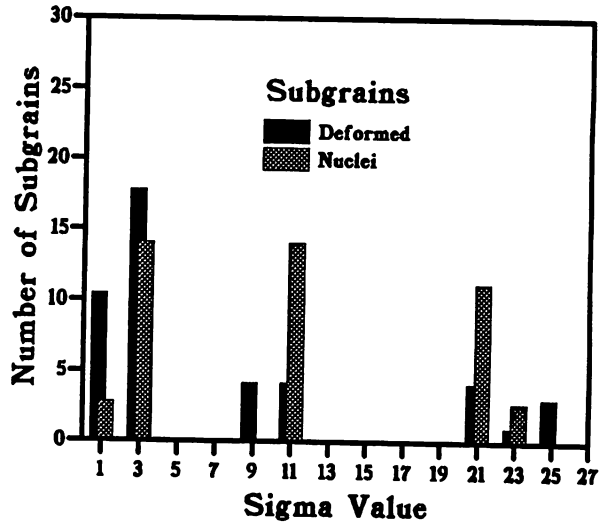

(b)

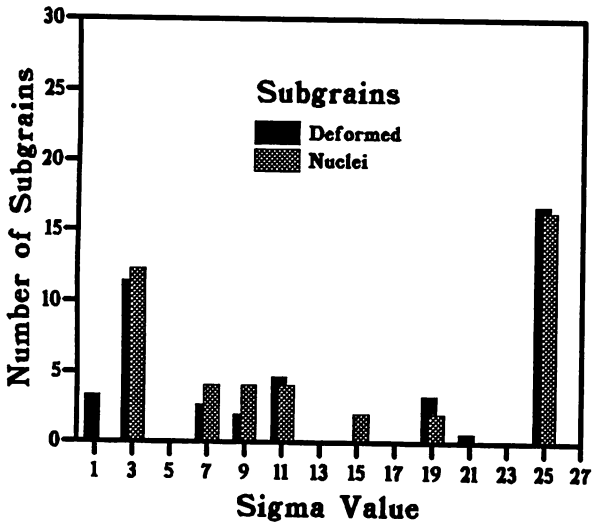

(c)

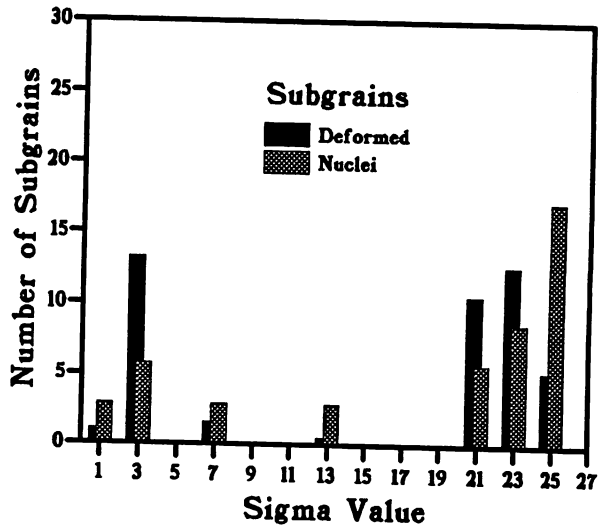

(d)

Figure 5.7 Frequency of Σ 'remote orientation' values in the Al–1.41 wt% Fe alloy (a) in the as–rolled condition, (b) annealed at 250°C for 30 minutes, (c) annealed at 250°C for 60 minutes and (d) annealed at 250°C for 90 minutes.

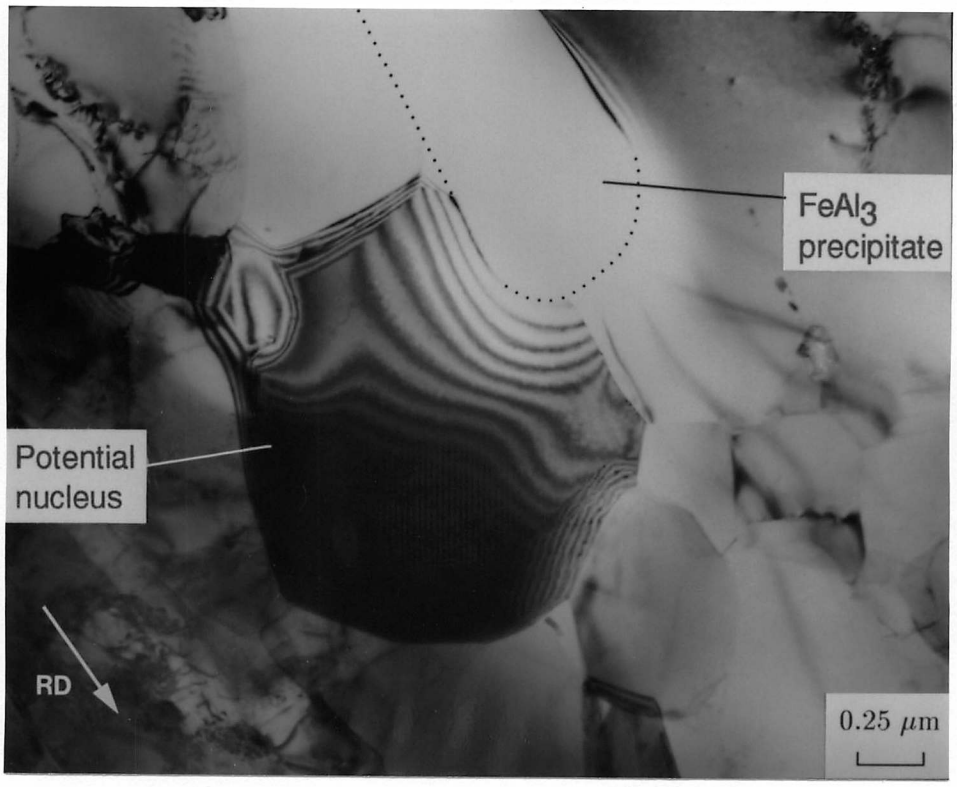

Figure 5.8 Transmission electron micrograph showing a potential nucleus which has grown to consume the immediate surrounding particle deformation zone in the Al–1.41 wt% Fe alloy annealed at 250°C for 90 minutes.

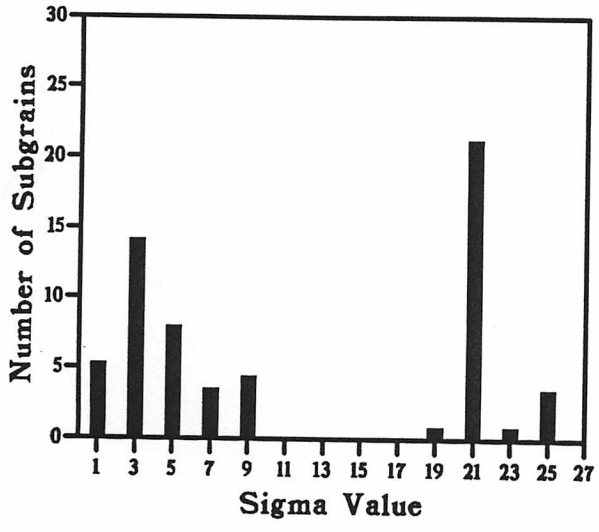

(a)

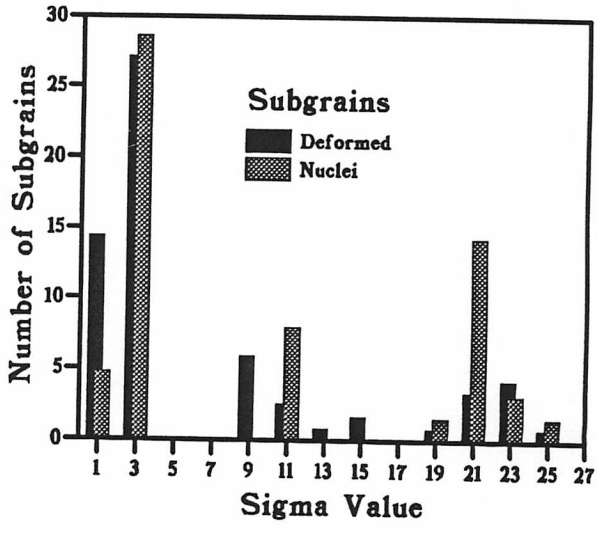

(b)

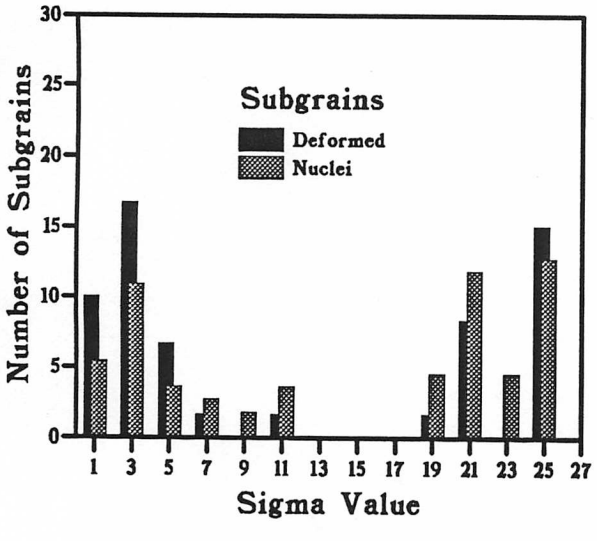

(c)

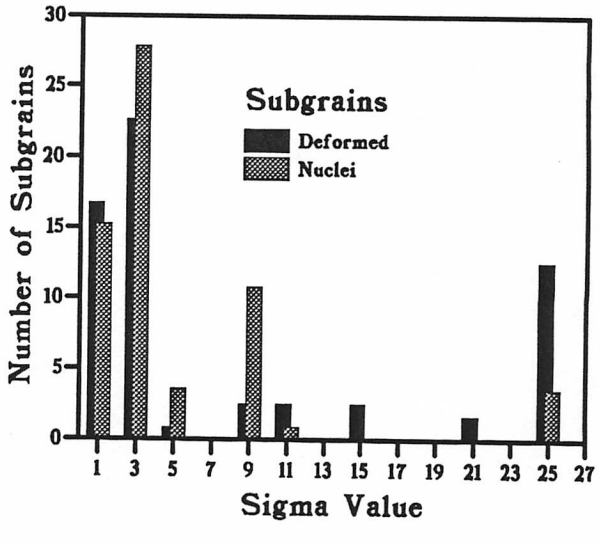

(d)

Figure 5.9 Frequency of Σ 'nearest neighbour' values in the Al–1.41 wt% Fe alloy (a) in the as–rolled condition, (b) annealed at 250°C for 30 minutes, (c) annealed at 250°C for 60 minutes and (d) annealed at 250°C for 90 minutes.

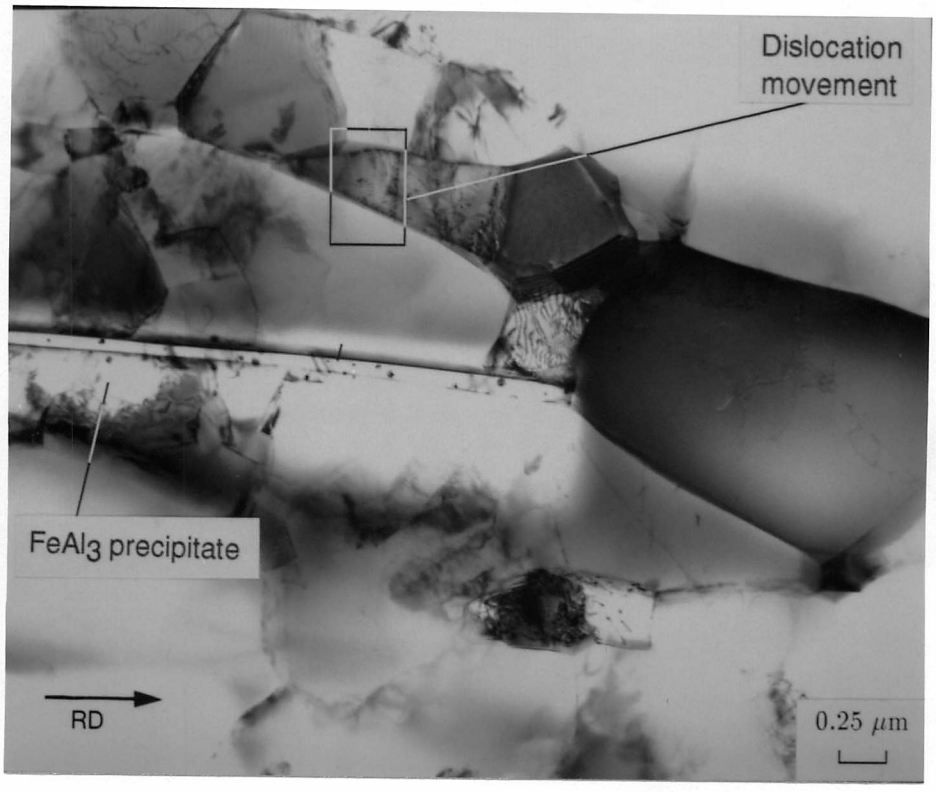

Figure 5.10 Transmission electron micrograph indicating the movement of dislocation lines within a boundary.

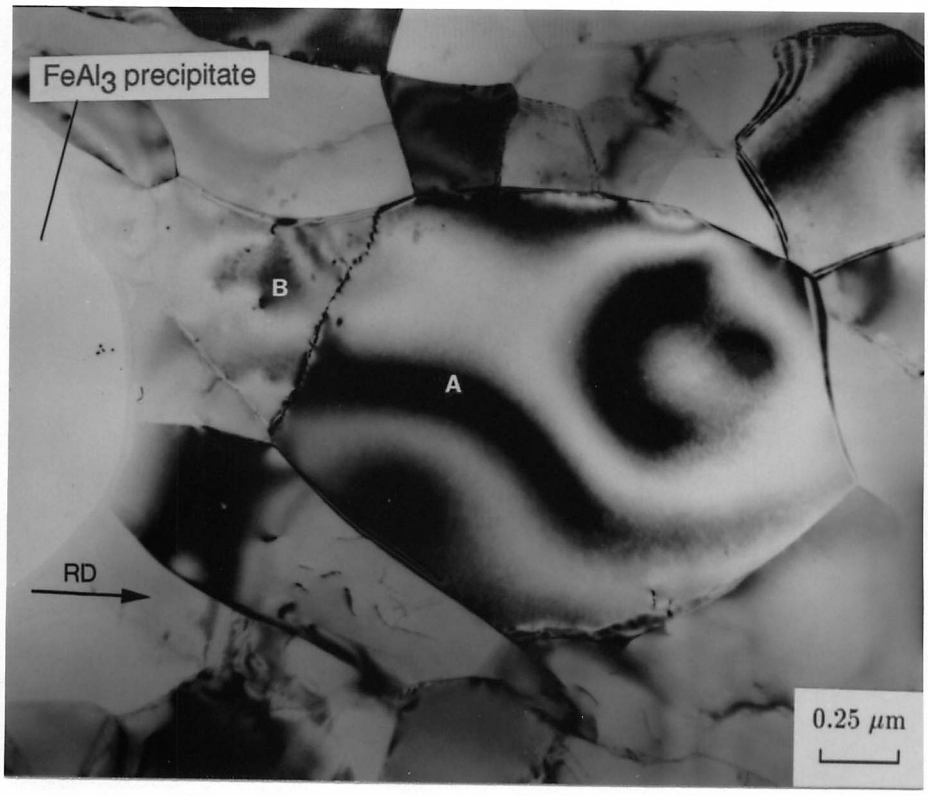

Figure 5.11 Transmission electron micrograph showing a potential nucleus A and neighbouring subgrain B under bright field illumination.

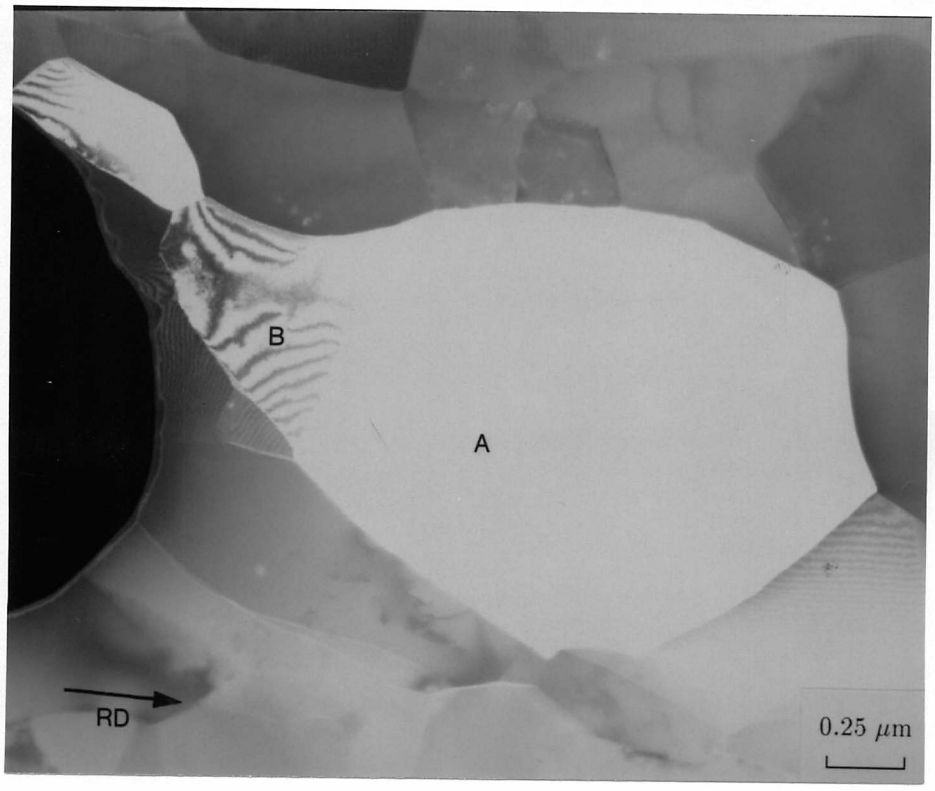

Figure 5.12 Transmission electron micrograph showing a potential nucleus A and neighbouring subgrain B under dark field illumination.

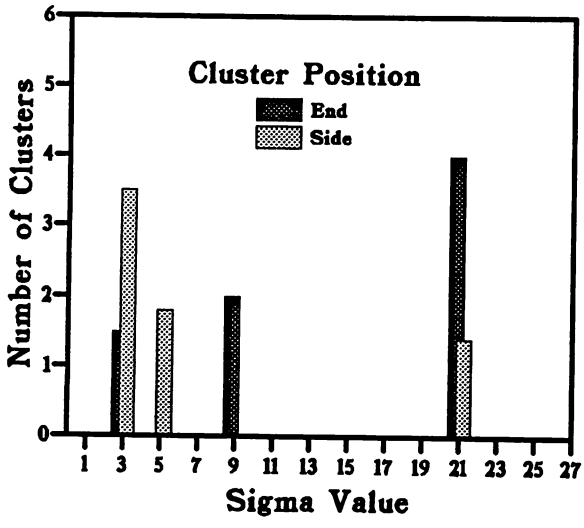

(a)

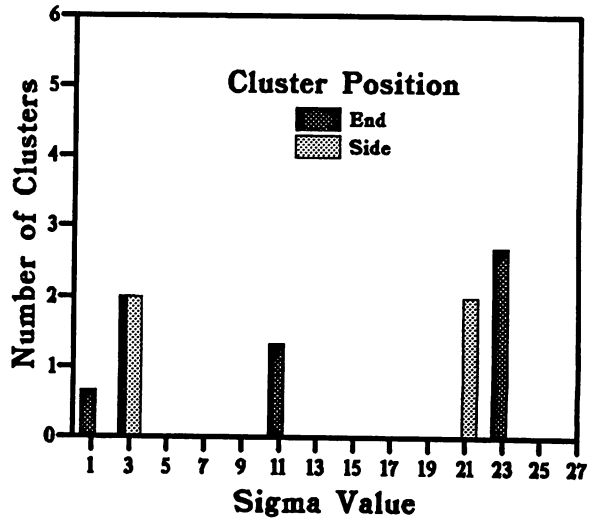

(b)

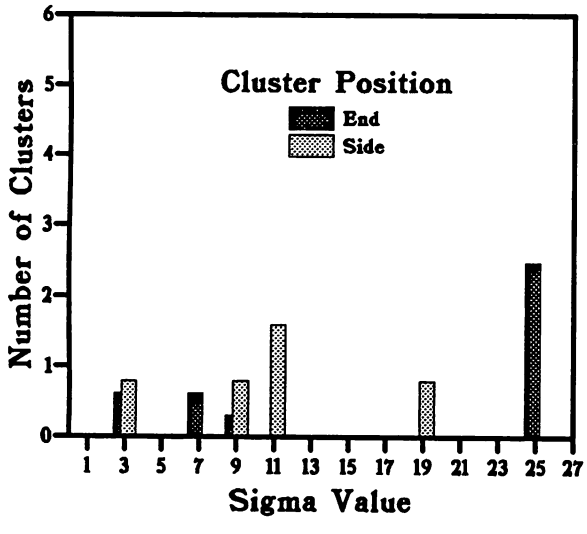

(c)

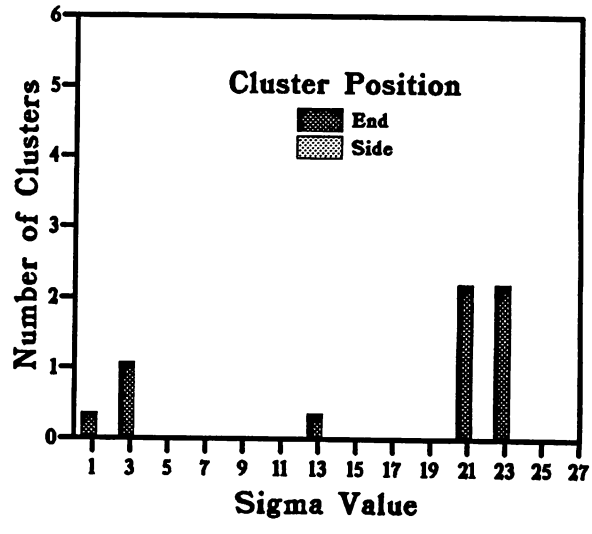

(d)

Figure 5.13 'Remote orientations' for subgrain clusters adjacent to particles in the Al–1.41 wt% Fe alloy, (a) as–deformed, (b) annealed at 250°C for 30 minutes, (c) annealed at 250°C for 60 minutes and (d) annealed at 250°C for 90 minutes.

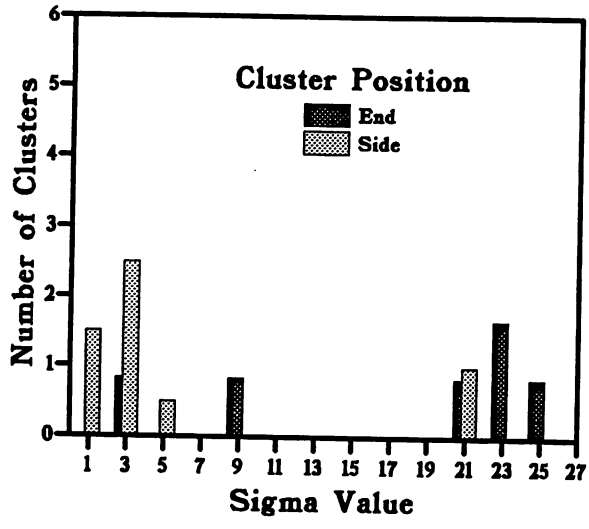

(a)

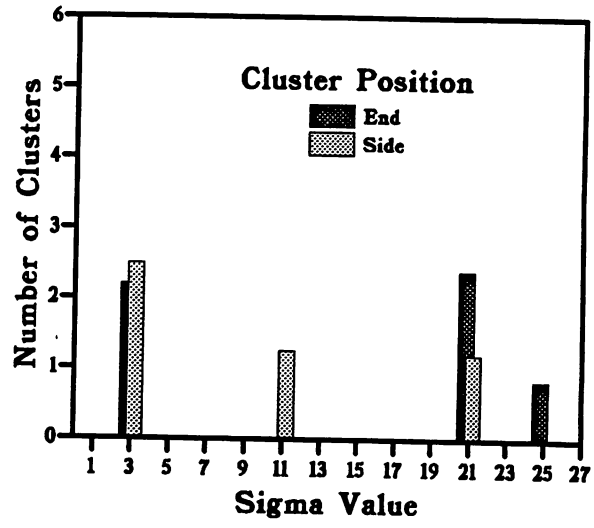

(b)

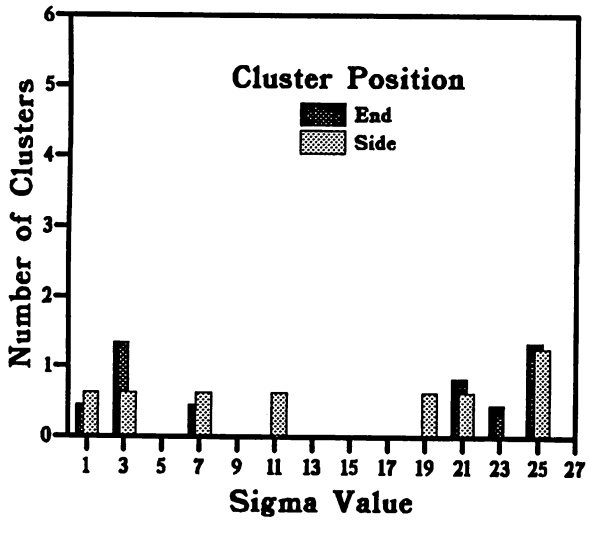

(c)

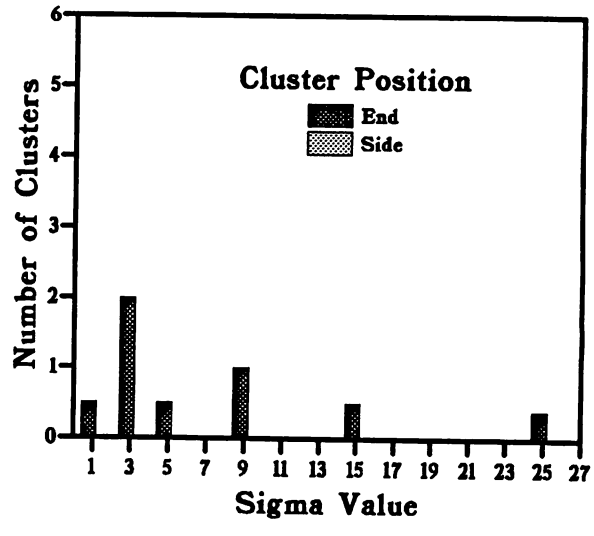

(d)

Figure 5.14 'Nearest neighbour' cluster data for subgrains adjacent to particles in the Al–1.41 wt% Fe alloy (a) as–rolled, (b) annealed at 250°C for 30 minutes, (c) annealed at 250°C for 60 minutes and (d) annealed at 250°C for 90 minutes.

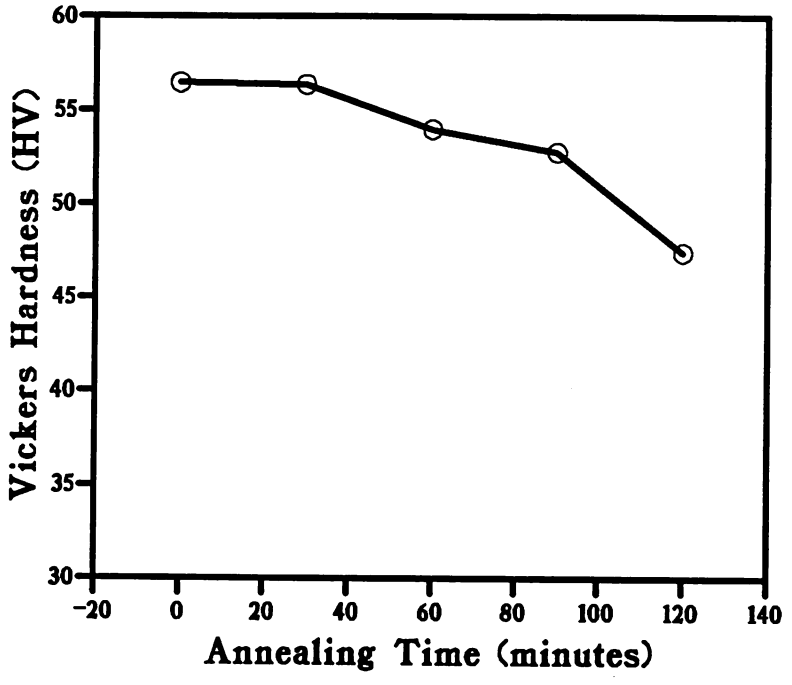

Figure 5.15 Changes in hardness in Al–1.41 wt% Fe alloy after annealing at 250°C for up to 120 minutes.

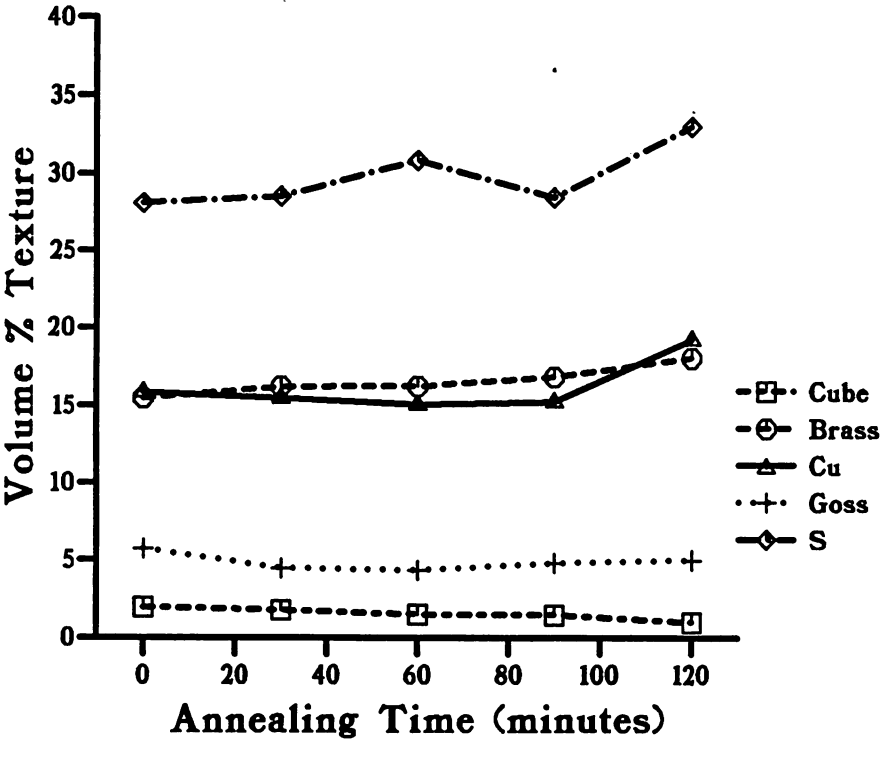

Figure 5.16 Changes in bulk texture types in Al–1.41 wt% Fe alloy after annealing at 250°C for up to 120 minutes.

5.2 Preferred Nucleation Sites

As has been discussed in the previous experimental section, the probability of the occurrence of potential nuclei at a subgrain cluster is linked closely to degree of deformation (the greatest deformation occurring at particle ends) and degree of misorientation with respect to the deformed matrix and between neighbouring subgrains in the cluster. This surely points to an importance of oriented nucleation since potential nuclei occur only selectively. The criterion for the appearance of a potential nucleus at a given particle deformation–zone cluster can be investigated further by combining the two types of axis angle pair measurements already discussed. For the purpose of characterisation of the different states in which a subgrain pair may occur with regard to one another and to the deformed matrix, the following abbreviations will be employed:

Σ–values measured between neighbouring subgrains, or 'nearest neighbour' data are designated N. Σ–values measured with respect to the deformed matrix, or 'remote misorientation' data are designated R. Those Σ–values less than 13 are 'low' and designated L. Those Σ–values greater than 13 are 'high' and designated H.

Now, a subgrain pair consisting of subgrain 1 and subgrain 2 can be fully characterised, for example:

Subgrain One	Subgrain Two
NH/RL	NH/RH

In this case, both of the subgrains are oriented at greater than Σ–13 with respect to each other (note that the nearest neighbour type must be identical for each subgrain) but subgrain 1 is oriented at less than Σ–13 to the deformed matrix and subgrain 2 is oriented at greater than Σ–13 to the deformed matrix.

We can go on to define a total of 8 subgrain pair types as given in table *5.3*. Note that pair types **2** and **6**, and **4** and **8** are synonymous since there is no distinction between subgrains 1 and 2 in terms of their recovered state. A number of physical consequences of these pair types must be noted before proceeding: Pair type **3**, in which both nearest neighbour and remote misorientations are low would not be expected to occur adjacent to particles if the deformation zone of a particle produces subgrain rotations away from the normal rolling texture types. That is, pair type **3** would only occur close to particles if the particles made no difference to the misorientation of subgrains during deformation. Pair type **5** would suggest that considerable subgrain rotation has been produced at the particle deformation–zone, both with respect to the deformed matrix and between adjacent subgrains.

In figure *5.18(a)* the subgrain pair types for the 1.41 wt% Fe as–rolled alloy are shown,

Table 5.3 Subgrain pair types according to 'nearest neighbour' and 'remote' coincidence–site lattice values.

Subgrain One	Subgrain Two	Pair Type Number
NH/RL	NH/RL	1
NH/RL	NH/RH	2
NL/RL	NL/RL	3
NL/RL	NL/RH	4
NH/RH	NH/RH	5
NH/RH	NH/RL	6
NL/RH	NL/RH	7
NL/RH	NL/RL	8

with distinction made between those occurring at the ends and those at the sides of particles. The data are displayed after two corrections had been made:

- Measurements taken at the very edge of the deformation zone (in which both subgrains could be said to be from the deformed matrix as opposed to the deformation zone) were removed, since these were found to be producing spurious pair type–**3** data.
- The data for pair types **4** and **8**, and **2** and **6** were combined, divided by two, and then simply displayed twice to complete the distribution and allow easier comparison with later graphs.

It can be seen that neither of the pair type values suggesting a low Σ–value with respect to the deformed matrix for both subgrains appear in the distribution (*ie.* pair types **1** and **3**). The dominant pair type is **5**, confirming the previously made observation that the presence of particles in the matrix produces major perturbations in texture.

In order to display the annealed data in a way in which the nature of the potential nuclei is illustrated, the same pair types are employed, but this time distinguishing between potential nuclei and as–deformed subgrains (shown in table *5.3*). In this case, pair types **2** and **6**, and **4** and **8** are not identical because theire is now a distinction between subgrains one and two. It should now be noted that pair types **5** to **8** are ones in which the potential nuclei have a high misorientation with respect to the deformed matrix, and assuming the previous conclusion concerning coalescence/recovery mechanism to be correct, are expected to be more favoured. In addition to this, pair type **7** shows a low nearest neighbour misorientation between the potential nucleus and its neighbour, which is expected to be favoured if coalescence is to occur. One further correction was made before displaying the annealed data, which was to remove pair–type data measured between two potential nuclei.

Figures *5.18(b)*, *(c)* and *(d)* show the pair type distributions for the 30, 60 and 90 minute

Table 5.4 Subgrain pair types according to 'nearest neighbour' and 'remote' coincidence site lattice values.

Potential Nucleus	As–Deformed Subgrain	Pair Type Number
NH/RL	NH/RL	1
NH/RL	NH/RH	2
NL/RL	NL/RL	3
NL/RL	NL/RH	4
NH/RH	NH/RH	5
NH/RH	NH/RL	6
NL/RH	NL/RH	7
NL/RH	NL/RL	8

anneals respectively. In the 30 minute anneal distribution the pair type **7** data have increased considerably from the as–rolled measurements, this being the type which shows low misorientation between potential nucleus and neighbouring subgrain, but high misorientation with respect to the deformed matrix. Some pair type **3** data have appeared, but these were found to be associated with subgrains occurring either at the very edge of the deformation zones, or within areas of tiny subgrains very close to the particle interface (figure *5.17*). The percentages of pair type data occurring at pairs of this kind as compared to 'normal' pairs are shown for all the data collected in table *5.5*.

Table 5.5 Percentages of pair type data associated with particular positions within the deformation zone (T.E. = Tiny subgrains at particle–End/matrix interface, T.S. = Tiny subgrains at particle–Side/matrix interface, E.E. = subgrains at the Edge of the deformation zone at particle End, E.S. = subgrains at the Edge of the deformation zone at particle Side, N. = Normal).

Pair Type	As–Rolled					Annealed				
	'T.E.'	'T.S.'	'E.E.'	'E.S.'	'N.'	'T.E.'	'T.S.'	'E.E.'	'E.S.'	'N.'
1	—	—	—	—	—	—	—	8.0	4.0	88.0
2	—	—	—	25.0	75.0	—	—	—	—	100.00
3	—	—	—	—	—	55.0	6.0	33.0	6.0	100.00
4	—	—	—	43.0	57.0	—	—	—	—	100.00
5	—	—	—	—	100.00	—	—	—	—	100.00
6	—	—	—	25.0	75.0	—	—	22.0	—	78.0
7	—	—	—	—	100.00	—	—	—	—	100.00
8	—	—	—	43.0	57.0	—	—	67.0	—	33.0

Moving on to the 60 minute anneal data, the pair–type **7** peak has increased further, and

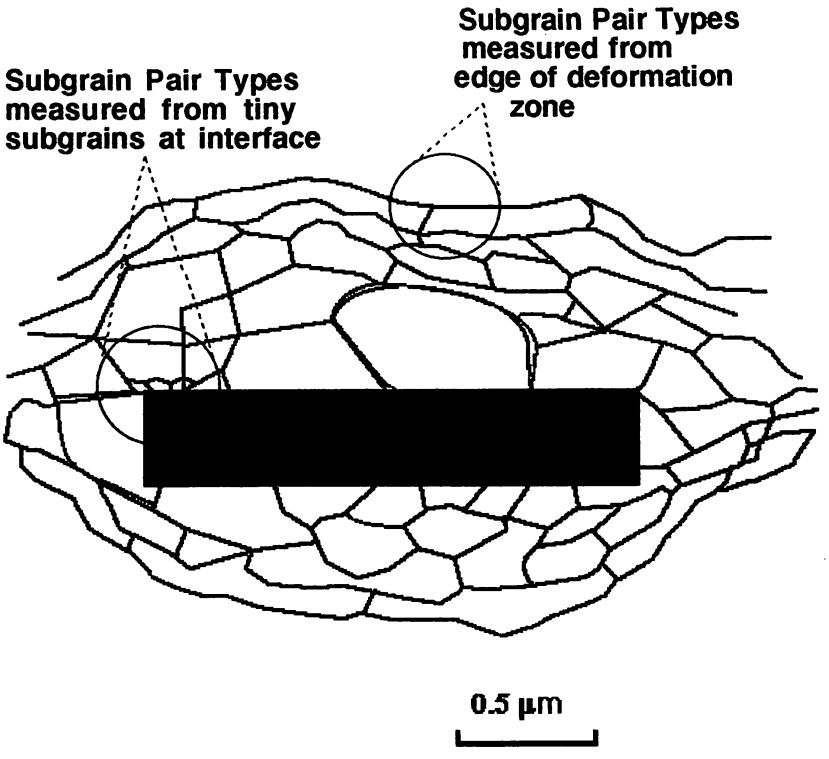

Figure 5.17 Schematic diagram showing the position of 'edge' subgrain pairs and 'small' subgrain pairs in the deformation zone of a particle.

the majority of potential nuclei now occur in pair–types **5** to **8**, where a high misorientation with respect to the matrix is displayed. The increase in pair–type **7** is expected if coalescence/recovery is the mechanism in progress, since subgrains will be expected to rotate towards the potential nuclei to give low nearest–neighbour misorientations. In conjunction with this, pair–types **5** and **6** are expected to decrease since these display high nearest–neighbour misorientations, and this does appear to be happening. In the data for 90 minutes annealing time, a further dramatic increase in pair type **7** is observed confirming the previous suggestion, and pair–types **5** and **6** have disappeared all together. Pair–type **2** has also disappeared, perhaps also due to subgrain rotations towards lower nearest–neighbour misorientations.

Once potential nuclei are established at the preferred sites already identified they develop into larger composite nuclei, consuming the surrounding subgrains in the deformation zone. It is likely however, that at this point a further selection process must come into play before growth beyond the deformation zone can occur, in which only those nuclei oriented in a preferred orientation for growth will be successful in the next stage of recrystallisation (discussed in chapter 6). It is therefore fair to say that both the oriented nucleation and oriented growth processes play a part in the recrystallisation of these aluminium–iron alloys.

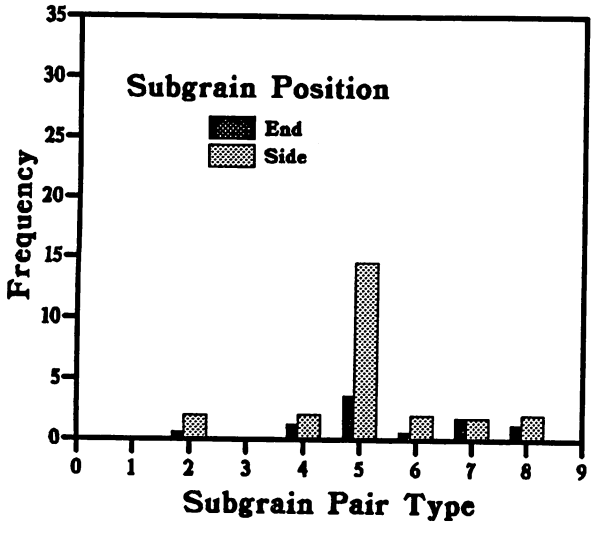

(a)

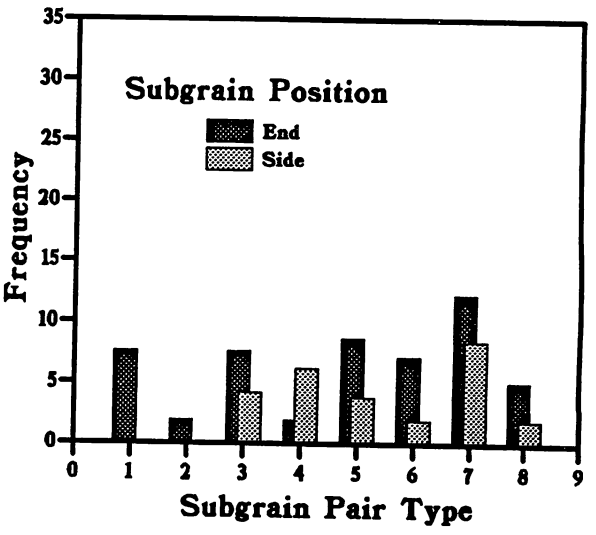

(b)

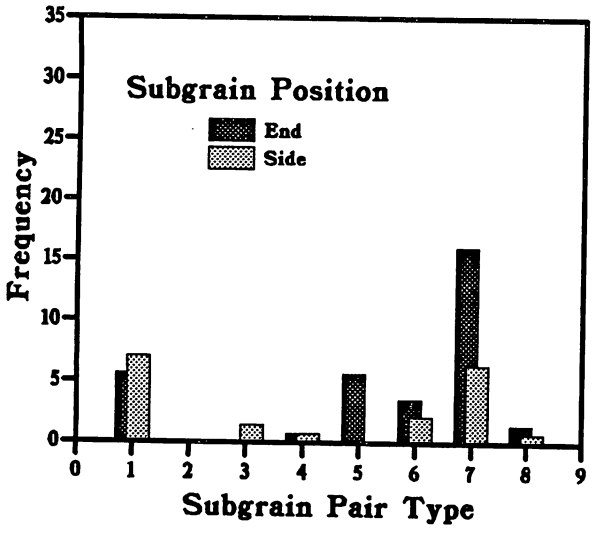

(c)

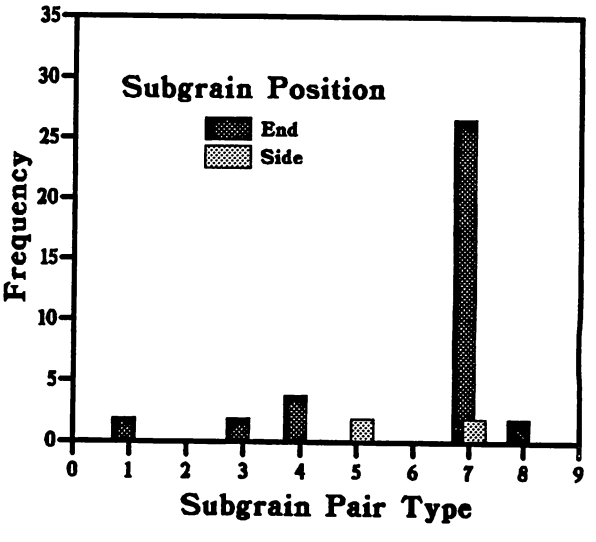

(d)

Figure 5.18 Σ–value subgrain pair type frequency distribution for the 1.41 wt% Fe alloy (a) as–rolled, (b) annealed at 250°C for 30 minutes, (c) annealed at 250°C for 60 minutes and (d) annealed at 250°C for 90 minutes.

5.2.1 *Low Iron–Content Alloy*

As shown in chapter 4, the particle deformation–zones in the 0.47 wt% Fe alloy are much smaller than in the 1.41 wt% Fe alloy, and display a less obvious distinction between side– and end–position clusters within the zones. Also, the wide seperation of particle bands and the close proximity of small particles within those bands is expected to produce a modification in the recrystallisation mechanisms observed.

Figure *5.19* shows the hardness curve for the 0.47 wt% Fe alloy annealed up to 120 minutes at 250°C, and when compared to the graph for the 1.41 wt% Fe alloy (figure *5.14(d)*) it can be seen that the recovery and recrystallisation occuring in the lower iron–content alloy is much slower. This is expected since the small particles of the 0.47 wt% Fe alloy were seen to produce much smaller deformation zones than those of the 1.41 wt% Fe alloy, and the lower volume–fraction of particles gives significantly fewer sites for accelerated polygonisation and recrystallisation nucleation to initiate. Thus, the period of development of 'potential nuclei', which can be thought of as being part of the incubation period for recrystallisation, is extended to longer times in the lower iron–content alloy. The bulk texture measurements for the alloy (figure *5.20* and table *5.6*) also illustrate this.

Table 5.6 Volume fraction percent changes in bulk texture types in 0.47 wt% Fe alloy after annealing at 250°C for up to 120 minutes.

Texture Type	As–rolled	30 minutes	60 minutes	90 minutes	120 minutes
$\{100\}\langle 001\rangle$ (Cube)	0.66	1.64	1.00	0.90	0.68
$\{110\}\ \langle 1\bar{1}2\rangle$ (Brass)	21.83	13.45	23.17	21.80	20.86
$\{121\}\ \langle 1\bar{1}1\rangle$ (Cu)	18.57	16.61	14.06	14.88	17.03
$\{110\}\ \langle 001\rangle$ (Goss)	3.88	4.79	3.83	4.36	4.86
$\{231\}\ \langle 3\bar{4}6\rangle$ (S)	34.11	25.92	33.21	34.51	32.22

Despite the smaller size of particles and associated deformation zones, potential nuclei were still observed to occur at only particles, and not other nucleation sites. Figure *5.21* shows a transmission electron micrograph of a particle occurring away from a particle band, with an associated potential nucleus. Within particle bands, growth of potential nuclei appeared to occur more readily, and figure *5.22* shows a group of particles surrounded by potential nuclei in the 0.47 wt% Fe alloy annealed for only 60 minutes. In general, the majority of potential nuclei were found to appear within particle bands at these low annealing times, and figure *5.23* shows a particle/potential nuclei band at low magnification in which the band has etched out. Figure *5.24* shows further evidence of the potential nucleus sites in the alloy annealed for 120 minutes.

The Σ–value data for the annealed specimens of the 0.47 wt% Fe alloy show similar trends as those discovered for the 1.41 wt% Fe alloy. The individual subgrain Σ–values recorded with respect to the remote matrix are illustrated in figures *5.25(a)* to *5.25(d)*. Generally the distributions given at each annealing stage are still comparable to the as–rolled data, but the 90 minute anneal distribution displays a very marked 'dual' nature of subgrains within particle deformation zones, split between Σ 3 and Σ 25. The 'nearest neighbour' data shown in figures *5.26(a)* to *5.25(d)*, as was found in the 1.41 wt% Fe alloy, show a dramatic drop in high Σ–value data at longer annealing times, although in this case the drop was seen at 60 minutes rather than 90 minutes. It was originally suggested that this drop was due to subgrain growth, but since in the 0.47 wt% Fe alloy softening was seen to be inhibited, if growth were indeed the cause for this drop in high Σ–values, it would be expected to occur beyond 90 minutes and not before. The suggestion made subsequently, that the drop was due to subgain rotation, is more likely and the process may be accelerated in the lower iron–content alloy due to the nature of the subgrain 'strips' described in chapter 4, which may facilitate the rotation mechanism. Although it could be said that any decrease in time taken for rotation should accelerate recrystallisation (and hence softening), it was observed that the potential nuclei produced within subgrain 'strips', although appearing at shorter times, were then inhibited in their growth by the very particles hemming them in which had formerly allowed their easier formation.

The 'remote orientation' cluster data for the 0.47 wt% Fe alloy are displayed in figure *5.27(a)* to *(d)*. As before, completely as–deformed clusters were not recorded in the annealed data. Again, a high number of clusters displaying high Σ–value orientations were recorded at longer annealing times supporting the observation that potential nuclei occur preferentially at high misorientations to the deformed matrix. In the 'nearest neighbour' data of figures *5.28(a)* to *(d)*, a reduction in high Σ–values is observed as annealing proceeds, again suggesting that subgrain rotation is in operation between adjacent subgrains in order to bring them into closer coincidence. This is underscored in the 90 minute anneal data, in which no high Σ–values were found.

Thus, at the early stages of recovery prior to the recrystallisation mechanism of abnormal grain growth, the 0.47 wt% Fe and 1.41 wt% Fe alloys behaved in a similar manner, although due to the low volume fraction of particles in the former, the number of potential nuclei formed in the lower iron–content alloy was greatly reduced.

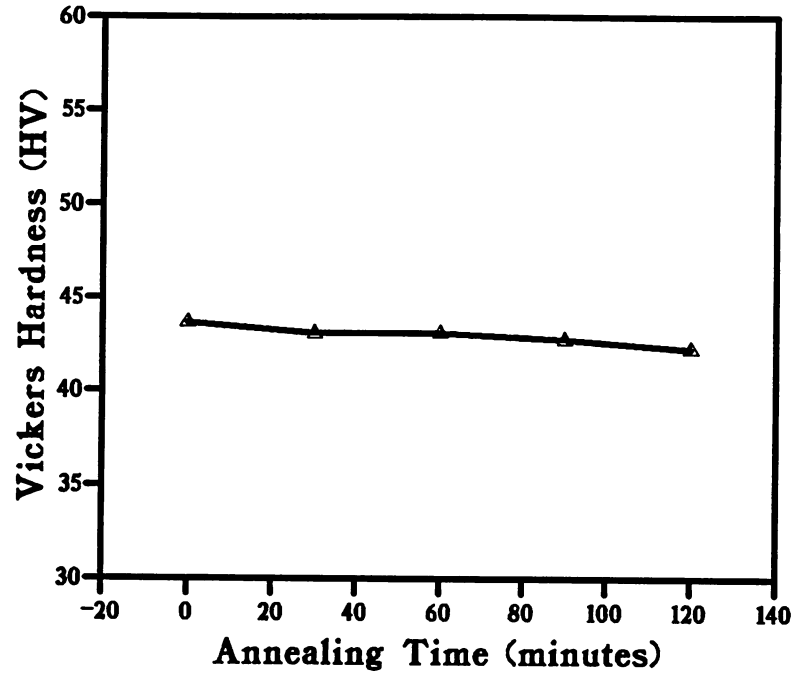

Figure 5.19 Changes in hardness in the Al–0.47 wt% Fe alloy after annealing at 250°C for up to 120 minutes.

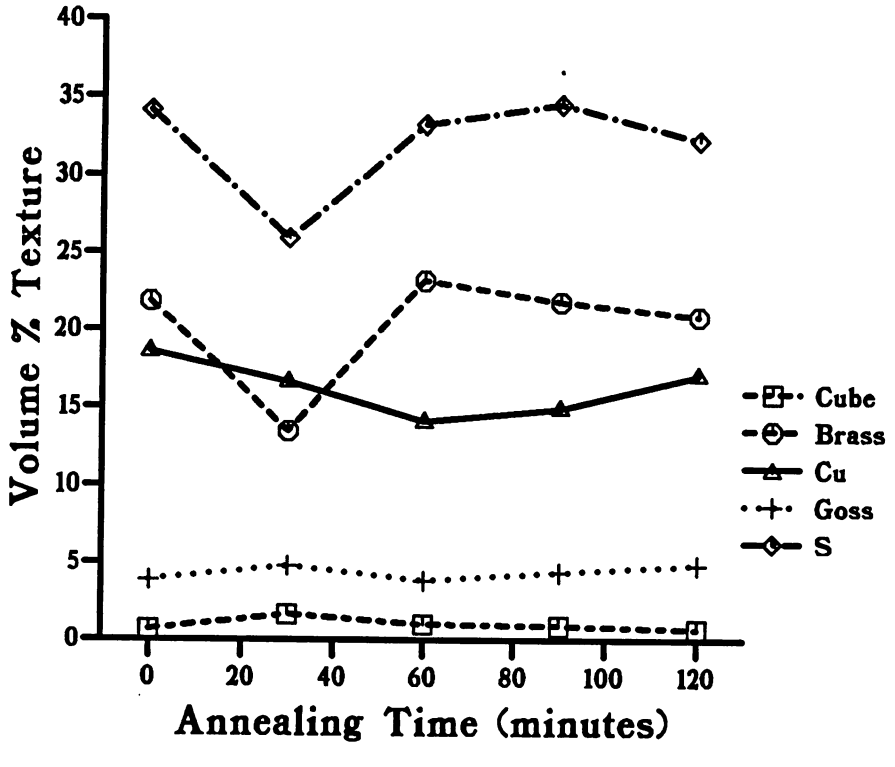

Figure 5.20 Volume fraction percent changes in bulk texture types in Al–0.47 wt% Fe alloy after annealing at 250°C for up to 120 minutes.

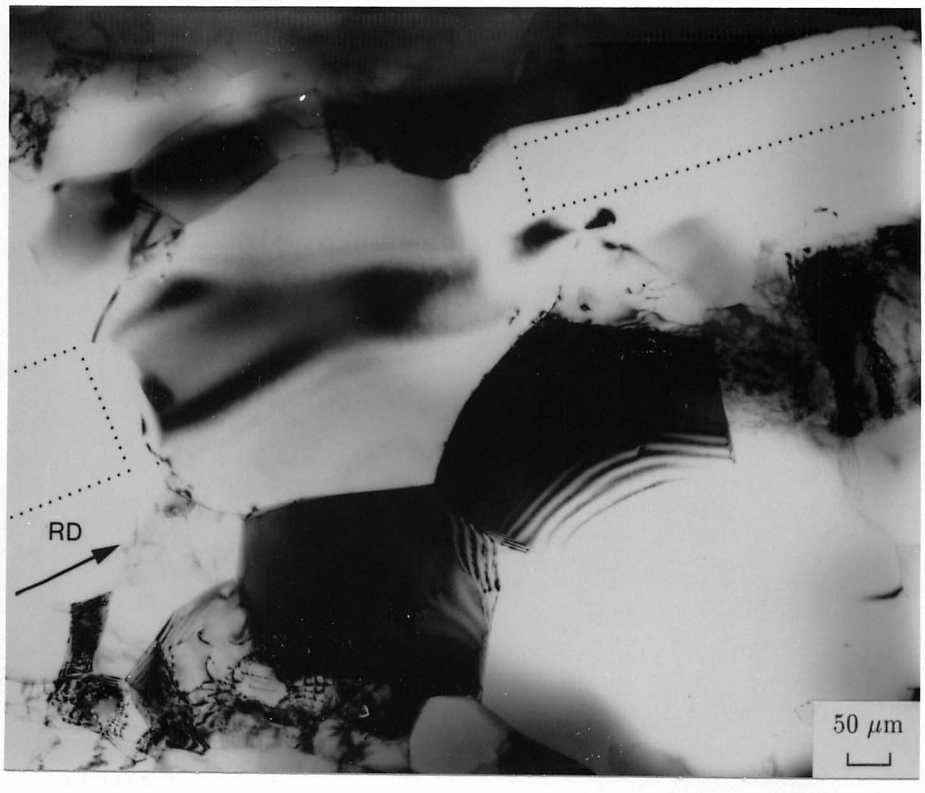

Figure 5.21 Transmission electron micrograph of the 0.47 wt% Fe alloy annealed at 250°C for 60 minutes showing an individual particle and potential nucleus.

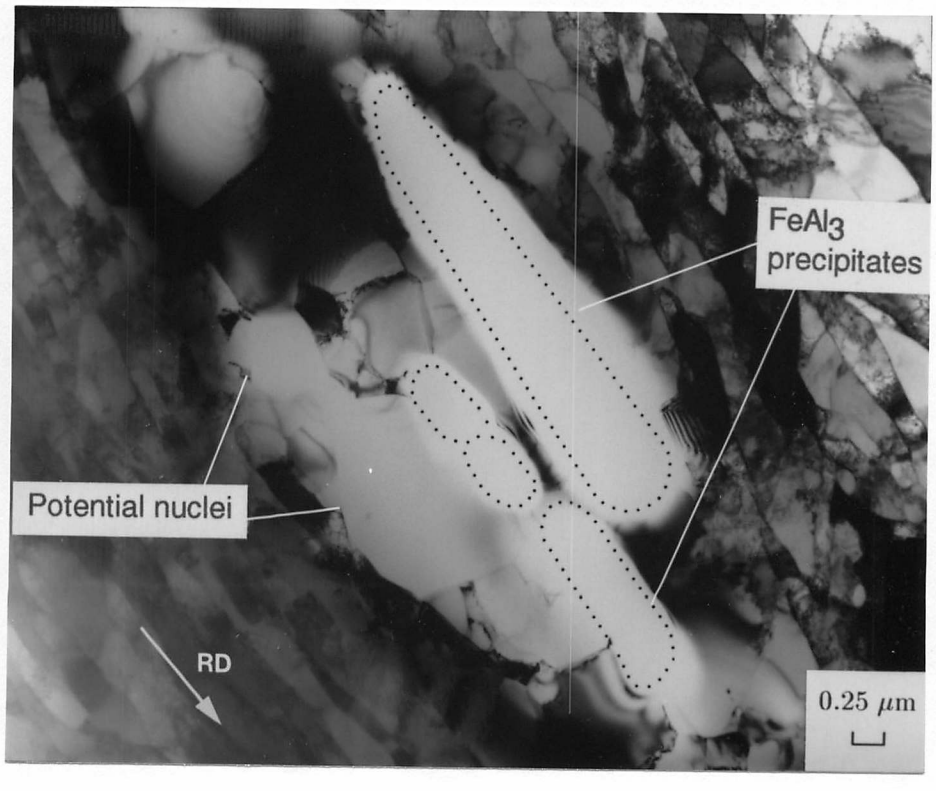

Figure 5.22 Transmission electron micrograph of the 0.47 wt% Fe alloy annealed at 250°C for 60 minutes showing a group of particles with associated potential nuclei.

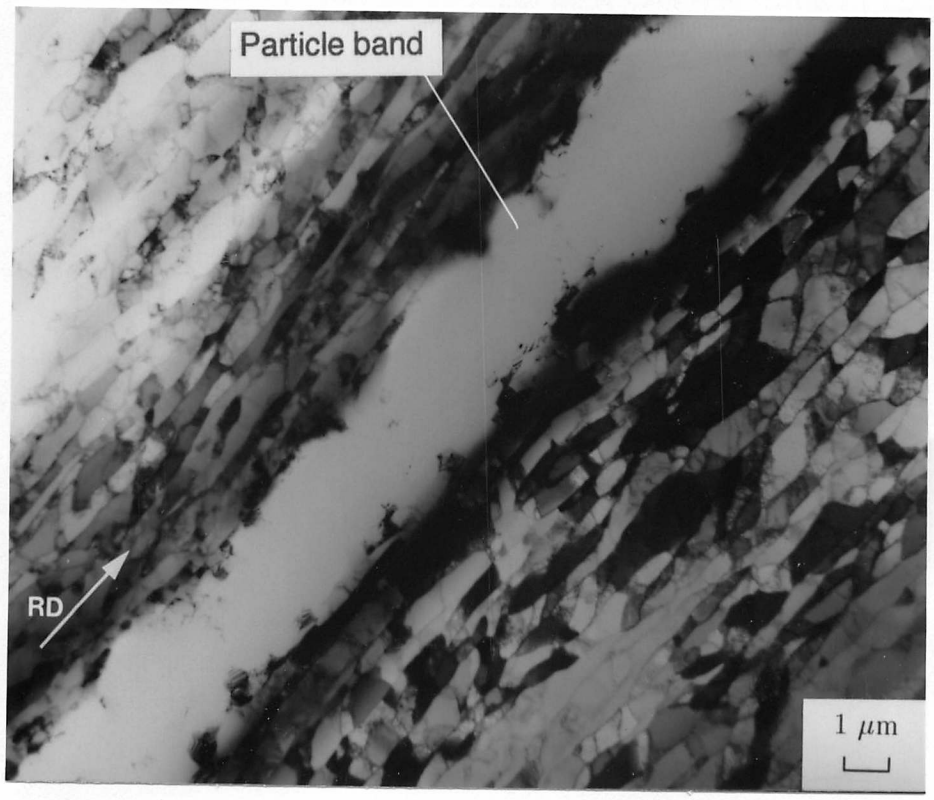

Figure 5.23 Transmission electron micrograph of the 0.47 wt% Fe alloy annealed at 250°C for 120 minutes showing a particle/potential nuclei band at low magnification.

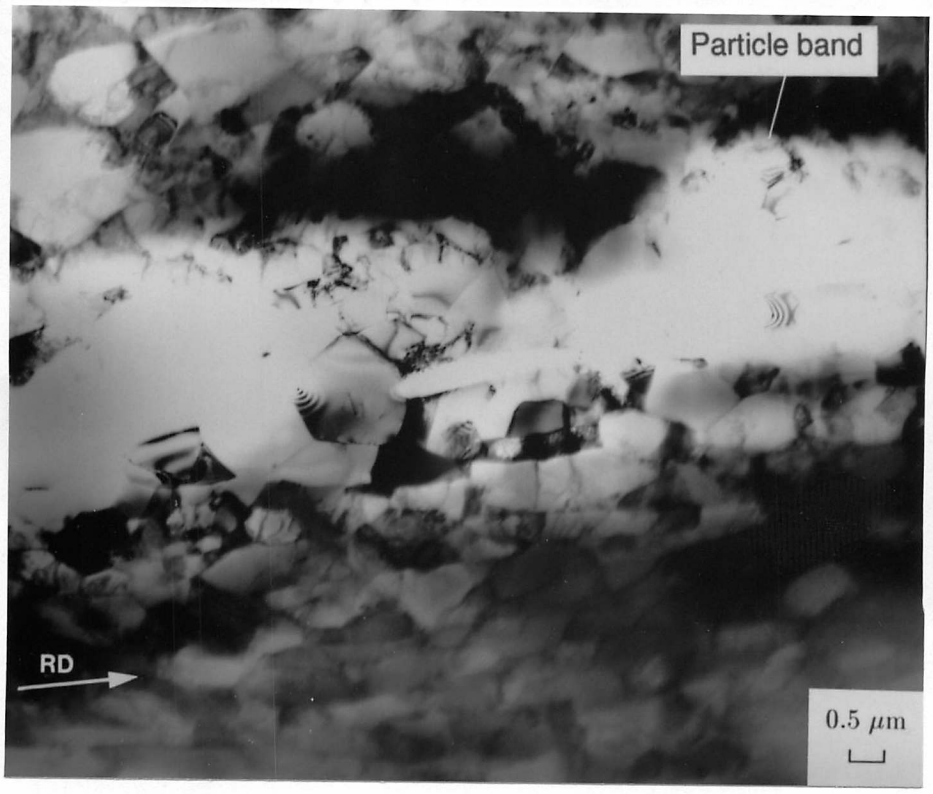

Figure 5.24 Transmission electron micrograph of the 0.47 wt% Fe alloy annealed at 250°C for 120 minutes showing a particle/potential nuclei band.

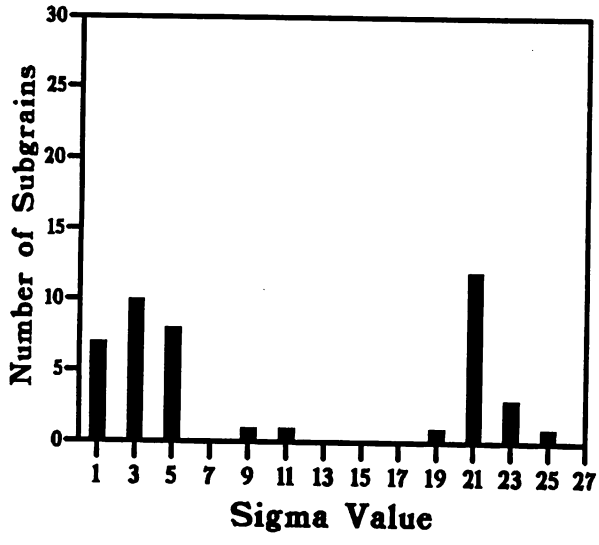

(a)

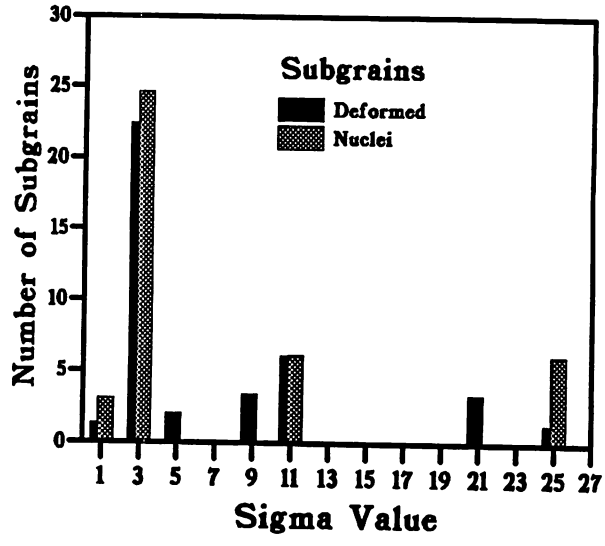

(b)

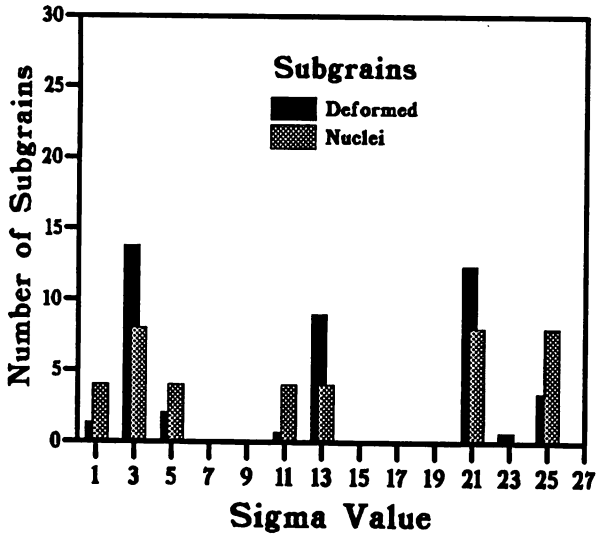

(c)

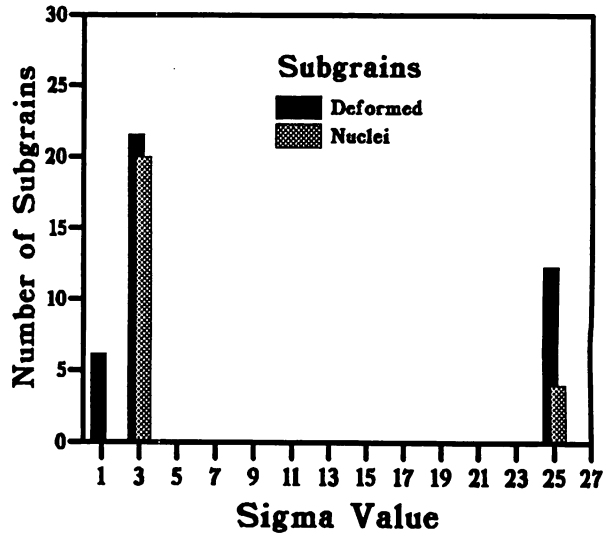

(d)

Figure 5.25 Frequency of Σ 'remote orientation' values in the 0.47 wt% Fe alloy in (a) the as-rolled condition, (b) annealed at 250°C for 30 minutes, (c) annealed at 250°C for 60 minutes and (d) annealed at 250°C for 90 minutes.

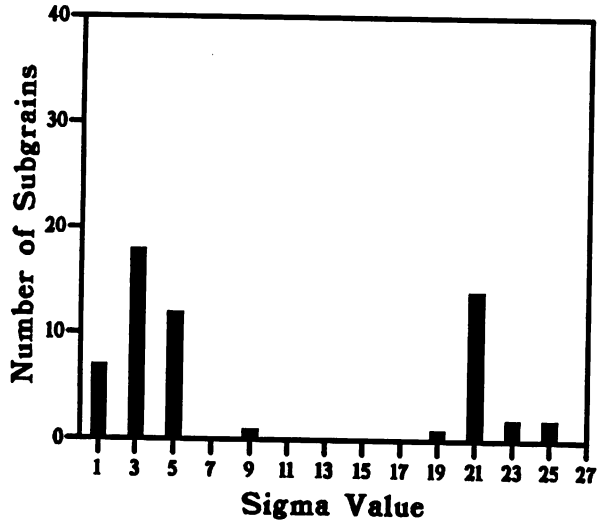

(a)

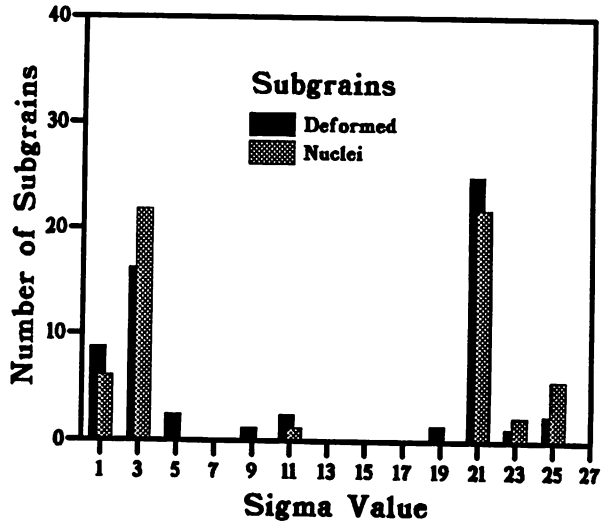

(b)

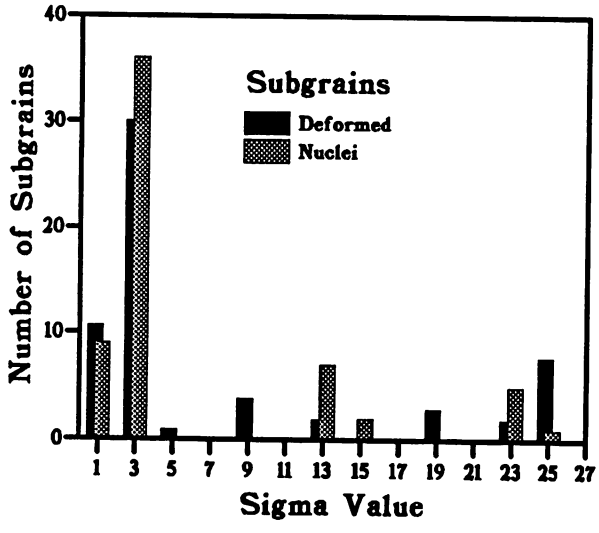

(c)

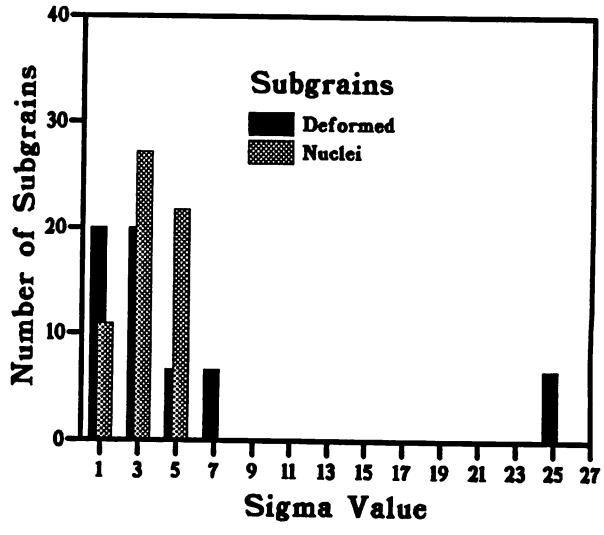

(d)

Figure 5.26 Frequency of Σ 'nearest neighbour' values in the 0.47 wt% Fe alloy in (a) the as-rolled condition, (b) annealed at 250°C for 30 minutes, (c) annealed at 250°C for 60 minutes and (d) annealed at 250°C for 90 minutes.

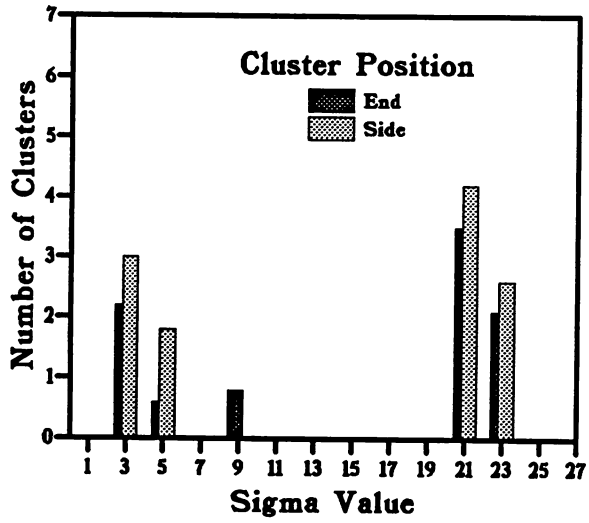

(a)

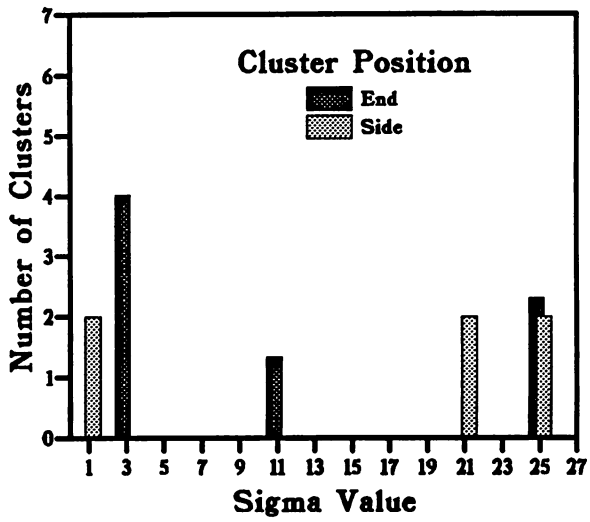

(b)

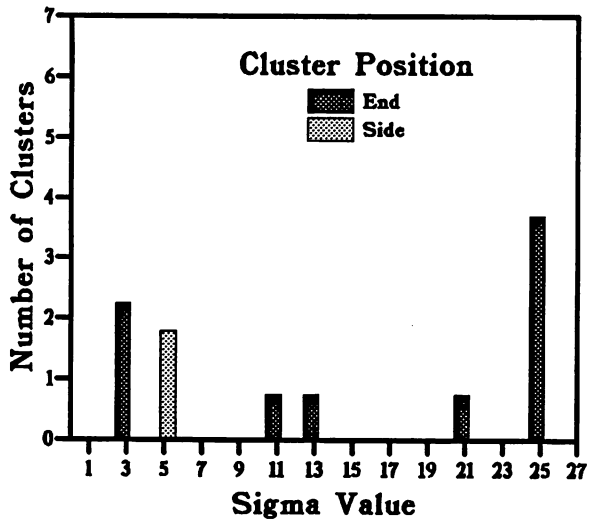

(c)

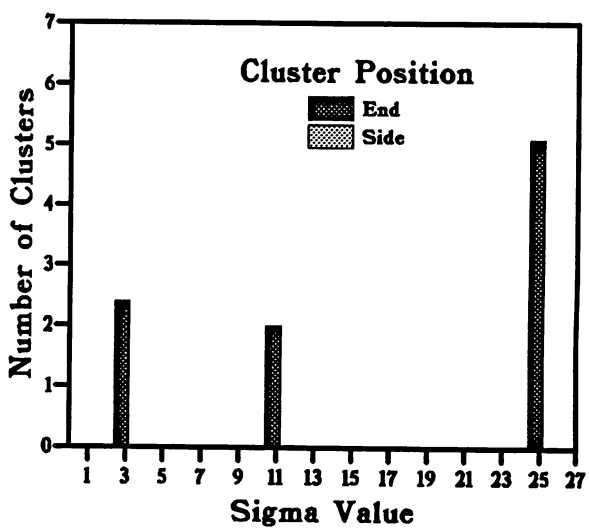

(d)

Figure 5.27 'Remote orientations' for subgrain clusters adjacent to particles in the 0.47 wt% Fe alloy, (a) as-deformed, (b) annealed at 250°C for 30 minutes, (c) annealed at 250°C for 60 minutes and (d) annealed at 250°C for 90 minutes.

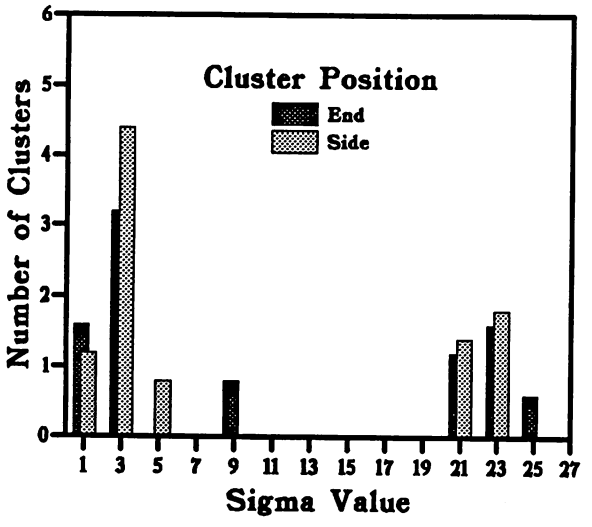

(a)

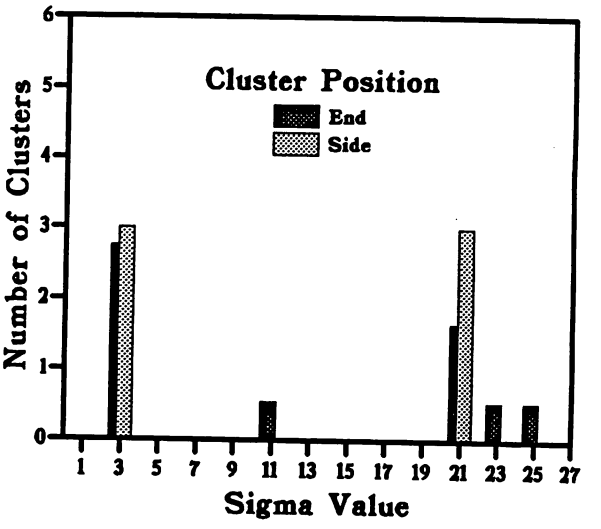

(b)

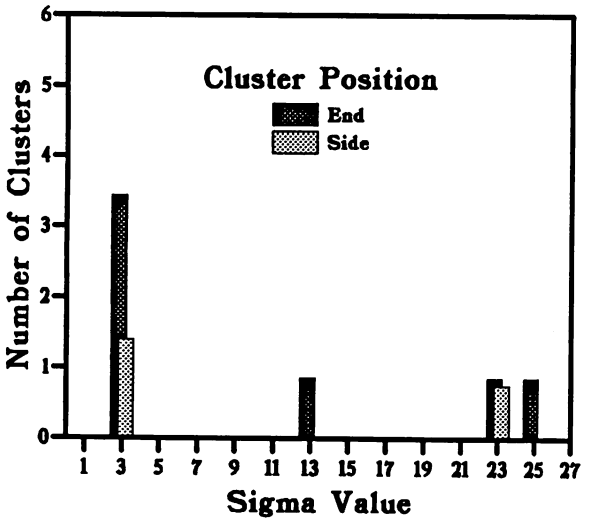

(c)

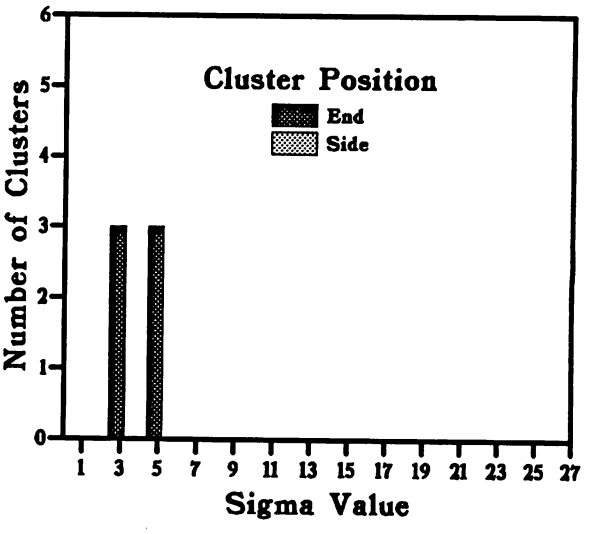

(d)

Figure 5.28 'Nearest neighbour' cluster data for subgrains adjacent to particles in the 0.47 wt% Fe alloy, (a) as–deformed, (b) annealed at 250°C for 30 minutes, (c) annealed at 250°C for 60 minutes and (d) annealed at 250°C for 90 minutes.

5.3 Conclusions

It has been demonstrated in this section of the work that the presence of clusters of subgrains in the deformation zones is important in allowing recrystallisation nuclei to form. Those clusters which display a small misorientation between their constituent subgrains, but which display a large misorientation with respect to the remote matrix, are those which promote nucleation. It is suggested that the mechanism involved in the production of a recrystallisation nucleus is one primarily of a recovery process rather than either a movement of boundaries under strain difference or a subgrain coalescence mechanism. Subgrain boundaries within subgrain clusters disappear by dislocation movement, and the resulting composite grain constitutes the new nucleus, which is able consume the entire deformation zone. The preference for low nearest–neighbour misorientations is therefore expected since this allows the reorganisation processes necessary for subgrain–boundary disappearance to occur. The prefernce for a high 'remote' misorientation is also expected, since this would suggest that the cluster in question is highly deformed, and contains enough stored energy for accelerated polygonisation to occur.

A similar result was seen in the lower iron–content alloy, but the kinetics involved were much slower, and fewer nuclei were formed due to the low volume–fraction of particles as compared to the 1.41 wt% Fe alloy.

This mechanism of local dislocation movements, subgrain boundary disappearance and nuclei growth, is only the first stage in recrystallisation, however, and annealing for longer periods is necessary to establish the mechanisms involved in growth beyond the deformation zone.

Chapter 6

PRIMARY RECRYSTALLISATION

After the initial stages of recrystallisation, in which the particle deformation zones of the Al–Fe alloys are consumed, recrystallisation proceeds relatively quickly, and the observation of this in the transmission electron microscope was not possible. Although potential nuclei have been observed to form at the $FeAl_3$ particles in the Al–Fe alloy matrix, it may be that other nucleation sites are activated at later stages of annealing. The successful nuclei will thus be those that have a sufficiently high mobility to dominate the recrystallisation kinetics. In order to be certain therefore, that the particles are indeed the sites for further nucleation, higher temperature anneals combined with optical–microscopy techniques were employed to follow the later stages of annealing.

6.1 Later Recrystallisation Stages

The 1.41 wt% Fe and 0.47 wt% Fe alloys of rolling schedule II were subjected to higher temperature heat treatments after first having been annealed at 250°C for 120 minutes in order to produce recrystallisation growth to a high enough degree to be viewed in the optical microscope. Each was heat treated at 300°C for 30 minutes, followed by 350°C for 30 minutes and then 400°C for 30 minutes, and the microstructures and hardness values after each stage were recorded. Figure *6.1* shows the hardness curves for the two alloys as annealing was carried out, with the higher annealing temperature treatments displayed as three consecutive 30 minute additions to the 250°C annealing curve. As can be gathered from the larger drop in hardness as compared with the 0.47 wt% Fe alloy curve, the 1.41 wt% Fe alloy has the fastest recrystallisation kinetics. If nucleation sites other than particles had been dominant during annealing, this difference between the two alloys would not have been observed. If particle stimulated nucleation is dominant, the 1.41 wt% Fe alloy, with its higher volume fraction of particles, would be expected to produce a greater number of potential nuclei from which recrystallisation may proceed and thus an acceleration in kinetics. This result therefore suggests that particle nucleation sites are dominant.

First, if the optical micorgraphs for the 1.41 wt% Fe alloy heat treatments are studied, the growth of recrystallised grains from the $FeAl_3$ particles can be followed. In figure *6.2* the alloy is shown in the rolling–plane after the 300°C treatment. The early stages of abnormal grain growth can be seen, and it is clear that the recrystallised grains are growing from particles only, and beginning to reach into the particle–free matrix. Within particle bands there are many small grains which will later compete for dominance, as shown in figure *6.3*. Still looking in the rolling–plane, after the 350°C anneal the grains have now grown to consume most of

the as–deformed matrix and, as can be seen in figure *6.4*, the largest grains occur in particle–free areas. It is clear that within particle bands the growth of recrystallised grains has been prevented by the pinning action of the particles, as indicated. Figure *6.5* shows the growth of grains from a string of particles, and figure *6.6* illustrates that the large grains appear to have developed from individual particles stranded away from particle bands. In the 400°C heat treated specimens, some further growth of grains has occurred, although this is not obvious from the rolling–plane micrographs, as shown in figure *6.7*. Many of the particles have begun to spheroidise and are less easy to distinguish. Figure *6.8* shows the duplex nature of the grain structure due to banding of the particles.

When viewed in the long transverse sections, the process of recrystallisation becomes more clear. Figure *6.9*, taken after the 300°C anneal, shows large as–deformed bands free of particles and recrystallising grains, separated by bands of particles, each with an associated nucleus. After the 350°C treatment, as shown in figure *6.10*, the grains have consumed the as–deformed material. Rather than appearing from nucleation sites other than $FeAl_3$ particles, the large grains away from the particle bands can be traced to particles at the edge of bands, or individual isolated particles. These isolated particles frequently appear within grains rather than at their boundaries, which suggests that the grains are nucleated from them rather than away from them, since in the latter case the particle would pin the approaching grain boundary and be left sitting on it. Figure *6.11* confirms the pinning powers of the particles in their limitation of grain sizes within the separation distance of particle strings, and figure *6.12* shows the positions of particles within new grains.

The 400°C anneal is shown in figure *6.13* in the long transverse section, and here a difference can be seen from the previous heat treatment, since some of the grains appear to have grown preferentially along the rolling direction where there is no obstruction from particles. This is shown again in figure *6.14*, in which a contrast can be seen with the equiaxed grains within the particle bands. Figures *6.15* and *6.16* show areas where this elongation is not prevalent, and particles can again be seen within the dominant grains.

The same heat treatments, carried out on the 0.47 wt% Fe alloy, reveal a more exaggeratedly duplex microstructure upon grain growth. The time taken for grain growth to proceed is longer than that of the 1.41 wt% Fe alloy, and this is illustrated in figures *6.17* and *6.18* taken in the rolling–plane after the 300°C treatment. Most of the as–deformed material is still in evidence, where the tiny recrystallised grains at the particles are as yet too small to view in the optical microscope.

After the 350°C treatment grain growth has begun in earnest, and already there can be seen a large range of grain sizes, as in figure *6.19*. As seen in the rolling–plane section, a few

of the already large grains cannot be traced to precipitates. However, no previous evidence had been found of other nucleation sites in operation, and the growth from any other sites would have to be extremely rapid to overtake the growth from particles. It may be that the grains observed have been nucleated from particles outside of the section viewed. Figure *6.20* shows the nucleation of grains from lines of particles extending into the deformed matrix, whilst areas free of particles are left untouched, thus strengthening the view that nucleation is only occurring from particles. Figures *6.21* and *6.22*, taken at higher magnification, show more clearly the recrystallised grains issuing from particle strings.

After 30 minutes at 400°C, many areas of the alloy are now fully recrystallised, as shown in figures *6.23* and *6.24*. Many small grains are seen close to the particle strings, but in the particle free areas the grains have grown to up to 200 μm in diameter. This is shown at higher magnification in figure *6.25* in which the small grains are more easily identified.

In the long transverse section it is easier to discern the nucleation sites of the recrystallised grains. Figure *6.26* shows the alloy after the 300°C treatment, and only very tiny grains can be discerned at particles. In figures *6.27* and *6.28* the 350°C treatment is shown, and large grains can be seen extending from particle strings, or from individual particles, their extended growth often inhibited by their impingement on particle strings. Viewed in this section, it can be seen that even after the 400°C treatment, the material is not fully recrystallised across the specimen. Figures *6.29* and *6.30* show the uneven nature of the recrystallisation process, and in both the strings of particles can be observed to be governing the final grain sizes. In this case, very few grains cannot be traced to associated particles.

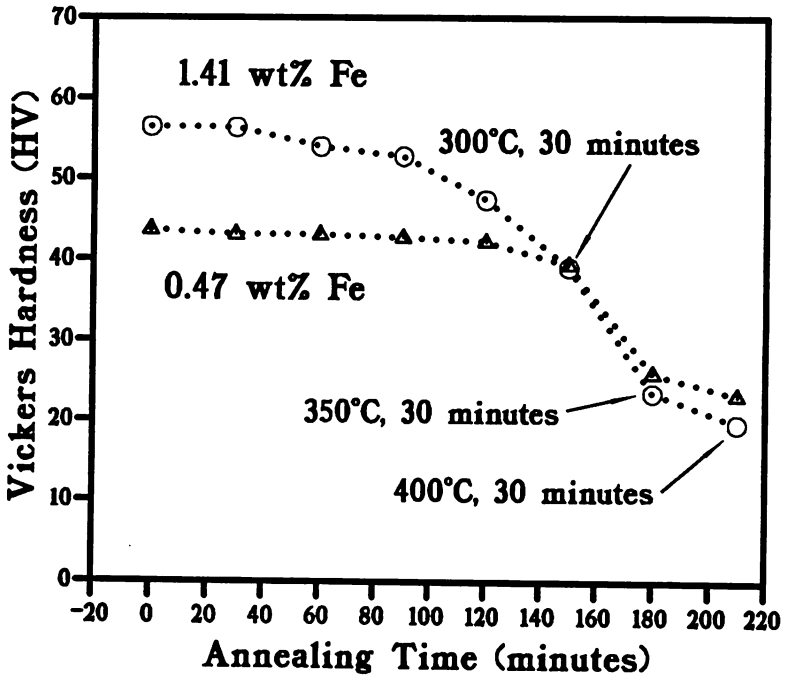

Figure 6.1 Hardness curves for the 1.41 wt% Fe and 0.47 wt% Fe alloys over higher annealing temperatures.

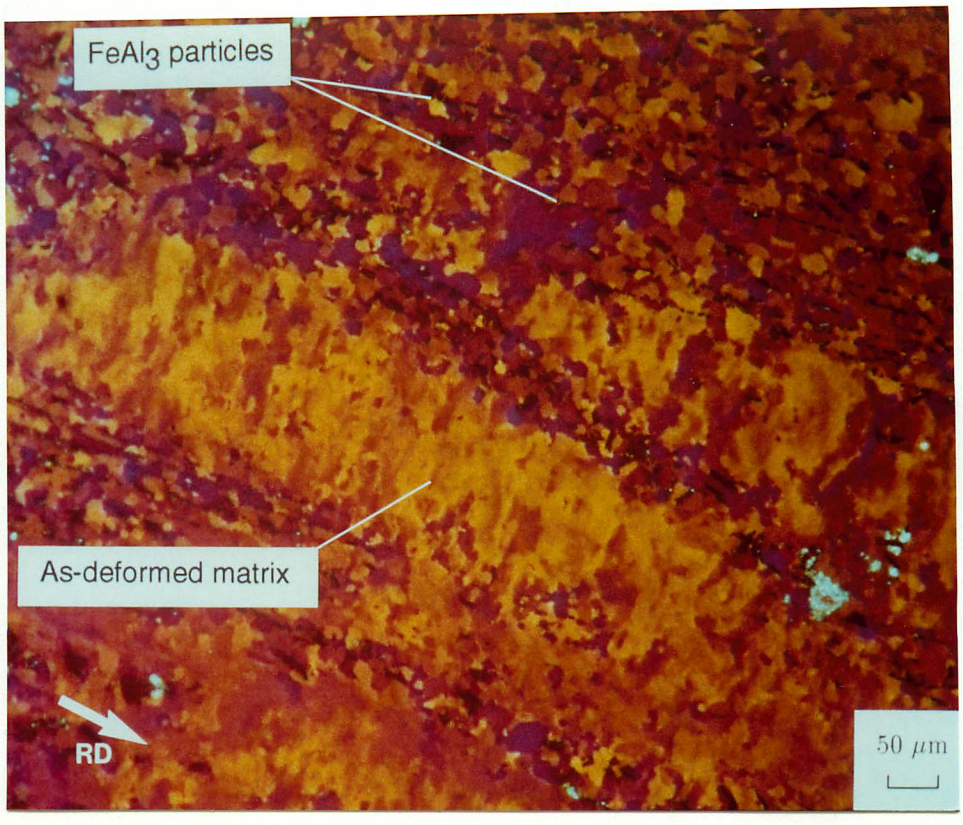

Figure 6.2 Optical micrograph in the rolling plane showing the 1.41 wt% Fe alloy heat treated at 250°C for 120 minutes followed by 300°C for 30 minutes.

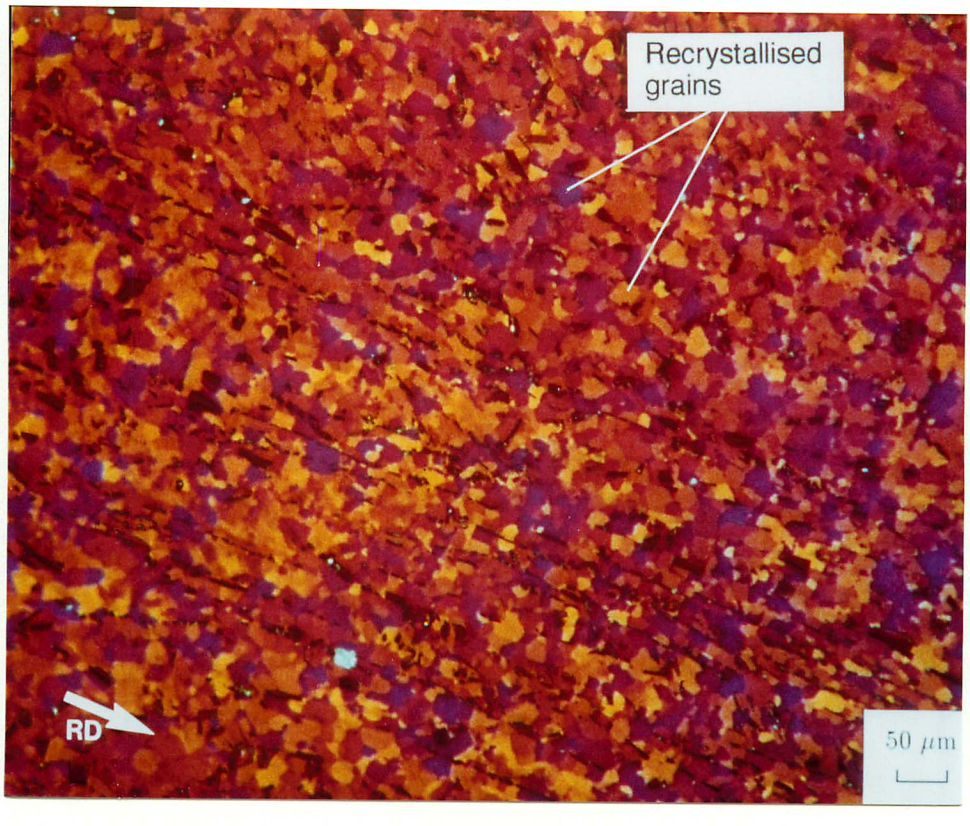

Figure 6.3 Optical micrograph in the rolling plane showing the 1.41 wt% Fe alloy heat treated at 250°C for 120 minutes followed by 300°C for 30 minutes taken within a particle band.

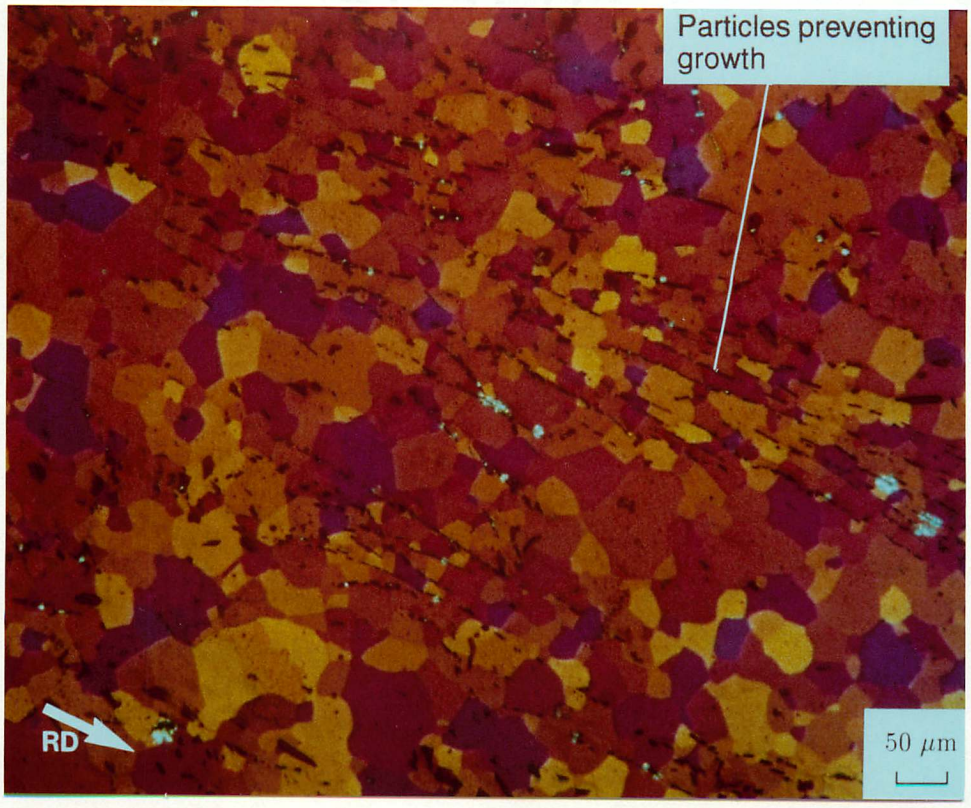

Figure 6.4 Optical micrograph in the rolling plane showing the 1.41 wt% Fe alloy heat treated at 250°C for 120 minutes followed by 350°C for 30 minutes showing complete recrystallisation.

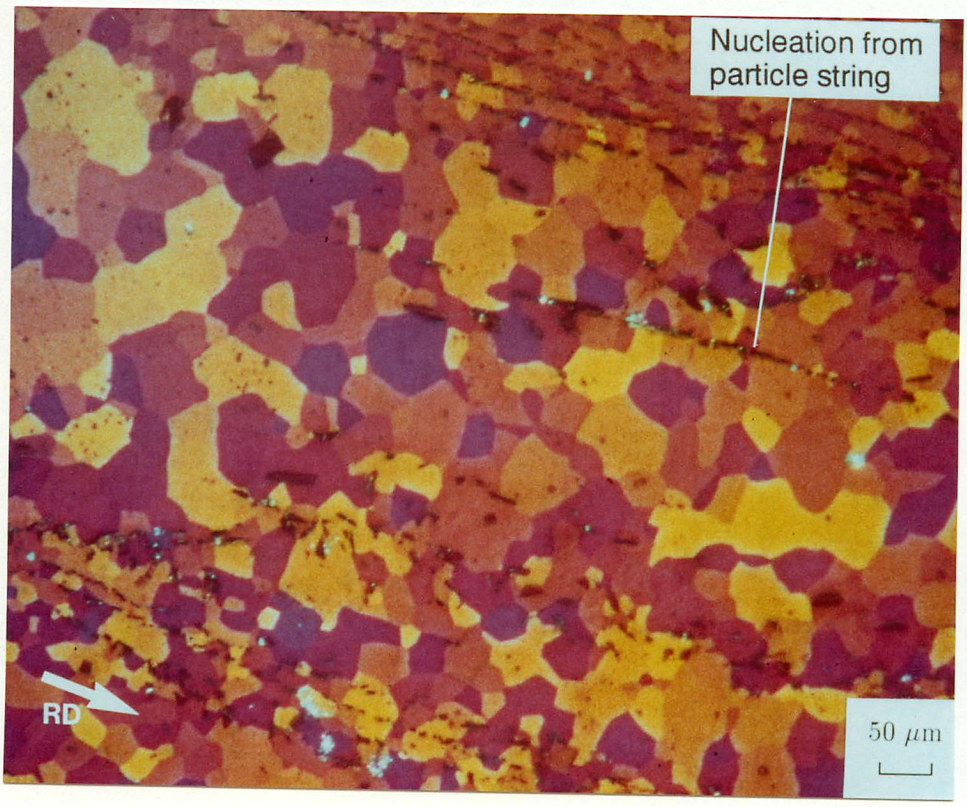

Figure 6.5 Optical micrograph in the rolling plane showing the 1.41 wt% Fe alloy heat treated at 250°C for 120 minutes followed by 350°C for 30 minutes.

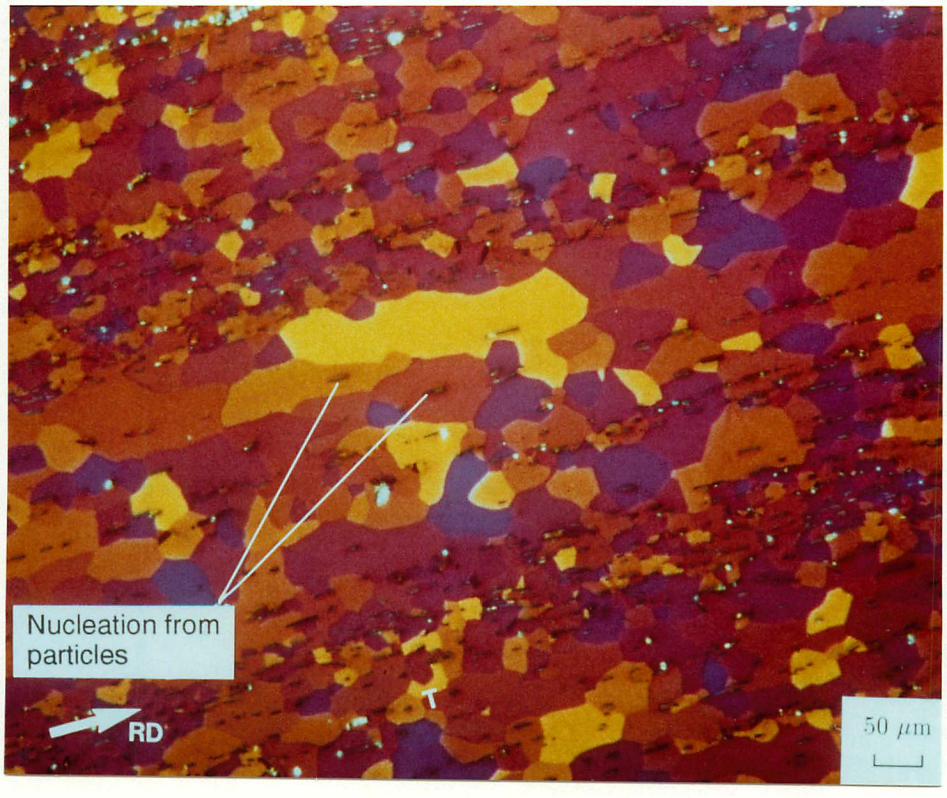

Figure 6.6 Optical micrograph in the rolling plane showing the 1.41 wt% Fe alloy heat treated at 250°C for 120 minutes followed by 350°C for 30 minutes.

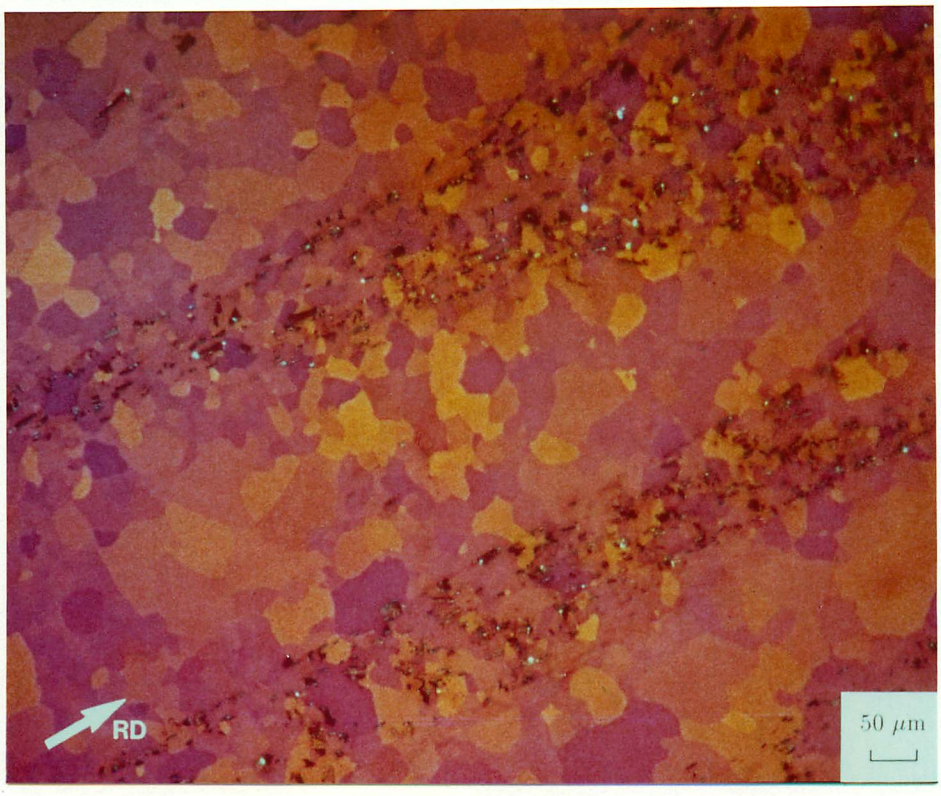

Figure 6.7 Optical micrograph in the rolling plane showing the 1.41 wt% Fe alloy heat treated at 250°C for 120 minutes followed by 400°C for 30 minutes.

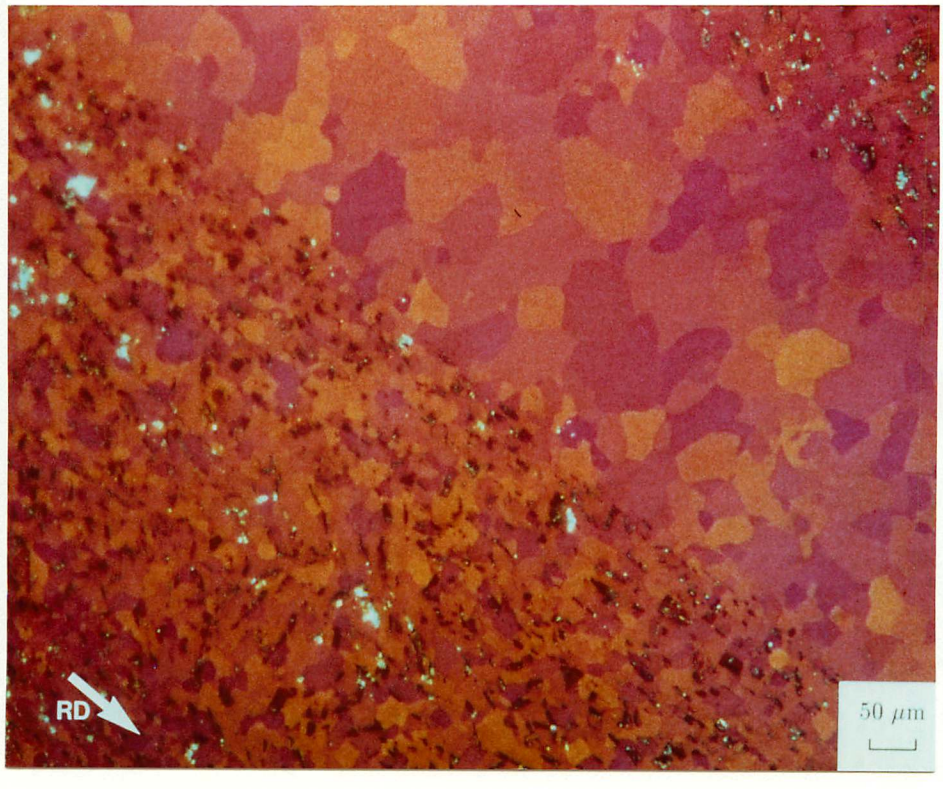

Figure 6.8 Optical micrograph in the rolling plane showing the 1.41 wt% Fe alloy heat treated at 250°C for 120 minutes followed by 400°C for 30 minutes.

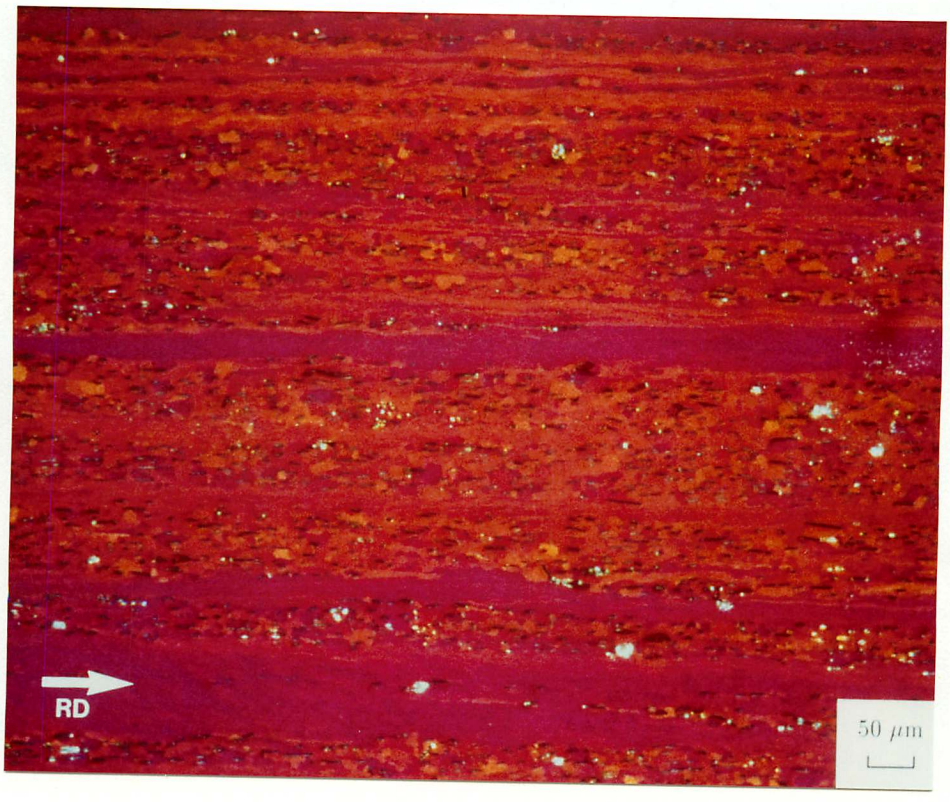

Figure 6.9 Optical micrograph in the long transverse section showing the 1.41 wt% Fe alloy heat treated at 250°C for 120 minutes followed by 300°C for 30 minutes.

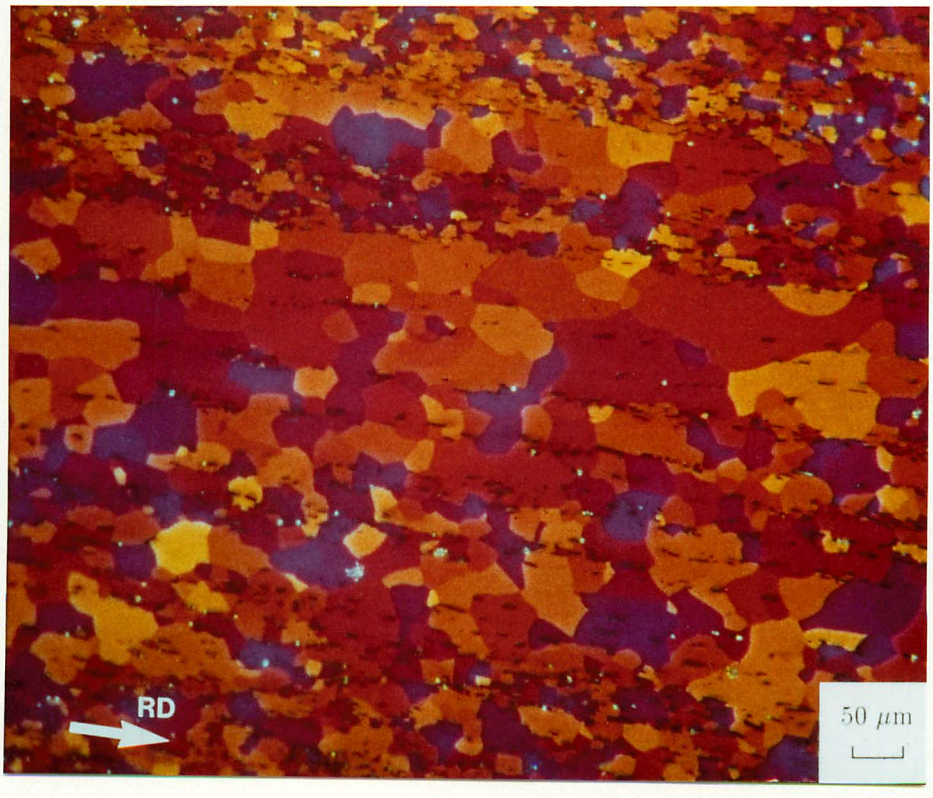

Figure 6.10 Optical micrograph in the long transverse section showing the 1.41 wt% Fe alloy heat treated at 250°C for 120 minutes followed by 350°C for 30 minutes showing particles occuring within new grains.

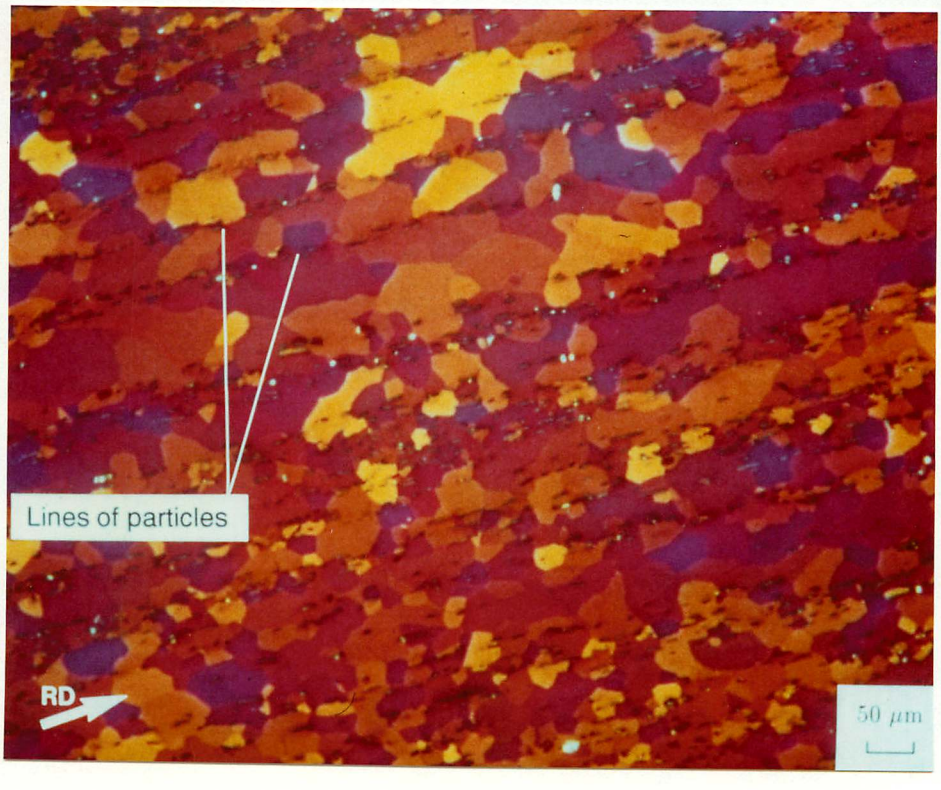

Figure 6.11 Optical micrograph in the long transverse section showing the 1.41 wt% Fe alloy heat treated at 250°C for 120 minutes followed by 350°C for 30 minutes.

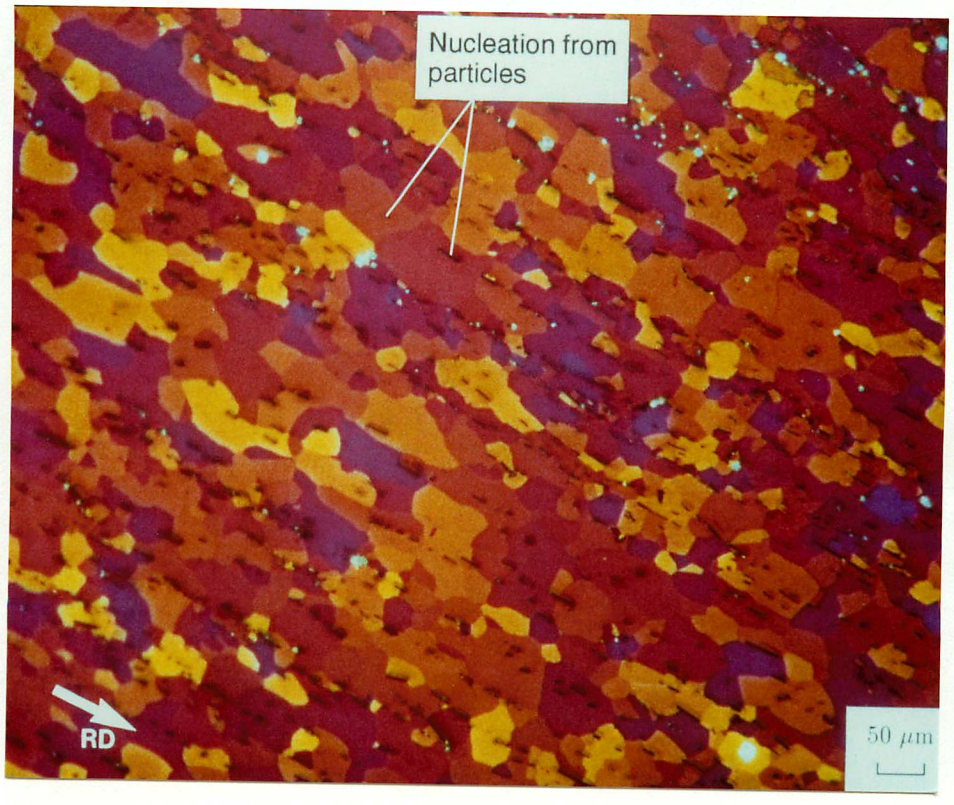

Figure 6.12 Optical micrograph in the long transverse section showing the 1.41 wt% Fe alloy heat treated at 250°C for 120 minutes followed by 350°C for 30 minutes.

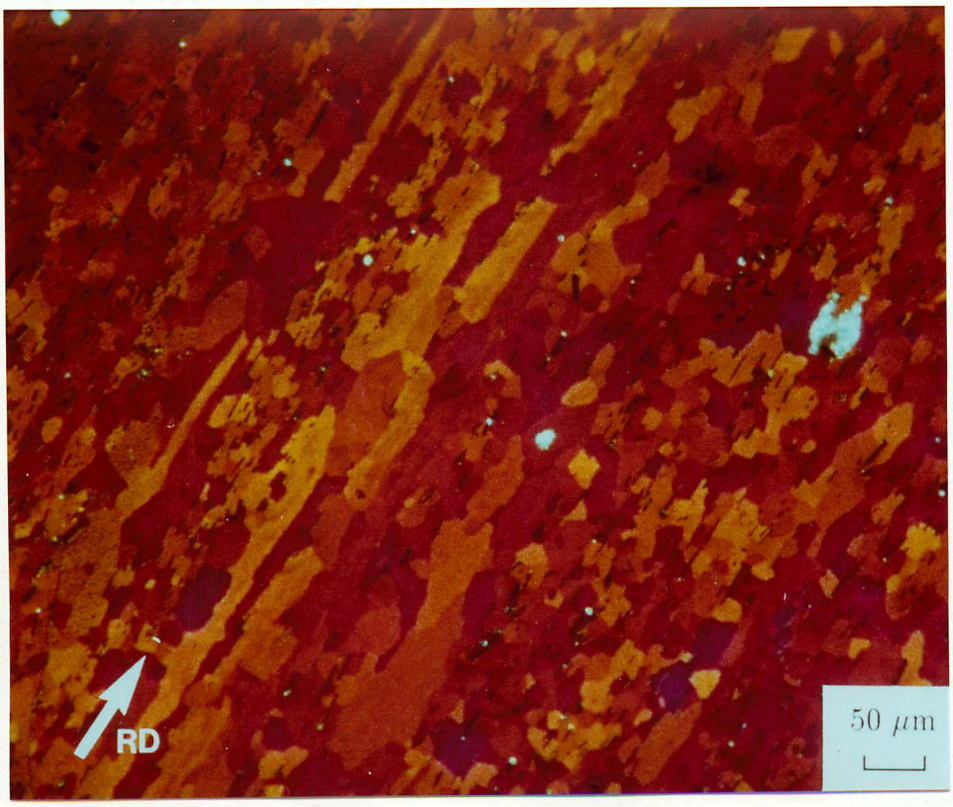

Figure 6.13 Optical micrograph in the long transverse section showing the 1.41 wt% Fe alloy heat treated at 250°C for 120 minutes followed by 400°C for 30 minutes.

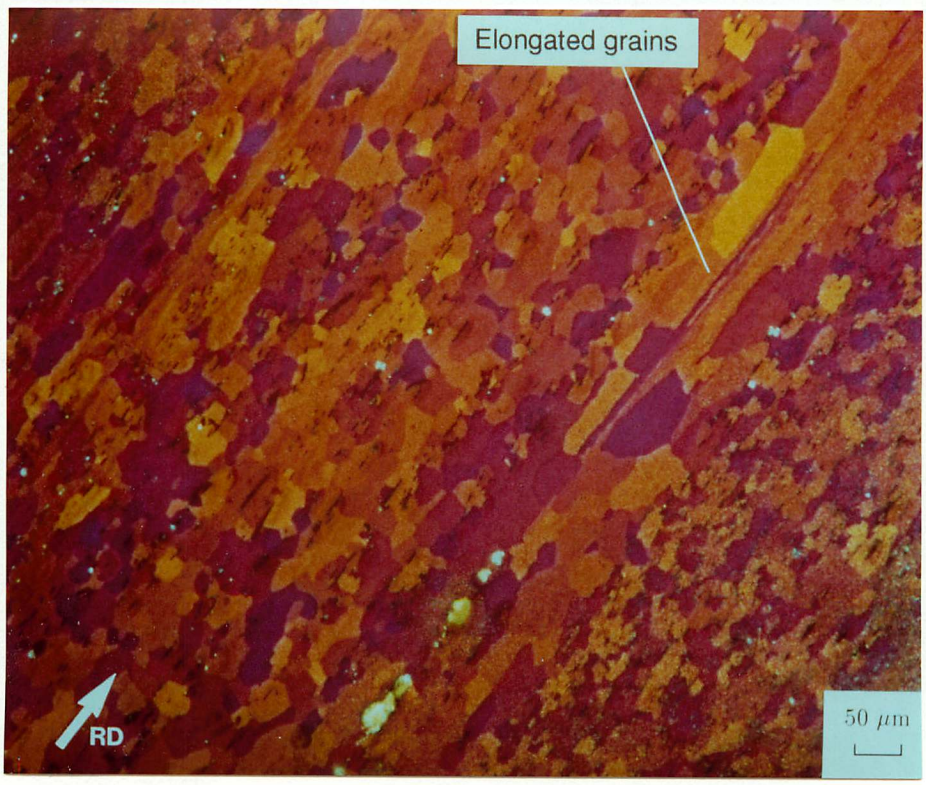

Figure 6.14 Optical micrograph in the long transverse section showing the 1.41 wt% Fe alloy heat treated at 250°C for 120 minutes followed by 400°C for 30 minutes.

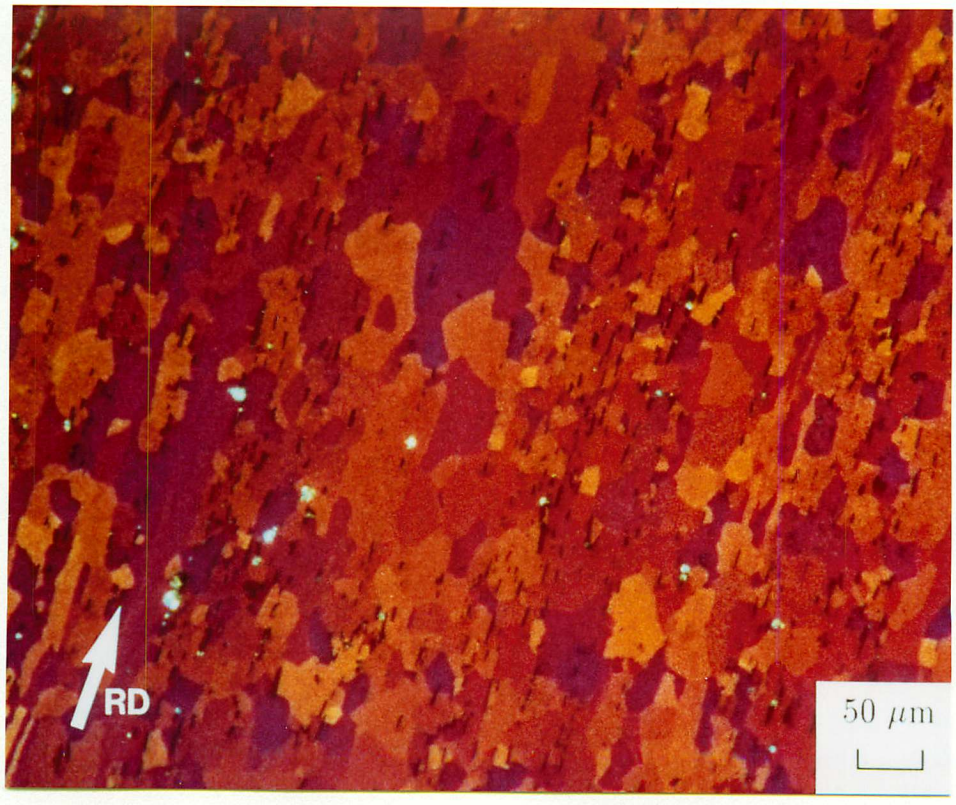

Figure 6.15 Optical micrograph in the long transverse section showing the 1.41 wt% Fe alloy heat treated at 250°C for 120 minutes followed by 400°C for 30 minutes.

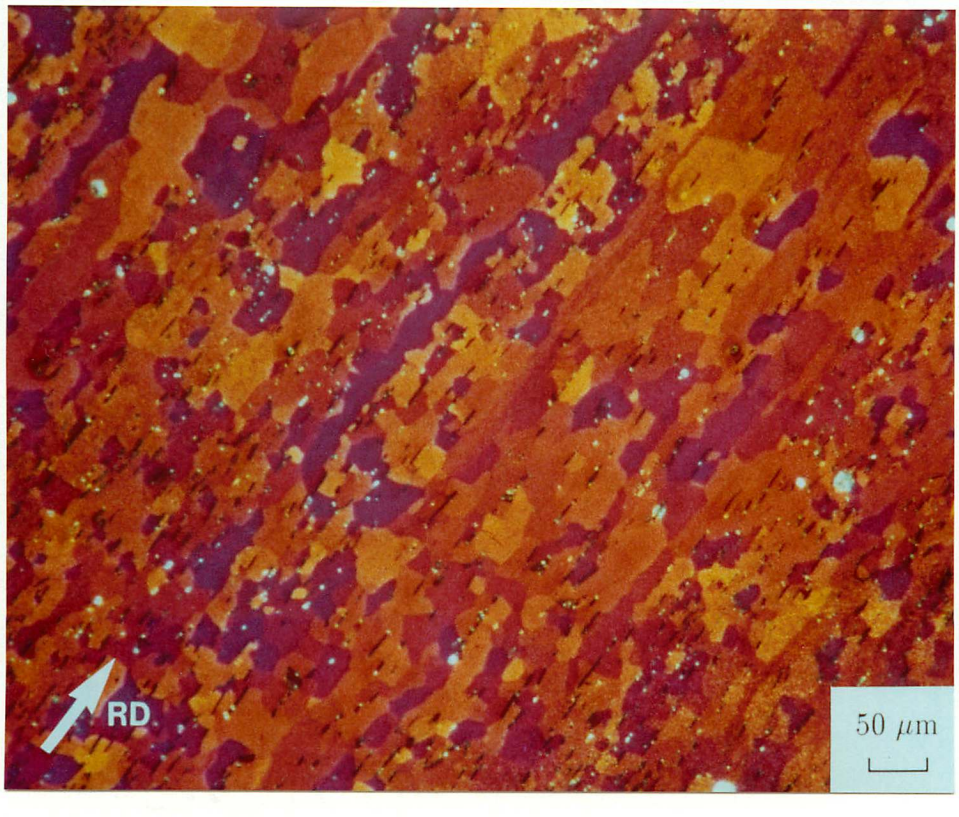

Figure 6.16 Optical micrograph in the long transverse section showing the 1.41 wt% Fe alloy heat treated at 250°C for 120 minutes followed by 400°C for 30 minutes.

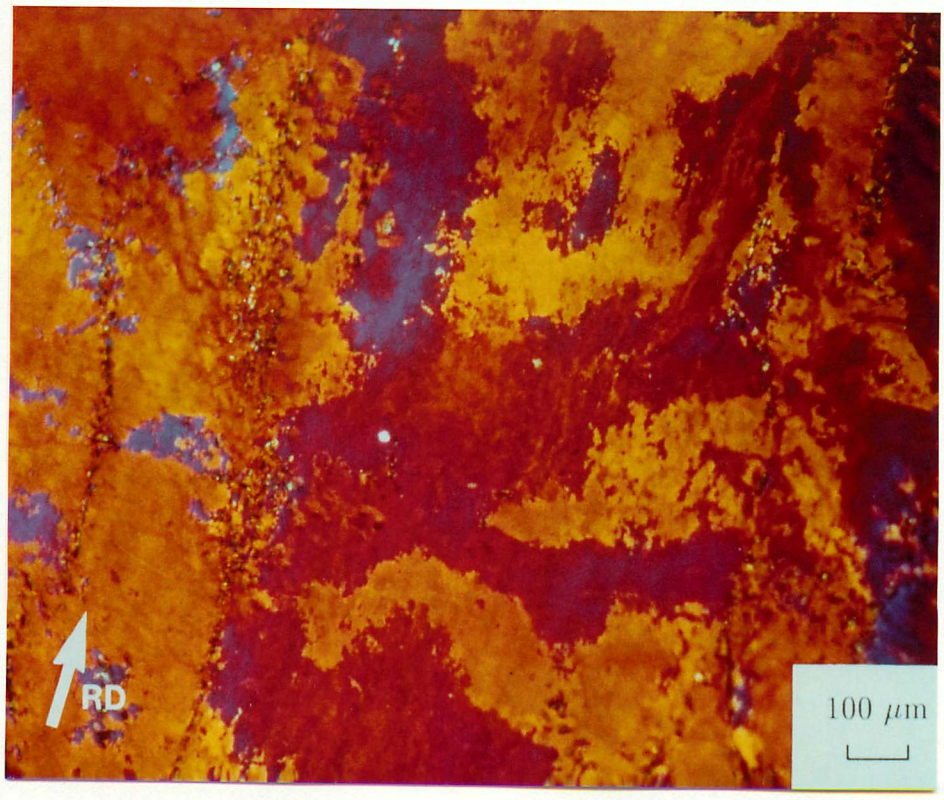

Figure 6.17 Optical micrograph in the rolling plane showing the 0.47 wt% Fe alloy heat treated at 250°C for 120 minutes followed by 300°C for 30 minutes showing predominantly as–deformed material.

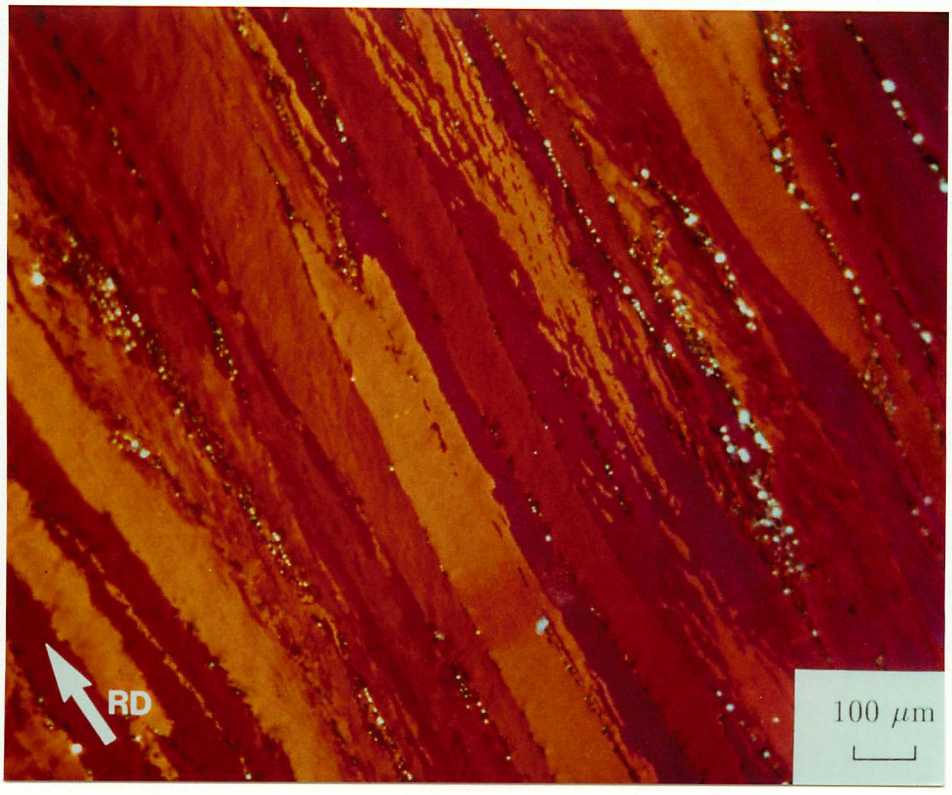

Figure 6.18 Optical micrograph in the rolling plane showing the 0.47 wt% Fe alloy heat treated at 250°C for 120 minutes followed by 300°C for 30 minutes.

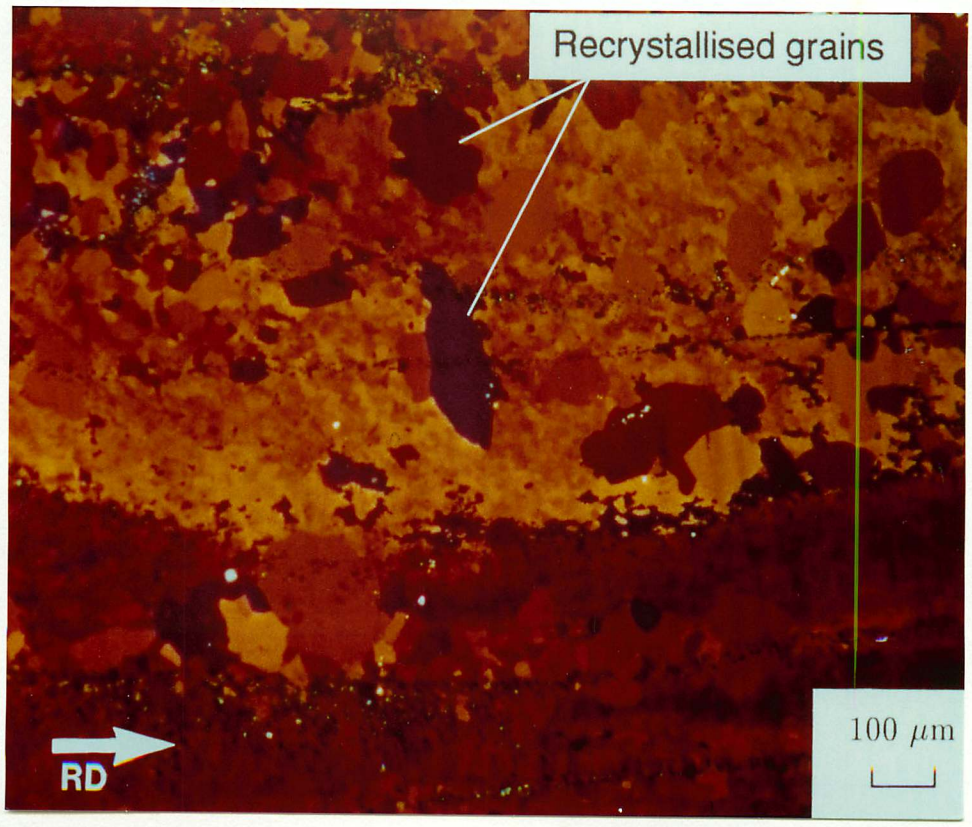

Figure 6.19 Optical micrograph in the rolling plane showing the 0.47 wt% Fe alloy heat treated at 250°C for 120 minutes followed by 350°C for 30 minutes.

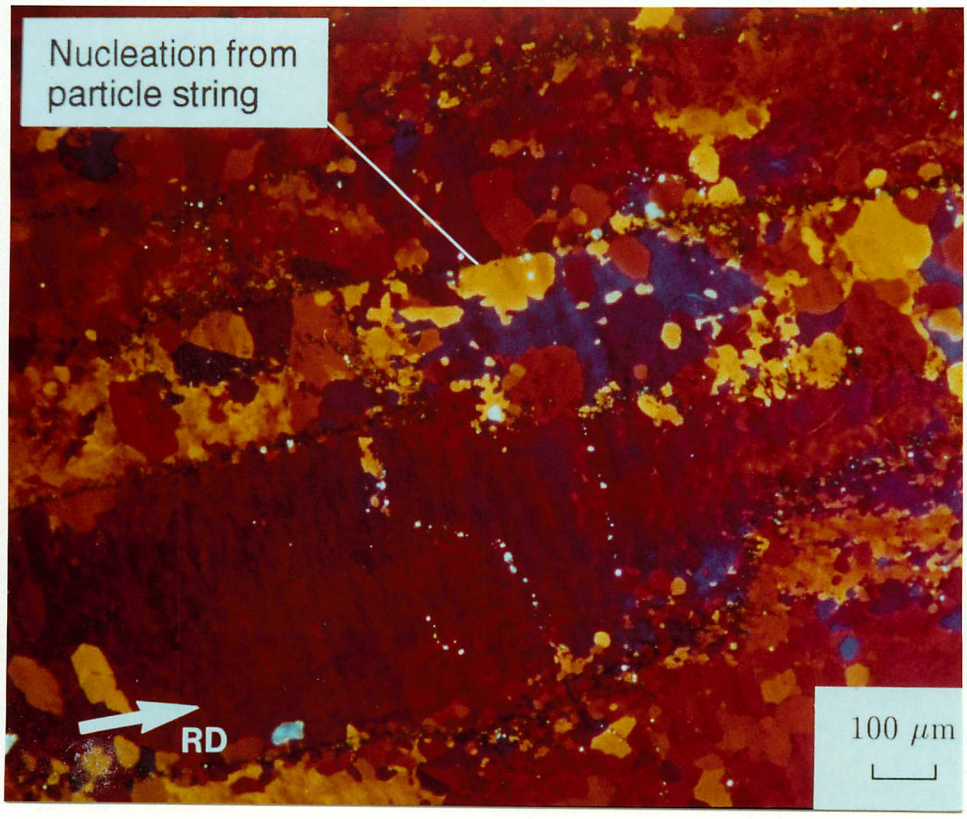

Figure 6.20 Optical micrograph in the rolling plane showing the 0.47 wt% Fe alloy heat treated at 250°C for 120 minutes followed by 350°C for 30 minutes.

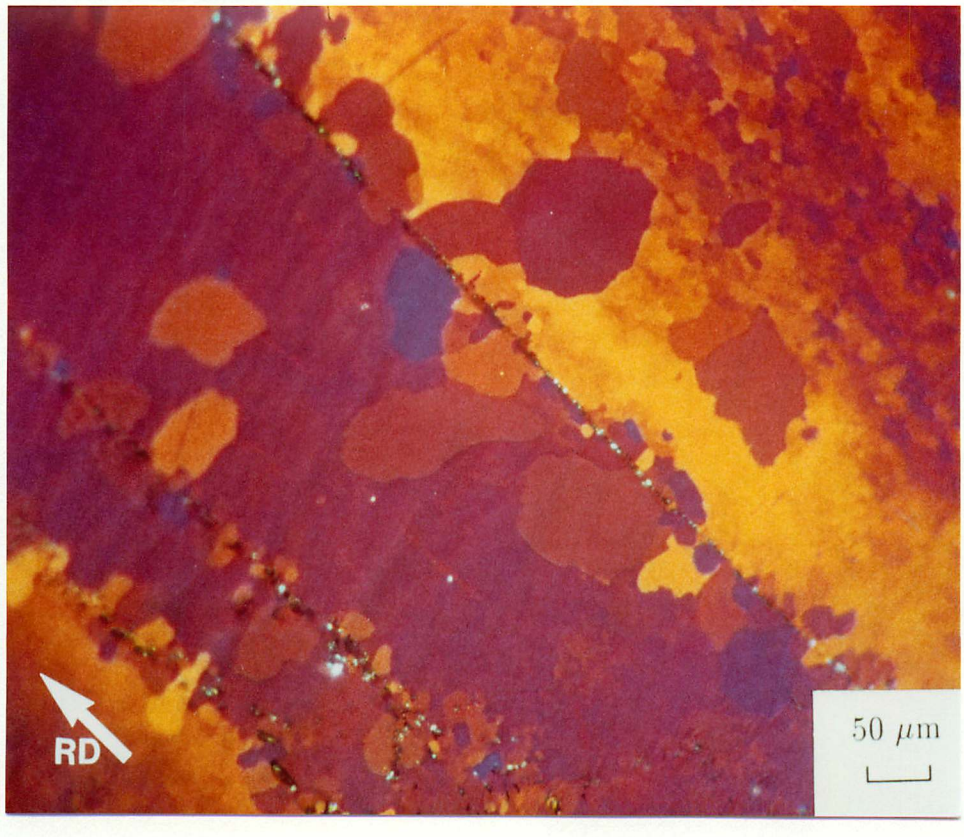

Figure 6.21 Optical micrograph in the rolling plane showing the 0.47 wt% Fe alloy heat treated at 250°C for 120 minutes followed by 350°C for 30 minutes shown at higher magnification.

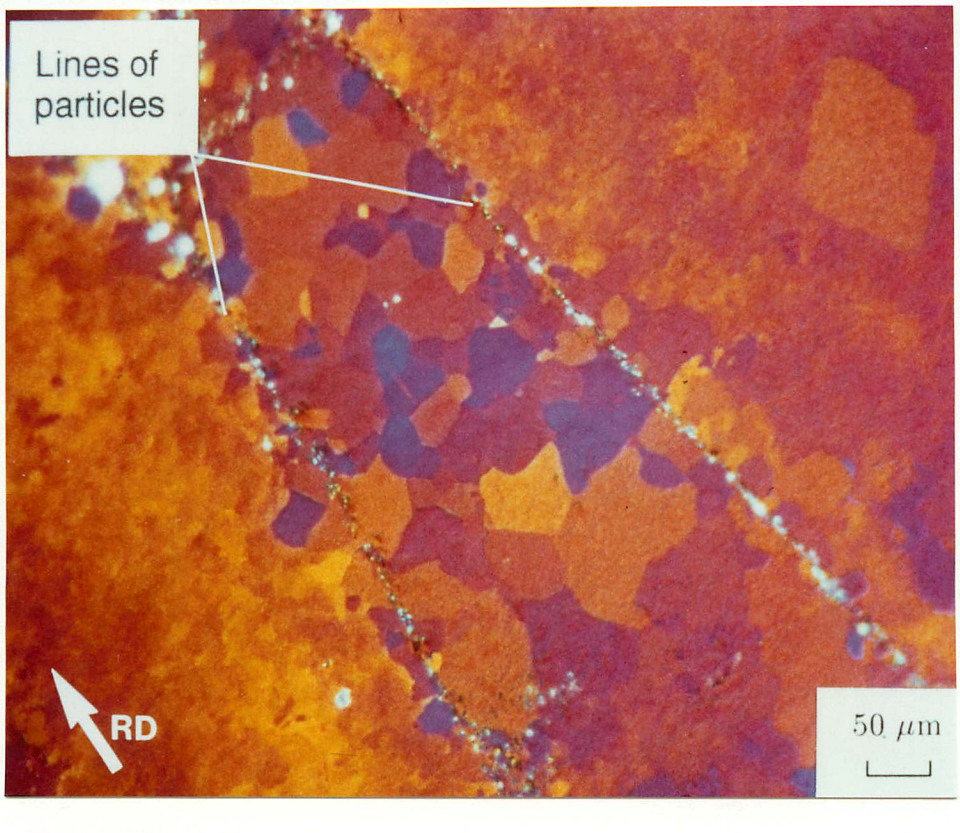

Figure 6.22 Optical micrograph in the rolling plane showing the 0.47 wt% Fe alloy heat treated at 250°C for 120 minutes followed by 350°C for 30 minutes shown at higher magnification.

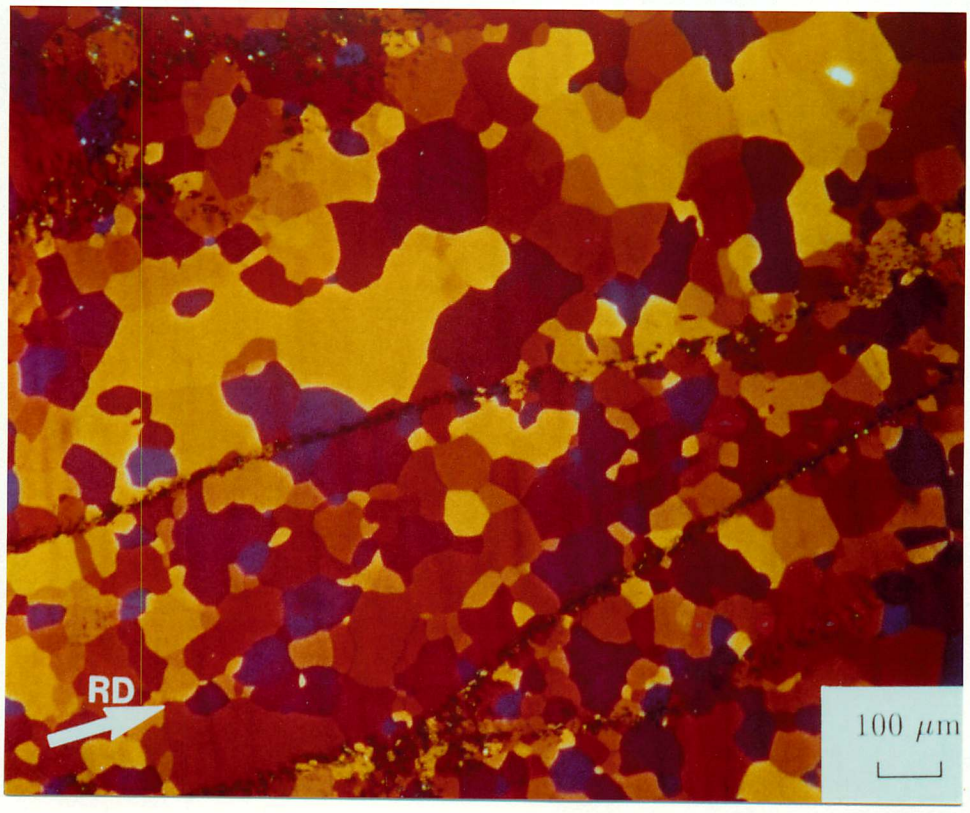

Figure 6.23 Optical micrograph in the rolling plane showing the 0.47 wt% Fe alloy heat treated at 250°C for 120 minutes followed by 400°C for 30 minutes showing full recrystallisation.

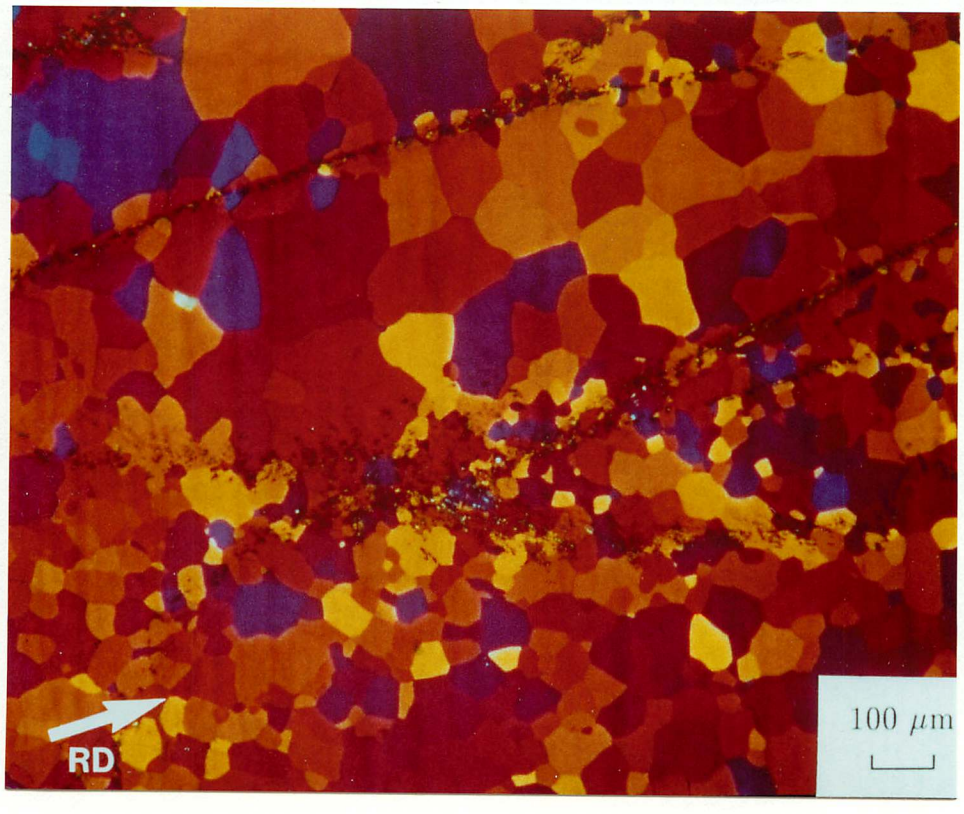

Figure 6.24 Optical micrograph in the rolling plane showing the 0.47 wt% Fe alloy heat treated at 250°C for 120 minutes followed by 400°C for 30 minutes.

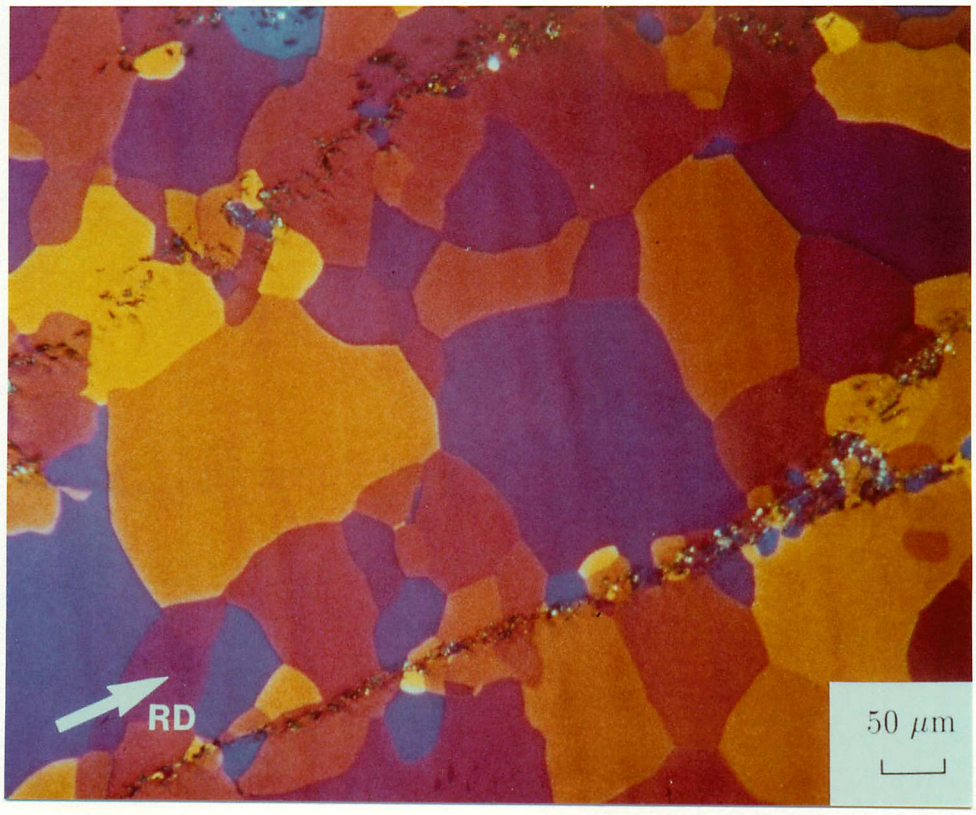

Figure 6.25 Optical micrograph in the rolling plane showing the 0.47 wt% Fe alloy heat treated at 250°C for 120 minutes followed by 400°C for 30 minutes at higher magnification.

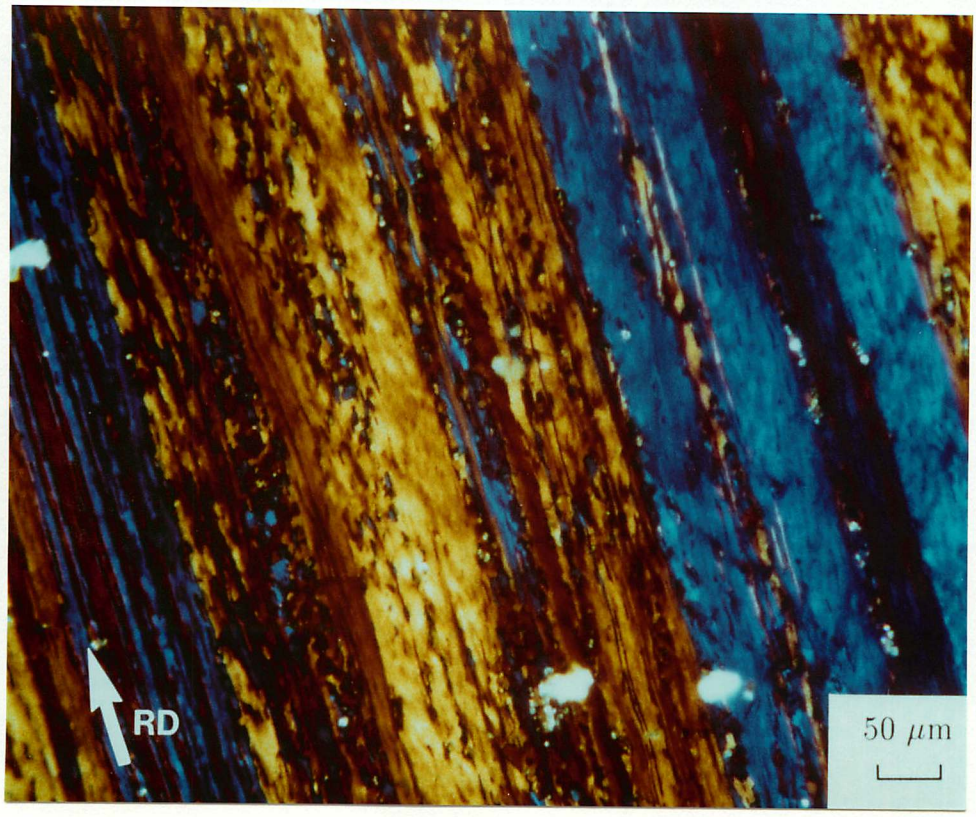

Figure 6.26 Optical micrograph in the long transverse section showing the 0.47 wt% Fe alloy heat treated at 250°C for 120 minutes followed by 300°C for 30 minutes.

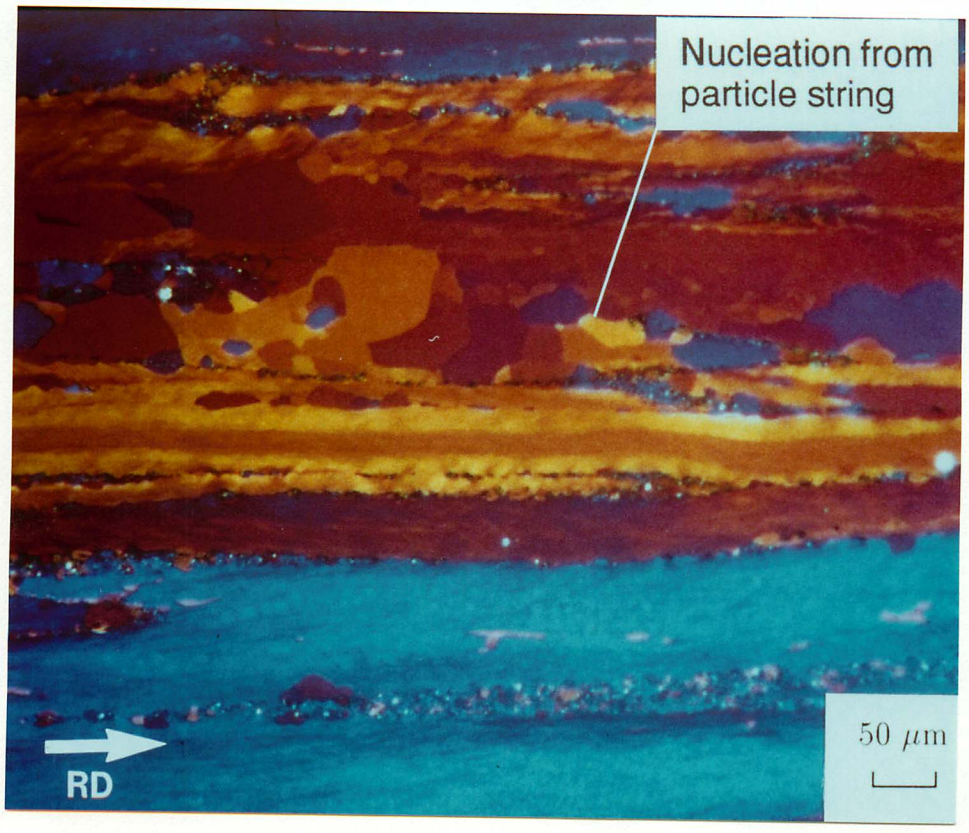

Figure 6.27 Optical micrograph in the long transverse section showing the 0.47 wt% Fe alloy heat treated at 250°C for 120 minutes followed by 350°C for 30 minutes.

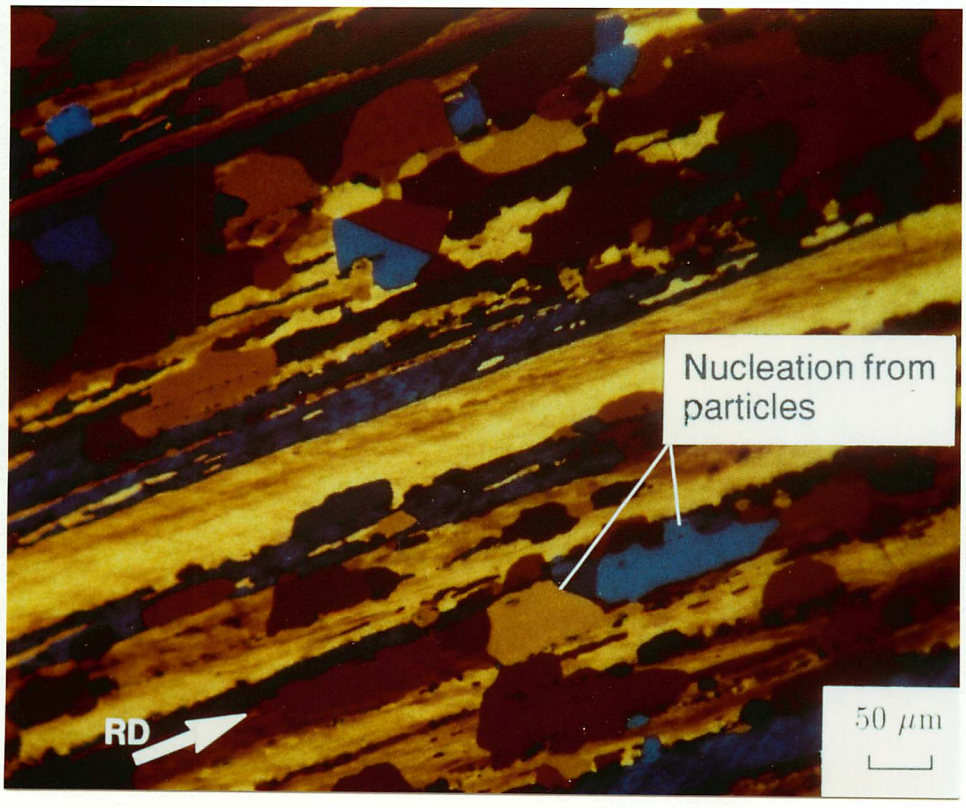

Figure 6.28 Optical micrograph in the long transverse section showing the 0.47 wt% Fe alloy heat treated at 250°C for 120 minutes followed by 350°C for 30 minutes.

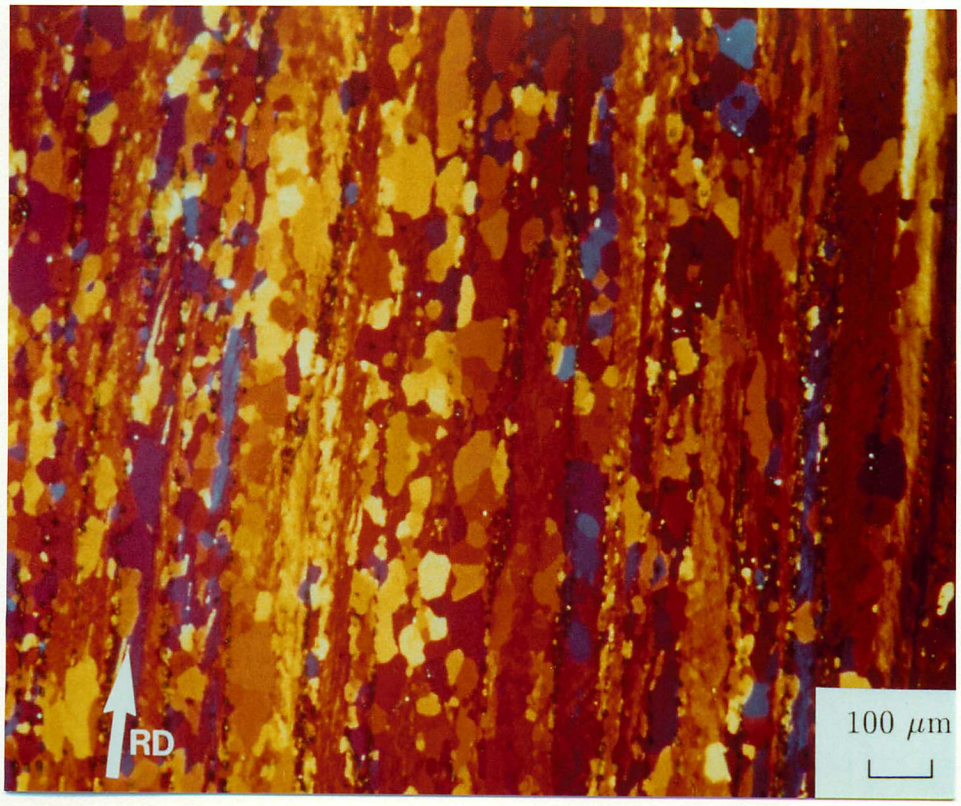

Figure 6.29 Optical micrograph in the long transverse section showing the 0.47 wt% Fe alloy heat treated at 250°C for 120 minutes followed by 400°C for 30 minutes.

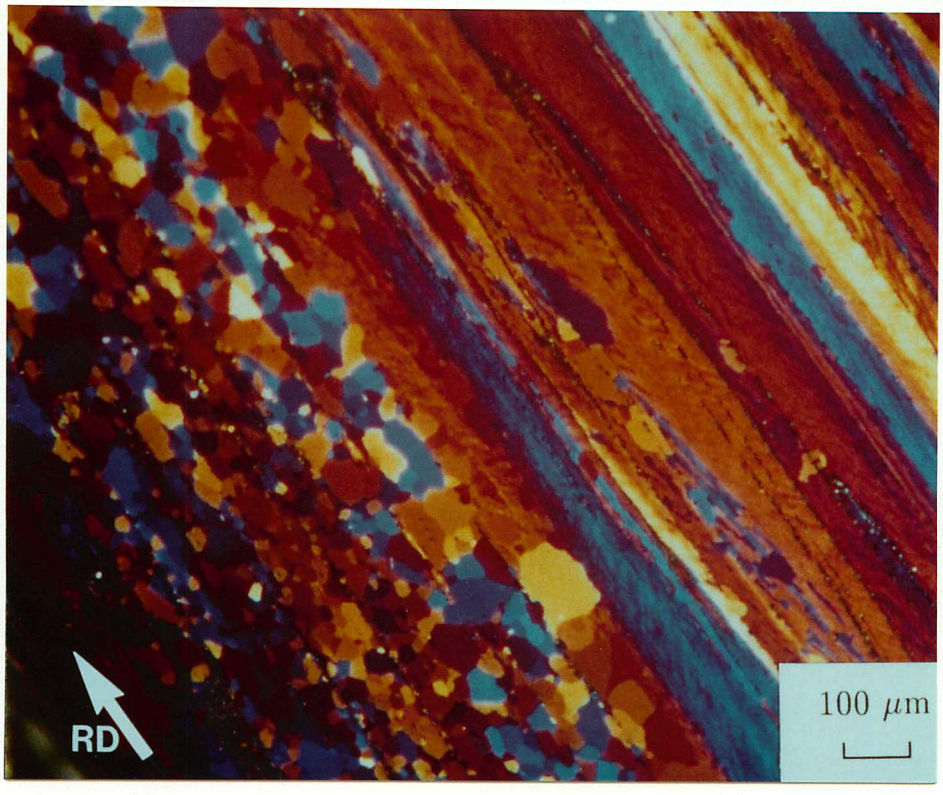

Figure 6.30 Optical micrograph in the long transverse section showing the 0.47 wt% Fe alloy heat treated at 250°C for 120 minutes followed by 400°C for 30 minutes showing uneven recrystallisation rate across the alloy.

6.2 Conclusions

The optical microscopy shown in this section suggests that not only are the further stages of recrystallisation initiated from particles, but that extended grain growth is prevented by particle–pinning mechanisms. Thus the final grain sizes are controlled by the particle spacings, and the quantities of nuclei are controlled by the particle number–density.

The recrystallisation kinetics of the lower iron–content alloy were much slower than the kinetics for the 1.41 wt% Fe alloy, giving weight to the theory that particles are the dominant nucleation sites in operation. In the low iron–content alloy therefore, a smaller number of very-large grains were observed on full recrystallisation as compared to a greater number of small grains in the high iron content alloy. In addition, the presence of particles in bands along the rolling direction gave rise to a bimodal grain size distribution, there being an opportunity for greater growth in areas away from particles. Particles which were stranded away from particle bands were observed to be the most successful in producing recrystallised grains, since the growth of these grains was not inhibited by closely neighbouring particles.

Chapter 7

ANEALING MECHANISMS IN A 6063AA + Mn ALLOY

The phenomenon of directional recrystallisation in rolled alloys has been linked in various materials to the effect of particles aligned along the rolling direction, inhibiting grain growth laterally. This leaves the recrystallised grains fewer degrees of freedom for grain boundary migration, and growth along the rolling direction, which is relatively uninhibited, is therefore promoted.

Particle pinning and any other factors which are likely to produce anisotropic growth are therefore important factors in the production of directionally–recrystallised materials.

In the case of the *6063AA* + Mn alloy studied, annealing is found to produce a stable microstructure of elongated grains. In the following investigations, the specific mechanisms involved in producing this final microstructure, along with an assessment of the role of particles in those mechanisms, are illucidated as far as possible.

7.1 Inhibition of Recrystallisation

Studies involving alloys hardened by disperse oxide–phases, including Al/Al_2O_3 alloys (Westerman & Lenel, 1960; Nobili & de Maria, 1965) have found that the resistance to recrystallisation is enhanced by the introduction of the dispersed phase. Nobili and de Maria (1965) have shown that the inhibition of recrystallisation gives an opportunity for recovery, and that extensive subgrain growth occurs, resulting in a subgrain diameter far exceeding particle spacing. It would appear that the extensive recovery reduces the inhomogeneity of the dislocation distribution, thus impeding the bulge and coalescence mechanisms of nucleation (figure *7.1*).

The cast aluminium–alloy utilised in this investigation has the commercial designation *6063*

AA and the chemical composition Al–0.5Mg–0.34Si–0.2Fe–0.29Mn–0.01Ti wt.%. During casting, coarse intermetallic compounds form interdendritically, giving particles typically 1 to 5 μm in diameter with compositions $FeAl_3$ and Mg_2Si. Fine dispersoids containing Mn and Si are also formed during the homogenisation heat–treatment (described below) and these are typically less than 0.5 μm in diameter and of uniform dispersion.

The cast alloy was homogenised at 500°C for three hours before being held at 400°C for one hour prior to rolling. Much of the precipitation is completed by the heat–treatment at 400°C. The blocks were then hot rolled down to 15 mm thickness followed by an anneal at 380°C for one hour. Finally, the thickness was reduced to 4 mm by cold rolling from 15 mm. During rolling, the hard intermetallic particles tend to break up and become aligned as stringers along the rolling direction.

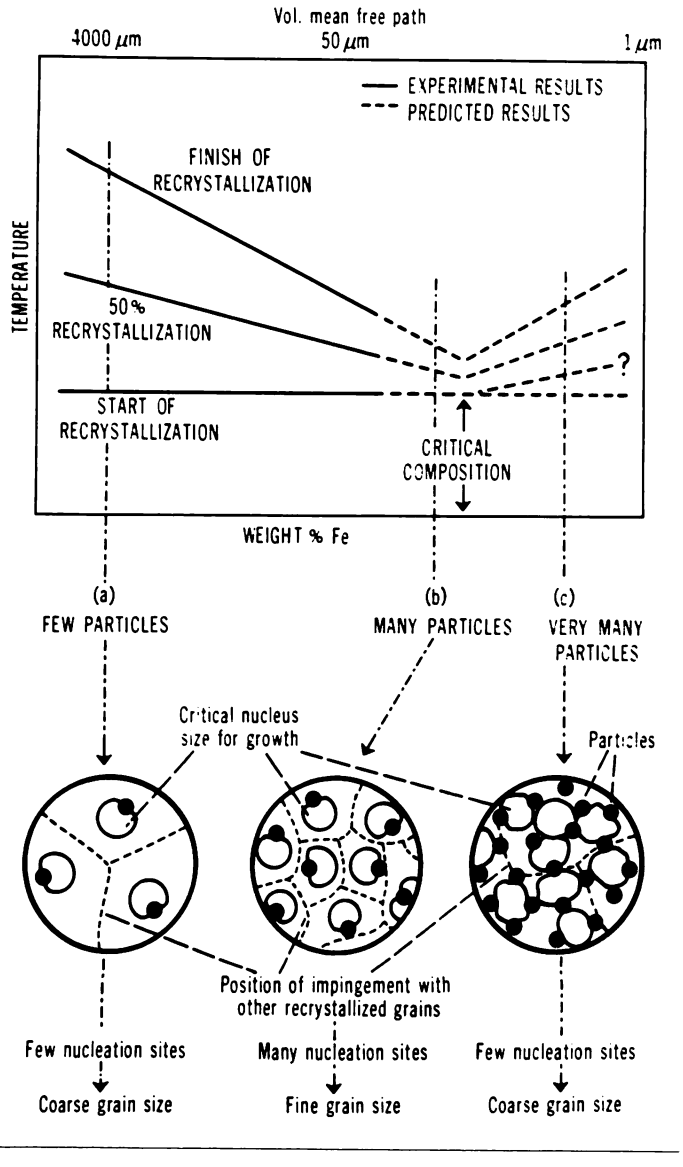

Figure 7.1 Diagram representing the influence of degree of dispersion of a second phase on the recrystallisation characteristics of cold–worked alloys (Cahn, 1965).

The rolled alloy was divided into eight specimens, with each sample being given a different heat–treatment as follows: four specimens were heated at 350°C for 30, 60, 120 and 240 minutes respectively, followed by water quenching to ambient temperature. Four further specimens were heated at 450°C for 30, 60, 120 and 240 minutes respectively. All of the specimens, together with some of the as–deformed material, were studied using transmission electron microscopy.

The as–cast microstructure consists of grains of approximate size 200 μm. The rolling process flattens these grains (figure *7.2*) into a thickness of about 20 μm, which is consistent approximately with the rolling reduction from 15 $\rightarrow$ 4 mm imparted to the cast billet. The transmission electron microstructure of the as–rolled material reveals a fine elongated structure (figure *7.3*) of subgrains within each of the coarser grains apparent in figure *7.2*. Another feature of the as–rolled microstructure is that although there appears to be an obvious alignment of coarse precipitate particles along the rolling plane (figure *7.2*) the smaller dispersoids are seen to be largely uniformly dispersed (figure *7.3*).

Hardness measurements using a 10 kg load revealed that annealing led to considerable softening, with this rate of softening decreasing drastically after about 30 minutes at the annealing temperature (figure *7.4*). On observing the optical microstructure of the samples in the long transverse section after 120 minutes of annealing, an elongated grain structure is visible. When compared to the as–rolled material it has relatively uniform anodised colour, as well as more sharply defined grain boundaries. The 350°C anneal is shown in figure *7.5*, where some areas of as–deformed material are still apparent, and the 450°C anneal is shown in figure *7.6* in which there are no as–deformed areas remaining. In both cases the new 'cleaner', more defined grains extend to a width of 20 to 60 μm. It may also be noted that in neither samples is there a particularly high incidence of association between the large particles and the new grain boundaries, suggesting that if recrystallisation and grain growth have occurred, nucleation of the former is not necessarily associated with the particles, and pinning of grain boundaries in the latter by these same particles is not effective. But if this is true, it becomes difficult to explain why the annealed microstructure is elongated.

The transition from as–rolled to annealed microstructure may also be observed in the rolling plane of the samples, in which the flat dimension of the 'pancaked' grains are observed. In figure *7.7* the as–rolled structure shows indistinctive boundaries and a wash of various shades of colour within grains, suggesting a range of subgrain orientations. After a short anneal (15 minutes) at 350°C, the grain colourings are still indistinct, but some grains appear to be developing more defined boundaries which are straight (figure *7.8*). After 30 minutes (figure *7.9*) greater distinction between grains is observed, in figure *7.10* 'clean' grains can be seen against the as–deformed matrix in the 60 minute anneal. At the longer annealing time of 120 minutes, a grain structure similar to the as–rolled microstructure, but with clean, well–defined grains, is now visible (figure *7.11*). As these micrographs illustrate, the grain boundaries of the new grains bear little relation to the positions of the strings of precipitates in the sample.

More information was gathered from the microstructures viewed in the transmission electron microscope. The alloy is shown in figure *7.12* in the long transverse section after annealing at 350°C for 30 minutes. In comparison with the optical micrographs, it can be seen that many of the large volume–fraction of small particles occur at subgrain boundaries or at dislocation tangles within subgrains. Although evidence of recovery can be observed, the particles appear to be inhibiting the process of boundary movement by pinning dislocation arrays. It would also be expected that the pinning of the subgrain boundaries would help to prevent the initiation of recrystallisation by any subgrain–bulging mechanisms. Figures *7.13* and *7.14* compare the bright field and dark field images of an area within the same sample. It can be seen that within some subgrain bands, the original subgrain boundaries have become indistinct, and are shown

to be of similar orientation from the dark field image. Many of these subgrain boundaries were pinned (as indicated) and it may be that rather than undergoing recrystallisation by a bulging mechanism, the dislocations within these boundaries have moved towards higher energy boundaries (such as grain boundaries) whilst a rotation mechanism has brought the orientations of the two subgrains either side of the boundary towards each other. This process is not dissimilar to the subgrain coalescence theory described in the previous chapters.

Upon further annealing this mechanism of dislocation movement can be seen to have advanced further as in figures *7.15* and *7.16*. In both, very distinct higher angle boundaries can be seen extending directly along the rolling direction, and are now extremely straight. On other boundaries, occurring at angles to the rolling direction, the greater separation of dislocations (figure *7.15*) and the movement of dislocation arrays (figure *7.16*) can be clearly seen. In other areas of the same samples a much more marked microstructural difference is observed. In figure *7.17* a band of elongated subgrains is isolated between two areas of highly–recovered regions in which no subgrain boundaries exist. It is assumed that these areas have undergone the process of dislocation movement and subgrain rotation to completion, and that by the same mechanisms they will eventually consume the as–deformed material. Figure *7.18* shows a recovered band encroaching on a partially recovered area, which are separated by a distinct boundary which displays some pinning. Figure *7.19* shows a fully recovered area next to a partially recovered area in which the rotation/boundary disappearance mechanisms are beginning.

At the longer annealing times, these recovered areas had increased in area considerably as shown in figure *7.20*, and only a few grain boundaries could be observed in one foil. Figure *7.21* shows a longer anneal at the higher annealing temperature of 450°C, and it can be noted that many dislocations are still apparent, stranded after the disentangling and rotation processes have occurred. Figures *7.22* and *7.23* show a remaining boundary section at low and high magnifications in the higher temperature anneal.

There is nothing new about this description of annealing; the process has been referred to as "continuous recrystallisation" (Köster & Hornbogen, 1968; Saji & Hornbogen, 1978), but this term is no longer considered suitable since recrystallisation must in modern terminology involve the motion of large misorientation grain boundaries. Thus, the annealing behaviour found here is simply one of recovery (here termed 'extended recovery'), and no evidence was found of recrystallisation proper. Nor were the large dispersoid particles seen to nucleate new recrystallised grains, as is often observed in particle containing systems (Lloyd, 1982; Humphreys, 1977). This behaviour is similar to that reported by Nobili and De Maria (1965), who found that in many cases, extensive recovery occurs before recrystallisation. The absence of recrystallisation, with annealing dominated by recovery, can occur due to a lack of sufficient stored–energy to drive

recrystallisation, a high rate of recovery, or an inhibition of large misorientation grain boundary migration by particle pinning. It is here suggested that in the alloy under examination the latter mechanism plays an important role in promoting recovery rather than recrystallisation.

The interpretation of the annealing process, as presented above, helps to identify the cause of the elongated grain structure in the annealed samples. As already pointed out, there are no indications of any non–uniformity in the distribution of the fine particles. Such particles can in principle retard grain boundary movement via Zener pinning (Zener, 1948). Any anisotropy in their dispersion would therefore lead to an anisotropy of grain growth (Lloyd, 1982; Baloch, 1989). The explanation of the observed elongated grain structure does not therefore lie in any anisotropic dispersion of pinning particles. On the other hand, if it is accepted that the annealing process considered here does not involve the motion of any large misorientation grain boundaries (*i.e.* those boundaries originating in the cast microstructure), then it follows that the final annealed grain structure must be elongated, with the thickness related to the rolling reduction. This is consistent with the experimental observations reported above.

If it is indeed true that the original scale of the flattened grain structure generated by deformation governs the thickness of the elongated grains observed in the annealed microstructure, then a change in the degree of deformation should lead to a corresponding change in the annealed microstructure. A larger, cold–rolling reduction from 15mm to 1mm was used to illustrate this. As predicted, the final annealed elongated grain–width still corresponded to the as–deformed grain width, which was found to be approximately 10–30 μm across. The two rolling reductions are compared in the long transverse section in figures *7.24* and *7.25*. It is interesting that elongated microstructures have recently been reported in another aluminium alloy where deliberate recovery heat–treatments were imparted prior to recrystallisation heat–treatment (Chang & Humphreys, 1991).

In order to ascertain the stability of the elongated microstructure obtained in the annealing treatments carried out, two further heat treatments were conducted, both at 600°C for 240 minutes, one on a specimen previously annealed at 350°C for 120 minutes, and one on a specimen previously annealed at 450°C for 120 minutes. The drops in hardness upon annealing at this temperature are shown in table *7.1*, and are seen to be negligible.

Table 7.1 Hardness data for the 6063 AA Mn alloy showing higher annealing temperature treatments. Measurements taken in the long transverse section.

1st Heat Treatment Temperature (°C)	HV after 1st Anneal	HV after 600°C Anneal
350	44.0	42.0
450	36.0	35.0

In addition, little or no change is seen in the optical microstructures other than a spheroidisation of the precipitates and a clearer and better defined grain structure, as shown in figures *7.26(a)* and *(b)* for the 350°C sample and in figures *7.27(a)* and *(b)* for the 450°C sample. Figure *7.28* shows the higher temperature anneal effects in the rolling plane.

If the assumptions made on the annealing processes involved in producing the elongated microstructure observed are correct, it would be expected that the texture of the fully annealed microstructure would not be dissimilar to that of the as–deformed alloy, since no movement of high energy boundaries will have occurred to produce a widely differing preferred orientation. Any subgrain rotations which may have taken place during the 'extended recovery' process would of necessity only be small, and the bulk texture observed would be preserved approximately during annealing. Figures *7.29(a)* and *(b)* and table *7.2* display the bulk texture–type volume fraction percentages for the samples dealt with.

Table 7.2 Bulk texture volume fraction percentages for the 6063 AA Mn alloy.

	Treatment				
Texture Type	As-Rolled	350°C, 30 minutes	600°C, 4 hours	450°C, 30 minutes	600°C, 4 hours
$\{100\}\ \langle 001\rangle$ (Cube)	1.67	1.82	2.15	4.67	5.34
$\{110\}\ \langle 1\bar{1}2\rangle$ (Brass)	24.64	24.60	24.55	7.04	6.18
$\{121\}\ \langle 1\bar{1}1\rangle$ (Cu)	11.37	13.57	18.43	3.89	5.74
$\{110\}\ \langle 001\rangle$ (Goss)	3.18	3.83	4.19	6.68	3.59
$\{231\}\ \langle 3\bar{4}6\rangle$ (S)	37.44	39.01	42.37	11.05	10.99

The figures and table show that there is in fact only a minimal change in texture in the case of the 350°C treated alloy, but the 450°C alloy appears to behave quite differently. Not only are the trends in texture–type volume–fraction changes much exaggerated in the higher temperature anneal over the first 30 minutes, but there is actually a decrease in S–type textures as opposed to an increase in the lower anneal. As annealing proceeds further, in the 450°C anneal, the decrease in percentage of the Cu texture is reversed, as is the increase in the Goss type, and this may be due to a change in annealing mechanism. The similarity between the as–rolled and 350°C annealed alloys, and the dissimilarity of the 450°C alloy can be seen more clearly in the 111 pole figures of the three shown in figures *7.30*, *7.31*, and *7.32*.

The higher annealing temperature may facilitate breakaway of subgrain and/or grain boundaries from pinning particles and hence allow for a strain–induced boundary–migration mechanism to give true abnormal grain growth. However, it would seem that the theory of 'extended recovery' postulated holds for the lower annealing temperature.

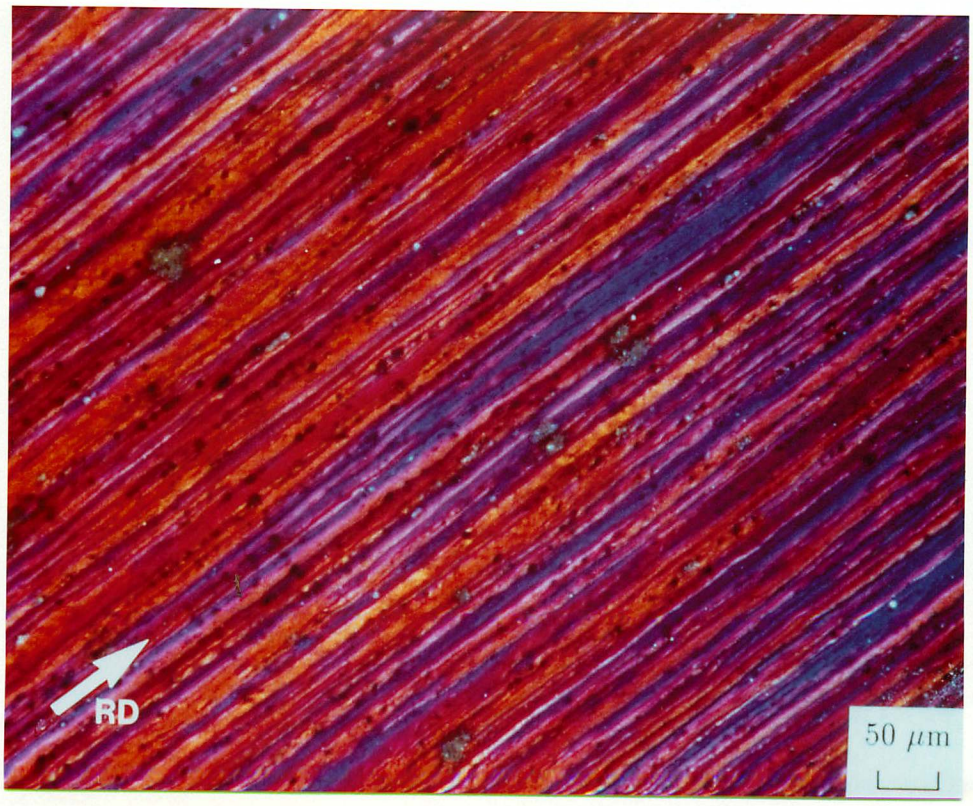

Figure 7.2 Optical micrograph in the long transverse section showing the microstructure after a rolling reduction from 15 to 4 mm thickness. Note that the microstructure consists of flattened grains approximately 20 μm in thickness.

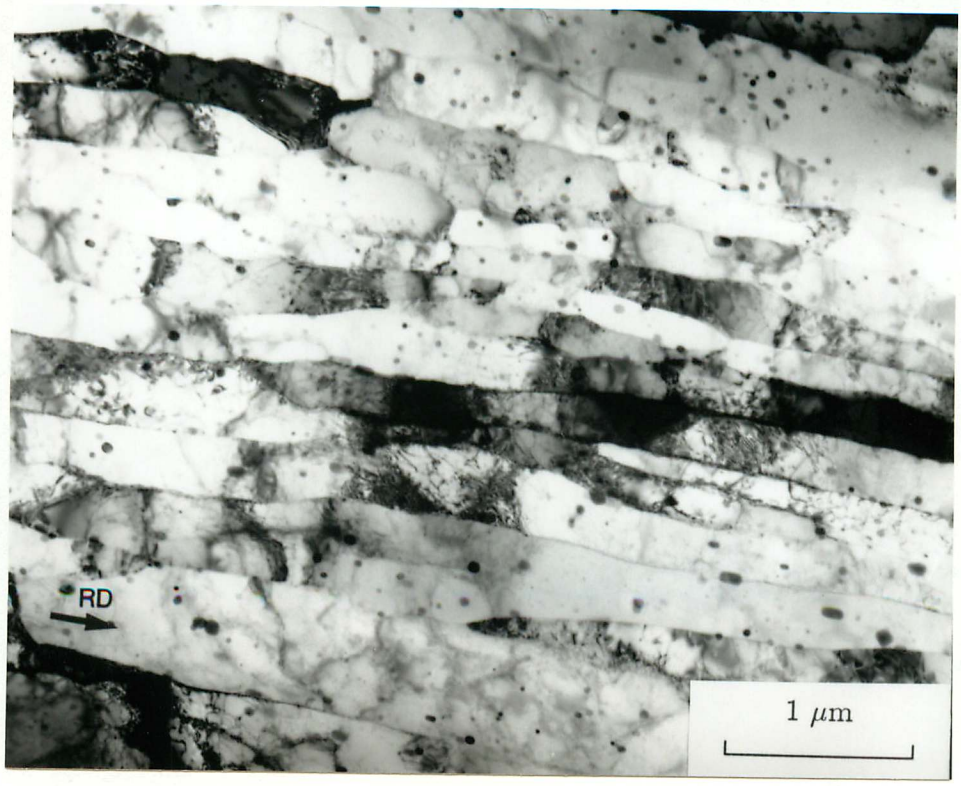

Figure 7.3 Corresponding transmission electron micrograph showing much finer subgrains within the coarser flattened grains apparent in the optical microstructure.

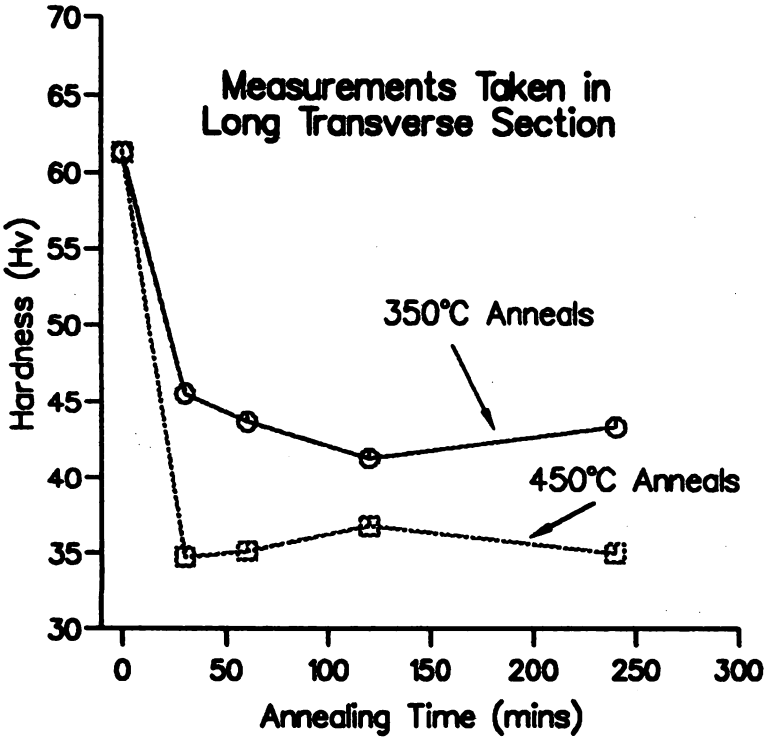

Figure 7.4 Microhardness curves for 6063 AA Mn alloy annealed at 350°C and 450°C.

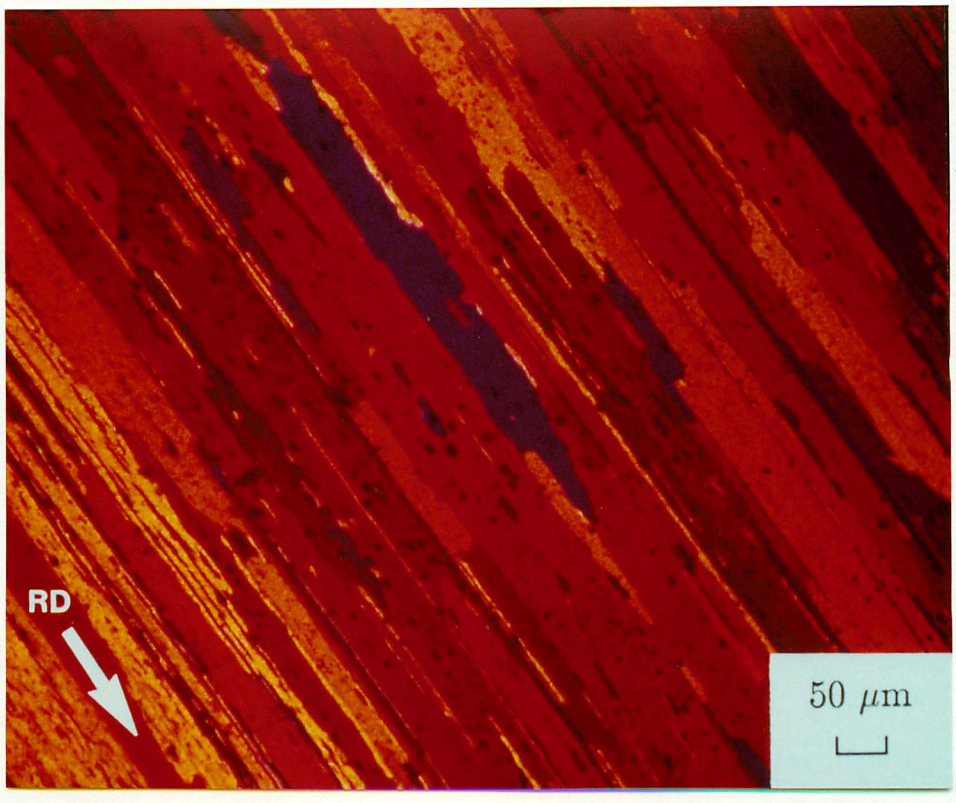

Figure 7.5 Optical micrograph showing the annealed microstructure in the long transverse section. Specimen annealed at 350°C for 120 mins.

Figure 7.6 Optical micrograph showing the annealed microstructure in the long transverse section. Specimen annealed at 450°C for 120 mins.

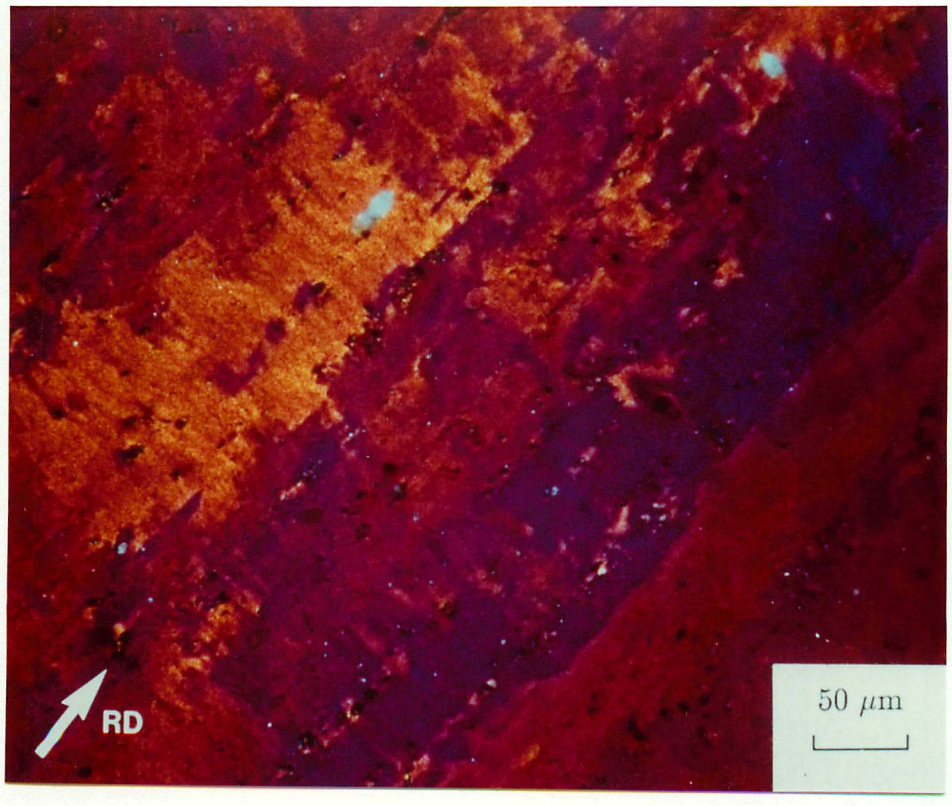

Figure 7.7 Optical micrograph showing the as-rolled microstructure in the rolling plane.

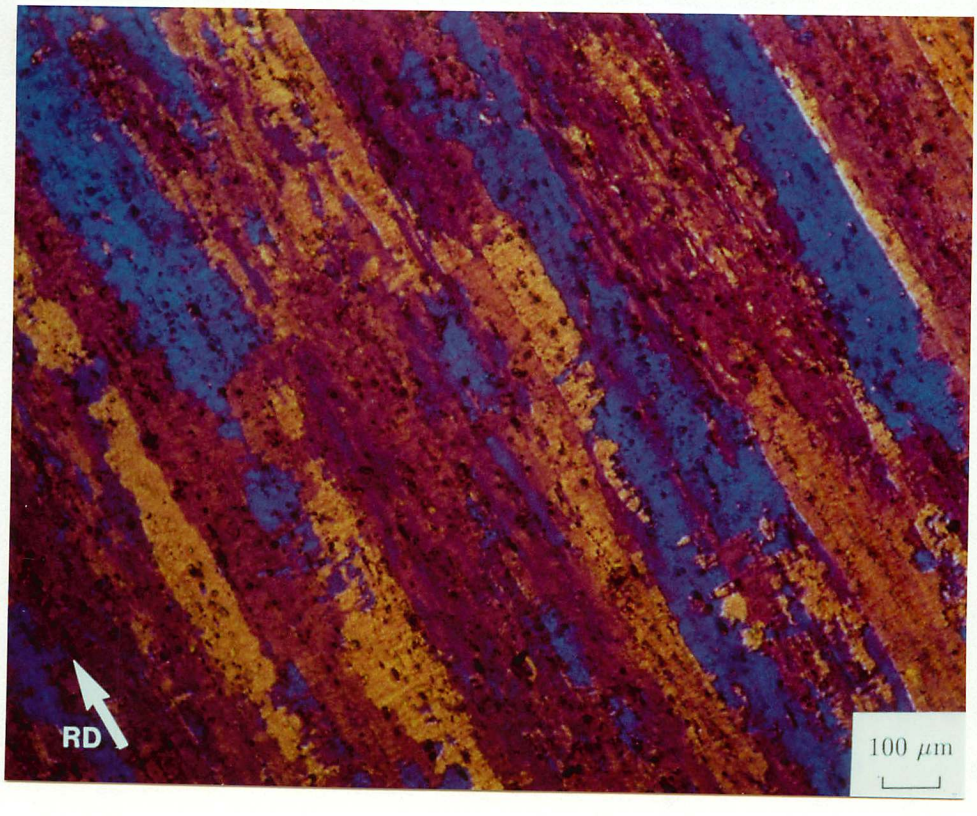

Figure 7.8 Optical micrograph showing the annealed microstructure in the rolling plane. Specimen annealed at 350°C for 15 mins.

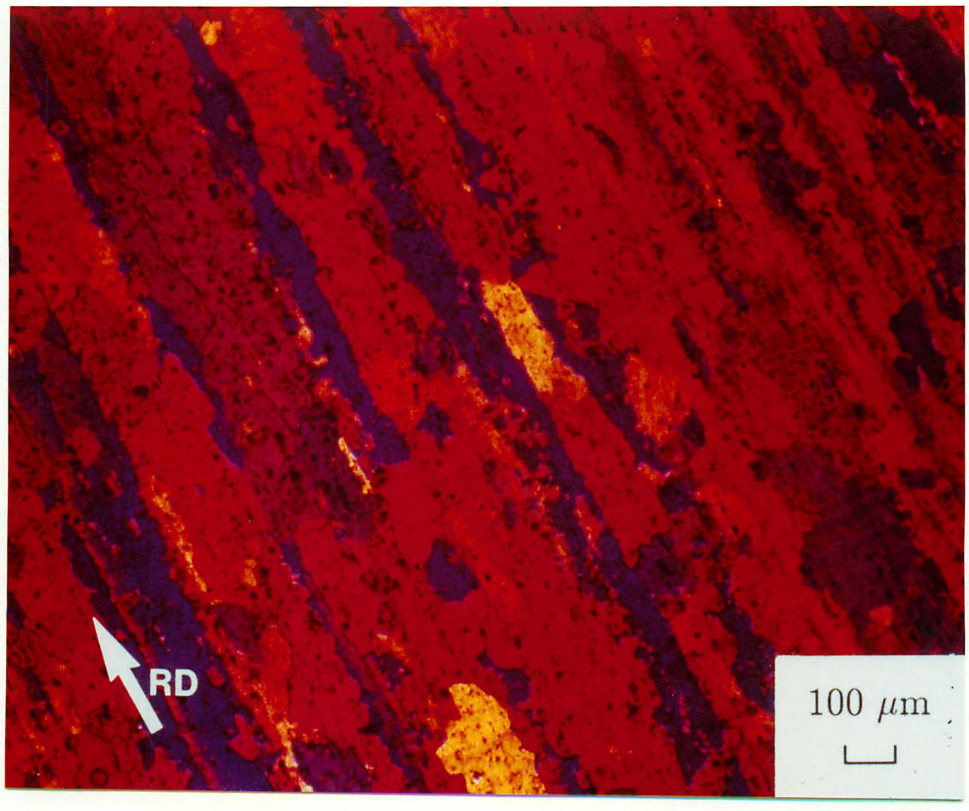

Figure 7.9 Optical micrograph showing the annealed microstructure in the rolling plane. Specimen annealed at 350°C for 30 mins.

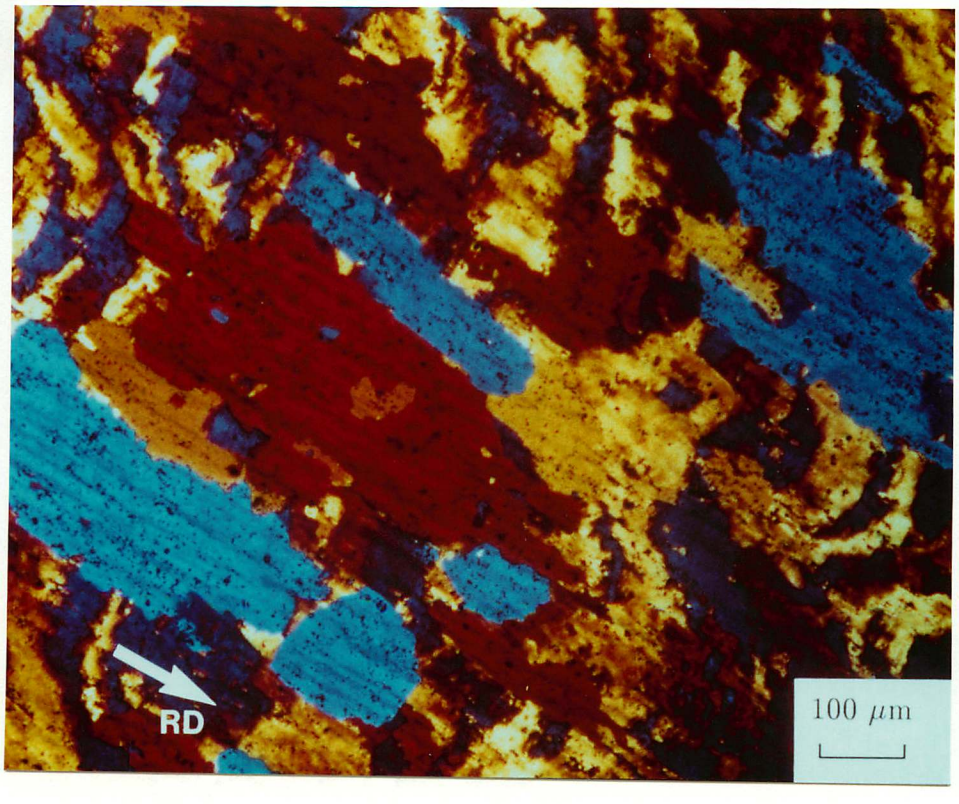

Figure 7.10 Optical micrograph showing the annealed microstructure in the rolling plane. Specimen annealed at 350°C for 60 mins.

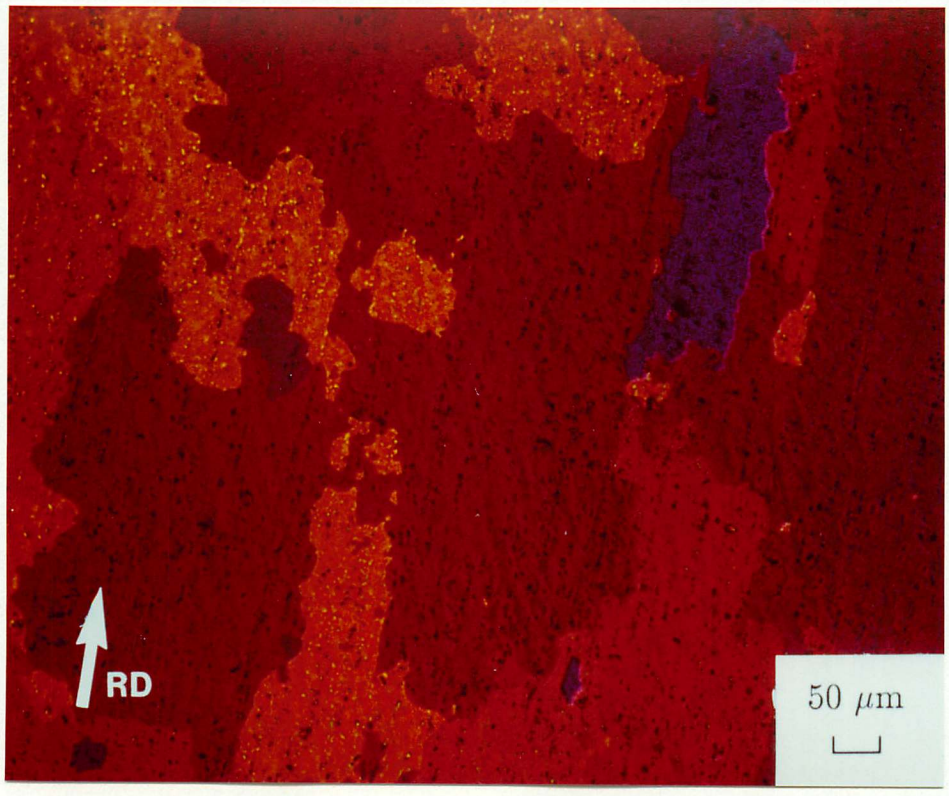

Figure 7.11 Optical micrograph showing the annealed microstructure in the rolling plane. Specimen annealed at 350°C for 120 mins.

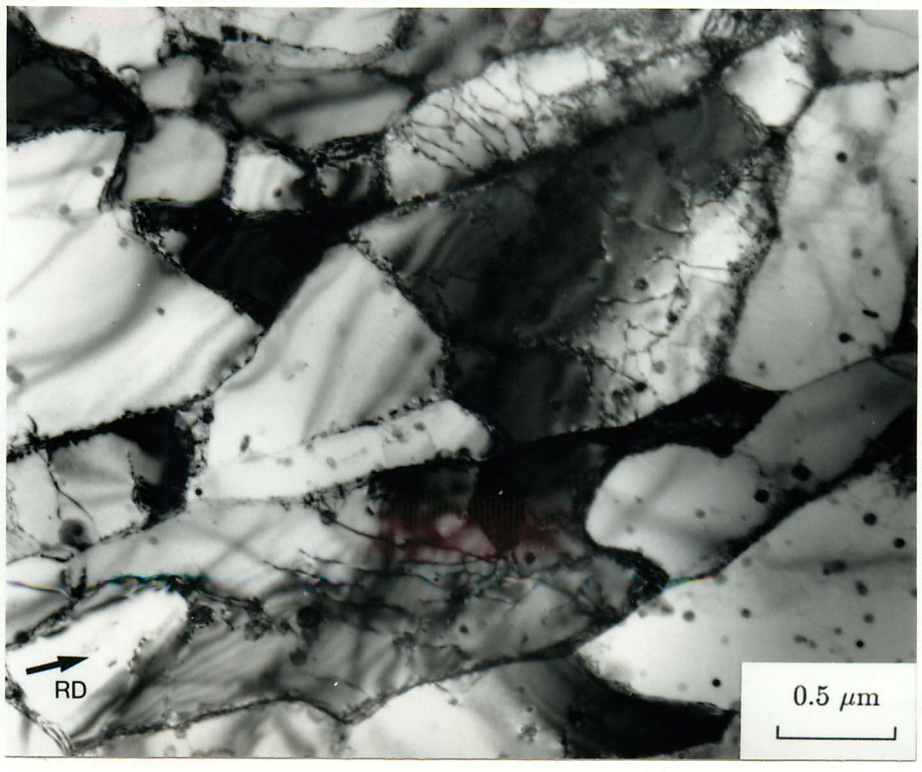

Figure 7.12 Transmission electron micrograph taken in the long transverse section showing pinning by small particles. Specimen annealed at 350°C for 30 mins.

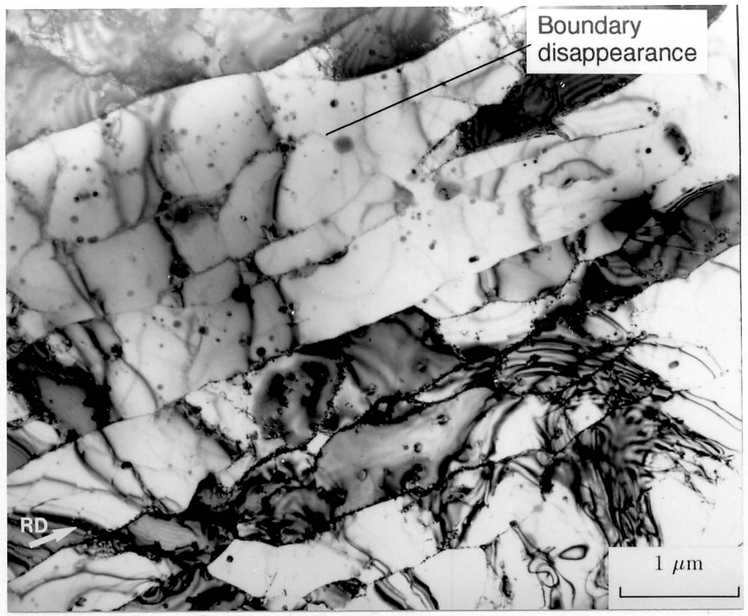

Figure 7.13 Transmission electron micrograph taken in the long transverse section showing disappearance of subgrain boundaries in bright field. Annealed at 350°C for 30 mins.

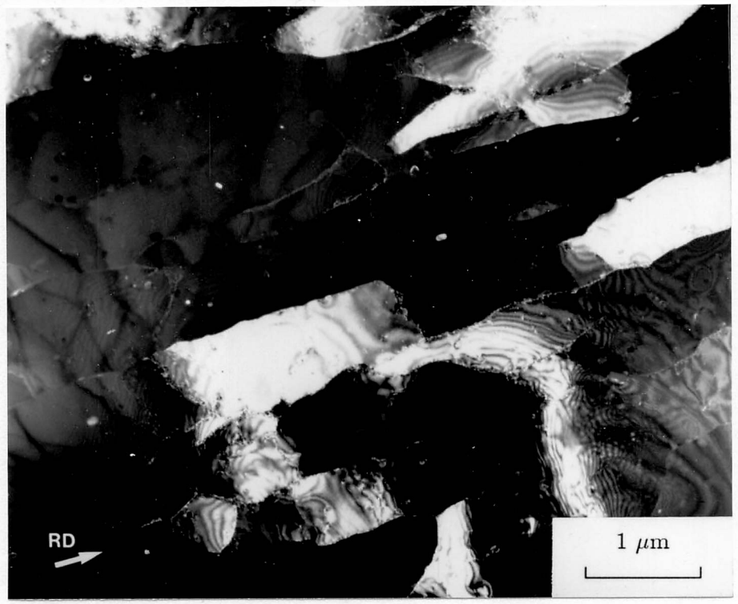

Figure 7.14 Transmission electron micrograph taken in the long transverse section showing disappearance of a boundaries between subgrains in dark field.

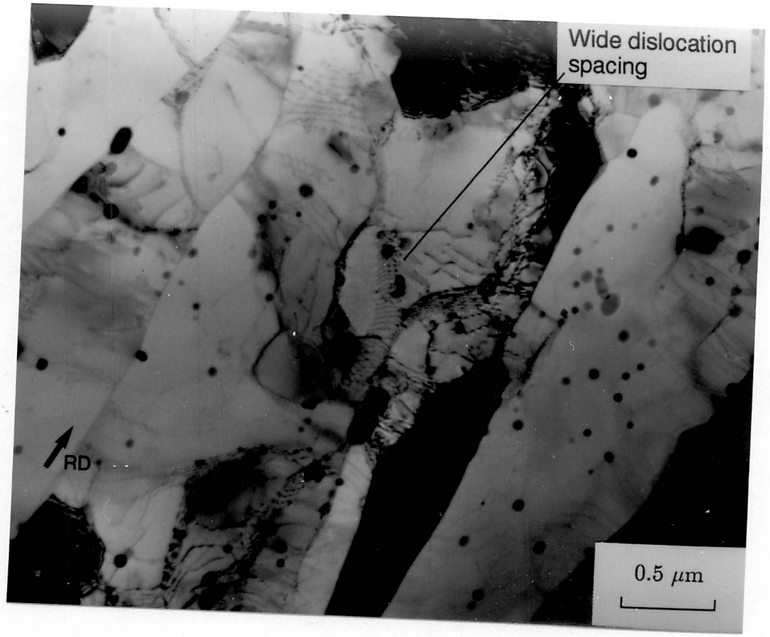

Figure 7.15 Transmission electron micrograph taken in the long transverse section. Annealed at 350°C for 60 mins.

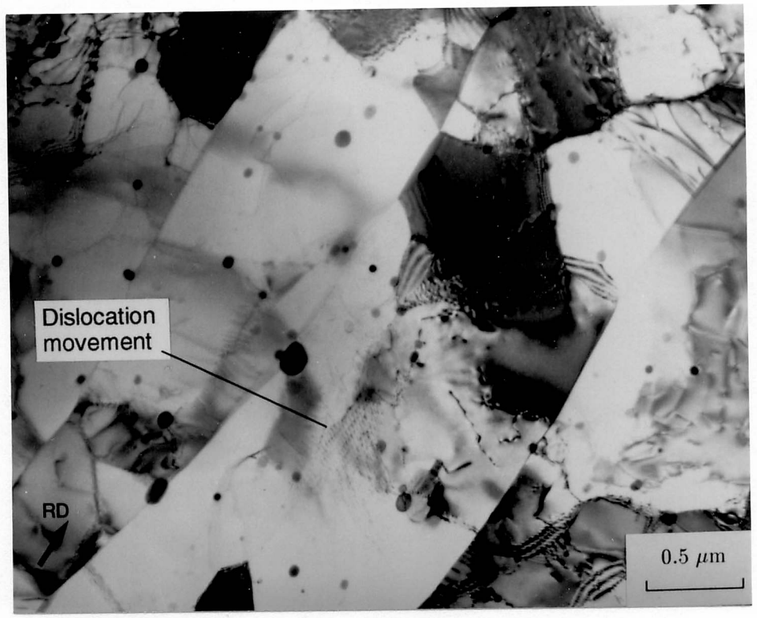

Figure 7.16 Transmission electron micrograph taken in the long transverse section. Annealed at 350°C for 60 mins.

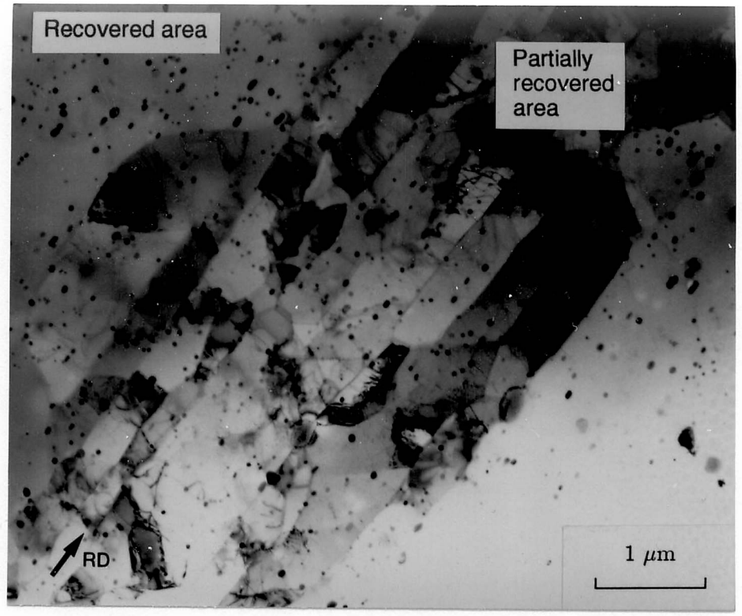

Figure 7.17 Transmission electron micrograph taken in the long transverse section showing areas of full recovery. Annealed at 350°C for 60 mins.

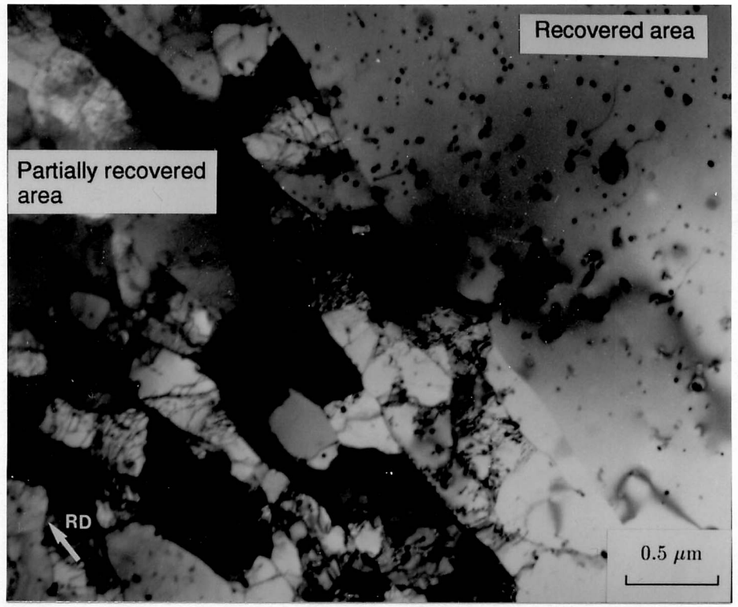

Figure 7.18 Transmission electron micrograph taken in the long transverse section showing some full recovery. Annealed at 350°C for 60 mins.

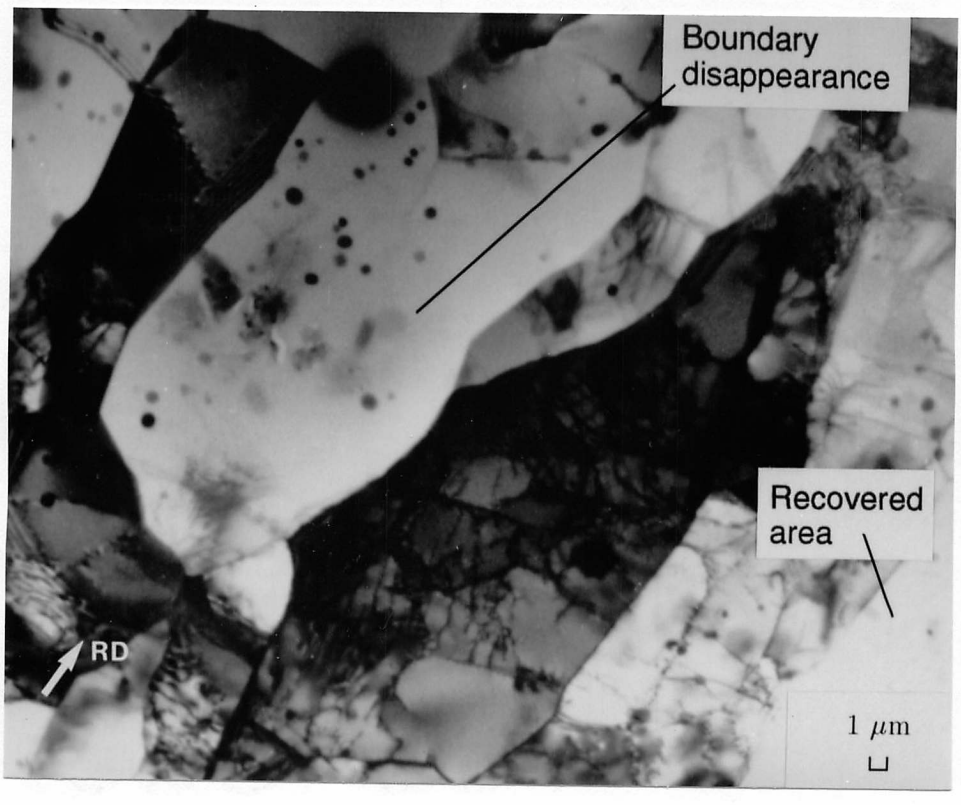

Figure 7.19 Transmission electron micrograph taken in the long transverse section showing early stages of extended recovery. Annealed at 350°C for 60 mins.

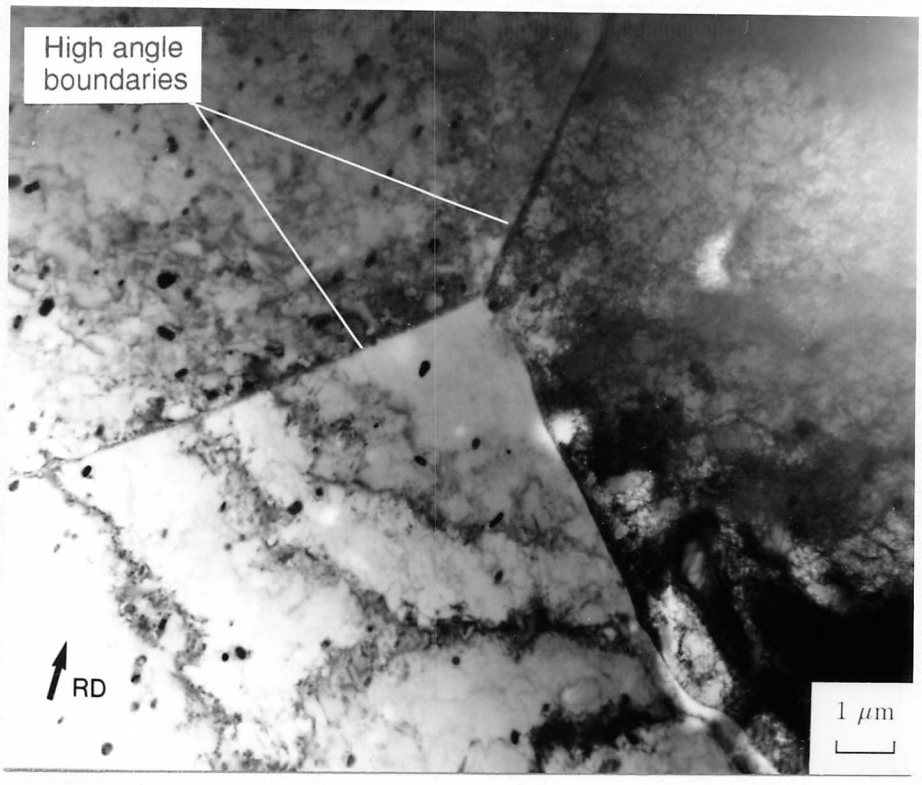

Figure 7.20 Transmission electron micrograph taken in the long transverse section showing complete recovery. Annealed at 350°C for 120 mins.

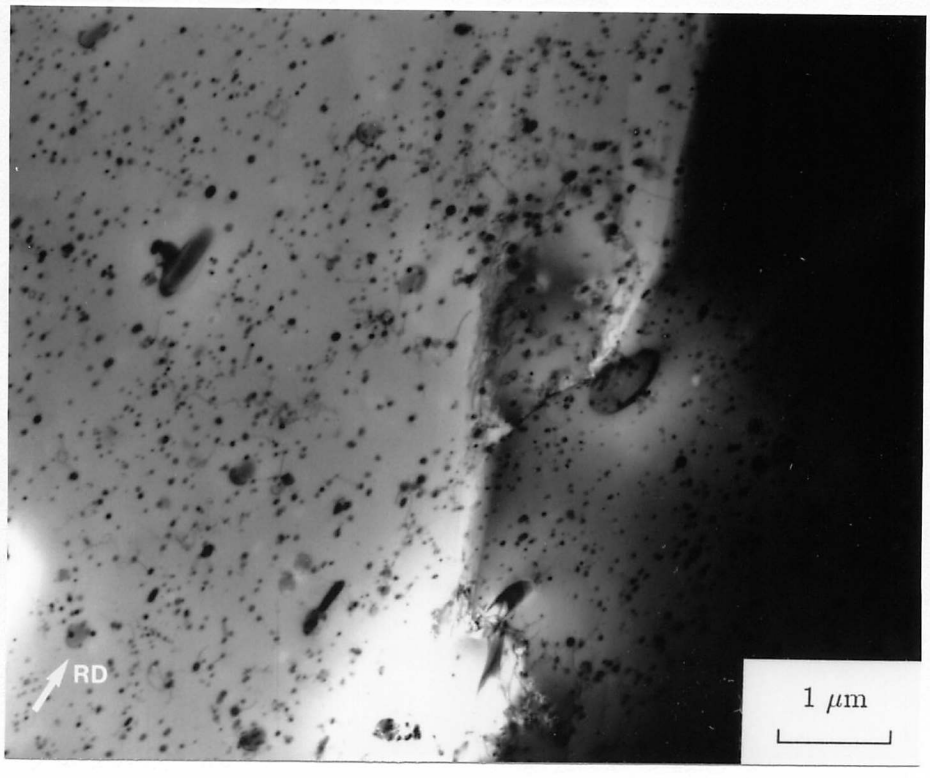

Figure 7.21 Transmission electron micrograph taken in the long transverse section showing complete recovery. Annealed at 450°C for 120 mins.

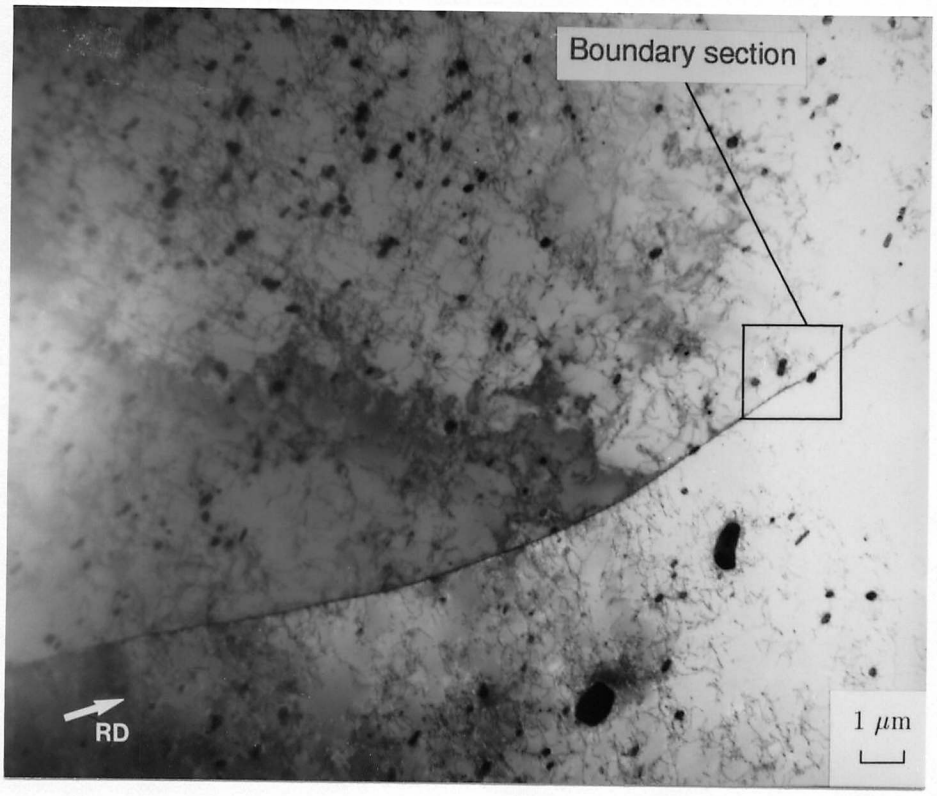

Figure 7.22 Transmission electron micrograph taken in the long transverse section showing a grain boundary at low magnification. Annealed at 450°C for 120 mins.

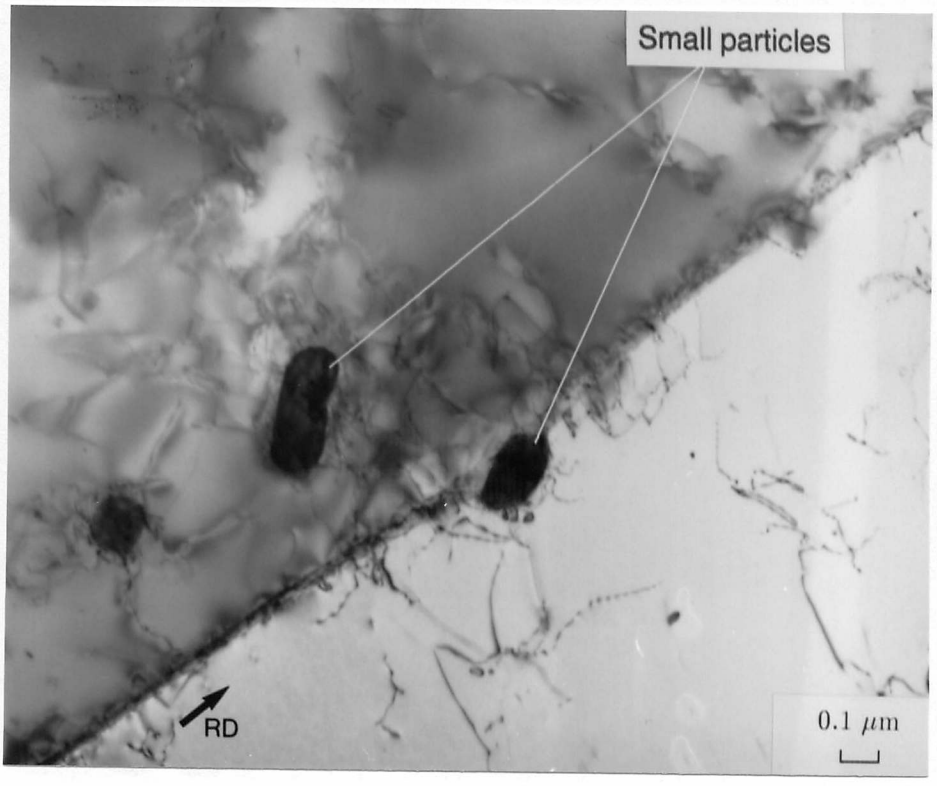

Figure 7.23 Transmission electron micrograph taken in the long transverse section showing a grain boundary at high magnification. Annealed at 450°C for 120 mins.

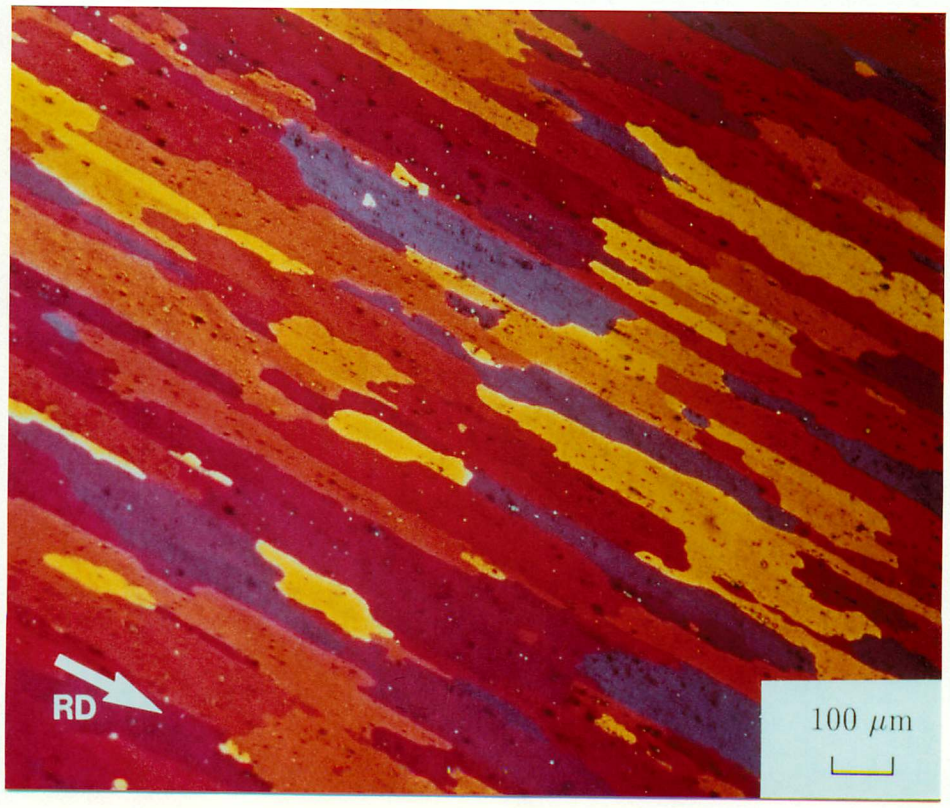

Figure 7.24 Optical micrograph taken in the long transverse section after cold rolling from 15 mm to 4 mm and annealing at 350°C for 120 minutes.

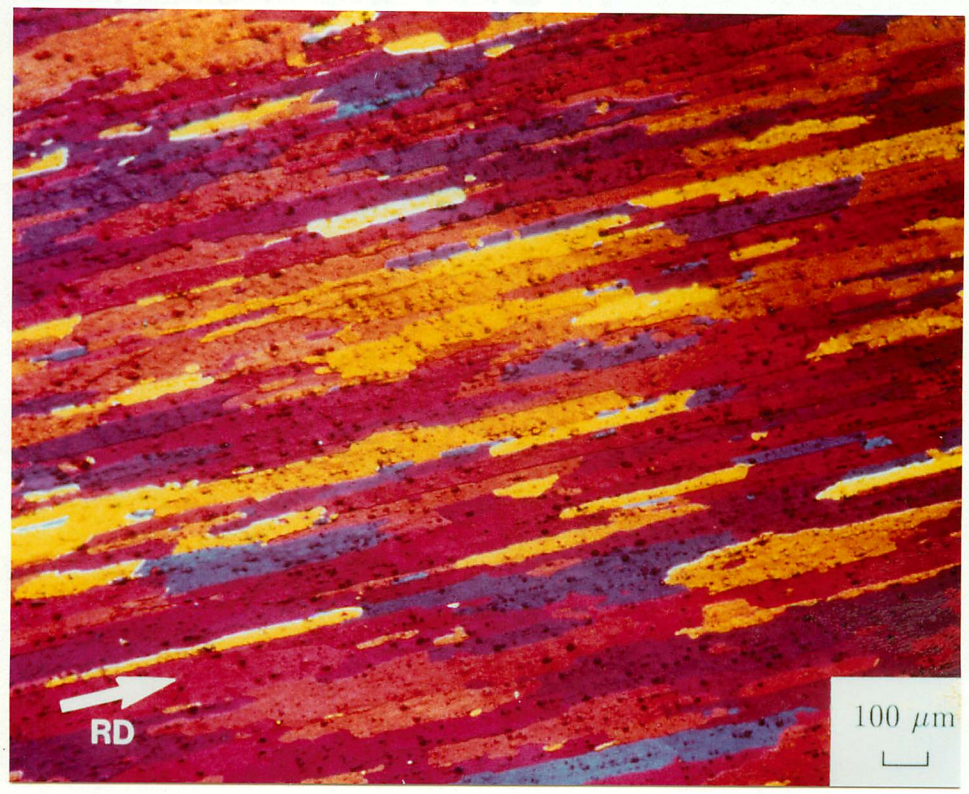

Figure 7.25 Optical micrograph taken in the long transverse section after cold rolling from 15 mm to 1 mm and annealing at 350°C for 120 minutes.

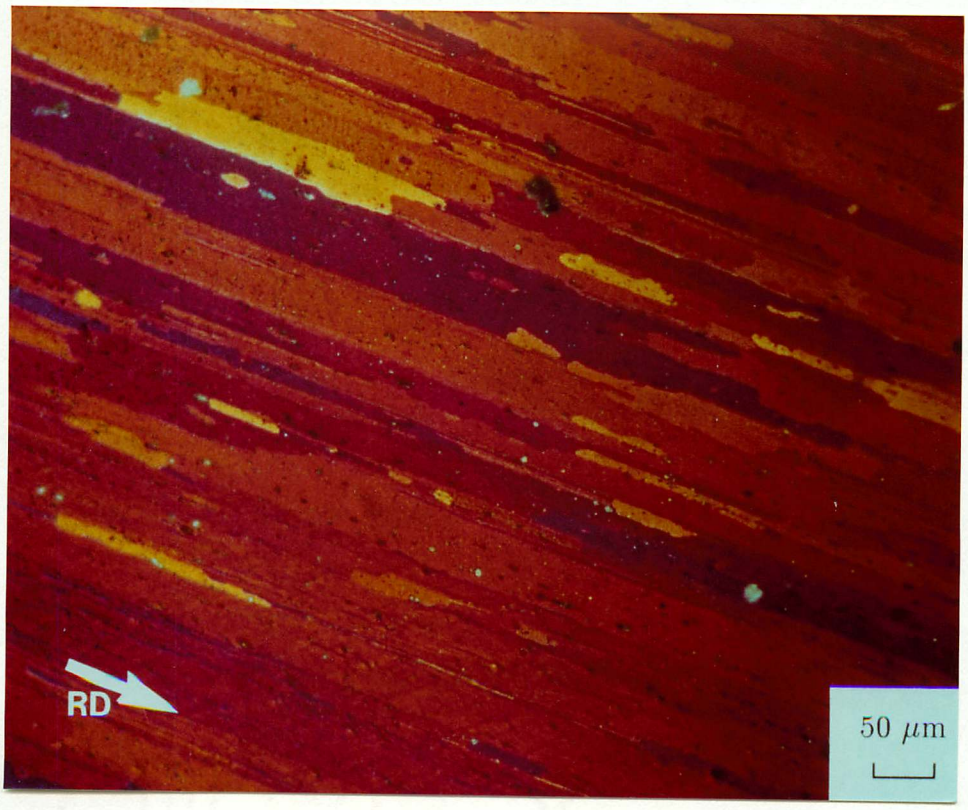

(a)

(b)

Figure 7.26 Optical micrographs taken in the long transverse section after (a) annealing at 350°C for 120 minutes, and (b) annealing at 350°C for 120 minutes followed by 4 hours at 600°C.

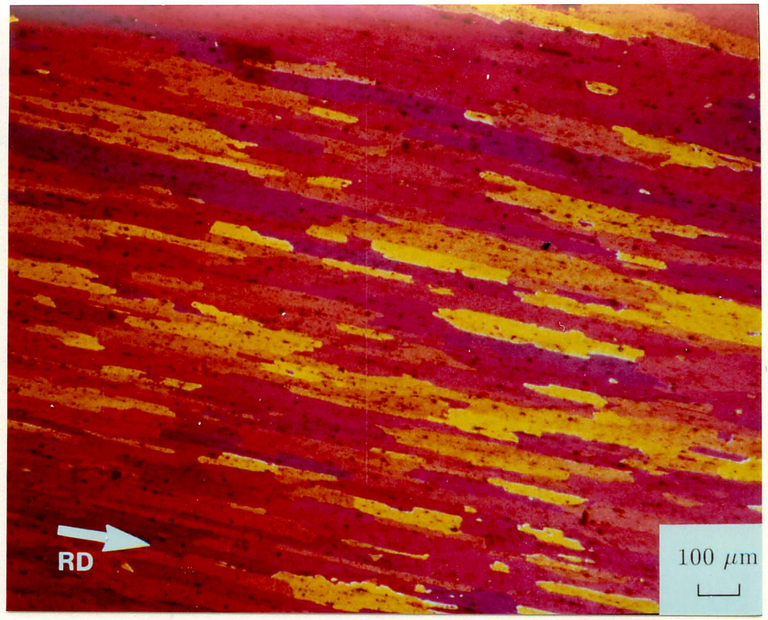

(a)

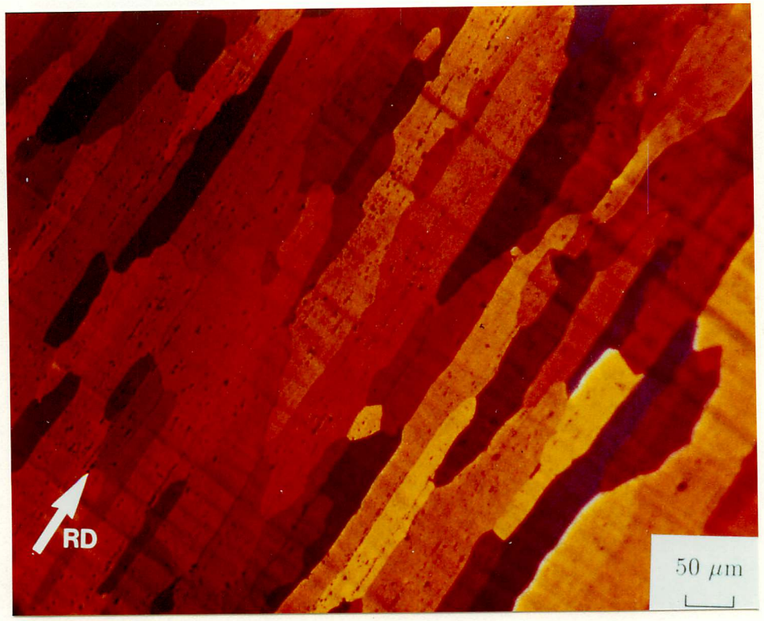

(b)

Figure 7.27 Optical micrographs taken in the long transverse section after (a) annealing at 450°C for 120 minutes, and (b) annealing at 450°C for 120 minutes followed by 4 hours at 600°C.

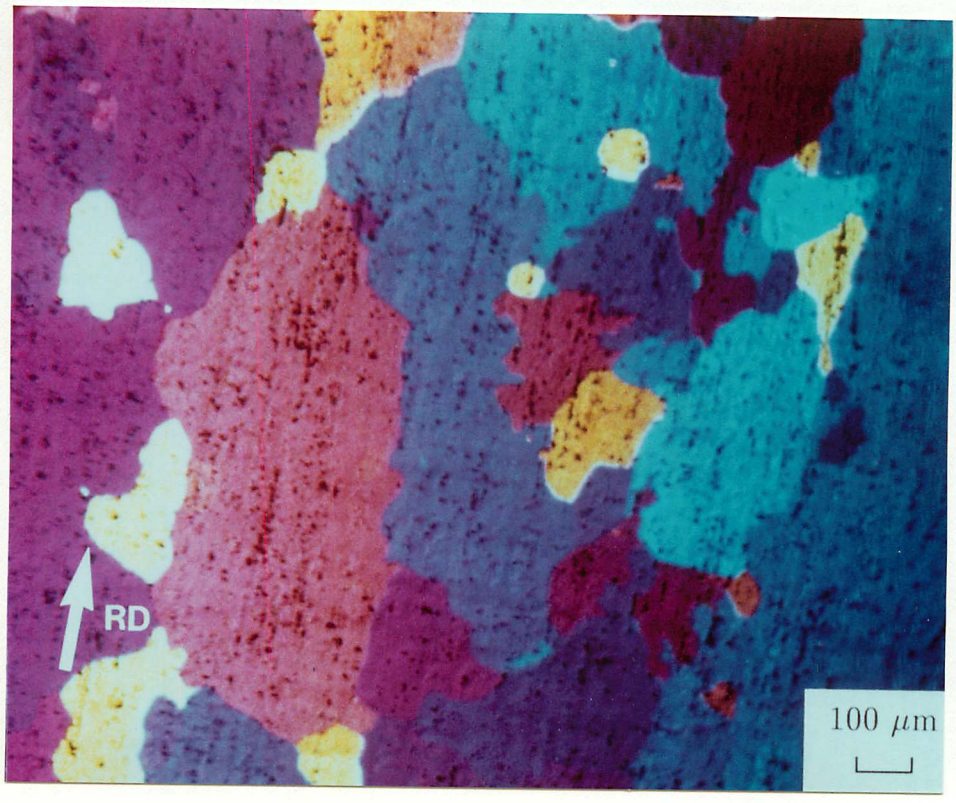

Figure 7.28 Optical micrograph taken in the rolling plane after annealing at 450°C for 120 minutes followed by 4 hours at 600°C.

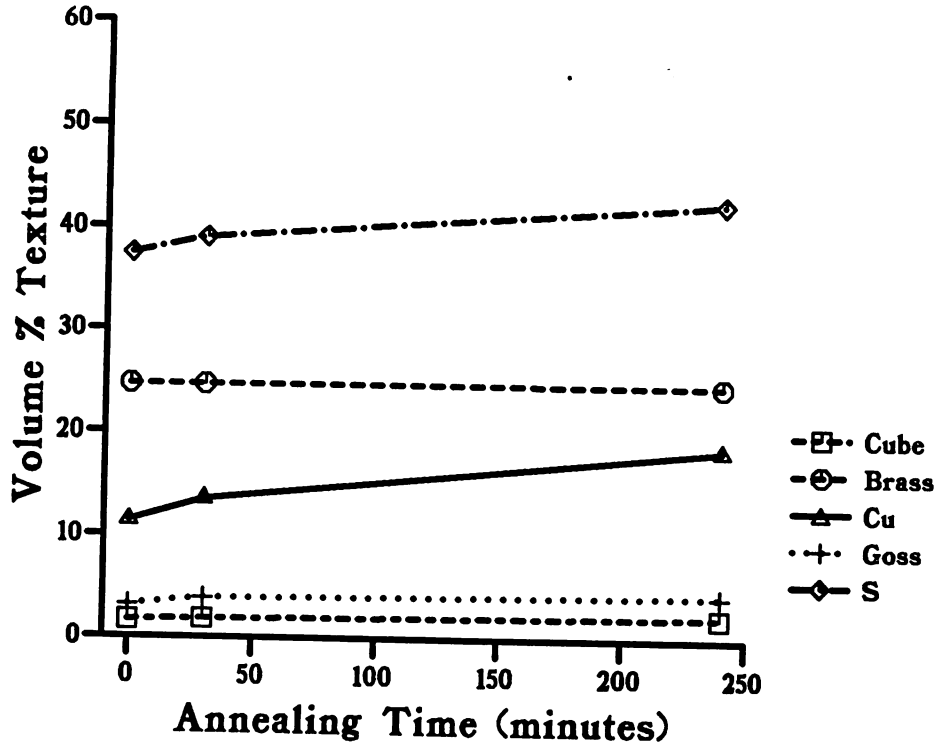

(a)

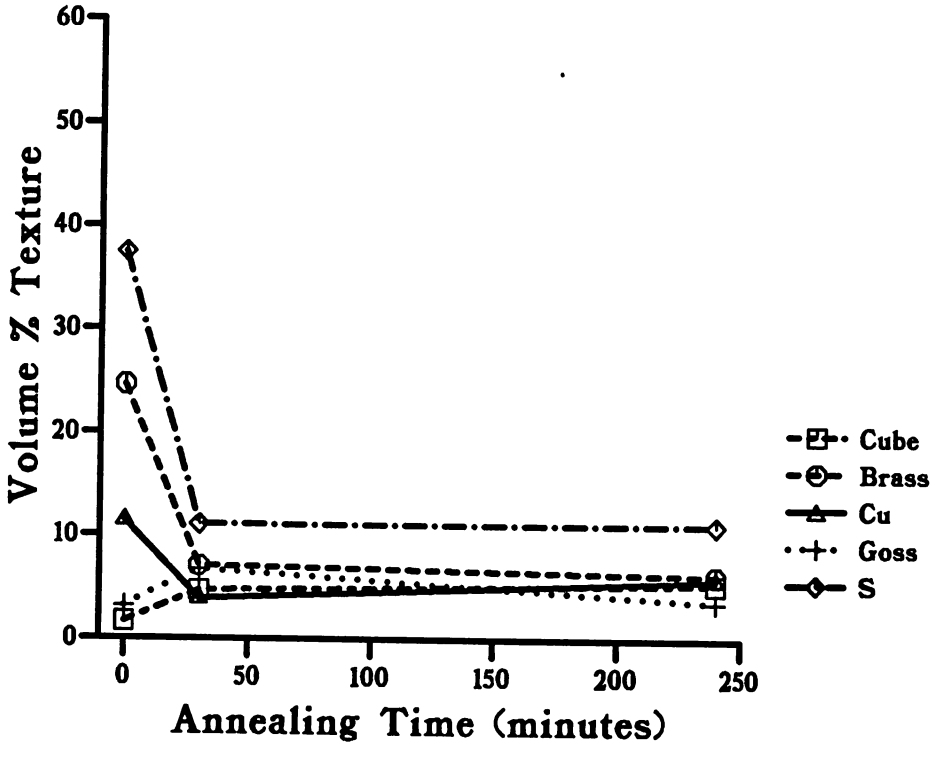

(b)

Figure 7.29 Bulk volume fraction texture changes in the 6063 AA Mn alloy during annealing at (a) 350°C and (b) 450°C for 4 hours. Measurements taken in the long transverse section.

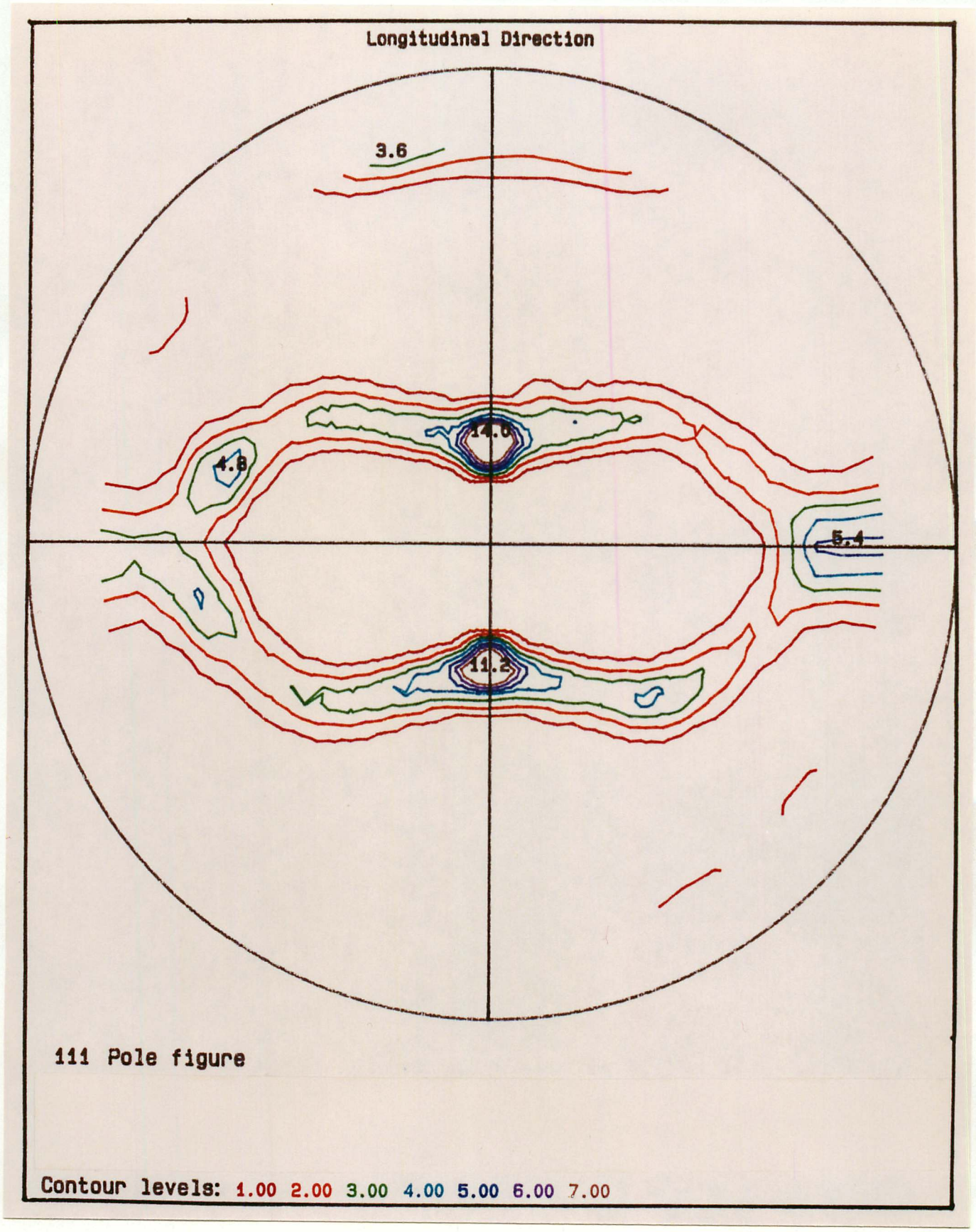

Figure 7.30 111 pole figure for the 6063 AA Mn alloy in the as-rolled condition.

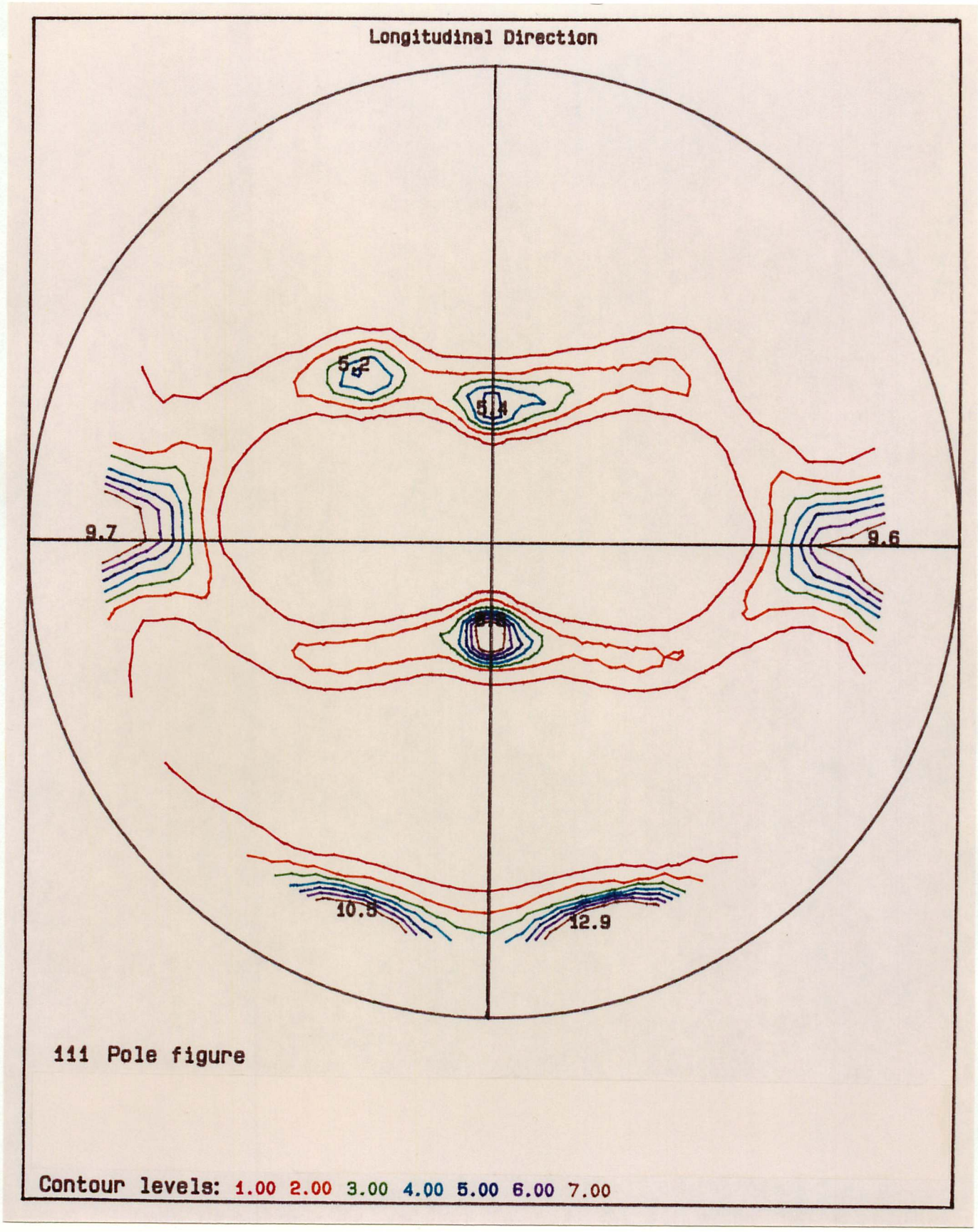

Figure 7.31 111 pole figure for the 6063 AA Mn alloy after annealing at 350°C for 4 hours.

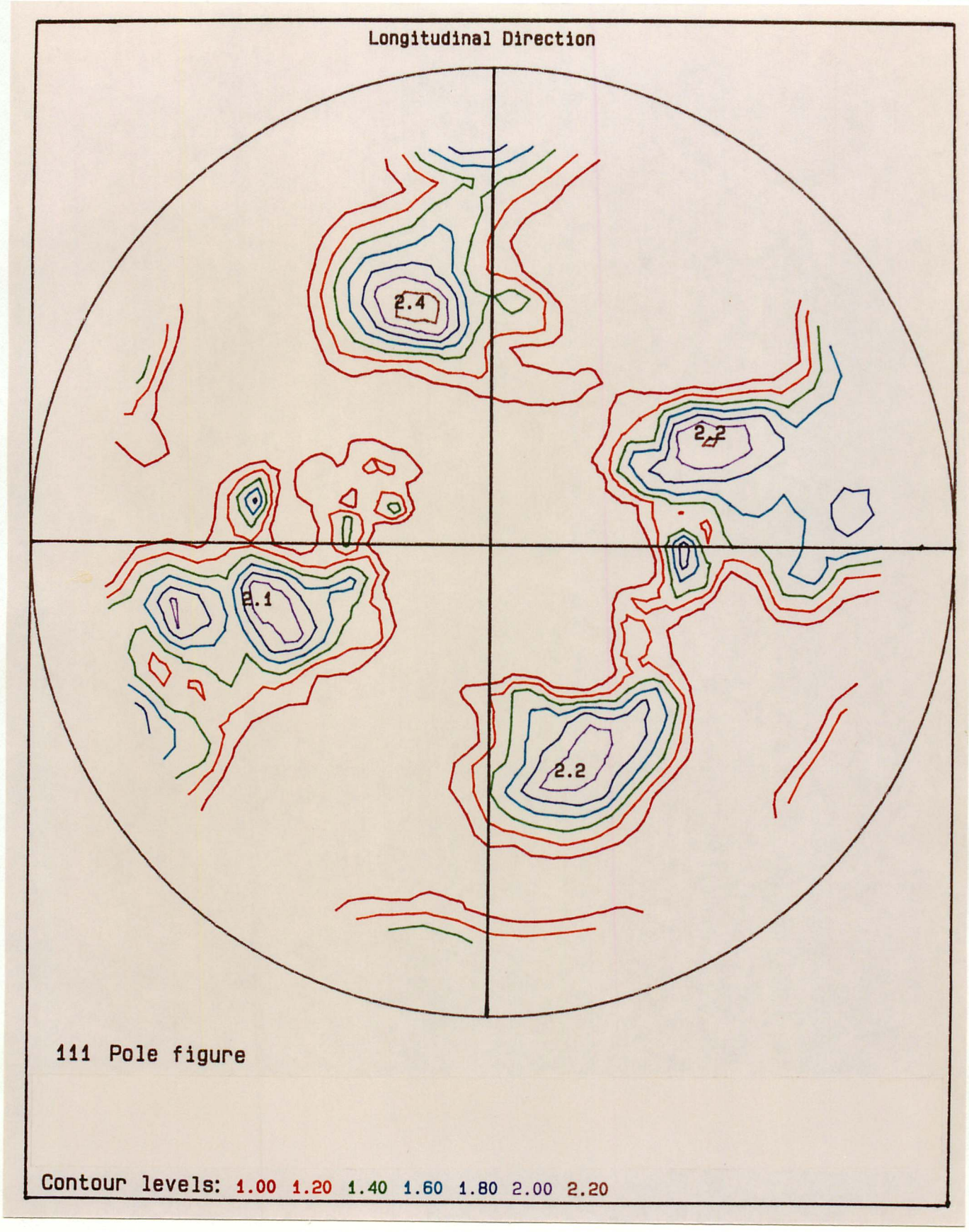

Figure 7.32 111 pole figure for the 6063 AA Mn alloy after annealing at 450°C for 4 hours.

7.2 Conclusions

It can be concluded that in a low temperature anneal (*ie.* less than 400°C) the annealing processes which produce an elongated microstructure in the *6063AA* + Mn alloy are essentially ones of recovery only, where the dispersion of small pinning particles are sufficient to prevent any true recrystallisation.

The thermomechanical processing is shown schematically in figure *7.33*, in which the as–cast equiaxed grain structure (a) is rolled down to give an elongated grain structure (b). Within these grains, the subgrains are also elongated, with a high dislocation density (c). During annealing, the small particles in the matrix pin these subgrain boundaries and dislocation networks whilst an extensive 'cleaning up' process occurs in which dislocations are anhilated, or migrate to higher angle boundaries (d). Eventually only the original grain boundaries remain (e) with the matrix now exhibiting a low dislocation–density and therefore a low–energy, stable state, and the microstructure is directly comparable to the as–rolled state (f).

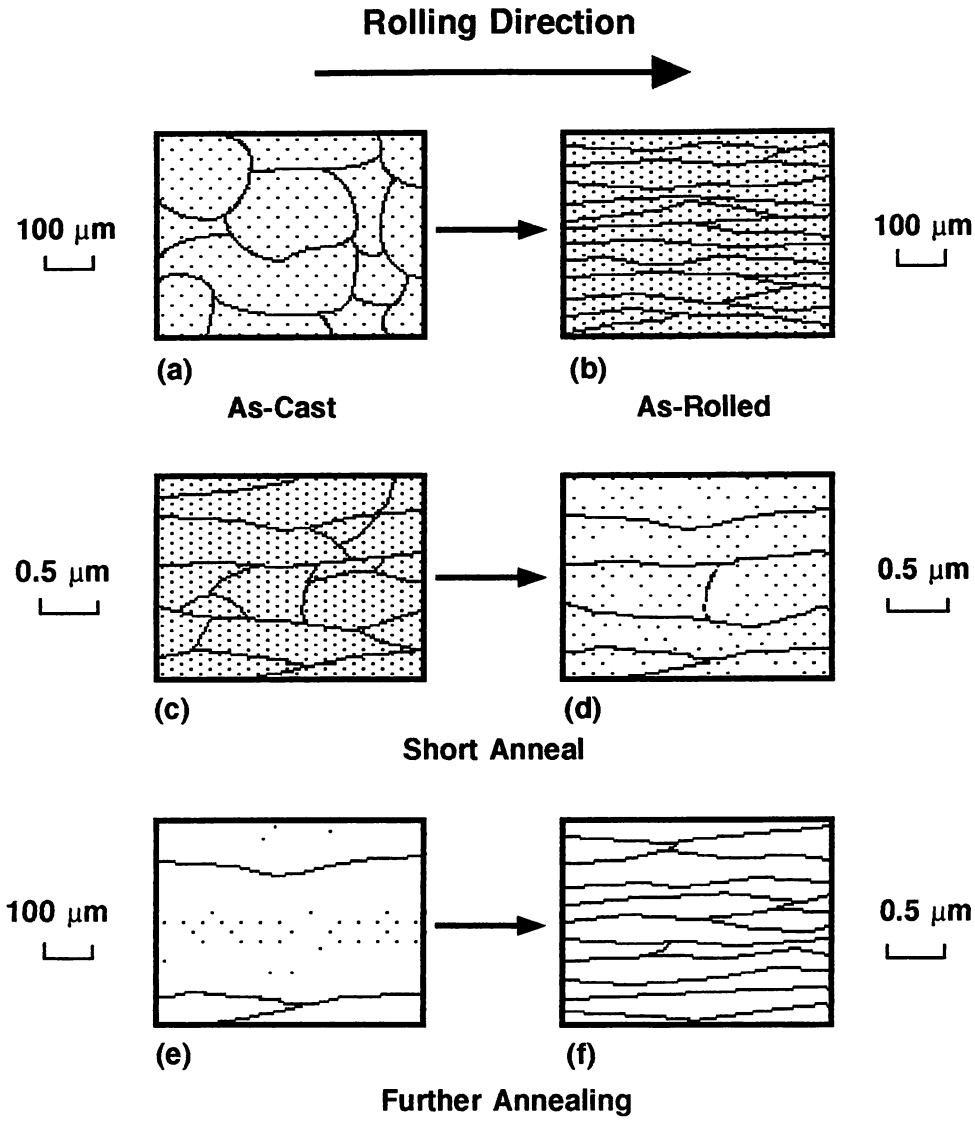

Figure 7.33 Schematic illustration of the annealing process referred to as 'extended recovery', which leads to the development of elongated grains in the final microstructure of the 6063 AA Mn alloy.

Chapter 8

CONCLUSIONS AND FURTHER WORK

8.1 Aluminium–Iron Alloys

Needle–like $FeAl_3$ particles present in aluminium alloys prior to cold–rolling have been found to develop associated deformation–zones in which the subgrains developed are small and equiaxed as compared to the elongated subgrains in the matrix, and exhibit a relatively high dislocation–density. Around particles of $1 - 7$ μm in length, the deformation zones extended to a distance of approximately 1.5 μm from the particle/matrix interface along the long dimension, and approximately 0.8 μm from the interface at the particle tips, where the subgrains were smaller and more highly deformed. The coincidence–site–lattice parameters for subgrains within these zones were large with respect to the deformed matrix as compared to the small values found between subgrains away from particles, underlying the role of the particles in producing major perturbations in deformation texture.

The formation of recrystallisation nuclei during annealing occurred only at particles in the alloy specifications studied, and this appeared to be helped by the high rate of polygonisation within the particle deformation–zones. Clustering of subgrain–orientation types within the deformation zone was found to be an important factor in promoting grain–boundary disappearance and local reorientation, and atomic reorganisation. This allowed one particular subgrain within a cluster to grow in size, thus becoming a potential nucleus for recrystallisation. During this stage, which can be described as a recovery mechanism within the zones, the potential recrystallisation nuclei grew in size until they had consumed the deformation zone. The nature of the zones allowed this process to happen due to the small size of subgrains involved, in addition to their high misorientation with respect to the deformed matrix but low misorientation between adjacent subgrains in clusters within the zones. These critera were fulfilled more often at particle tips, and nucleation from these areas was seen more frequently than from particle sides.

Decreases in subgrain CSL values are likely to be due predominantly to the movement of dislocations away from the subgrains in question, which makes local atomic reorganisation necessary to accomodate fewer dislocations. Large rotations of the neighbouring subgrains is not necessary if their original misorientation with respect to each other is not large (which is true within clusters), therefore a true 'subgrain–coalescence' mechanism theory is not necessary to describe the process involved.

In the low iron–content alloy, deformation zones at particles were smaller, with less highly deformed subgrains. However, recrystallisation still nucleated at particles, and the mechanism

involved could again be described as a localised recovery mechanism.

Once these nuclei are established at particles, it is likely that a further stage of grain growth will proceed, in which a selection process comes into play. Those nuclei which occur at more favourable orientations for growth will then dominate the grain growth stage. This grain growth stage consumed the surrounding deformed matrix to give a completely recrystallised microstructure. Particles occurring within bands produced only small recrystallised grains, since neighbouring particles inhibited further grain growth by pinning of grain boundaries. Particles which were relatively isolated from these bands or at band edges initiated recrystallised grains which were able to grow more extensively, and so a duplex microstructure resulted. In the low iron–content alloy this effect was exaggerated since most of the low volume–fraction of particles were situated within thin bands in which the particle spacing was very small and the bands occurred at large separations.

As part of a further investigation of these alloy annealing–mechanisms, it is suggested that TEM–diffraction data should be used to produce accurate axis–angle pair measurements between neighbouring subgrains within the particle deformation–zones in order to observe more closely the mechanisms proceeding during annealing. The nature of CSL values means that a boundary characterised by one CSL value could actually be one of a number of misorientations. The results described therefore are essentially qualitative, and have allowed a clearer understanding of the nucleation mechanisms involved at needle–like particles.

The use of Kikuchi line diffraction–patterns in order to calculate orientations with respect to the rolling direction would be of interest in order to ascertain more accurately and distinctively not only the nature of the deformation zones, but also the preferred microtexture for nucleus formation. In addition to this, it would be of interest to watch the stages of grain growth immediately beyond the deformation zones in conjunction with measuring the orientation of those grains which are successful in doing so. Since the small thin–area of foils used in transmission electron microscopy make these observations difficult, scanning electron microscopy techniques and the use of electron back–scattering patterns would be more convenient.

8.2 Aluminium 6063 AA + Mn Alloy

Strain–induced precipitation of small particles during processing is an extremely efficient method of retarding recrystallisation in subsequent static anneals. In the case of the *6063AA* alloy with added manganese, it was found that the effect of pinning of subgrain boundaries by the Mn and Si particles is so dramatic, that recrystallisation is prevented altogether, allowing extended recovery to occur to completion. There is also an important effect brought about by the relatively uniform distribution of particles, since this prevents development of heterogeneities in dislocation density and subgrain microstructures. Thus, the differences in stored

energies across boundaries required for recrystallisation are prevented. It is this 'extended recovery' process which produces an elongated grain structure upon heat treatment. The coarse $FeAl_3$ and Mg_2Si particles aligned along the rolling direction have little or no role to play in microstructural development.

In any further work carried out it would be necessary to investigate the influence of annealing temperature on the recovery mechanisms involved, since an increase in temperature in this investigation appeared to produce widely differing bulk–texture results. Also, the effect of prior deformation is likely to be an important factor in determining the efficiency of the small particles in inhibiting recrystallisation, and therefore would be useful to investigate further.

REFERENCES

ASHBY, M.F., (1970,)
The deformation of plastically non–homogeneous materials *Phil. Mag.* **21**, 399-424

ASTROM, H.U., (1955,)
Isothermal measurements on the release of energy stored in cold-worked aluminium *Arkiv f Fysik* **10**, 197-211

AUST, K.T. and RUTTER, J.W., (1960,)
Annealing twins and coincidence–site boundaries in high–purity lead *Trans. AIME* **218**, 1023-1028

AUST, K.T. and RUTTER, J.W., (1961,)
Some annealing phenomena in high–purity metals *in Ultra High Purity Metals (ASM),* 115-148

AVRAMI, M., (1941,)
Granulation, phase change and microstructure. Kinetics of phase change III *J. Chem. Phys.* **9**, 177-184

BAILEY, J.E., (1960,)
Electron microscope observations on the annealing processes occuring in cold–worked silver *Phil. Mag.* **5**, 833-842

BAILEY, J.E., (1963,)
in Electron Microscopy and the Strength of Crystals (ed. G.Thomas and G.Washburn) N.Y., 131-145

BAILEY, J.E. and HIRSCH, P.B., (1962,)
The recrystallisation process in some polycrystalline metals *Proc. Roy. Soc.* **267A**, 11-30

BALL, C.J., (1957,)
Surface distributions of dislocations in metal, II *Phil. Mag.* **2**, 977-984

BALL, C.J. and HIRSCH, P.B., (1955,)
Surface distributions of dislocations in metal, I *Phil. Mag.* **46**, 1343-1352

BALOCH, M., (1989,)
Ph.D. Thesis *University of Cambridge*

BAY, B. and HANSEN, N., (1979,)
Initial stages of recrystallisation in aluminium of commercial purity *Metall. Trans.* **10A**, 279-288

BAY, B. and HANSEN, N., (1984,)
Recrystallisation in commercially pure aluminium *Metall. Trans.* **15A**, 287-297

BECK, P.A., (1949,)
Effect of a dispersed phase on grain–growth in Al-Mn alloys *Trans. AIME* **185**, 310-315

BECK, P.A., (1954,)
Annealing of cold–worked metals *Advanc. Phys.* **3**, 245-324

BECK, P.A., HOLZWORTH, and SPERRY, P.R., (1949b,)
Effect of a dispersed phase on grain growth in Al–Mn alloys *Trans. AIME* **180**, 163-192

BECK, P.A. and HU, H., (1966,)
The origin of recrystallisation textures *in Recrystallisation, Grain Growth and Textures (ed Margolin), ASM Metals Park, Ohio.* 393-433

BECK, P.A., KREMER, J.C., DEMER, L.J., HOLZWORTH, M.L., (1948,)
Grain growth in high–purity aluminium and in an Al-Mn alloy *Trans. AIME* **175**, 372-400

BECK, P.A. and SPERRY, P.R., (1949a,)
Effect of recrystallisation texture on grain–growth *Metall. Trans.* 240-241

BECK, P.A. and SPERRY, P.R., (1950,)
Strain–induced grain–boundary migration in high–purity aluminium *J. Appl. Phys.* **21,** 150-152

BELLIER, S.P. and DOHERTY, R.D., (1977,)
The structure of deformed aluminium and its recrystallisation - investigations with transmission Kossel diffraction *Acta. Met.* **25,** 521-538

BLECK, W. and BUNGE, H.J., (1981,)
The recrystallisation of Al–Mn investigated with pole figures by number *Acta. Met.* **29,** 1401-1412

BROWN, L.M. and STOBBS, D.W., (1971,)
The work–hardening of copper–silica. I The role of plastic relaxation *Phil. Mag.* **23,** 1201-1233

BROWN, L.M. and STOBBS, D.W., (1976,)
The work–hardening of copper–silica. V Equilibrium plastic–relaxation by secondary dislocations *Phil. Mag.* **34,** 351-372

BUNGE, H.J., (1969,)
Texture Analysis in Materials Science - Mathematical Methods *translated to English 1982 (Butterworth & Co.)*

BURGERS, W.G., (1941,)
in Handbuch der Metallphysik (ed Masing), Akad. Verl., Leipzig.

BURGERS, W.G. and LOUWERSE, P.C., (1931,)
On the deformation and recrystallisation of aluminium *Z. Physic.* **67,** 605-678

BURKE, J.E. and TURNBULL, D., (1952,)
Recrystallisation and grain growth *in Prog. in Met. Phys. (London, Pergamon Press)* **3,** 220-292

CAHN, J.W., (1949,)
Recrystallisation of single crystals after plastic bending *J. Inst. Met.* **76,** 121-143

CAHN, R.W., (1950,)
A new theory of recrystallisation nuclei *Proc. Phys .Soc. (London)* **A60,** 323-336

CAHN, J.W., (1962,)
The impurity–drag effect in grain–boundary motion *Acta. Met.* **10,** 789-798

CAHN, J.W., (1965,)
Recrystallisation mechanisms *in Recrystallisation, Grain Growth and Textures (ed. Margolin) ASM Metals Park, Ohio* 99-127

CHANG, S.K. and HUMPHREYS, F.J., (1991,)
Effect of recovery treatment on recrystallisation of Al–4wt%Cu *Mat. Sci. & Tech.* **7,** 357-359

CHAPMAN, P.F. and STOBBS, W.M., (1969,)
The measurement of local rotations in the electron microscope *Phil. Mag.* **19,** 1015-1030

CHRISTIAN, J.W., (1965,)
Theory of Transformation in Metals and Alloys *Oxford, Pergamon Press.*

COTTRELL, A.H., (1953,)
Dislocations and Plastic Flow in Crystals *Oxford,* 51-57

DETERT, K., (1971,)
Secondary recrystallisation *in Recrystallisation of Metallic Materials (ed. F. Haessner, Dr.) Riederer-Verlag GMBH, Stuttgart,* 97-109

DEW-HUGHES, D. and ROBERTSON, W.D., (1960,)
Dispersed particle–hardening of Al–Cu alloy single–crystals *Acta. Met.* **8,** 147-155

DINGLEY, D.J., (1984,)
Diffraction from submicron particles using electron–backscatter reflection *in Scanning Electron Microscopy* **11,** 569-575

DOHERTY, R.D., (1974,)
The deformed state and nucleation of recrystallisation *Metal Sci. J.* **8,** 132-142

DOHERTY, R.D. and CAHN, R.W., (1972,)
Nucleation of new grains in recrystallisation of cold–worked metals *J. Less Common Metals* **28,** 279-296

DOHERTY, R.D. and MARTIN, J.W., (1963,)
The effect of a dispersed second–phase on the recrystallisation of Al–Cu alloys *J. Inst. Metals* **91,** 332-338

DOHERTY, R.D. and MARTIN, J.W., (1964,)
Recrystallisation in two–phase Al–Cu alloys *Trans. Am. Soc. Metals* **57,** 874-884

DUGGAN, B.J., SINDEL, M., KÖHLOFF, G.D. and LÜCKE, K., (1990,)
Oriented nucleation, oriented growth and twinning in cube–texture formation *Acta. Met.* **38,** 103-111

DUNN, C.G. and WALTER, J.L., (1965,)
Secondary recrystallisation *in Recrystallisation, Grain Growth and Textures (ed. Margolin), Metals Park, Ohio* 461-521

ENGLISH, A.T. and BACKOFEN, W.A., (1964,)
Recrystallisation in hot–worked Si–Fe *Trans. Met. Soc. AIME* **230,** 396-407

ERBSLÖH, H.W., BRONDER, P. and LÜCKE, K., (1984,)
ICOTOM 7 *7th Inter. Conf. on Texture of Materials.* 221-229

ES-SAID, O.S. and MORRIS, J.G., (1986,)
The effect of second phase particles on the recrystallisation behavior, texture and earing behavior of strip cast 3004 Al alloy *in Aluminium Alloys, Their Physical and Mechanical Properties.* **EMAS,** 451-472

ES-SAID, O.S., MORRIS, J.G. and MERCHANT, H.D., (1988,)
The influence of particles on the recrystallisation of aluminium alloys *in Homogenisation and Annealing of Aluminium and Copper Alloys. (Eds. Merchant, Crane, Chia), The Met. Soc.,* 183-207

FERRAN, G.L., DOHERTY, R.D. and CAHN, R.W., (1971,)
The Kossel–line determination of the orientation of new grains formed by recrystallisation of aluminium *Acta. Met.* **19,** 1019-1028

FUJITA, H., (1961,)
Direct observation of subgrain–growth of cold–worked aluminium by means of electron microscopy *J. Phys. Soc. Japan* **16,** 397-406

GAWNE, D.T. and HIGGINS, G.T., (1971,)
Associations between spherical particles of two dissimilar phases *J. Mat. Sci.* **6,** 403-412

GORDON, P. and VANDERMEER, R.A., (1962,)
The mechanism of boundary migration in recrystallisation *Trans. AIME* **224,** 917-928

HAESSNER, F., (1971,)
Systematic survey and fundamental problems of recrystallisation *in Recrystallisation of Metallic Materials, 1st Edition, Stuttgart* 5-20

HAESSNER, F., HORNBOGEN, E. and MUKHERJEE, M., (1966,)
Retardation of recrystallisation by a small second–phase *Z. Metallk.* **57**, 171-175

HAM, R.K., (1962,)
On the loss of dislocations during the preperation of thin–films *Phil. Mag.* **7**, 1177-1182

HERBST, P. and HUBER, J., (1978,)
in Proc. 5th Inter. Conf. on Textures. (ed Gottstein and Lücke), Berlin, 453-467

HILLERT, M. and SUNDMAN, B., (1976,)
A treatment of the solute–drag on moving grain–boundaries and phase interfaces in binary alloys *Acta. Met.* **24**, 731-743

HIRSCH, J.R., (1990,)
Correlations of deformation and texture and microstructure *Mat. Sci. & Tech.* **6**, 1048-1057

HIRSCH, P.B, HORNE, R.W. and WHELAN, M.J. (1957,)
Direct observations of the arrangement and motion of dislocations in aluminium *in Dislocations and Mechanical Properties of Crystals, Wiley & son, New York* 92-113

HONEYCOMBE, R.W.K., (1968,)
The Plastic Deformation of Metals *Arnold.*

HU, H., (1959,)
Observations on the recrytallisation of a Si–Fe crystal in a polygonized matrix *Trans. AIME* **215**, 320-326

HU, H., (1962,)
Direct observations on the annealing of a Si–Fe crystal in the electron microscope *Trans. AIME* **224**, 75-84

HU, H., (1963,)
Annealing of silicon–iron single crystals *in Recovery and Recrystallisation of Metals. (ed. L.Himmel) N.Y.,* 311-362

HUMPHREYS, F.J., (1977,)
The nucleation of recrystallisation at second–phase particles in deformed aluminium *Acta. Met.* **25**, 1323-1344

HUMPHREYS, F.J., (1978,)
The deformation structure and the recrystallisation behaviour of two–phase alloys *Met. Forum* **1**, 123-135

HUMPHREYS, F.J., (1979,)
Local lattice–rotations at second–phase particles in deformed metals *Acta. Met.* **27**, 1801-1814

HUMPHREYS, F.J., (1984,)
The determination of local texture by electron diffraction methods. *Proc. 5th RISØ Symp., (Eds. Hessel et al, Roskilde,Denmark* 35-50

HUMPHREYS, F.J. and KALU, (1990,)
The plasticity of particle–containing polycrystals *Acta. Met. Mater.* **38**, 917-930

HUMPHREYS, F.J. and STEWART, A.T., (1972,)
Dislocation generation at SiO_2 particles in an α–brass matrix on plastic deformation *Surf. Sci.* **31**, 389-421

HUTCHINSON, B. (1974,)
Development of textures in recrystallisation *Met. Sci.* **8**, 185-196

IBE, G. and LÜCKE, K., (1964,)
Technical rep. to *ARO(D)* from *Institute fur Allgemeine Metallphisik der Technischen Hochschulen, Aachen.*

ITO, K., MUSICK, R. and LÜCKE, K., (1983,)
The influence of iron content and annealing temperature on the recrystallisation textures of high purity aluminium-iron alloys *Acta. Met.* **31,** 2137-2149

JENSEN, D.J., HANSEN, N. and HUMPHREYS, F.J., (1985,)
Texture development during recrystallisation of aluminium containing large particles *Acta. Met.* **33,** 2155-2162

KAHN, J.W. and HUMPHREYS, F.J., (1988,)
A microtexture investigation of the deformation and recovery of particle–containing alloys *in Proc. 8th ICOTOM Met. Sci. AIME* 511-516

KEH, A.S. and WEISSMAN, S., (1963,)
in Electron Microscopy and Strength of Crystals, Interscience, New York 231-267

KELLER, J.N., HIRSCH, P.B. and Thorp, J.S., (1950,)
An X–ray microbeam examination of a plastically–deformed metal *Nature, Lond.* **165,** 554-556

KOSTER, U. and HORNBOGEN, E., (1968,)
Electron microscopy of Al-Cu single crystals *Z. Metallkunde* **59,** 792-799

LEIBMANN, B. and LÜCKE, K., (1956a,)
Measurement of grain–growth rates in recrystallisation *Trans. Amer. Inst. Min. Engrs.* **206,** 1413-1416

LEIBMANN, B., LÜCKE, K. and MASING, G., (1956b,)
Orientation of nuclei during primary recrystallisation of aluminium *Z. Metallk.* **47,** 57-63

LESLIE, W.C., PLECITY, F.G. and MICHALAK, J.T., (1961,)
Recrystallisation of iron and iron–manganese alloys *Trans. AIME* **221,** 691-700

LI, J.C.M., (1962a,)
Possibility of subgrain rotation during recrystallisation *J. Appl. Phys.* **33,** 2958-2965

LI, J.C.M., (1962b,)
Comments *in Direct Observation of Imperfections in Crystals, Interscience, New York* 234-238

LI, J.C.M., (1963,)
Discussion on grain–boundary migration *in Recovery and Recrystallisation of Metals, Interscience, New York,* 160-164

LI, J.C.M., (1965,)
Recovery processes in metals *Recrystallisation, Grain Growth and Textures. AIME Metals Park, Ohio* 45-97

LIU, L., JENSEN, D. J. and HANSEN, N., (1989,)
Recrystallisation microstructure in cold–rolled aluminium composites reinforced by Si–C whiskers *Met. Trans.* **20A,** 1743-1753

LLOYD, D.J., (1982,)
Recrystallisation of unhomogenized aluminium–manganese alloys *Met. Sci.* **16,** 304-308

LÜCKE, K., (1984,)
Proc. 7th Int. Conf. on Textures of Materials. Noordwijkerhout, Holland. (Eds. Brakman et al), 195-212

LÜCKE, K., POSPIECH, J., VIRNICH, K.H. and JURA, J., (1981,)
On the problem of the reproduction of the true orientation distribution from pole figures *Acta. Met.* **29,** 167-185

LÜCKE, K. and STUWE, H.P., (1967,)
On the theory of grain–boundary motion *in Recovery and Recrystallisation of Metals. (ed. L.Himmel) (Interscience, N.Y.),* 171-210

LYTTON, J.L., WESTMACOTT, K.H. and POTTER, L.C., (1965,)
The relation between flow stress and dislocation structure during recovery of high–purity aluminium *Trans. AIME* **233,** 1757-1765

McKIE, D. and McKIE, C., (1986,)
Essentials of Crystallography *Blackwell.*

McQUEEN, H.J., CHIA H., and STARKE, E.H., (1985,)
The microstructural strengthening mechanisms in dilute Al–Fe conductor alloys *in Microstructural Control in Aluminium Alloys: Deformation, Recovery and Recrystallisation. Eds Chia and McQueen* 1-18

MICHELS, L.C. and RICKETTS, B.G., (1967,)
Nucleation of recrystallisation in cold-worked aluminium and nickel *Trans. AIME* **239,** 1841-1847

NES, E., (1980,)
Recrystallisation and bimodal particle–distribution *in Recrystallisation and Grain Growth of Multiphase and Particle Containing Materials. (Eds. HANSEN, Jones and Leffers) RISØ, Denmark,* 85-95

NIELSEN, J.P., (1954,)
Mechanism for the origin of recrystallisation nuclei *Trans. AIME* **200,** 1084-1088

NOBILI, D. and DE MARIA, R., (1965,)
Isochronal recovery of work–hardening in aluminium–alumina alloys *J. Nucl. Mat.* **17,** 5-19

POLMEAR, I.J., (1981,)
Metallurgy of the Light Metals *Arnold*

RIDHA, A.A. and HUTCHINSON, W.B., (1982,)
Recrystallisation mechanisms and the origin of cube texture in copper *Acta. Met.* **30,** 1929-1939

SAJI, S. and HORNBOGEN, E., (1978,)
Combined recrystallisation and precipitate reactions in a Cu–4wt% Ti alloy *Z. Metallk.* **69,** 741-746

SANDSTRÖM, R., (1980,)
Influence of a distribution of coarse particles on the recrystallisation kinetics. Application to Al–Fe alloys. *Z. Metallk.* **71,** 741-751

SCHWARZER, R.A. and WEILAND, H., (1986,)
Electron–diffraction polefigure measurements *in Experimental techniques of texture analysis., Ed. Bunge* 287-300

SPEICH, G.R. and FISHER, R.M., (1965,)
Recrystallisation of a rapidly heated 3.25% Si steel *in Recrystallisation, Grain Growth and Textures, AIME, Metals Park, Ohio* 563-598

THURBER and McHARGUE, (1960,)
Deformation textures in aluminium–uranium alloys *Trans. AIME* **218,** 141-144

TOWNER, R.J. and BERGER, J.A., (1960,)
X-Ray studies of polygonisation and subgrain–growth in aluminium *Trans. AIME* **218,** 611-617

VANDERMEER, R.A. and GORDON, P., (1963,)
The influence of recovery on recrystallisation in aluminium *in Recovery and Recrystallisation of Metals, Interscience, New York* 211-239

WALTER, J.L. and KOCH, E.F., (1962,)
Electron microscope study of the structure of cold–rolled and annealed (100)[001] crystals of high–purity silicon–iron *Acta. Met.* **10,** 1059-1075

WALTER, J.L. and KOCH, E.F., (1963,)
Substructures and recrystallisation of deformed (100)[001] oriented crystals of high–purity silicon–iron *Acta. Met.* **11,** 923-938

WESTERMAN, E.J. and LENEL, F.V., (1960,)
Recrystallisation of cold–drawn sintered aluminium powder *Trans AIME* **218,** 1010-1014

ZENER, (1948,)
Private communication to C.S. Smith (Grains, phases and interfaces: an interpretation of microstructure) *Trans. AIME* **175,** 15-51

APPENDIX III

The following computer program is used to calulate the axis–angle pair relationship between two adjacent grains, and to also match that axis–angle pair to the appropriate sigma value.

```
* MAIN PROGRAM - AXIS ANGLE PAIRS
. . . . . .
* This program is designed to produce the rotation matrix
* required to bring two crystals into coincidence, in addition
* to the axis of rotation and the angle of rotation required.
. . . . . .
* It will then choose the sigma value which most accurately
* corresponds to the 28 equivalent axis-angle pairs produced.
. . . . . .

      IMPLICIT REAL(A-H,K-Z), INTEGER(I,J)
      DIMENSION BEC(24,9),B(9),AA(9),R(9),AINVR(9),AX(24,3),ANGS(24)
27    WRITE(*,26)
      WRITE(*,25)
26    FORMAT(///////)
25    FORMAT(///////
     + 20X,' 2B 2A 1B'/
     + 20X,' — / '/
     + 20X,' — / '/
     + 20X,' — / '/
     + 20X,' — / '/
     + 20X,' ——— 1A '/
     + //10X,' Arrange your data according to this diagram '//
     + 19X,' VECTORS 1A & 2A are from CRYSTAL A'/
     + 19X,' VECTORS 1B & 2B are from CRYSTAL B'/
     + 19X,' You also need the acute angle between 2A & 2B'/
     + 50X,' ...Press Return when ready')
20    FORMAT(25X,' Components of VECTOR 1A ?'/)
23    FORMAT(25X,' Components of VECTOR 2A ?'/)
21    FORMAT(25X,' Components of VECTOR 1B ?'/)
24    FORMAT(25X,' Components of VECTOR 2B ?'/)
22    FORMAT(25X,' Acute angle (degrees) between ',
    + ' VECTORS 2A and 2B ?'/)
8967  FORMAT(' ****************************************',
     + '*******************************'/)
      READ(*,*)
. . . . . .
      WRITE(*,20)
      READ(*,*) H,K,L
      WRITE(*,23)
      READ(*,*)H1,K1,L1
      WRITE(*,21)
```

```
      READ(*,*) U1,V1,W1
      WRITE(*,24)
      READ(*,*)U,V,W
      WRITE(*,22)
      CALL REED(PHI)
      WRITE(6,3)PHI
3     FORMAT(10X,' Angle between VECTORS 2A & 2B = ',F5.1,' DEGREES'/)
      WRITE(6,4)H,K,L,H1,K1,L1,U1,V1,W1,U,V,W
4     FORMAT(10X, ' VECTOR 1A =', 3F10.4/
     +  10X, ' VECTOR 2A =', 3F10.4/
     +  10X, ' VECTOR 1B =', 3F10.4/
     +  10X, ' VECTOR 2B =', 3F10.4/)
      PHI=PHI*2.0*3.14159/360.0
      CALL NORM(H,K,L)
      CALL NORM(H1,K1,L1)
      CALL NORM(U1,V1,W1)
      CALL NORM(U,V,W)
. . . . . .
* The following section calculates the rotation matrix
* required to bring the two crystals into coincidence
* as well as the axis-angle pairs
. . . . . .
      H2=K*L1-L*K1
      K2=L*H1-H*L1
      L2=H*K1-K*H1
      CALL NORM(H2,K2,L2)
      Q=H*H1+K*K1+L*L1
8     Q=ACOS(Q)
      M=U*U1+V*V1+W*W1
10    M=ACOS(M)
      P=M-PHI
      A1=H2
      A2=K2
      A3=L2
      A4=H1
      A5=K1
      A6=L1
      A7=H
      A8=K
      A9=L
      C2=COS(PHI)
      C3=COS(PHI+Q)
      C4=COS(P)
      C5=COS(Q-P)
      B(1)=A5*A9-A6*A8
      B(2)=A6*A7-A4*A9
      B(3)=A4*A8-A7*A5
      B(4)=A8*A3-A9*A2
      B(5)=A9*A1-A7*A3
      B(6)=A7*A2-A8*A1
      B(7)=A2*A6-A3*A5
```

```
      B(8)=A3*A4-A1*A6
      B(9)=A1*A5-A2*A4
      C=A1*B(1)+A2*B(2)+A3*B(3)
      DO  11 I=1,9
          AA(I)=B(I)/C
11    CONTINUE
      H3=AA(4)*C2+AA(7)*C3
      K3=AA(5)*C2+AA(8)*C3
      L3=AA(6)*C2+AA(9)*C3
      H4=AA(4)*C4+AA(7)*C5
      K4=AA(5)*C4+AA(8)*C5
      L4=AA(6)*C4+AA(9)*C5
      CALL NORM(H3,K3,L3)
      CALL NORM(H4,K4,L4)
      X=(K4-V1)*(L3-W)-(L4-W1)*(K3-V)
      Y=(L4-W1)*(H3-U)-(H4-U1)*(L3-W)
      Z=(H4-U1)*(K3-V)-(K4-V1)*(H3-U)
      C10=(H4+U1)*(H3-U)+(K4+V1)*(K3-V)+(L3-W)*(L4+W1)
      X=X/C10
      Y=Y/C10
      Z=Z/C10
      M=SQRT(X*X+Y*Y+Z*Z)
      N=2.0*ATAN(M)
      N1=N*360.0/(2.0*3.14159)
      CALL NORM(X,Y,Z)
      WRITE(6,12)X,Y,Z,N1
      12 FORMAT(' ******',11X,' Rotation Axis = [',3F8.4,']'/
     +  ' ****** Right-handed rotation angle =',F7.1,' Degrees'/)
* The 28 equivalent axis-angle pairs are also calulated
      CALL ROT(X,Y,Z,N,R)
. . . . . .
* The following section compares the 28 equivalent axis-angle
* pairs to those of the sigma values, and chooses that sigma
* value which displays the best fit
. . . . . .
      AX(1,1) = X
      AX(1,2) = Y
      AX(1,3) = Z
      ANGS(1) = N1
      XXX=X
      YYY=Y
      ZZZ=Z
      NNNN1=N1
      DO  450 I20=1,24
          DO  451 I21=1,9
              BEC(I20,I21)=0.0
451       CONTINUE
450   CONTINUE
      CALL ORIENT(BEC)
. . . . . .
      WRITE (6,15)
```

```
      WRITE(6,16)R(1),R(2),R(3)
      WRITE(6,16)R(4),R(5),R(6)
      WRITE(6,16)R(7),R(8),R(9)
16    FORMAT(3F12.6)
15    FORMAT(' Rotation Matrix')
* CALL SIG(R,SI,9)
      WRITE(6,*) 'SIGMA=', SI
      CALL DET(R,DETS)
      WRITE(6,*) 'DETERMINANT =',DETS
800   FORMAT(' Inverse of Rotation Matrix')
      CALL INVERS(AINVR,R)
      WRITE(6,800)
      WRITE(6,16)AINVR(1),AINVR(2),AINVR(3)
      WRITE(6,16)AINVR(4),AINVR(5),AINVR(6)
      WRITE(6,16)AINVR(7),AINVR(8),AINVR(9)
      CALL ROTAT(XXX,YYY,ZZZ,NNNN1,BEC,AX,ANGS)
      CALL ASIG(AX,ANGS)
      WRITE(*,8967)
      WRITE(*,8967)
      WRITE(*,28)
28    FORMAT(10X,' Continue Analysis? (1 = Yes, 0 = No)')
      CALL REEDI(JYES)
      CALL TRY(2,1.0,JYES)
      IF(JYES .EQ. 1)GOTO 27
      STOP
      END
. . . . . .

. . . . . .
      SUBROUTINE ORIENT(BEC)
      DIMENSION BEC(24,9)
      BEC(2,2)=1.0
      BEC(2,6)=1.0
      BEC(2,7)=1.0
      BEC(3,3)=1.0
      BEC(3,4)=1.0
      BEC(3,8)=1.0
      BEC(4,1)=-1.0
      BEC(4,6)=-1.0
      BEC(4,8)=-1.0
      BEC(5,2)=-1.0
      BEC(5,4)=-1.0
      BEC(5,9)=-1.0
      BEC(6,3)=-1.0
      BEC(6,5)=-1.0
      BEC(6,7)=-1.0
      BEC(7,1)=1.0
      BEC(7,6)=1.0
      BEC(7,8)=-1.0
      BEC(8,3)=1.0
      BEC(8,5)=1.0
```

```
BEC(8,7)=-1.0
BEC(9,2)=1.0
BEC(9,4)=1.0
BEC(9,9)=-1.0
BEC(10,3)=-1.0
BEC(10,4)=-1.0
BEC(10,8)=1.0
BEC(11,2)=-1.0
BEC(11,6)=-1.0
BEC(11,7)=1.0
BEC(12,1)=-1.0
BEC(12,5)=-1.0
BEC(12,9)=1.0
BEC(13,1)=1.0
BEC(13,6)=-1.0
BEC(13,8)=1.0
BEC(14,3)=1.0
BEC(14,5)=-1.0
BEC(14,7)=1.0
BEC(15,2)=1.0
BEC(15,4)=-1.0
BEC(15,9)=1.0
BEC(16,2)=-1.0
BEC(16,6)=1.0
BEC(16,7)=-1.0
BEC(17,3)=-1.0
BEC(17,4)=1.0
BEC(17,8)=-1.0
BEC(18,1)=-1.0
BEC(18,5)=1.0
BEC(18,9)=-1.0
BEC(19,3)=-1.0
BEC(19,5)=1.0
BEC(19,7)=1.0
BEC(20,1)=-1.0
BEC(20,6)=1.0
BEC(20,8)=1.0
BEC(21,2)=-1.0
BEC(21,4)=1.0
BEC(21,9)=1.0
BEC(22,2)=1.0
BEC(22,6)=-1.0
BEC(22,7)=-1.0
BEC(23,3)=1.0
BEC(23,4)=-1.0
BEC(23,8)=-1.0
BEC(24,1)=1.0
BEC(24,5)=-1.0
BEC(24,9)=-1.0
RETURN
END
```

```
      SUBROUTINE DET(G,DEL)
      REAL G(9),DEL
      DEL=G(1)*(G(5)*G(9)-G(6)*G(8))
     +  +G(2)*(G(6)*G(7)-G(4)*G(9))
     +  +G(3)*(G(4)*G(8)-G(7)*G(5))
      RETURN
      END
```

```
      SUBROUTINE ROT(P1,P2,P3,THETA,R)
      REAL P1,P2,P3,THETA,A5
      DIMENSION R(9)
      A5=1.0
      R(1)=P1*P1*(A5-COS(THETA))+COS(THETA)
      R(2)=P1*P2*(A5-COS(THETA))-P3*SIN(THETA)
      R(3)=P1*P3*(A5-COS(THETA))+P2*SIN(THETA)
      R(4)=P2*P1*(A5-COS(THETA))+P3*SIN(THETA)
      R(5)=P2*P2*(A5-COS(THETA))+COS(THETA)
      R(6)=P2*P3*(A5-COS(THETA))-P1*SIN(THETA)
      R(7)=P3*P1*(A5-COS(THETA))-P2*SIN(THETA)
      R(8)=P3*P2*(A5-COS(THETA))+P1*SIN(THETA)
      R(9)=P3*P3*(A5-COS(THETA))+COS(THETA)
      RETURN
      END
```

```
* The vectors must be normalised -
      SUBROUTINE NORM(X,Y,Z)
      REAL X,Y,Z,C
      C=SQRT(X*X+Y*Y+Z*Z)
      X=X/C
      Y=Y/C
      Z=Z/C
      RETURN
      END
```

```
      SUBROUTINE REEDI(I)
      INTEGER I
996   READ(*,*,ERR=999)I
      GOTO 998
999   WRITE(*,997)
997   FORMAT(19X,' Incorrect Input. Try again'/)
      GOTO 996
998   RETURN
```

```
      END
. . . . . .

. . . . . .
      SUBROUTINE TRY(I,A,J)
      IMPLICIT REAL(A-H,K-Z),INTEGER(I,J)
5     IF(I .EQ. 1)GOTO 1
      IF(I .EQ. 2)GOTO 20
      IF(I .EQ. 3)GOTO 30
      IF(I .EQ. 4) GOTO 40
      IF(I .EQ. 5) GOTO 50
1     IF(A .LE. 0.0 .OR. A .GE. 180.0) GOTO 2
      GOTO 3
20    IF(J .LT. 0 .OR. J .GT. 1)GOTO 2
      GOTO 3
30    IF(J .LT. 1 .OR. J .GT. 12) GOTO 2
      GOTO 3
40    IF(J .LT. 1 .OR. J .GT. 6) GOTO 2
      GOTO 3
50    IF(J .LT. 0 .OR. J .GT. 2) GOTO 2
      GOTO 3
2     WRITE(*,4)
4     FORMAT(/20X,'****** Incorrect input. Try again. ******'/)
      IF(I .EQ. 1)GOTO 10
      IF(I .GT. 1)GOTO 11
10    CALL REED(A)
      GOTO 5
11    CALL REEDI(J)
      GOTO 5
3     RETURN
      END
. . . . . .

. . . . . .
      SUBROUTINE REED(A)
      REAL A
996   READ(*,*,ERR=999)A
      GOTO 998
999   WRITE(*,997)
997   FORMAT(19X,' Incorrect Input. Try again'/)
      GOTO 996
998   RETURN
      END
. . . . . .
```